Fused Deposition of Ceramics:

A Comprehensive Experimental, Analytical and Computational Study of Material Behavior, Fabrication Process and Equipment Design

A Thesis

Submitted to the Faculty

of

Drexel University

by

Anna Bellini

in partial fulfillment of the

requirements for the degree

of

Doctor of Philosophy

September 2002

Dedications

To my wonderful parents:
my mother Vittoria
and
my father Alberto
...with love.

Acknowledgement

Many people have to be acknowledged for the completion of this thesis. First of all, many thanks go to Dr. Selçuk I Güçeri not only as a mentor and supervisor in the technical area, but also for his friendship, support and encouragement during all these years. His enthusiasm in his job and his love for research has always been stimulating even in the hardest moments.

Deep gratefulness goes to Dr. Mun Y. Choi, who has been a kind listener and an important source of suggestions; his dedication to students and his driving personality have always been encouraging.

I would also like to thank especially Dr. Yuri Gogotsi and Dr. Alan Lau, who have been very supporting respectively in the first and in the last part of this research. They have guided me in the most difficult parts of the project, both reassuring me as well as urging me to keep focus.

I would like to extend my appreciation to the other members of my doctoral committee: Dr. Wei Sun who has shown great interest in the project and with whom I really wish to collaborate in the future; Dr. Giuseppe R. Palmese for his availability and quiet support.

I also would like to thank Defense Advanced Research Projects Agency (DARPA) and Office of Naval Research (ONR), especially Dr. Ralph Wachter, for the funding provided during the course of the study and for the interest they had always shown in the developments of the project. This work was supported by the DoD

Multidisciplinary University Research Initiative (MURI) program administered by the Office of Naval Research under Grant N00014-96-1-1175.

Many constructive discussions with other MURI team members, notable with Drs Danforth, Safari and Jafari of Rutgers University and Dr. Chou of University of Delaware, are also acknowledged.

Very special thanks go to Wilma and Carlo Geneletti, Gaurav Bajpai and Nick Gialias for their kind love and friendship, which enriched my life outside the laboratory. Their presence and our talks have reduced the nostalgia of my family.

I am sincerely thankful to my friends, Daniel Norlen, Almila and Yigit Yazicioglu, Stefan Pettersson, Andrea Irrera, Lauren Shor, Carl Imhauser, Dave Lenhert, Ahmet Yozgatligil, Stacie Ringleb, Jhonatan Thomas, Simon Chung, Murat Aktas, Chris Kennedy, John Thinnes and many others for their love and respect.

I would like to give a particular thank to Uno Thörnborg who especially in the last months have been extremely supportive and patient.

Special thanks go to my parents, for their patience, understanding and love as well as for their keen criticisms and spurs that have been so important for the success of this work.

Table of Contents

List of Tables

List of Figures

Abstract

Fused Deposition of Ceramics:
A Comprehensive Experimental, Analytical and Computational Study of
Material Behavior, Fabrication Process and Equipment Design
Anna Bellini
Selçuk I. Güçeri, PhD

Customer-driven product customization and continued demand for cost and time savings have generated a renewed interest in agile manufacturing based on improvements on Rapid Prototyping (RP) technologies. The advantages of RP technologies are: 1. ability to shorten the product design and development time, 2. suitability for automation and decrease in the level of human intervention, 3. ability to build many geometrically complex shapes.

A shift from "prototyping" to "manufacturing" necessitates the following improvements:

- Flexibility in choice of materials;
- Part integrity and built-in characteristics to meet performance requirements;
- Dimensional stability and tolerances;
- Improved surface finish.

A project funded by ONR has been undertaken to develop an agile manufacturing technology for fabrication of ceramic and multi-component parts to meet various needs of the Navy, such as transducers, etc. The project is based on adaptation of a layered manufacturing concept since the program required that the new technology be developed based on a commercially available RP technology.

Among various RP technologies available today, Fused Deposition Modeling (FDM) has been identified as the focus of this research because of its potential versatility in the choice of materials and deposition configuration. This innovative approach allows for designing and implementing highly complex internal architectures into parts through deposition of different materials in a variety of configurations in such a way that the finished product exhibit characteristics to meet the performance requirements. This implies that, in principle, one can tailor-make the assemble of materials and structures as per specifications of an optimum design.

The program objectives can be achieved only through accurate process modeling and modeling of material behavior. Oftentimes, process modeling is based on some type of computational approach where as modeling of material behavior is based on extensive experimental investigations. Studies are conducted in the following categories:

- Flow modeling during extrusion and deposition;
- Thermal modeling;
- Flow control during deposition;
- Product characterization and property determination for dimensional analysis;
- Development of a novel technology based on a mini-extrusion system.

Studies in each of these stages have involved experimental as well as analytical approaches to develop a comprehensive modeling.

CHAPTER 1: INTRODUCTION

Layered Manufacturing (LM) introduced a nearly unique way of producing prototypes, tooling and functional parts by integrating the computer technology with the manufacturing hardware. The fundamental paradigm of production is to break down the complicated three-dimensional geometry into building blocks that may have several levels of organization. Typically, three-dimensional objects are reduced to a collection of two-dimensional planar slices, which may or may not be further divided into curvilinear streaks or droplets. Hardware developed for layered manufacturing is capable of producing these unit geometries rapidly. Computer automation of the LM equipment enables the production and assembly of unit geometries repetitively to produce the three-dimensional geometry [42].

In Fused Deposition (FD), specifically, every slice is built as an assembly of filaments of thermoplastic material. Objective of the current project is to extend this technology to fabrication of ceramic, metallic and even components that have composite material architectures by utilizing feed filaments that are filled with particles of corresponding materials.

The system builds the part by extruding a bead of semi-molten thermoplastic material, from a computer-controlled nozzle and depositing it on a workspace. Since a typical FD part contains hundreds of *road* segments each, a typical engineering object may contain tens of thousands of discrete units to make up the entire part. Consequently the connectivity of the building blocks (the *roads*) is of significance since these are the trace of the manufacturing sequence of the part. Moreover, the bonds between the roads

are strictly depending on their cross-sectional shapes (i.e. round shapes will lead to a one point contact, while square shapes will result in a more desirable line contact).

Since during the process each point is exposed to the influence of the heated depositing nozzle multiple times, the material properties in the work volume change during the production. In particular, changes in temperature, viscosity, mass and boundary conditions, cause a continuous evolution of the shape of the deposited roads during the process.

Because of the importance of the single road and of its stackable property, the main focus of this research has been on the process modeling and experimentation of the extrusion, deposition, thus formation of the road of material. Since these roads are the fundamental building blocks of the process, the final quality and performances of the built product are strictly dependent on their sizes, formation and evolution.

1.1 Motivation

The increasing demand of customized products with more complex designs and smaller feature, raise the interest in the application of the Solid Freeform Fabrication (SFF) techniques, generally used for rapid prototyping purposes, as technology for fabrication of the final product. Moreover, the specific characteristics of fused deposition (FD), such as:

- The capability of depositing different materials in the same layer, according to complex architecture;
- The possibility of remote controlled process;

- The use of small building blocks, i.e. *roads,* which can be combined in several toolpaths providing the ability of building any complex shape starting from a computer file;

made the FD technique an appealing alternative to traditional manufacturing processes.

However, since it was developed for rapid prototyping applications, the technology used in FD needs to be improved in order to satisfy the more restrictive manufacturing requirements, such as dimensional stability, tolerances and product performance. Consequently important scientific and engineering issues need to be addressed before considering FD for the fabrication of products for final use. Among these issues there are:

- Improved integrity, hence performance, of the part;
- Increased flexibility in material selection;
- Improved the surface finish and quality.

Giving the opportunity of tailor-making products with performance, complex characteristics through the deposition of several materials in composite structures, FD reduces the limitations common to the use of monolithic materials in manufacturing. As the technology develops further, the strong coupling between fabrication and part configuration, as well as the flexibility that will become available, are expected to lead to new design paradigms.

1.2 Contribution of the thesis

In order to enhance the performance of fused deposition (FD) technology for direct manufacturing, the study presented in this thesis was focused on process modeling. Research reported in this dissertation has focused in the following studies with the aim of developing a complete and realistic model:

- Characterization of material and process behavior through *experimental testing* and development of empirical relations;
- Development of *process analysis and simulation tools*, which are in terms of complex differential equations that require numerical solution.

As result of these studies, models were developed to provide:

- Guideline to engineer the product and consequently predict performances of the part;
- Control functions for equipment operation and intelligent fabrication;
- Flexibility for different material system and part configurations;
- Guidelines to significantly improve part quality.

Using these models as an integral part of the process planning is expected to accomplish much needed improvements for product quality and performance to meet the manufacturing requirement.

Moreover, a new equipment design, which was developed as part of the efforts to broad the choice of material selection, opens up the applicability of FD in fields not

possible before. Eliminating the filament feeding system, the novel micro-extruder design brings to FD the necessary flexibility to be considered as a realistic alternative to traditional manufacturing technologies.

1.3 Organization of the thesis

The rest of the thesis is organized as follows. In order to provide an easier and streamlined reading of the thesis, each chapter was written as a self-standing paper, that presents its own abstract, introduction and conclusion.

Chapter 2 presents description of fused deposition modeling (FDM) and fused deposition of ceramics (FDC) processes in order to give an insight of the characteristic of the techniques that have been studied.

In chapter 3 the study accomplished to determine the mechanisms that affect the evolution of road shape is presented. Consequently the model developed, based on the experimental data, to control the mentioned mechanisms is extensively described.

In chapter 4 the experiments performed to investigate the relation between hardware design, i.e. nozzle, and road shape are incorporated. Moreover, the model that was developed, based on the experimental data, to predict the road shape is described and the conducted parametric study is presented.

Chapter 5 discusses the analysis of liquefier dynamics towards establishing strategies for flow control during the extrusion phase. It will be shown that improvements in the control of the evolution of the road will reduce the defects typical of parts built in FD.

In chapter 6 the investigation of the relation between mechanical performance of the part and building orientation is explained in order to emphasize the need of an extensive process planning before going to manufacture the final product.

In chapter 7 a description of a novel system developed as part of the effort to improve the flexibility of material selection is described. Experimental data to study the influence of process and material parameters is incorporated as well.

Chapter 8 presents a comprehensive summary, emphasizing the achievements obtained in this study in order to bring FD to the level of maturity needed to consider it as a new manufacturing process.

CHAPTER 2: PROCESS OVERVIEW

The objective of this project, supported by ONR under the MURI program was to develop an agile manufacturing technology for fabrication of ceramic and other multi-component parts.

The project was required to be based on adaptation of a commercially available Layered Manufacturing technology, in order to take advantages of the fact that:

1. They typically are additive processes, so there is a minimum waste of bulk material;
2. The development time for building a product is short compare to subtractive technique, like CNC machining;
3. They are automatic processes, hence they require a minimum human intervention;
4. They can be controlled remotely;
5. They have the ability of building any object starting from a computer file.

Among all the available techniques, Fused Deposition Modeling (FDM) process was chosen because of its capability to build any complex shape, with any complex structure, with theoretically any material.

In order to give an insight of the developing world of solid freeform fabrication techniques, a brief overview of the many existing forms of Layered Manufacturing processes is given in section 2.1. Section 2.2 is dedicated more specifically to the

description of FDM, while section 2.3 introduces the Fused Deposition of Ceramics (FDC) process, which was developed as part of this MURI project.

2.1 Layered manufacturing techniques

Rapid prototyping (RP) and solid freeform fabrication (SFF) techniques offer an alternative route of computer automation for mechanical component fabrication. Physical RP builds tangible objects from computer data without the need of jigs or fixtures or NC programming. In this technology, also called layer manufacturing (LM), or material addition manufacturing, the computer analyses the 3D CAD model and slices it into cross sections. The cross sections are recreated by adding raw material either in form of solid sheet or through the solidification of liquids and/or powders. A distinct advantage of creating a part layer-by-layer is that it allows for building complex shapes that would be virtually impossible to machine (i.e. with a CNC machine), in addition to the more simple design [11].

There are a large number of LM processes currently available. Since the development of many of these technologies occurred simultaneously, there are numerous similarities as well as differences between them [37]. While there are many ways in which one can classify the numerous RP systems in the market, one of the best ways is to classify RP systems broadly by the initial form of its material.

In this manner, all RP technologies can be categorized into: (1) liquid-based, (2) solid-based (solid sheet) and (3) powder –based [33]. Detailed reviews of the processes of some basic technologies are reported below in Figure 2.1.

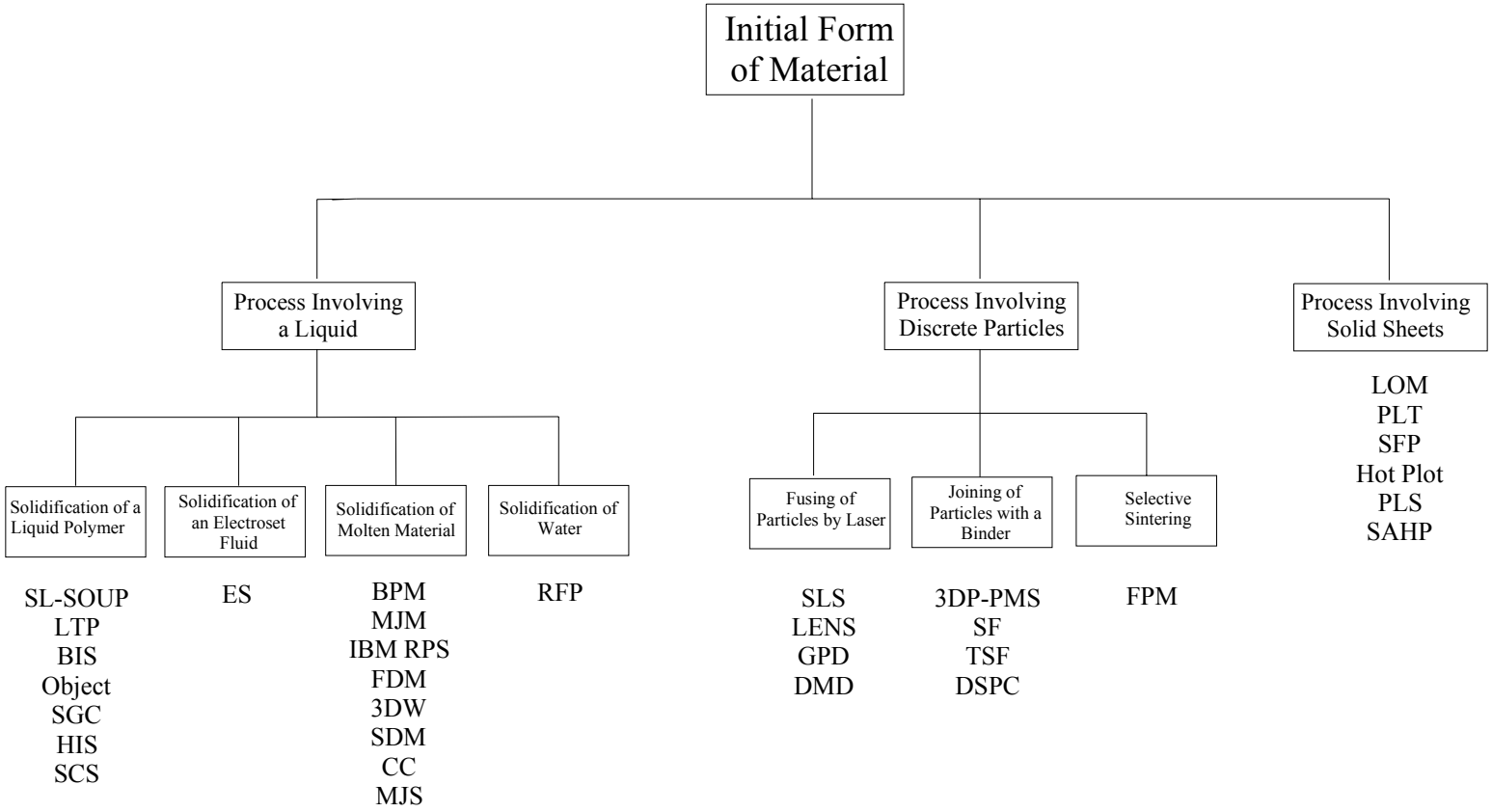

Figure 2.1: Diagram of RP techniques available today

2.1.1 Liquid-based

Liquid-based processes entail the solidification of a resin on contact with a laser, the solidification of an electrostatic fluid, or the melting, thus subsequent solidification, of the prototype material [50].

2.1.1.1 Stereolithography (SL)

Stereolithography, developed by C. Hull in 3D System, was the first RP process to reach the market in 1987. This was in the same time frame when the development of *solid modeling* in the CAD industry allowed to produce true three-dimensional objects in electronic format. Thus it became possible to assign material properties, such as mass and density, to a solid model, represented no more by wireframes and surfaces, but by an enclosed volume.

SL process relies on photosensitive liquid resin which polymerize when expose to ultraviolet (UV) light. Thanks to the light energy, which acts like a catalyst, during the polymerization phase small molecules (monomers) link to larger chain molecules (polymers). The result is then a solid cross-link polymer. Due to the absorption and scattering of the beam, this reaction takes place only near the surface and produces voxels which are characterized by their horizontal line-width and vertical cure depth.

The process start with a solid model in CAD format and proceeds transforming it into a standard STL file. The control unit then slices the model in a series of cross sections (from 0.1 to 0.5 mm thick) and creates the tool-path for each section. The motion commands are thus sent to the SL machine, which consist of (1) a platform mounted in a

vat of resin, (2) a UV Helium-Cadium or Argon ion laser (see Figure 2.2). The computer-controlled optical scanning system directs the focused beam so that it solidifies the 2-dimensional cross-section corresponding to the slice. Once the scanned layer has solidified, the platform is lowered enough to cover the part with another layer of liquid resin. A leveling wiper moves across the surfaces so that exactly one layer thickness remains above the part. The laser then draws the next layer. This procedure continues until when the part is completely built.

The advantages of SLA are that (1) it yields a surface finish comparable to that of numerical controlled milling; (2) it is a well proven system; (3) it has an accuracy of $\pm 100 \mu m$ and it can achieve layers of 25 μm thick.

The disadvantages are that (1) the material is expensive and toxic and it must be shielded from light to avoid premature polymerization; (2) there is only a limited choice of resins; (3) the part may be brittle and they need supports which may affect the surface finish when removed; (4) changing the resin in the vat is a lengthy and costly procedure.

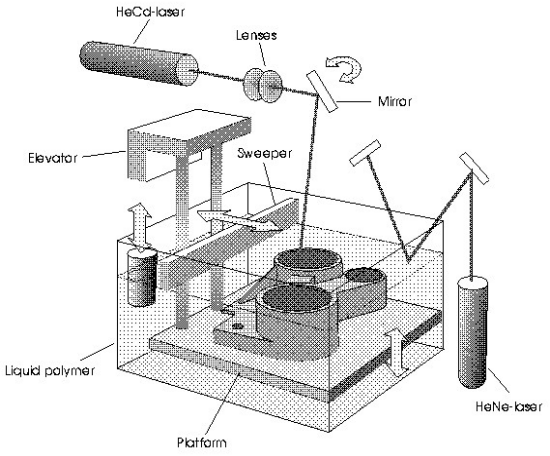

Figure 2.2: Stereolitography process

2.1.1.2 Multi-phase jet solidification (MJS)

The multi-phase jet solidification (Figure 2.3), developed in Germany by Fraunhofer-Gessellschaft, is a process able to produce metallic or ceramic parts. It uses low-melting point alloys or powder-binder mixtures, which is squeezed out through a computer-controlled nozzle to build the part layer by layer [33]. The process constitutes of 2 phases: data preparation and model building. During the data preparation the CAD model is sliced in layers of uniform thickness. This information together with the process parameters, such as machining speed and material flow, are thus sent to the controller of the machine. During the building phase the material is heated up beyond its solidification point in a chamber. Then it is squeezed through a computer-controlled nozzle by the use of a pumping system. The material solidify when it get in contact with the platform or with the previous generated “roads”. Because of the contact with the liquefied material, the top layer is subjected to a partial remelting, which leads to a good bonding with the new layer. Once a layer is finished, the extrusion jet moves up in the z-direction of exactly the same amount of one layer thickness. The most important advantage of MJS is mainly the fact it can produce high-density metallic and ceramic parts [62]. However, the biggest disadvantage of this process is its discontinuity. The chamber must be filled, usually with cartridges, before the beginning of the process and must contain enough material to complete the part.

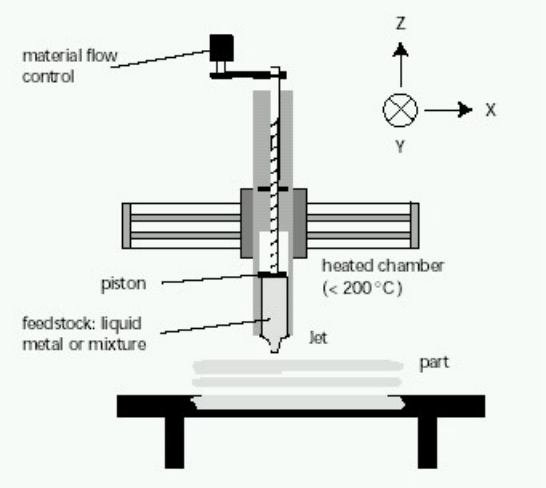

Figure 2.3: Principle of the MJS process

2.1.1.3 Ballistic particles manufacturing (BPM)

Ballistic Particle Manufacturing (Figure 2.4), developed in 1995 by BPM Technology, can be considered the pioneers of ink-jet based, office-friendly RP systems. It indeed uses non toxic material and its system is extremely compact.

The process consists in ejecting a stream of molten material from a nozzle. During the ejection, the material separates into droplets, which hit the substrate and immediately cold weld to form the part. In order to maintain a continuous jet, the nozzle is excited by a piezoelectric transducer at a frequency of about 60 Hz. With this mechanism is possible to insure regular droplets with uniform spacing and distance. Furthermore, the use of the piezoelectric system allows the user to control the size of the drops, their velocity and the spacing between consecutive drops just adjusting the frequency and the wave of the perturbation. When the drop leaves the nozzle, it is electrostatically charged. Applying a

difference in voltage between the nozzle and the substrate it is thus possible to control the deposition of the same drop. The quality of the part strictly depends on the speed of the jet and the temperature of deposition. For example if the jet is moving too slow, the placement accuracy will be poor, if it moves too fast the droplet will be deformed on impact.

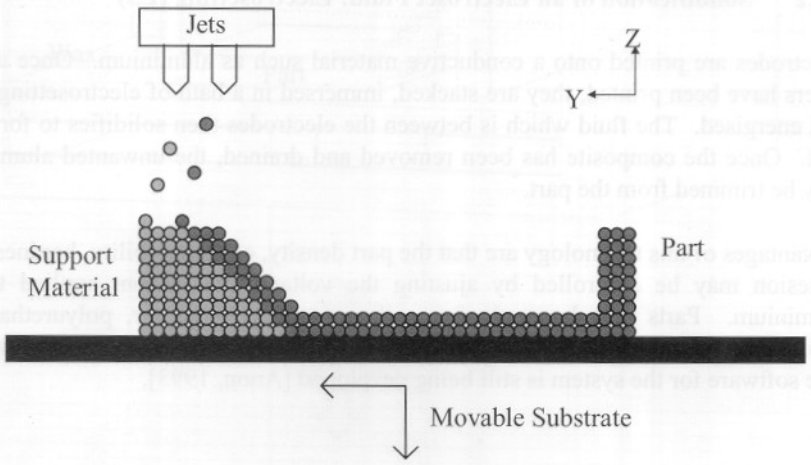

Figure 2.4: Ballistic particle manufacturing process

2.1.2 Solid-based

Those processes which use solid-based materials, bond together solid-sheets with a laser or with an adhesive.

2.1.2.1 Laminated object manufacturing

LOM, which has been developed and commercialized by Helysis, is a RP technique which produces three-dimensional models with foils of paper, plastic or composites (see Figure 2.5). It can be considered a hybrid between subtractive and

additive processes: the models are indeed built up with layers (like additive processes), but each layer is individually cut by a laser (subtractive process) in the shape of the cross section of the part [11].

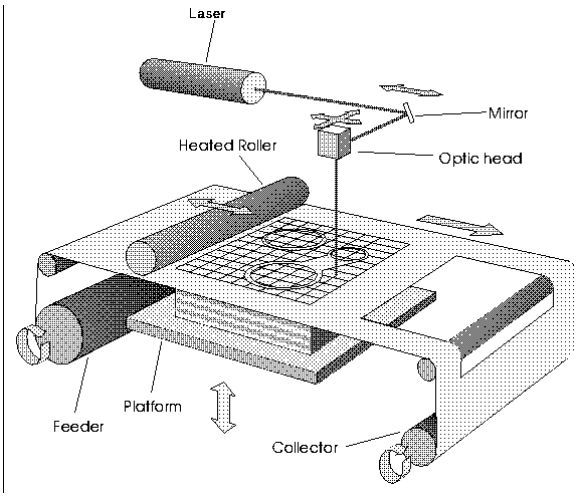

Figure 2.5: Laminated object manufacturing

The paper is unwound from a feed roll onto the stack and bonded to the previous layer using a heated roller, which melts a plastic coating on the bottom side of the paper. The profiles are then traced by an optics system that is mounted to an X-Y stage [25]. Unwanted material is trimmed into rectangles to facilitate its later removal but remains in place during the build to act as supports [50]. The sheets of papers are wider than the part itself, so that when a slice is created its edges remain intact. After lowering the part, the roll of material can be advanced by winding the excess edges onto a second roller, thus the whole process can be repeated. Once the part is made, it should be sealed by the use

of epoxy resin spray or silicon fluid, in order to prevent later distortion through water absorption.

Variations on this method have been developed by many companies and research groups. Kira's Paper Lamination Technology (PLT) uses a knife to cut each layer instead of a laser and applies adhesive to bond layers using the xerographic process. There are also variations which seek to increase speed and/or material versatility by cutting the edges of thick layers diagonally to avoid stair stepping.

The advantages of this technique are (1) the wide range of cheap materials, such as paper, plastic or fiber-reinforced glass ceramic; (2) dimensions of the part, that can be consider large compared to the products of other RP techniques; (3) the speed which is 5-10 times grater than in other processes.

The drawback is the difficulties encountered in removing the extra material. This leads to serious problems with undercuts and reentrant features. Another important disadvantage is the need of a controlled environment filled with inert gas estinguishers because of fire hazards.

2.1.2.2 Hot plot (HP)

Sparx AB of Molndal, Sweden, introduced and commercialized Hot Plot technology, a RP system very similar to LOM. Even if it was the least expensive commercial system, it required a considerable amount of operator assistance. For this reason it never really became successful. The machine consists of a flat-bed plotter equipped with a heated cutting elecrode and a mounting fixture.

The process begins with the mathematical generation of cross-sectional data from the three-dimensional CAD model. Next a polystyrene sheet material, previously coated with pressure sensitive adhesive and backed by removable foil, is *manually* positioned on the plotter bed. The electrode cuts the outline of the cross-section, then the operator picks up the sheet representing the layer and affixes it on a mounting fixture. The foil backing is peeled off to expose adhesive for the next layer. Excess material is manually removed from the plotter bed to accommodate the next sheet.

This system is best suited for visual modeling than for manufacturing, because of the thickness (0.04 in) of the layer and its poor mechanical properties [26].

2.1.2.3 Selective adhesive and hot press

The Kira Solid Center system consists of a PC, a photocopy printer, a paper alignment mechanism, a hot press and a mechanical cutter plotter. The SAHP process includes six steps (see Figure 2.6): generating a model and printing resin powder, hot pressing, cutting the contour, completing block, removing excess material and post processing.

- Firstly the computer generates a layer and then the resin powder (like a toner) is applied on a sheet of paper using a typical laser stream printer.
- Secondly, a sheet alignment mechanism adjusted the printed sheet onto the previous layer. A hot press moves on top of the new layer so to melt the toner, which adheres the sheet together. It must be noticed that the hot press also flattens the top surface and prevents the formation of bubbles.

- Thirdly, the PC commands a mechanical cutter to move along the contour of the section in order to cut the top layer.

The three steps are repeated until when the part is done. When printing, hot pressing and cutting are completed, the model block is removed and unnecessary portions of the paper are disconnected quickly.

It has been shown that the tensile and bending strength of the composite material made by SAHP process is approximately one-half that of wooden (LOM) models. However the final product does not reach the necessary mechanical properties for manufacturing, thus it is used mostly for visualization [33].

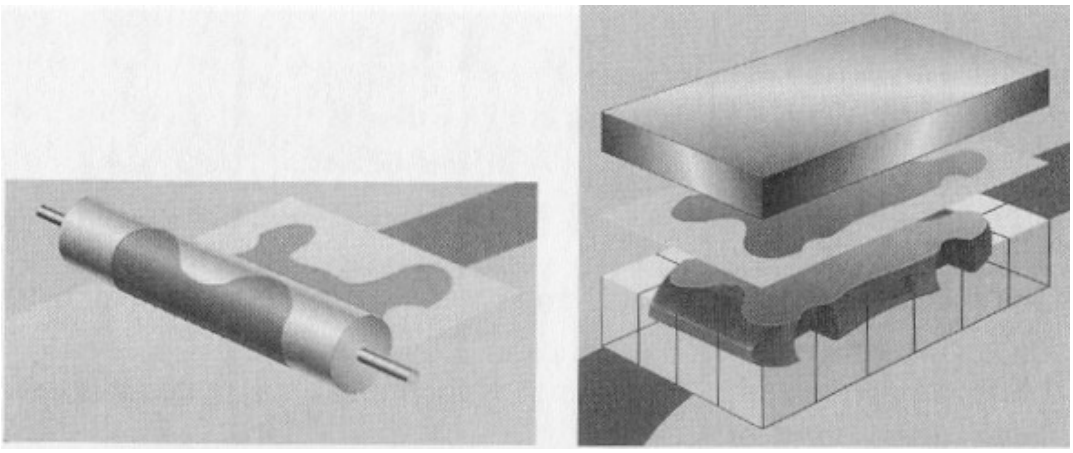

Printing of toner

Hot pressing

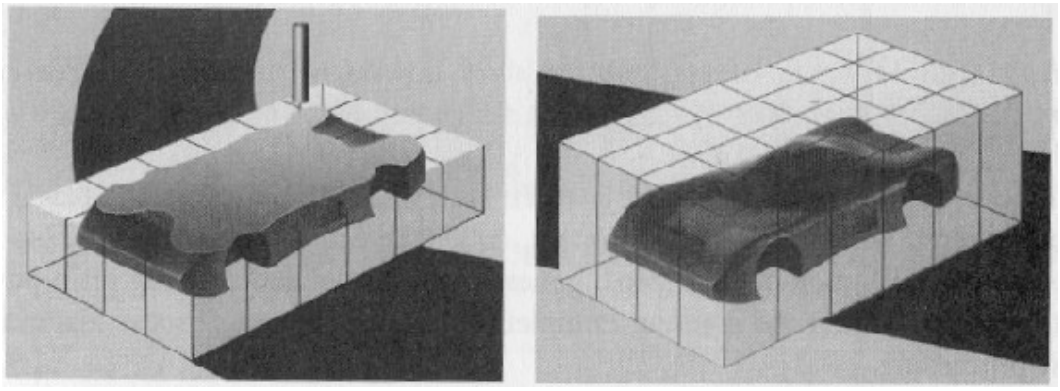

Cutting the contour

Completing the block

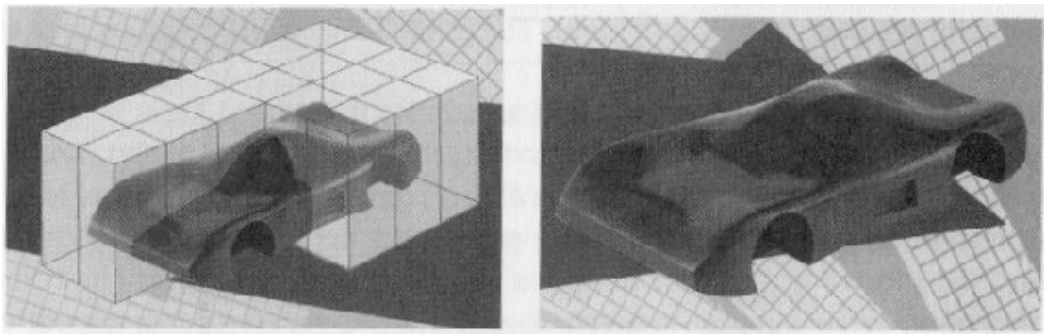

Removal of excess material

Post processing

Figure 2.6: Selective adhesive and hot press process

2.1.3 Powder-based

In the strict sense, powder is definitely in the solid state. However it is created as a category because of the importance, for some technologies, of the grain-like form material. These processes aggregate the powders with a laser or by the selective application of binding agents.

2.1.3.1 Selective laser sintering

SLS, developed by the University of Texas and commercialized by DTM in 1987, is a RP technique that uses fine powders as a build media. The powder is fused together by a powerful carbon dioxide laser.

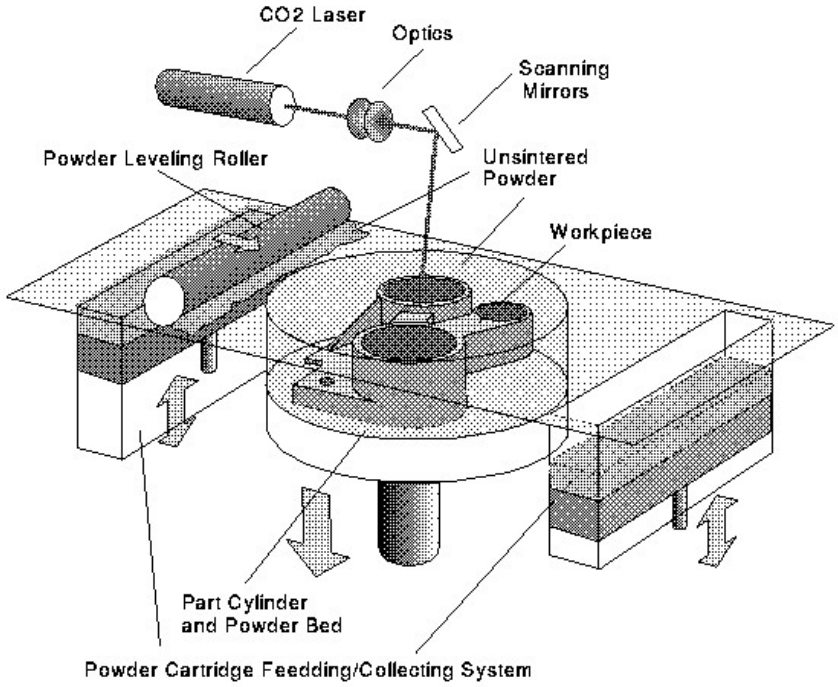

Figure 2.7: Selective laser sintering process

The process starts heating up the entire power bed (see Figure 2.7), in order to minimize thermal distortion and facilitate fusion to the previous layer.

With the build piston on the top, a thin layer of powder is spread across the build area by a roller/sweeper from one of the feed pistons. The computer-controlled laser draws the desired tool-path, thus builds one layer by curing the powder. The piston is than lower and more powder is deposited. The process is repeated until when the part is completed. At this point the part is moved to the Break Out Station (BOS) where the extra powder is manually removed with brushes.

The advantages of this technique are (1) the wide range of build materials, (2) the high throughput capability, (3) self-supporting build envelope. However the disadvantages are (1) the high initial and maintenance cost, (2) the need of peripherals, such as BOS table, air handler and sifter (to filter the dust particles from the area).

2.1.3.2 Laser engineering net shaping and direct metal deposition

The LENS process, developed by Sandia National Laboratories and commercialized by Optomec Design Co. in 1997, is an RP technique capable of creating fully dense metal or cermet parts by fusing powders within the focal zone of a laser beam. Like all RP processes, LENS also incorporates an additive building process. The high-powered laser beam (see Figure 2.8) is focused onto a substrate where metallic powder is injected under computer guidance [27], [50]. Once a layer is built, the stage is lowered in order to prepare the process for the next layer.

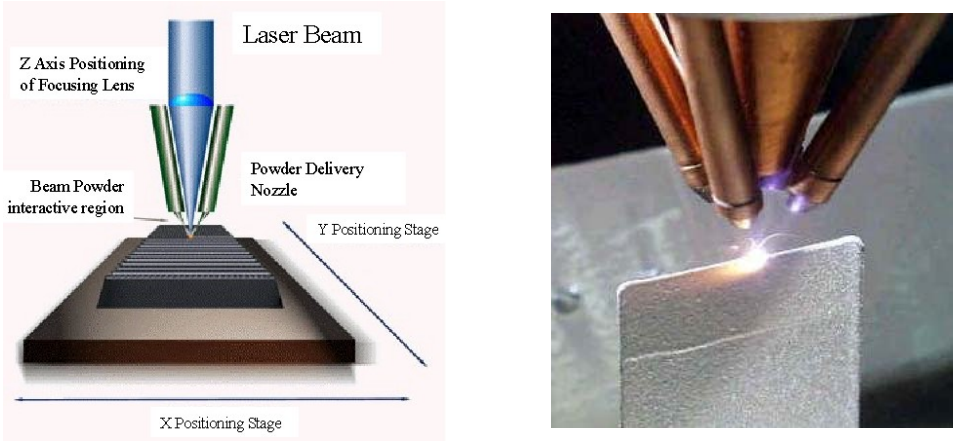

Figure 2.8: LENS process (courtesy of Optomec Design Co)

As the focus of the laser moves, rapid solidification occurs creating a fully dense material. All of this occurs within a build chamber that maintains an inert atmosphere. Additionally, powder that is not consumed by a layer may be recovered and used again. Due to the rapid solidification superior strength and ductility are achieved.

The advantage of the LENS process is that it allows for the creation of a fully dense component fabricated from the powder of a single material with no further heat treating; this is quite unique in the field of RP. Furthermore, it offers the ability to use varying compositions of powder (i.e. metal particles mixed with ceramic particles) hence allowing us to create cermets, multi-metal, and gradient materials. Hence, you can produce a part with varying materials and properties in order to meet the requirements of a specific application, such as die cast tooling.

In 2000 Precision Optical Manufacturing (POM) in Michigan patented a closed-loop optical feedback system for the LENS process (see Figure 2.9) [35]. With this optical feedback the process can be continuously controlled and optimized.

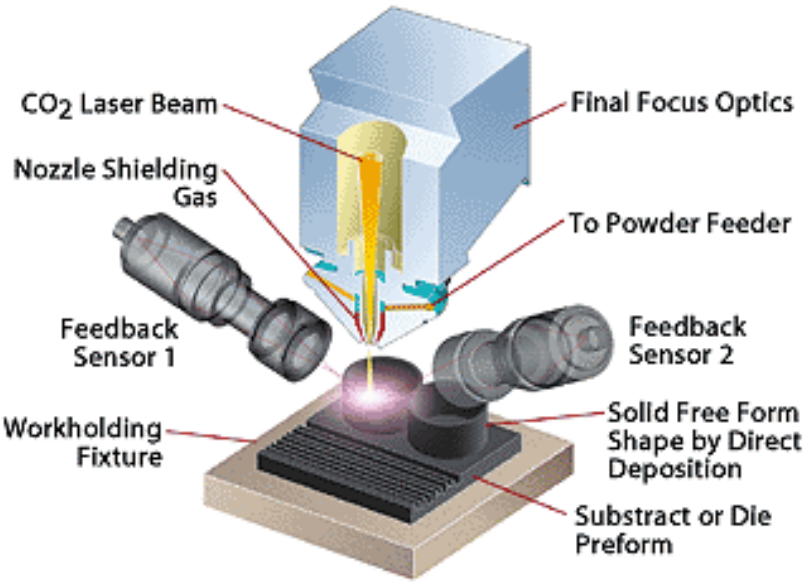

Figure 2.9: DMD process (courtesy of Precision Optical Manufacturing)

2.1.3.3 3D printer and ProMetal system

In the 3D printer process, developed by MIT and commercialized by Z Corporation in 1994, layers of powders are applied to a substrate and subsequently joined together applying a binder sprayed through a nozzle (see Figure 2.10). The part is built in the layer by layer fashion, thus after every layer, the piston is lowered and new powder is added. After building the part, the excess powder, which was supporting the model, is removed. In order to remove the powder captured inside the model, parts need to include a hole.

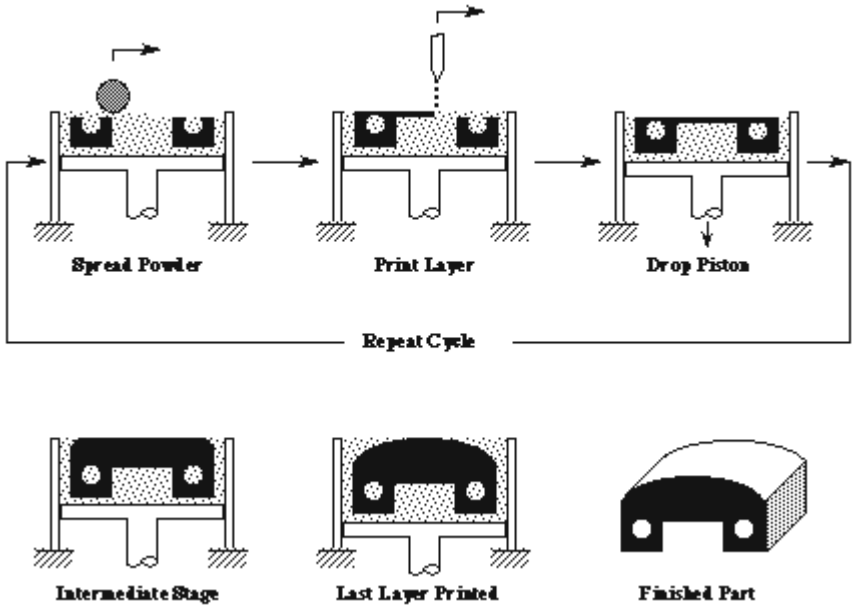

Figure 2.10: 3DP process (courtesy of MIT)

2.2 Overview of FDM

FDM, developed in 1989 and marketed in 1990 by Stratasys Inc., is the second most widely used rapid prototyping technology today, after stereolithography. In FDM a plastic filament is unwound from a coil and is fed into a liquefier where it is melted. The solid portion of the incoming filament serves as a "plunger" to extrude the material through a nozzle.

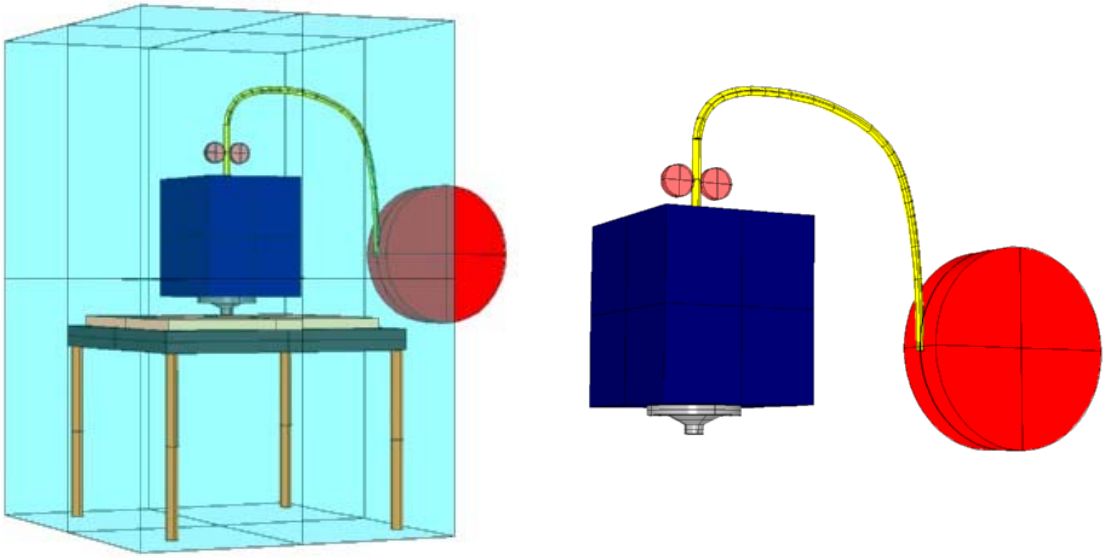

(a) FDM Hardware Architecture (b) Feeding system

Figure 2.11: FDM hardware

The nozzle is mounted to a mechanical stage, which can be moved in the *xy* plane. As the nozzle is moved over the table in a prespecified configuration, it deposits a thin bead of extruded plastic to form a road. Stocking of roads side-by-side in a rastering configuration produces each layer (see Figure 2.12). The polymer hardens immediately after being extruded through the nozzle and bonds to the layer below. Once a layer is

built, the platform is lowered in the *z* direction in order to prepare the workstation for the next layer.

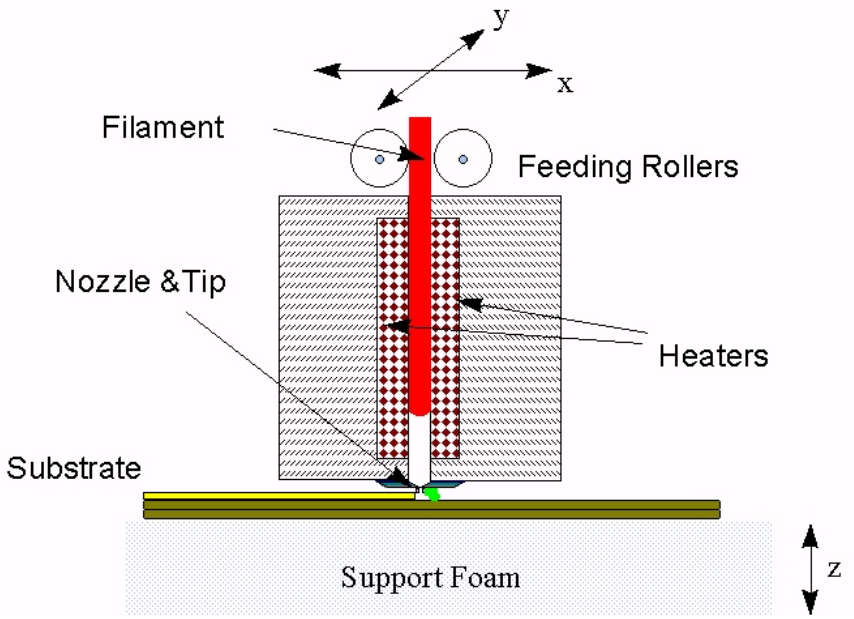

Figure 2.12: FDM material deposition system

The entire system is contained within a chamber (see Figure 2.11), which provides a temperature controlled environment with temperatures just below the melting point of the polymer. This allows the layers to bind together more effectively.

Several materials are commercially available for this process including ABS and investment casting wax. ABS offers good strength, and more recently polycarbonate and polysulfone materials have been introduced which extend the capabilities of the method further in terms of strength and temperature range. Support structures are fabricated for overhanging geometries and are later removed by breaking them away from the object. A water-soluble support material, which can simply be washed away, is also available.

The method is office friendly and quiet (see Figure 2.13). FDM is fairly fast for small parts on the order of a few cubic inches, or those that have tall, thin form-factors. It can be very time consuming for parts with wide cross sections, however.

Figure 2.13: Stratasys 1650 FDM machine

2.3 Overview of FDC

The process of Fused Deposition of Ceramics, developed at Rutgers University by S. C. Danforth *et. al.* [14], is similar to the FDM technique. The main difference consists in the feedstock material.

To produce the final products using Layered Manufacturing, S.C. Danforth *et al.* developed the idea of substituting the commercial feed material, i.e. the filament, with a thermoplastic filament loaded with ceramic powder (see Figure 2.14).

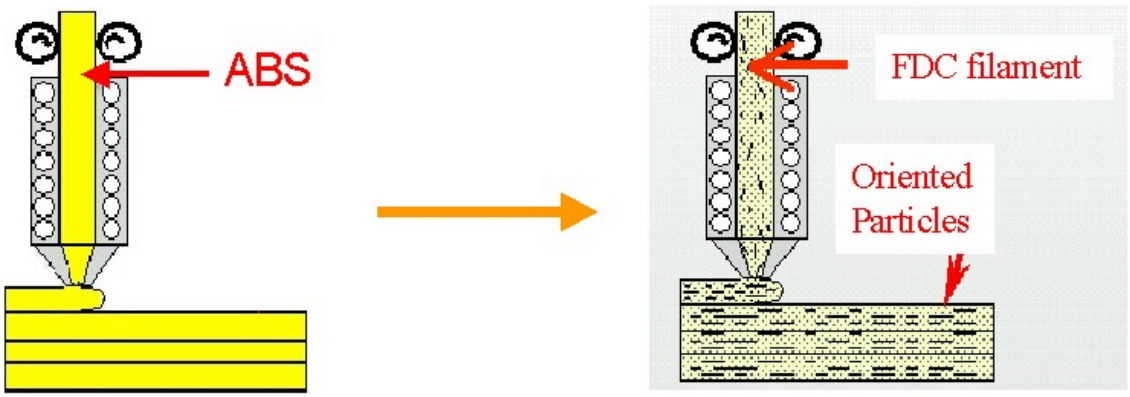

Figure 2.14: From FDM to FDC

Similar to the FDM process, the filament is mechanically driven into a liquefier, where the binder melts and flows through a nozzle. During this process the ceramic powder, dispersed in the binder, is forced to follow the streamline of the flow, thus is deposited on the substrate. Once the "green body" is built, the part goes through a binder removal phase where the thermoplastic binder material disintegrates and is removed. At this stage, the part, constituted by powder of ceramic, becomes very fragile. In order to obtain a dense object with the desired mechanical properties, the brown body is thus moved to the sintering phase, where the application of heat dandifies the powder into a cohesive mass (see Figure 2.15).

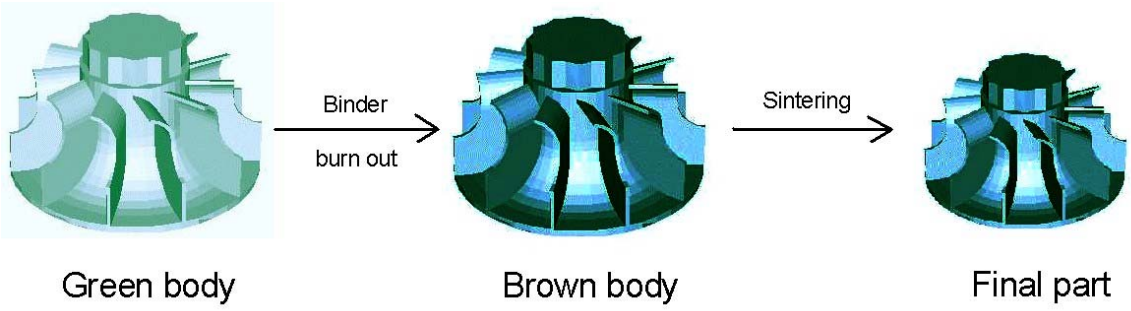

Figure 2.15: Post process phases in FDC

CHAPTER 3: COMPUTATIONAL-SIMULATION OF THERMO FLUID BEHAVIOR IN FDC

3.1 Abstract

Fused deposition of ceramics (FDC) is an evolution of fused deposition modeling (FDM) process (see sections 2.2 and 2.3). As such, it is part of the Layered Manufacturing (LM) technologies, where the part is built in layers. While most of the previous LM technologies focused on building "prototypes" many recent approaches, including the current project, try to achieve an agile fabrication technology to produce the final product directly.

In FDC, parts are fabricated by stacking layers each of which is produced using roads in a configuration rastering cross sectional surfaces that are obtained by slicing 3-dimensioanl solid models. As it was explained in section 2.3, unlike in rapid prototyping applications, "roads" are formed by extruding a mixture of the ceramic particles and a thermoplastic carrier/binder.

Once a part is fabricated using this particle-binder mixture, subsequent binder removal and sintering steps result in the finished product (see Figure 2.15). Since parts are fabricated on an "evolutionary" fashion road-by-road and layer-by-layer, the part integrity of the finished product greatly depends on the void formation and inter road, inter layer bonding during manufacturing. Presence of voids and/or poor inter-layer and inter-road bonding parameters result in undesirable mechanical performance characteristics and cracks in the finished part, mainly due to exposure to high temperature thermal cycles.

The aim of the study presented in this chapter is to determine the parameters that affect the characteristics (i.e. shape, temperature, viscosity etc.) during road deposition and formation of layers. Once these mechanisms are known, it will be possible to actively control and optimize the most influencing parameters in order to enhance the quality of the built part.

3.2 Introduction

In fused deposition process the feed material that undergoes twice through phase transition is subjected to very complex thermal and flow boundary conditions that continually affect and alter its thermo fluid dynamic state.

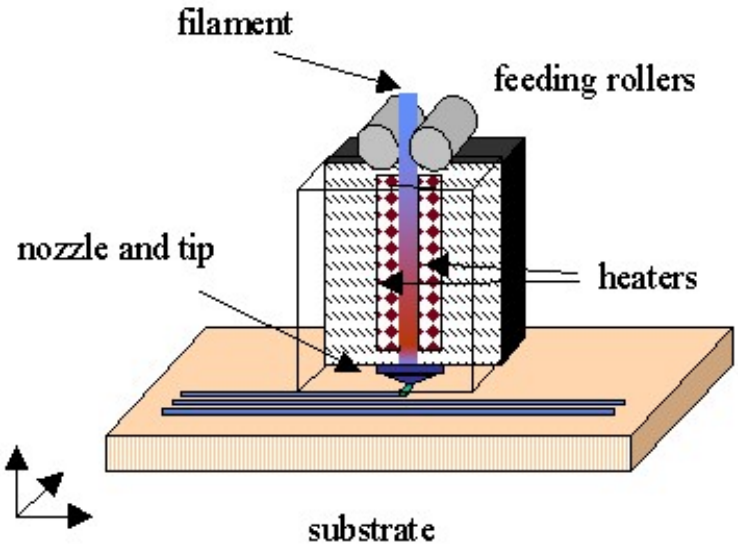

Figure 3.1: Schematic of the FD process

In the very first step the material is in solid state in the form of a filament that can be easily wounded and stocked in the back of the working volume (see Figure 2.11(a)). This assures continuity, thus automation to the process.

Then the filament is mechanically pushed into the *liquefier* where it melts with the application of heat generated by a current-carrying coil wrapped around the metallic chamber (see Figure 3.1). The melt, subjected to the pressure applied by the incoming material, is consequently extruded through the *nozzle.* Because of the adhesion of the material to the walls, the velocity field of the melt has a parabolic profile (fully developed flow). Furthermore, because of the small area of the orifice of the nozzle, the velocity distribution presents a large gradient in the radial direction. At the exit of the nozzle, where no forces are applied, the flow quickly assumes the conditions typical of a plug flow causing a radial expansion of the melt (the so called swelling phenomenon).

The second phase transition takes place when the extruded thermoplastic material touches the platform and quickly solidifies according to the temperature and the thermal conductivities properties of the substrate. Because of the different thermal boundary conditions, such as different thermal inertia of the substrate, it was observed that the evolution of roads in the *first deposited layer* considerably differs from *layers deposited successively* [64].

From these observations it is evident that to assure the quality of the final product, it is important to monitor and possibly control the thermal fluid dynamic state of the material at any stage of the process. For this reason in the current study the entire process has been ideally divided in five consecutive regions/steps:

1. Melt flow in the liquefier;
2. Extrusion through the nozzle;
3. Free extrusion and swelling of the melt at the exit of the nozzle;

4. Evolution of the road in the first deposited layer;
5. Evolution of the road in the successively deposited layers.

For simplicity first each step was studied independently; successively its correlations and influences on the others were considered.

3.3 Experimental approach

In order to provide the data for the development of a realistic model, capable to simulate the process and to predict the material behavior, an experimental study was conducted at first.

In this section the hardware and the conditions of the experimental set up, as well as the observations captured during the analysis have been reported. With the purpose of simplifying the reading, the explanation of the performed test have been subdivided according to the five steps mentioned in section 3.2: 1. Melt flow in the liquefier;2. Extrusion through the nozzle; 3. Free extrusion and swelling of the melt at the exit of the nozzle; 4. Evolution of the road in the first deposited layer; 5. Evolution of the road in the successively deposited layers.

3.3.1 Melt flow in the liquefier

In the equipment used to conduct the experiments reported in this paper (a modified Stratasys 1650), the liquefier consists of a 15 cm long aluminum tube with an internal bore diameter of 1.83 mm. A current-carrying coil, wrapped helically around the liquefier, provides the heat necessary to melt the filament.

Inserted into the liquefier wall, at the exit end, there is a thermocouple, which is monitored by a dedicated temperature controller. The temperature regulator adjusts the heater power based on the variation between the thermocouple measurements and the desired temperature, manually set by the operator. A separate control circuit is also installed to regulate the temperature of the building volume, see Figure 2.11(a).

3.3.1.1 Thermal conditions

The liquefier temperature is chosen according to the rheological properties (i.e. the dependence of the viscosity on the temperature) and the melting temperature of the thermoplastic material. It is determined as a compromise between: 1. the need of low viscosity of the melt in the liquefier, in order to facilitate the extrusion through the nozzle; 2. the need to remelt the previously deposited layer to assure strong intra layer bonding; 3. the need of higher viscosity at deposition in order to assure a self-supporting road with enough adhesive properties.

3.3.1.2 Observations

It was observed that the quality of the deposited layers is strongly affected by the length of the liquefier. For the creation of a single layer, an ensemble of segments of different lengths generally constitutes a typical raster configuration (see Figure 3.2).

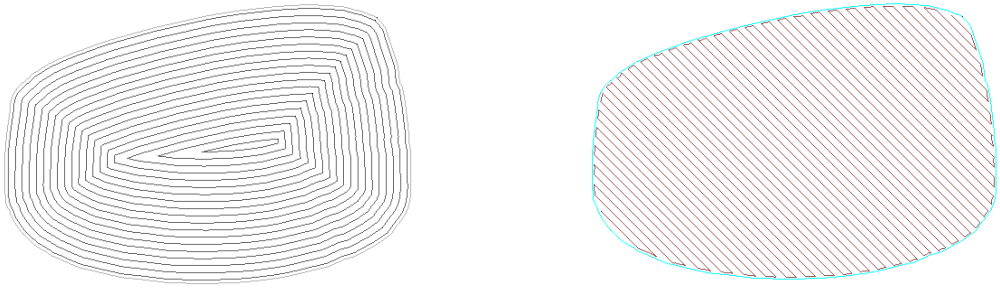

(a) (b)

Figure 3.2: Different toolpath configurations

Since the speed of the head varies considerably during the path (it accelerates at the beginning of a segment, reaching a cruise velocity at the center and decelerating in proximity of the end), the flow of the melt in the liquefier must vary accordingly in order to assure a constant, linear mass deposition rate. A mismatch between speed of the head and flow results in over deposition and/or under deposition of material, which lead to the so called *start-stop defects* (see Figure 3.3)

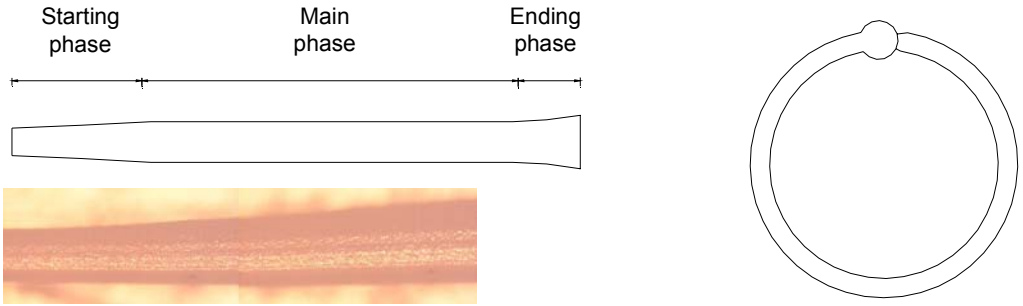

Figure 3.3: Evidence of start-stop defects

In the configuration of the machine used for these experiments, the flow of the melt is controlled by varying the speed of the pair of counter rotating rollers at the entrance of the liquefier (Figure 3.1), where the actual deposition of the melt takes place at the exit of the nozzle. The effect of a change in the motion of the rollers is thus delayed of a time proportional to the uncontrolled volume of material, which depends on the length of the liquefier [3]. A reduction of this length will improve the control of the deposition rate and it will insure a uniform section of the road along the path.

A model capable to predict the thermal fluid dynamic conditions of the flow in the liquefier will be useful for the determination of the optimal design. It will provide the tool for the calculation of the shortest length, according to the heat flux provided and material properties, that will insure the melt of the material as well as a fully developed flow at the entrance of the nozzle [31].

3.3.2 Extrusion through the nozzle

The nozzle attached at the end of the liquefier has the function to reduce the cross sectional area of the melt as well as to shape the thermoplastic material according to the desired road configuration. For the commercially available FDM machine, the nozzles are made in steel and have the configuration shown in Figure 3.4.

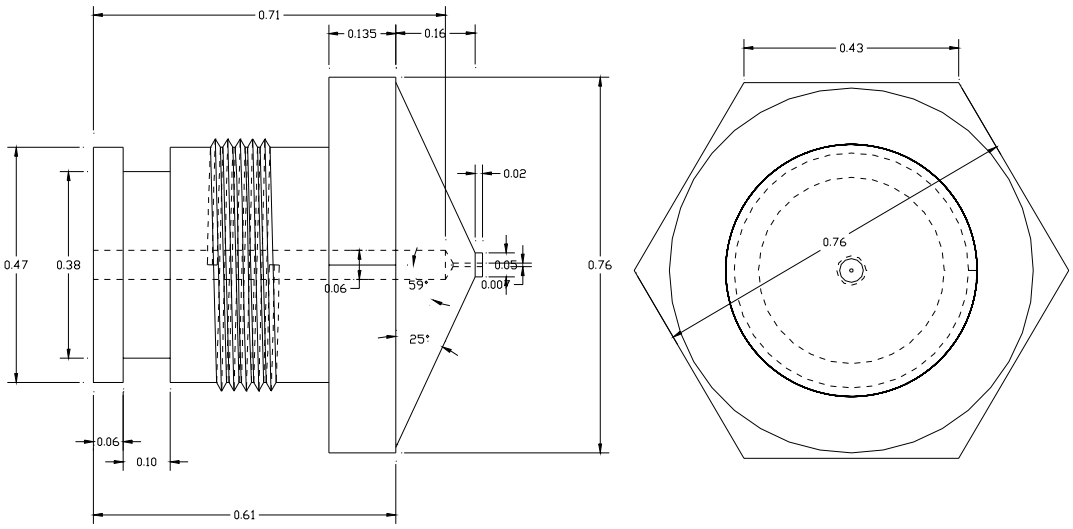

Figure 3.4: Typical nozzle geometry (dimensions are in inch)

3.3.2.1 Thermal conditions

A thermocouple is placed at the end of the liquefier, few millimeters above the threaded opening for the attachment of the nozzle. This assures that at the entrance of the nozzle the temperature of the melt corresponds to the value set by the operator (i.e. the melting temperature). The upper half of the nozzle is insulated using Teflon coating, while the lower one is subjected to heat convection.

3.3.2.2 Observations

The effect of the shape of the orifice on the final shape of the road is evident in Figure 3.5. The picture shows a micrograph of a cross-section of a fiber deposited using a round nozzle.

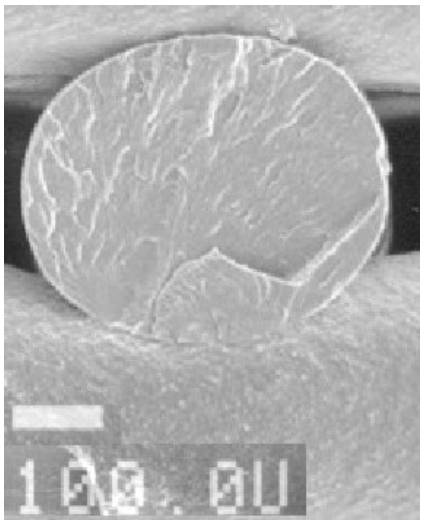

Figure 3.5: Road made with a round nozzle

Although various shaped nozzles have been tested, the focus of this study was concentrated on nozzles with round cross-sectional orifices and on the identification of those parameters that affect the most the success of the process.

It was observed that often in FDM a successful "green part" can not be built because of the continuous buckling failure of the filament. Acting like a plunger the incoming solid filament provides indeed the pressure that is needed for the extrusion of the melt through the small orifice. However, the high values of backpressure encountered during deposition often reach the critical limits of the material, causing the buckling of the filament at the entrance of the liquefier (see Figure 3.6).

In addition, it was observed [60] that the buckling problem limits the percentage of ceramic powder in the filament, hence it reduces the probability of success in the sintering phase. It was demonstrated that in order to avoid buckling failures the ratio E/η_a (where E represents the elastic modulus, while η_a is the apparent viscosity) of the

material has to be less than a certain critical value, which depends on the process parameters. Since the ratio E/η_a is proportional to the powder volume fraction, a limitation of its value results in a limitation of the quantity of powder in the filament.

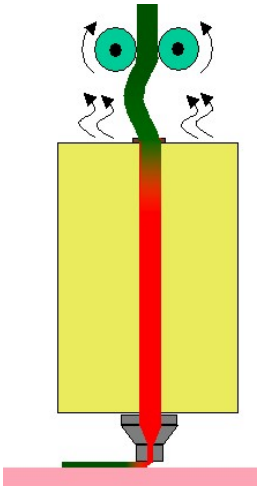

(a) Buckling of the filament

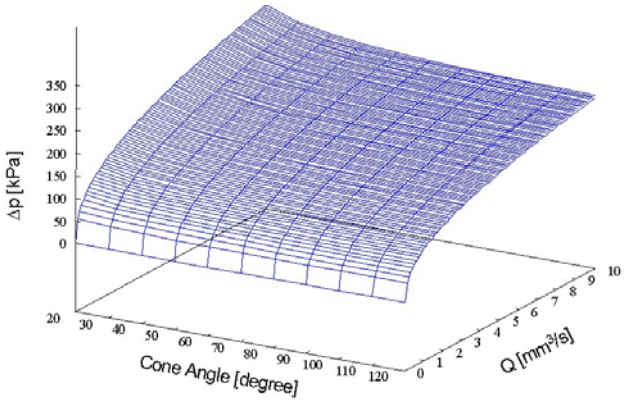

(b) Typical pressure drop values

Figure 3.6: Observed backpressure

In conclusion, a reduction of the pressure drop will improve the performance of the technique in term of continuity of the process and success of the sintering phase. Having observed [61] that approximately 85% of the pressure drop occurs in the nozzle, where the material flows through the converging section, it is possible to conclude that the backpressure is strongly dependent on the parameters α, *L* and *D* depicted in Figure 3.7.

A model capable to calculate the pressure drop for a given a nozzle configuration according to the material properties of a melt will be useful to predict the buckling of a filament. Furthermore, it will provide the tool for a parametric study (i.e. on α, *L* and *D*)

for the determination of a nozzle design that, reducing the backpressure, will prevent the failure.

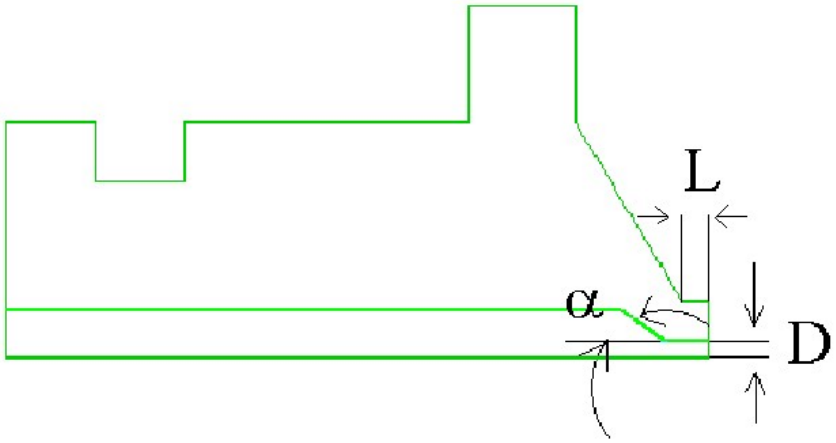

Figure 3.7: Parameter that most changes in different nozzles sizes

3.3.3 Free extrusion and swelling of the melt at the exit of the nozzle

In order to facilitate the extrusion through the nozzle, where high share rate values are observed, the melt used in FD processes are characterized by a shear-thinning behavior. This means that the viscosity of the material decreases with increasing shear rate [7]. This particular behavior of the melt, as well as the non-uniformity of the velocity field in the cross-sectional area of the nozzle, causes the swelling of the material at the exit.

3.3.3.1 Thermal conditions

At the exit of the nozzle, the surface of the melt is subjected to heat convection. The high temperature difference between the material and the air in the working volume causes a quick drop of the surface temperature. Meanwhile, at the core of the strand, the

heat supplied by heat conduction keeps the core of the filament at high temperature. Since high temperature values correspond to low viscosity of the thermoplastic material, the heat provided by conduction phenomena allows a continuous flow despite the formation of a “crust” on the surface of the strand.

3.3.3.2 Observations

In order to determine the importance of the swelling phenomenon, experiments were conducted using the FDC process with a nozzle of 0.406 mm in diameter and using PZT/ECG9 combination (see appendix 1). The liquefier was raised high above the platform to avoid any contact of the extruded strand with its surface. The extrusion process was conducted for a time sufficient to achieve a steady state condition.

The collected strands were then divided in 2 cm long segments and dipped in a 1.5 cm-high cup, containing epoxy. During the solidification of the epoxy particular attention was taken in order to keep the strand straight.

The sample was then cut approximately at half its high and it was polished with sandpaper in order to provide a flatter surface. The micrograph taken with an SEM microscope is shown in Figure 3.8.

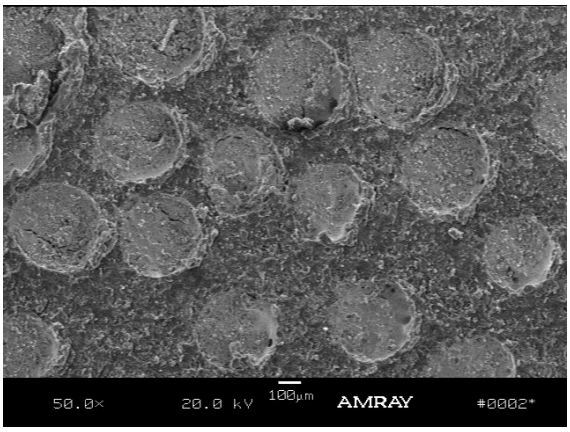

Figure 3.8: Micrograph of the section of free extruded strands

Using the scale at the bottom of the micrograph, the diameter of all the sections was manually measured and registered. The average diameter of the cross-section of the strands was then calculated to be D_{av} *=0.428 mm.*

In order to quantify the importance of the swelling phenomenon, the coefficient *s*, defined as the ratio of the diameter of the strand (D_{av}) and the diameter of the nozzle (D_{nozz}), was calculated:

$$s = \frac{D_{av}}{D_{nozz}} = \frac{0.428mm}{0.406mm} = 1.054 \tag{3.1}$$

Although the swelling phenomenon is not very pronounced during the extrusion of PZT/ECG9 ($s \approx 1$), it was observed that it cannot be completely neglected. It will be shown in chapter that the swelling of the melt originates cross sections characterized by rounded corner when the material is extruded through square nozzles. Consequently, in order to obtain square shaped strands it is necessary to manufacture complex shaped

nozzles (i.e. star shape) that compensate the swelling of the melt at the corners (see chapter 4).

3.3.4 Deposition of the first layer

In order to provide the best surface quality, to reproduce tiny features and to reduce the "stairs effect", along the boundaries and external surfaces, that are typical of LM techniques [41], in FD the standard thickness of a layer is about *0.254 mm*. The nozzle is maintained very close to the substrate, so that its tip touches and thermally irradiates the deposited road (see Figure 3.9). The platform is constituted by a foam with low thermal conductivity. The foam facilitates the separation of the object from the support after the cooling of the built part; the low thermal conductivity allows for a slower solidification rate of the road avoiding the formation of thermal stresses in early layers.

3.3.4.1 Thermal conditions

The envelope temperature (i.e. the temperature of the working volume, see Figure 3.1) is chosen as a compromise between: (1) the need of a fast solidification of the part, to insure the desired shape and good surface quality (in this case the working volume temperature should be the lowest possible); (2) the need of strong bonds between inter and intra layers roads, to improve the mechanical properties of the final product. Since self-adhesion of thermoplastic materials has been identified as the basic mechanism for the development of part strength, the envelope temperature should be kept at a level as high as possible in order to develop strong inter-roads bonds. According to Wool and

coworkers indeed [63], the degree of interface healing, defined as the ratio of interface mechanical strength to bulk material strength, depends on ¼ power of residence time *t* spent above a critical bonding temperature:

$$\alpha = \frac{\sigma_i}{\sigma_b} = K(T_i) \cdot t^{\frac{1}{4}} \tag{3.2}$$

The healing function K, dependent on the interface temperature T_i, has the following form:

$$K(T_i) = \begin{cases} A(T_c)\exp\left(\left(\frac{E_a}{R}\right)\left(\frac{1}{T_c} - \frac{1}{T_i}\right)\right), T_i > T_c \\ 0 \qquad\qquad\qquad\qquad\qquad\quad , T_i < T_c \end{cases} \tag{3.3}$$

where A and E_a are material constants indicating rate of healing at critical bond temperature and activation energy for healing process, R is the universal gas constant and T_c is the material dependent critical bonding temperature (it can be consider as the melting temperature).

3.3.4.2 Observations

Because of the very small dimensions, typical of the FDC, a high magnification, high-speed Kodak camera was used to monitor the deposition process in situ. Figure 3.9 shows one frame of a movie taken during the deposition of the third layer of a part built with PZT/ECG9.

Observing the figure it is clear that the tip is in contact with the deposited road as soon as the material is extruded from the nozzle. The results of tests conducted using various nozzle configurations show that the effect of the tip is beneficial for the final

quality of the road. More specifically, when a nozzle with no tip was adopted, it was experienced an interference with the surface of the still hot road: the depositing material got often attached to the external surface of the nozzle causing damage on previously deposited roads. Exercising mechanical pressure and supplying heat flow, through heat conduction and irradiation, the tip enhances the stability and the flatness of the layer, during the first critical moments of road evolution.

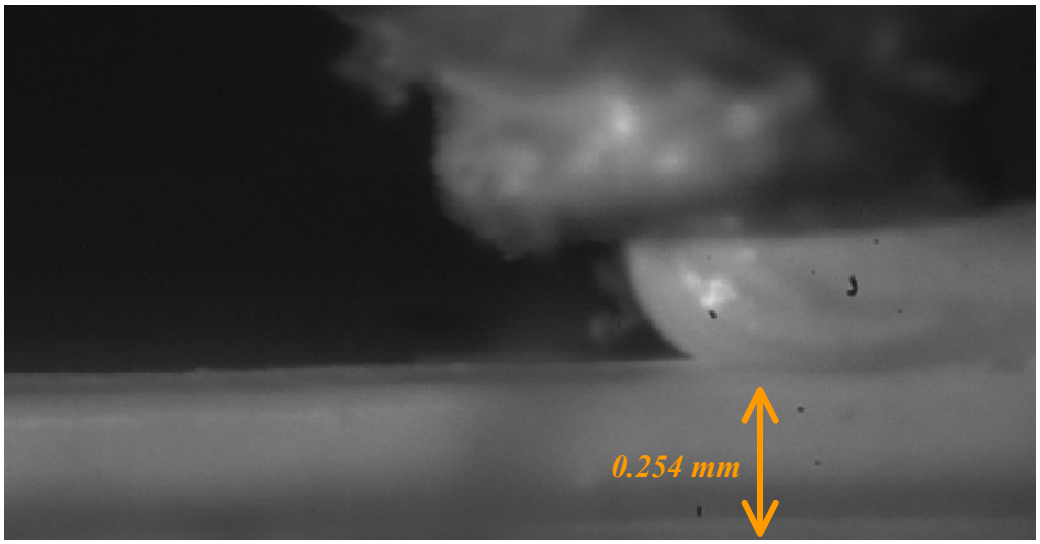

Figure 3.9: Snap shot of the deposition process using PZT/ECG9

Moreover, it was observed [29], [49] that in FDC randomly oriented particles present in the binder assume a certain orientation after extrusion and deposition of the material (see Figure 3.10). This means that the movement of the nozzle, the pressure of the tip and the viscosity of the thermoplastic material originate a flow characterized by longitudinal streamlines approximately parallel to the substrate.

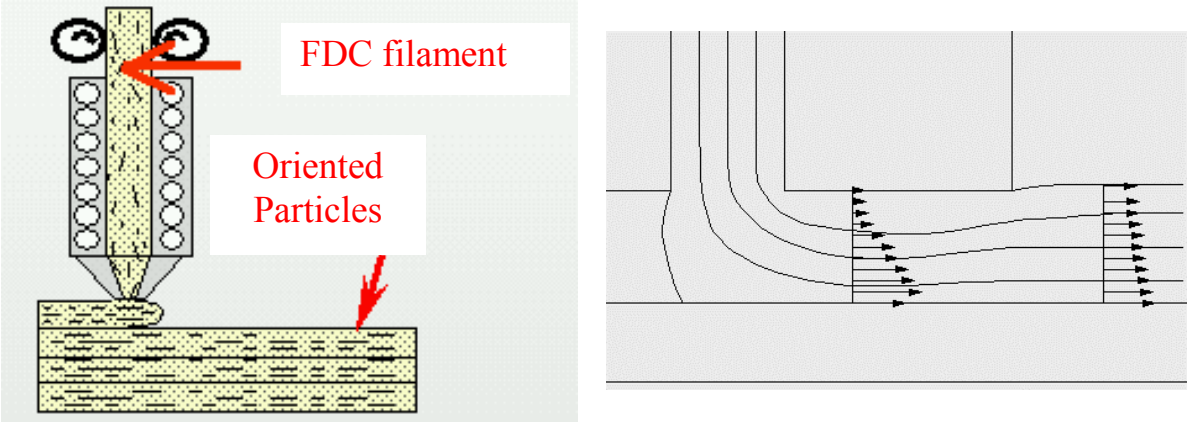

(a) Particle orientation

(b) Hypothesized flow streamlines (nozzle is assumed fixed and platform moving)

Figure 3.10: Orientation of particles and hypothesized flow streamlines

Because of the strong influence of the temperature both on the viscosity of the material as well as on the strength of the inter-layer and/or intra-layers bonds, particular attention was given to the temperature evolution of the road. For this reason the experimental set-up schematically represented in Figure 3.11 was adapted [64] during the deposition of PZT/ECG9 melt.

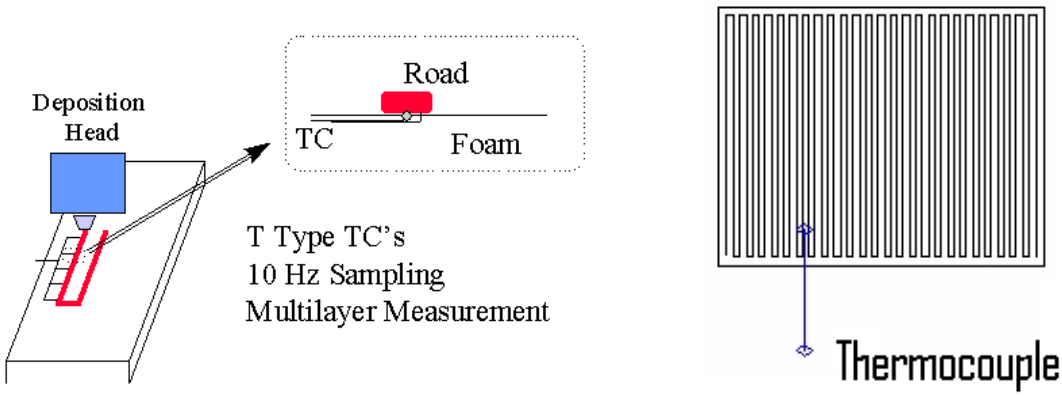

(a) Schematic of experimental set-up

(b) Thermocouple placement for temperature measurements

Figure 3.11: Experimental set-up for temperature measurements

In the experiment an array of T type thermocouples was inserted into the supporting foam, flush with the foam surface. Thermocouple signals were recorded during deposition using a stand-alone data acquisition system (TempScan1100, Omega Engineering) connected to the host computer via RS232 connection. In all instances a sampling frequency of 10 Hz was utilized, which was also the sampling limit of the instrument.

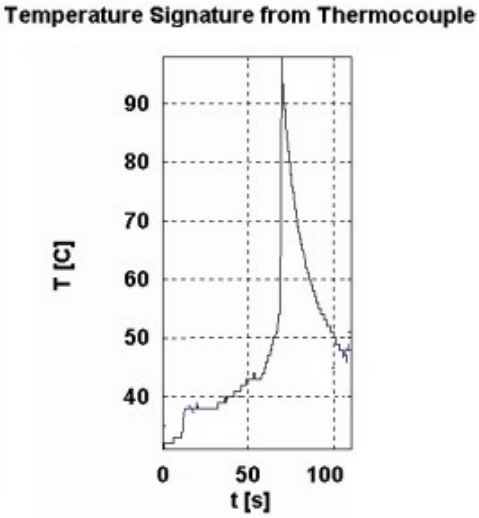

Figure 3.12: Temperature history for a material point on short raster part

The temperature history registered by the thermocouple is presented in Figure 3.12. From the collected data it is possible to observe that the temperature of a material point drops rapidly with time, according to an exponential decay function.

It should be noticed that in the experiment the highest temperature value registered by the thermocouple is about 100^{o}C. The mismatch between this value and the value (140 ^{o}C) provided by the probe placed at the exit of the liquefier (two centimeters above the platform) is due to the heat dispersion through the thermocouple inserted in the

foam. In order to reduce the fin effect of the thermocouple, smaller and insulated thermocouples would be necessary to better monitor the temperature history of a given point. To give a measure of the importance of the fin effect, with respect to the low thermo mass of the deposited road, it is sufficient to consider that most commonly utilized road sizes are *0.020"x0.010",* which will not tolerate thermocouples with weld diameters larger than *0.005"*.

A model for the deposition of the early roads will be useful, not only for the evaluation of the final road shape or the strength of the interface between roads given certain process parameters, but also for the prediction of the parameter optimal values, i.e. the envelope temperature that will assure the desired performance of the part. Without a comprehensive process model, these values have often to be determined through a time-consuming trial-and-error approach.

3.3.5 Successively deposited layers

The deposition of the next layers takes place under the same overall condition described for the deposition of the first layer. The main difference consists in the substrate and its thermal behavior.

3.3.5.1 Thermal boundary conditions

The deposition of the second and subsequent layers takes place on top of previously deposited sections. According to the thermodynamics state of the substrate, which depends on the toolpath configuration, the conditions of the intra-layer bonds can vary considerably.

3.3.5.2 Observations

In order to better understand the structure and the properties of parts built with FD process, micrographs of the cross section of the specimens have been taken and reported in Figure 3.13. In this experiment a block of 2 cm x 2 cm x 1 cm was built with a 0/90 raster configuration using PZT/ECG9. Once solidified and cooled, the part was dipped in liquid nitrogen and quickly cut in two parts by manually applying a bending momentum. This method allowed to obtain a straight, sharp fracture without affecting/deforming the shape of the single roads.

From the micrographs it is possible to observe that the internal architecture of a part fabricated using layered manufacturing resembles to the structure of a fiber reinforced composite. Using this "similitude" the air would "represent" the matrix, while the deposited roads would "represent" the fibers.

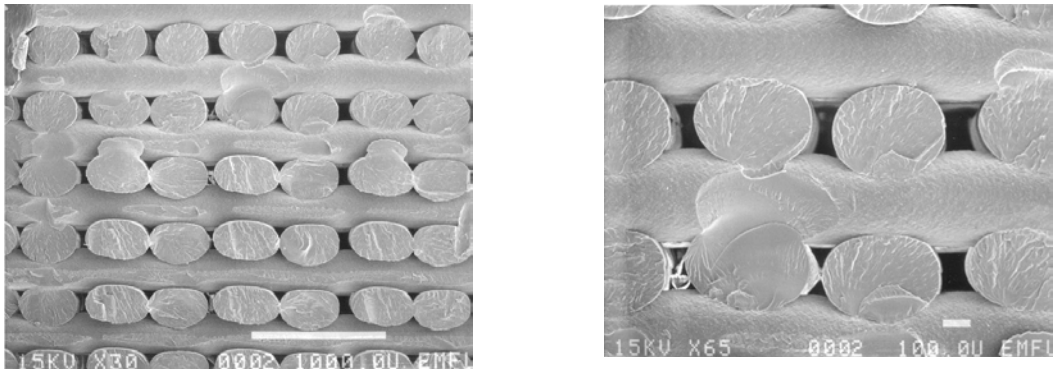

(a) Overview (b) Close up

Figure 3.13: Cross-sectional view of ABS part built with 0/90^{o} rasters ($1u = 1\mu m$)

It is because of this particular architecture that parts manufactured with LM technique show anisotropy due to property variations along direction of the roads and across the roads [4].

Furthermore it was observed that inter road adhesion, which strongly dependents on the temperature signature of the road (see equation (3.2) and (3.3)), governs the strength of the final part. In order to better understand the influence of the temperature on the quality of the part, several experiments were conducted with various toolpaths. Results show that the temperature distribution, thus the quality of the inter and intra layer bonds is strongly effected by the toolpath chosen for the fabrication of each layer. More precisely it was observed that short raster produce significantly more uniform thermal histories for the entire part and more isotropic properties [1].

A model capable to describe the formation of successively deposited layers should be able to capture:

- The effects of substrate on the new road formation;
- The influence of the incoming material on the evolution of the previously deposited road.

This model will provide a powerful tool for the determination of all the process parameters needed to insure the required performance of the final product. Once incorporated as an integral part of the process planning, the model will provide the FDC process with those characteristics required to be considered as a real alternative manufacturing technique.

3.4 Process modeling

In FD the evolution of the road during deposition, hence the quality of the final part, is strongly affected by the thermal fluid conditions of each step:

1. Melt flow in the liquefier,
2. Extrusion through the nozzle;
3. Free extrusion and swelling of the melt at the exit of the nozzle,
4. Evolution of the road in the first deposited layer,
5. Evolution of the road in the successively deposited layers.

In order to provide an exhaustive process planning tool, five different sub-models have been developed. For this purpose a finite elements approach was adopted because of the complexity of the problem, which involves:

- a viscous material, characterized by highly non-linear behavior;
- a process characterized by non-isothermal conditions that affect the thermodynamic state of the melt;
- a flow subjected to high shear rate and characterized by complex boundary conditions, i.e. free surface.

Having conducted a comparative evaluation on the capabilities of various commercially available codes, Polyflow was chosen due to its extensive libraries. The viscoelastic models implemented in Polyflow made it a suitable choice for the development of a FD model.

3.4.1 Melt flow in the liquefier

The model for the simulation of the melt flow in the liquefier was developed taking into account the axis symmetric properties of the geometry as well as of the boundary conditions. This particular characteristic of the physical problem allows us to consider and consequently mesh only a radial of the entire geometry, reducing the number of variables involved in the calculation.

Since the location of the melt flow was unknown, no distinctions were made in the sizes of the elements according to the different regions in the liquefier. In the opposite case, a refinement of the mesh in proximity of the melt flow, where higher gradients are usually present, could be considered.

Figure 3.14 depicts the geometry, the mesh and the boundary conditions considered for the simulation: 4200 quadrilateral elements with four nodes were used, resulting in a total number of 4808 nodes for the entire problem.

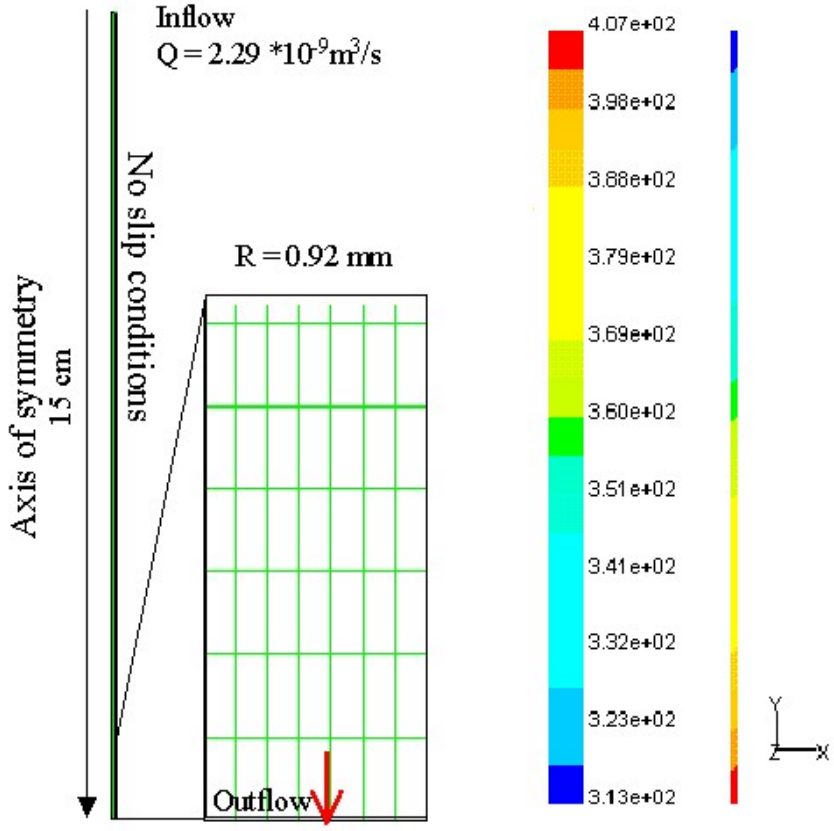

Figure 3.14: Geometry of the liquefier and calculated temperature distribution

3.4.1.1 Thermal and flow boundary conditions

The flow and thermal conditions imposed at the entrance of the liquefier are described below.

1. In order to simulate the fact that at the entrance the material is still solid, the incoming flow was modeled with normal velocity (*plug flow*) constant one the entire surface. A flow rate of $Q = 2.29 \times 10^{-9} m^3 / s$ was applied because it

describes a typical process condition using a T12 nozzle (with diameter $D = 12\ mills = 0.3048\ mm$):

a. Velocity of deposition: $v_{dep} = 25\ mm/s$;

b. Deposited road cross-section: $A = 0.088\ mm^2$;

c. Velocity of the filament: $v = 0.86\ mm/s$;

d. Velocity of the melt at the exit of the T12 nozzle: $v = 31.4\ mm/s$;

2. Since the liquefier is fed with filament that was previously stocked in the working chamber, a temperature $T = 40^o C$ was assumed at the entrance. This value corresponds to the actual envelope temperature when PZT/ECG9 is used.

For the surface at the exit of the liquefier, surface that corresponds also to the entrance of the nozzle, the flow and thermal conditions are as following:

1. No normal surface forces applied: $f_n = 0$ and zero tangential velocity $v_s = 0$. These conditions correspond to the case called “outflow”.

2. Temperature $T = 140^0 C$: this condition simulates the fact that a thermocouple, placed at the exit of the liquefier, assures the achievement of the melting temperature applied by the operator.

For the wall of the liquefier it was considered that:

1. The melt *adheres* to the wall, thus $v_s = v_n = 0$. This case corresponds to the "*no-slip*" conditions.

2. The current-carrying coil provides a constant heat flux, through the liquefier walls. The heat flux assumed was calculated considering the heat needed to raise the melt temperature from temperature at the entrance ($T_{entrance}$) to temperature at the exit (T_{exit}):

$$Q = C_p * \left(T_{exit} - T_{entrance}\right)$$

and through a parametric study. During this study, several simulations were conducted increasing the value of Q_w until when the temperature in proximity of the exit of the liquefier was constant and identical to the desired value (i.e. 140°C). This procedure best simulated the temperature control loop of the commercial Stratasys machine.

In order to describe the shear thinning behavior of the melt, the *power law* shear–rate dependence of the viscosity was considered in combination with the *Arrhenius relation* (for the temperature dependence):

$$\eta(\dot{\gamma}, T) = K\left(\dot{\gamma}\right)^{n-1} * H(T) = 633 * \left(\dot{\gamma}\right)^{0.6-1} * H(T) \tag{3.4}$$

$$H(T) = \exp\left[\alpha\left(\frac{1}{T} - \frac{1}{T_\alpha}\right)\right] = \exp\left[19{,}800\left(\frac{1}{T} - \frac{1}{413}\right)\right] \tag{3.5}$$

where η represents the viscosity, $\dot{\gamma}$ the shear rate, *H(T)* describes the Arrhenius relation, α represents the activation energy and T_α is the reference temperature, for which *H(T) = 1* [22]. The values for the material properties, such as *K, n* and *α*, were determined following the procedure described in appendix 1.

3.4.1.2 Results

The temperature distribution, obtained with the mentioned model, is represented in Figure 3.15. In term of the velocity field and flow conditions, the results showed that the melt reaches a steady laminar flow condition only after few centimeters from the entrance of the liquefier. Because of the small diameter, the hydrodynamic entry length is of the order of [31]:

$$\left(\frac{x_{fd,h}}{D}\right) = 10 \quad \Rightarrow \quad x_{fd,h} \cong 18\,mm \tag{3.6}$$

The results show that since in the upper *12 cm* of the liquefier, the temperature of the material does not reach 387 K, which is considered as the melting temperature for PZT/ECG9, the polymer can still be considered “semi-solid”. This result implies also that a quicker heating of the material, achieved through an increase of the heat flux Q_w, could allow a reduction of the length of the liquefier.

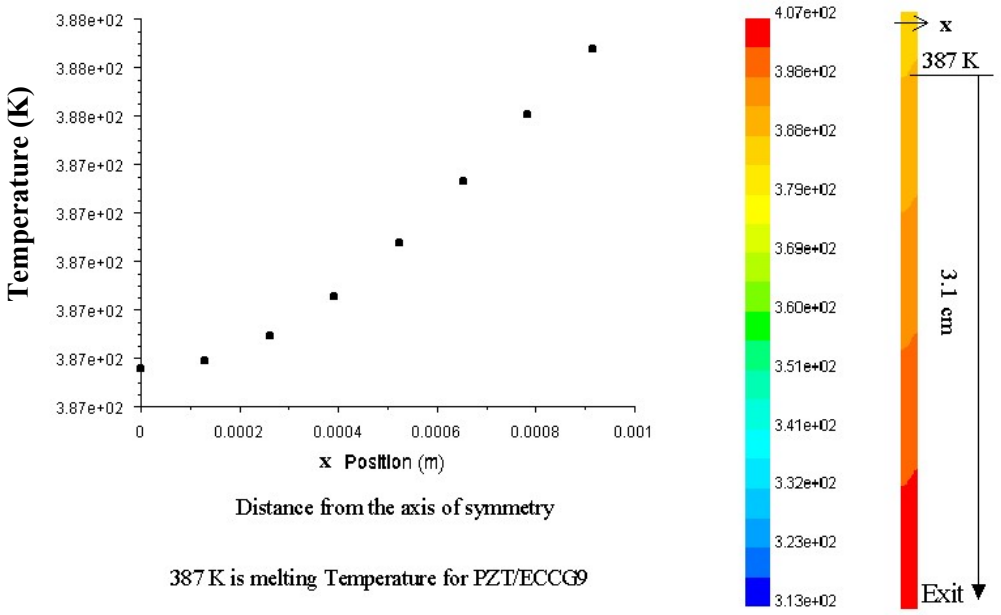

Figure 3.15: Distance of the PZT/ECG9 melt flow from the exit of the liquefier

The adoption of a smaller liquefier will consequently cause shortening of the time delay between the action of the roller at the inlet and the extrusion of the material through the nozzle (see section 3.3.1), hence a better control of the flow. The improvement in the control of the deposition process, achieved with the new design of the liquefier, will lead to improvements in term of surface quality and part performance.

3.4.2 Extrusion through the nozzle

For the generation of the data for the model of the extrusion process, a T12 nozzle (with diameter $D = 12\ mills = 0.3048\ mm$) was utilized.

In the creation of the model for a round nozzle it was taken into account that geometry and boundary conditions are axis symmetric with respect to the centerline. This characteristic of the physical problem allowed for the consideration of only one radial of

the entire geometry. In order to carefully capture the changes in the flow due to the conical section of the nozzle, the mesh was refined in that area.

Figure 3.16 depicts the geometry, the mesh and the boundary conditions considered for the simulation: 283 quadrilateral elements with four nodes were used, resulting in a total number of 333 nodes for the entire problem.

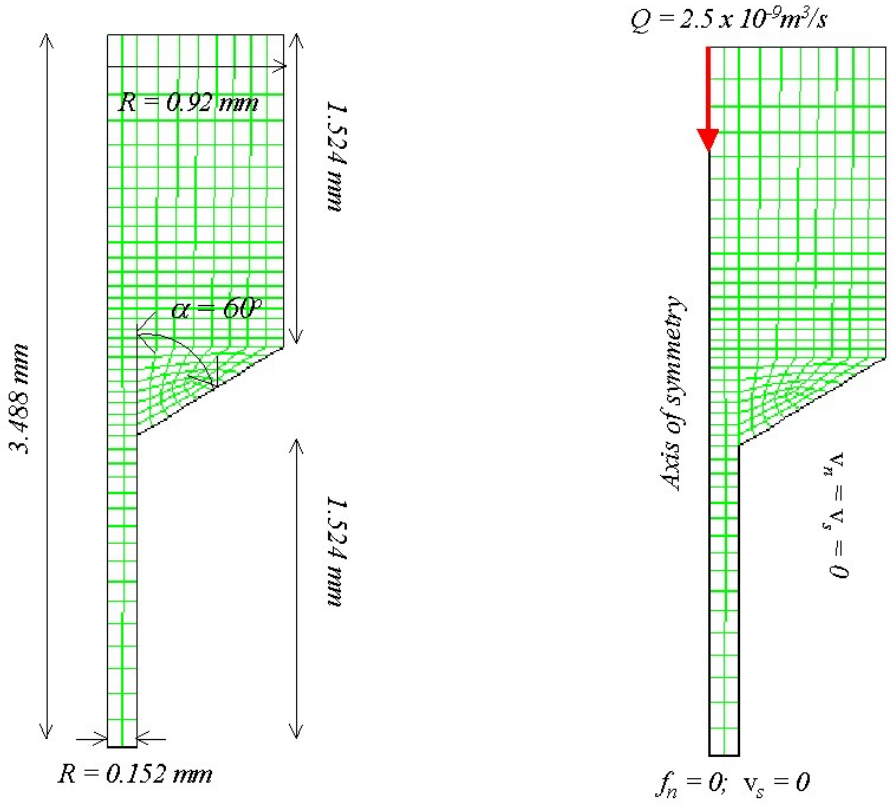

Figure 3.16: Geometry and boundary conditions in the nozzle

3.4.2.1 Thermal and flow boundary conditions

Considering that the part of the nozzle subjected to heat convection with air at $T = 40\ ^{o}C$ is about *7.5 mm* long and that the nozzle is directly connected to the liquefier, thus

it is subjected to high heat conduction rate, the melt was consider in a steady thermal state at $T = 140^{o}C$.

The fluid dynamics state of the melt was simulated applying the following boundary conditions:

1. At the entrance of the nozzle the flow is fully developed. Since this surface corresponds to the surface at the exit of the liquefier, this condition is a consequence of the results obtained with the model developed for the liquefier;
2. On the surface of the nozzle the velocity vector of the flow is zero because of the adhesion of the melt to the wall;
3. At the exit of the nozzle there are no normal forces acting perpendicular to the surface and the direction of the flow must be perpendicular to the same surface (outflow conditions, see section 3.3.1).

3.4.2.2 Results

Because of the small size of the mesh and the fact that the flow was considered isothermal and in steady state conditions, the computation converged in only six seconds of CPU time.

The pathlines obtained for the flow under the conditions described previously have been presented in Figure 3.17. From this figure it is possible to observe that there is a small stagnating flow region at the entrance of the converging section. Once past this zone, the melt flows smoothly into the last “cylindrical” part of the nozzle.

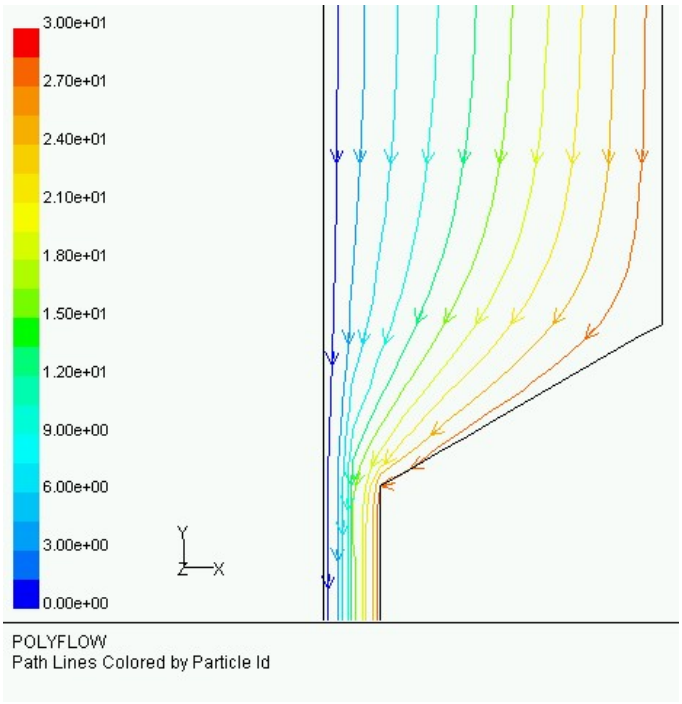

Figure 3.17: Calculated pathlines in the nozzle

The plots of velocity profile and of the pressure distribution have been presented in Figure 3.18.

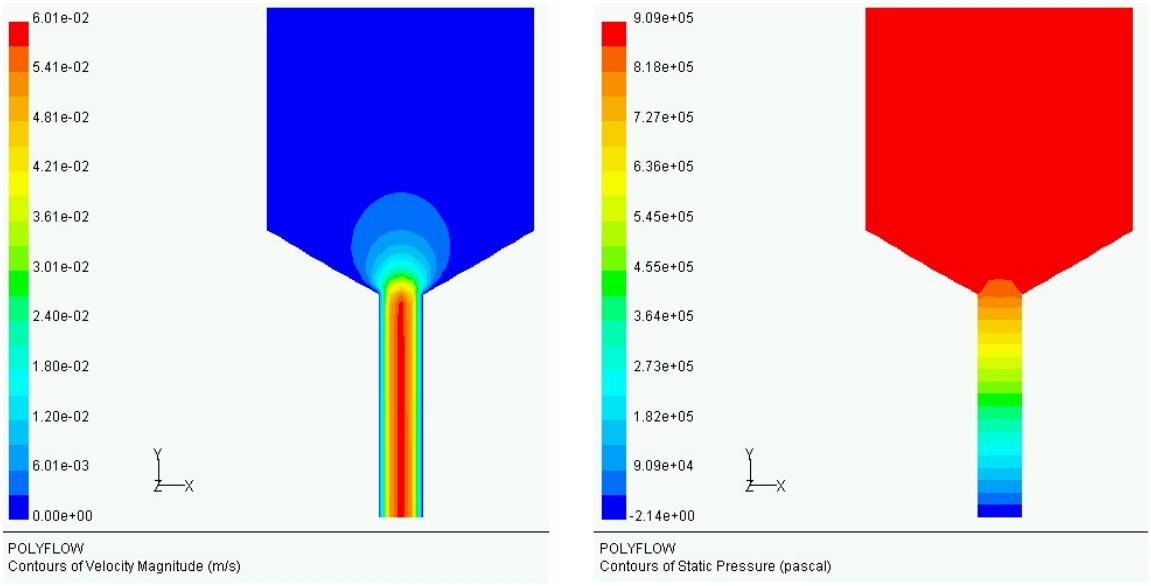

Figure 3.18: Contours plots of temperature and pressure calculated in the nozzle

From these plots it is observable that the steady state condition of the flow recovers quickly once past the convergence section.

The fact that the pressure drop, obtained with the finite element simulation (the right hand plot in Figure 3.18) for a T12 nozzle, match well with the values obtained with an analytical approach (the right hand plot in Figure 3.6) is a proof of the validity of the developed model.

3.4.3 Free extrusion and swelling of the melt

Since also in the case of free extrusion through a T12 round nozzle geometry and boundary conditions are characterized by axis symmetric properties, only a radial section has been considered in the model (see Figure 3.19).

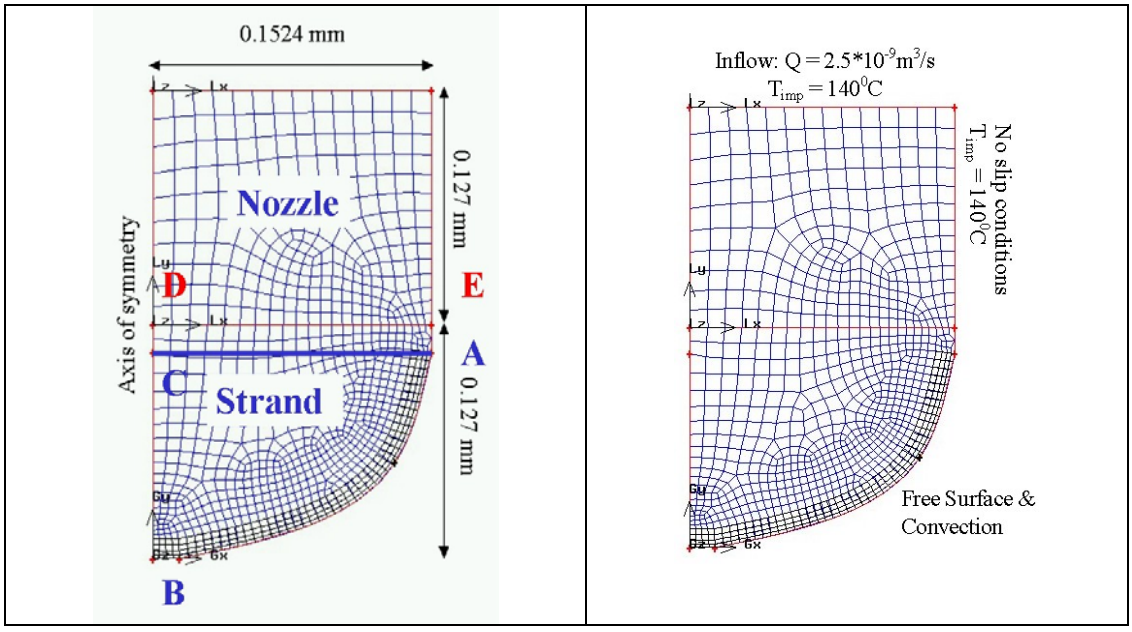

Figure 3.19: Mesh and boundary conditions applied for free extrusion simulation

In order to predict the evolution of the geometry, the simulation was conducted using a time dependent approach. Expecting very large displacements, boundary layers have been used, in proximity of the free surface, in order to avoid too distorted elements.

Boundary layers are indeed layers of elements that allow to [64]:

- Produce high quality cells near boundary.
- Allow resolution of flowfield effects with fewer cells than would be required.

The described mesh is constituted by:

- The cylindrical upper part, that represents the end of the tip of the nozzle (see Figure 3.19.a);
- The lower "semi-spherical" part, which describes the free surface of the extruded strand (see Figure 3.19.a).

Quadrilaterals elements with four nodes (see Figure 3.19) are applied. The total number of elements is 887, while the total number of nodes is 943.

In order to determine the final shape of the extruded melt, a remeshing technique was applied on the *ideal* sub-domain, limited by the segments AB, BD, DE, and EA (Figure 3.19.a). This *fictitious* domain, where a segment EA was purposely added (even though it does not have a physical meaning), was created to satisfy the requirements for the Thompson mapping transformation (see appendix 3).

3.4.3.1 Thermal and flow boundary conditions

In order to keep consistent in all the models, the thermal and flow results obtained at the exit of the nozzle were imported on the top surface of the mesh considered for the simulation of the free extrusion. The two surfaces correspond to the same ideal section of the physical problem. More precisely, it was applied:

1. Fully developed inflow with $Q = 2.5 \times 10^{-9}\ m^3/s$;
2. Temperature $T = 140^oC$.

On the wall of the nozzle (the upper cylindrical part in Figure 3.19.a) no-slip conditions as well as constant temperature $T = 140^oC$ were considered.

For the extruded melt, represented by the *semi-spherical* lower part of the mesh (see Figure 3.19.a), it was considered that:

1. The volume and surface forces acting on the melt are:
   - The gravitational force;
   - The surface tension, which is direct *tangent* to the outer surface. Its amplitude σ (see appendix 3), surface tension coefficient, was considered to be $\sigma = 0.05 \frac{N}{m^2}$ for PZT/ECG9 (see appendix 1).

   In order to calculate the final shape of the strand, some conditions on the displacement of the free surface need to be imposed and an arbitrary Lagrangian Eulerian Formulation needs to be applied [30]. In this model it was assumed that:

- Since the point A of Figure 3.19.a belongs both to the free surface and to the wall of the nozzle, its position must be kept fixed during the evolution;
- Since the point B in Figure 3.19.a is part of the axis of symmetry, it can move only in the vertical direction.

2. The free surface is subjected to heat convection with air at $40^{o}C$. Since typical values for the convection heat transfer coefficients for gases [31] are in the range of $2 < h < 25 \frac{W}{m^2 K}$, and since a ventilation system in the chamber creates a slightly moving air flow, the h value used in the simulation was: $h = 20 \frac{W}{m^2 K}$.

3.4.3.2 Results

In Figure 3.20 the evolution of the geometry of the extruded melt has been reported as snap shots for several consecutive instants.

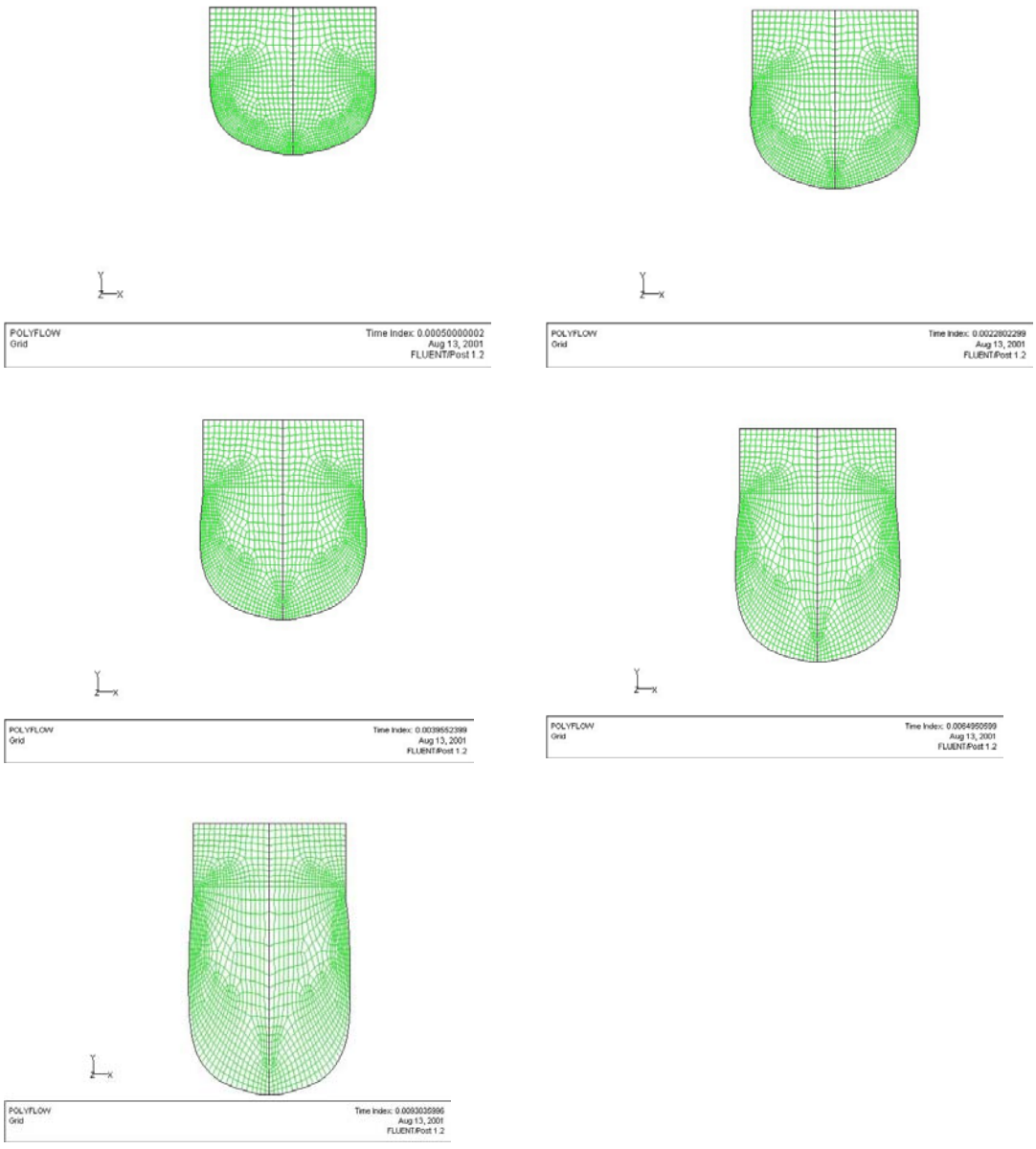

Figure 3.20: Mesh evolution for the extrusion problem

For the purpose of this study the simulation was stopped at $t = 0.06$. From the geometry of the strand resulted at $t=0.01$, when the section of the extruded material reaches a steady state condition, the diameter OB was calculated and the swelling phenomenon was determined (see Figure 3.21):

$$s = \frac{OB}{OA} = \frac{2*1.624*10^{-4}}{2*1.524*10^{-4}} = 1.063 \tag{3.7}$$

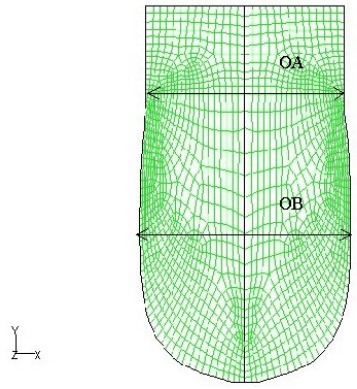

Figure 3.21: Determination of the calculated swelling phenomenon

The fact that the value of the swelling coefficient s calculated with the numerical approach (see equation (3.7)) is close to the measured value (see equation (3.1)), confirm the validity of the developed model.

In Figure 3.22, the evolution of the temperature distribution during the process has been also presented. Because of the *high* thermal conductivity of the material ($k = 1.5\frac{w}{mK}$, while usually in the deposition processes the material is characterized by $k = 0.2\frac{w}{mK}$) the temperature of the melt decreases slowly during the free extrusion, thus the viscosity remains low and the flow can proceed.

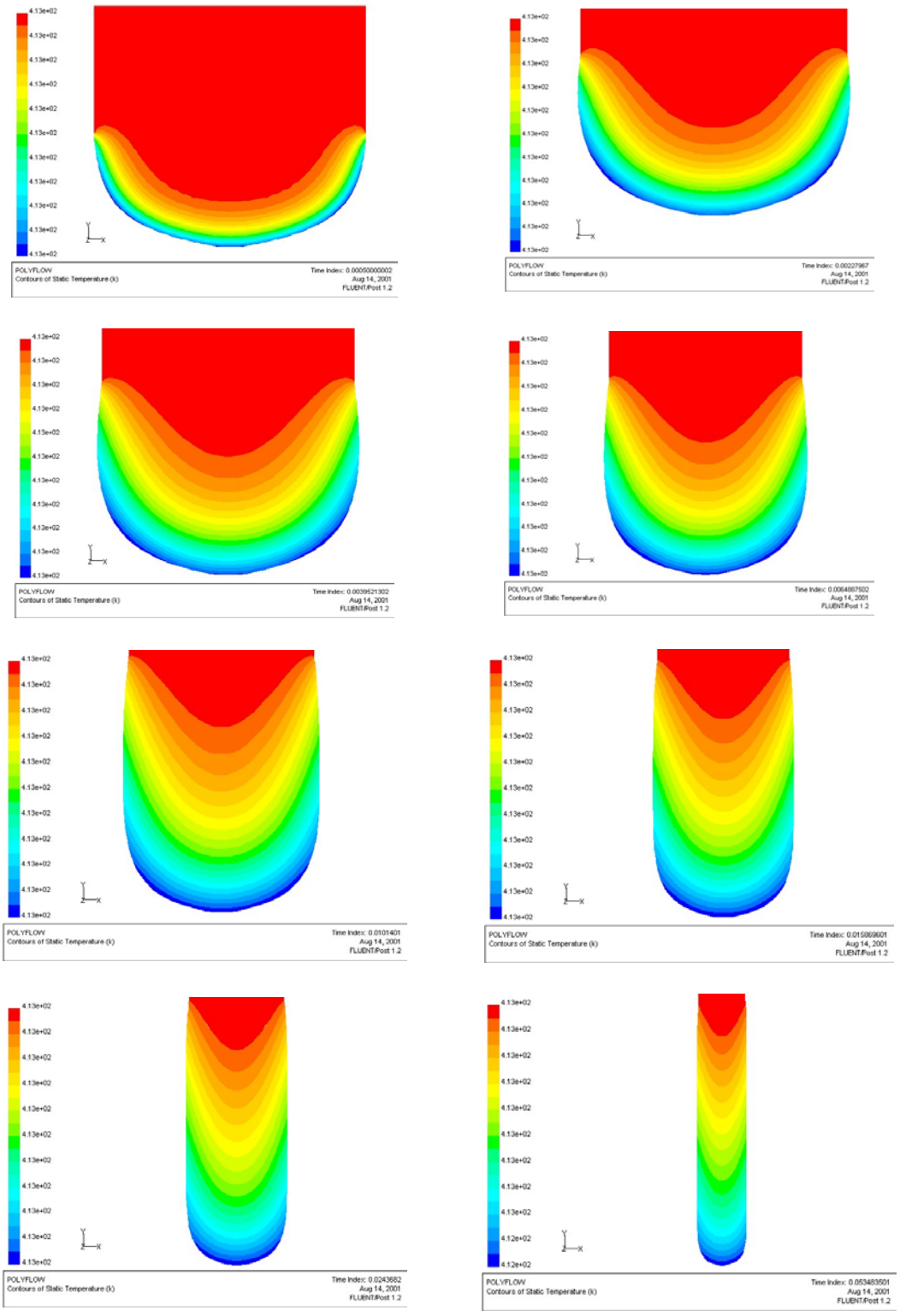

Figure 3.22: Evolution of the temperature distribution in the strand (note that the scale is different in all the images)

3.4.4 Evolution of the road in the first deposited layer

In the deposition phase the flow field of the melt is more complicated. In a first moment the extruded thermoplastic polymer is moving through the nozzle in the vertical direction; when it reaches the platform, the motion of the nozzle and the forces acting on the road are such that the material points align long horizontal pathlines (see Figure 3.10.b).

In order to simulate this behavior of the melt, without incurring in computer memory limitation and excessive computational time requirements typical of three-dimensional models, a two-dimensional geometry was adopted. It should be considered that when a two-dimensional problem is set up, the simulation is performed considering one-unit width geometry, where the end effects are neglected.

For the purpose of determining the role of the nozzle tip configuration on the deposited road, two different geometries were considered (see Figure 3.23 and Figure 3.24). In one case the tip of the nozzle was not modeled, consequently the flow was free to expand in the vertical direction; in the other case the tip of the nozzle was included in the simulation and a contact condition was imposed.

Quadrilaterals elements with four nodes (see Figure 3.23) are applied. The total number of elements is 3418, while the total number of nodes is 4046.

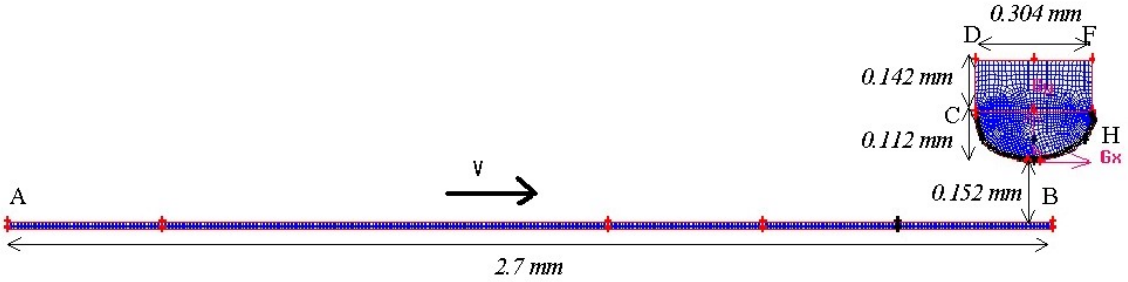

Figure 3.23: Mesh adopted without considering the effect of the nozzle

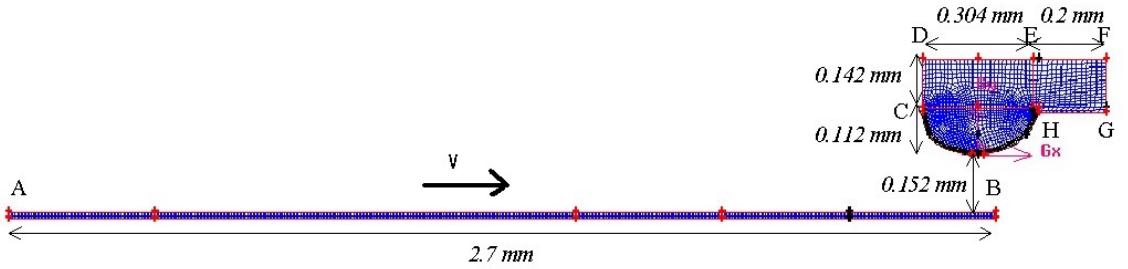

Figure 3.24: Mesh adopted when considering the effect of the nozzle

In order to clarify the geometry of the model, in Figure 3.24:

- The line AB represents the top surface of the platform;
- The line CH represents the free surface of the extruded melt;
- The area CDEH represents the volume of the melt in the tip of the nozzle;
- The area EFGH represents the right half of the tip of the nozzle, which is the only part that "*interferes*" with the deposition of the road.

3.4.4.1 Thermal and flow boundary conditions

In order to simulate the relative motion between the platform and the nozzle, it was considered that the nozzle was maintained fixed, while the platform was translating in the *x direction* with a velocity of $v_{dep} = 5 \times 10^{-3}\ m/s$. This value of the velocity, which falls in the lower part of the typical range for the deposition process, was used in order to facilitate the convergence of the simulation.

On the surface represented by DE the following conditions were applied:

1. Because of the results obtained from the model of the nozzle (see section 3.3.2) the flow rate $Q = 1.3 \times 10^{-6}\ m^3/s$ was considered fully developed. The value of the flow rate was chosen according to the thickness of the road $th = 0.26 \times 10^{-3}\ m$ (equal to the distance of the nozzle from the platform), the width of the road which is *1 unit* (because of the two-dimensional representation), and the velocity of deposition $v_{dep} = 5 \times 10^{-3}\ m/s$, thus $Q = A_{dep} \times v_{dep} = 1.3 \times 10^{-6} m^3/s$;

2. To keep consistent with the model developed for the nozzle, the temperature was assumed to be $T = 140^{o}C$.

The conditions on the walls of the tip (represented by CD and EH) were taken as:

1. No-slip conditions, thus $v_n = v_s = 0$;

2. Constant temperature $T = 140^{o}C$.

On the free surface CH the same conditions reported in section 3.4.3 were applied:

1. Surface tension $\sigma = 0.05 \frac{N}{m^2}$;

2. Heat convection with air.

For the free surface, two contact problems were considered:

- Contact detection with the surface AB of the platform;

- Contact detection with the surface GH of the nozzle.

The average temperatures $T=140^oC$ and $T=40^oC$ were applied respectively for the nozzle and the platform. Moreover, for the nozzle it was considered that the parameter α for the determination of the heat flux

$$Q = \alpha\left(T - T_{mold}\right) \text{ was } \alpha = 10^4 \frac{W}{m^2 K} \tag{3.8}$$

This high value of the parameter α simulates the high thermal conductivity of the steel. For the contact with the platform two simulations were conducted:

- With $\alpha = 10^3 \frac{W}{m^2 K}$, for simulation of material with medium-high thermal conductivity;

- With $\alpha = 10 \frac{W}{m^2 K}$, for simulation of material with low thermal conductivity (insulating material).

3.4.4.2 Results

The results obtained with the developed model explained the beneficial effects of the presence of the tip of the nozzle (see also observation in page 43). A comparison between Figure 3.25 and Figure 3.7 show that this particular feature adds stability to the flow.

In Figure 3.25, it is possible to notice that the top surface of the road is not completely flat: a distortion is particularly evident in the last frame. Given the small dimension of the thickness of a road (about 0.26 mm), and the stoking of consecutive roads, which results in the summation of the defects of each layer, a small deflection from the flat surface can cause the final rejection of the part. The final product could present delaminations or poor mechanical properties due to the presence of voids (under-filling) or of excess of material (over-filling).

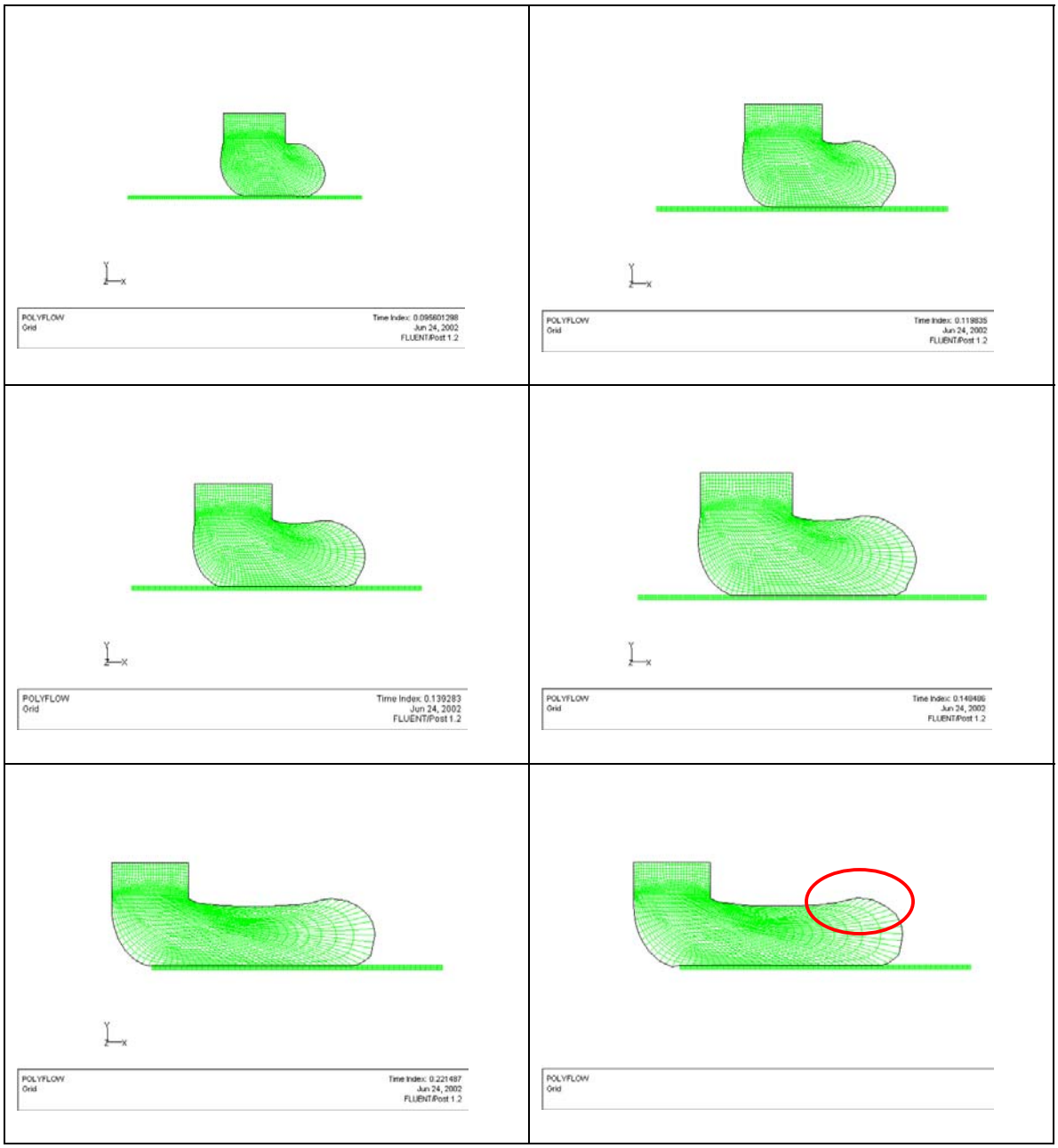

Figure 3.25: Evolution of the road shape during deposition of a first road (considering contact on the substrate and no presence of the tip of the nozzle)

When the presence of the nozzle is taken into account, the evolution of the road is controlled by the contact with the tip (see Figure 3.26).

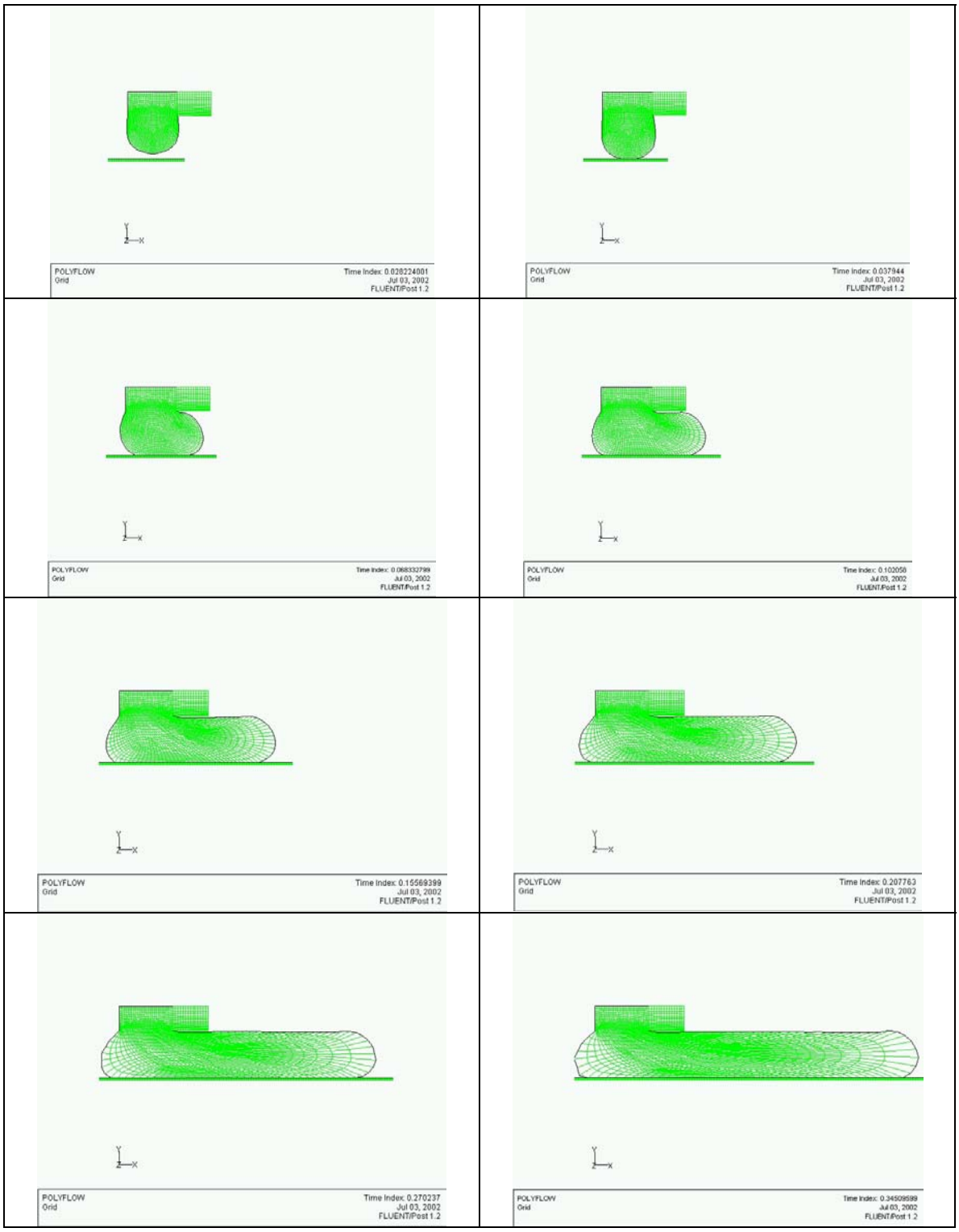

Figure 3.26: Evolution of the road shape during deposition of a first road (considering contact on the substrate as well as on the tip of the nozzle)

In this case the thickness of the "*fiber*" remains constant, insuring flatness to the deposited layer.

After having demonstrated the advantages of the presence of the tip of the nozzle, the attention of the study was focused on the determination of the effects of the thermal properties of the platform on the road formation. The results obtained with different values of the parameter α (see equation (3.8)) and the sub-section 3.4.4.1) are reported in Figure 3.27 and Figure 3.28.

A comparison between the two figures reveals, as expected, that a substrate with higher thermal conductivity causes a faster cooling of the road. In the case of $\alpha=10^3$ W/m^2K, for example, the results show that the temperature of the road can drop 20^o in only *1 mm*. Considering that the performance of a part built with an LM process strictly dependents on the inter-roads and inter-layers bonds, whose strength is effected by the residence time above a certain critical temperature (see equations (3.2) and (3.3)), a supercooling of the road will lead to poor mechanical properties of the final object.

Since in the physical problem the support consists of an insulating foam, the results obtained imposing $\alpha=10\ W/m^2K$ seem to closer simulate the real process.

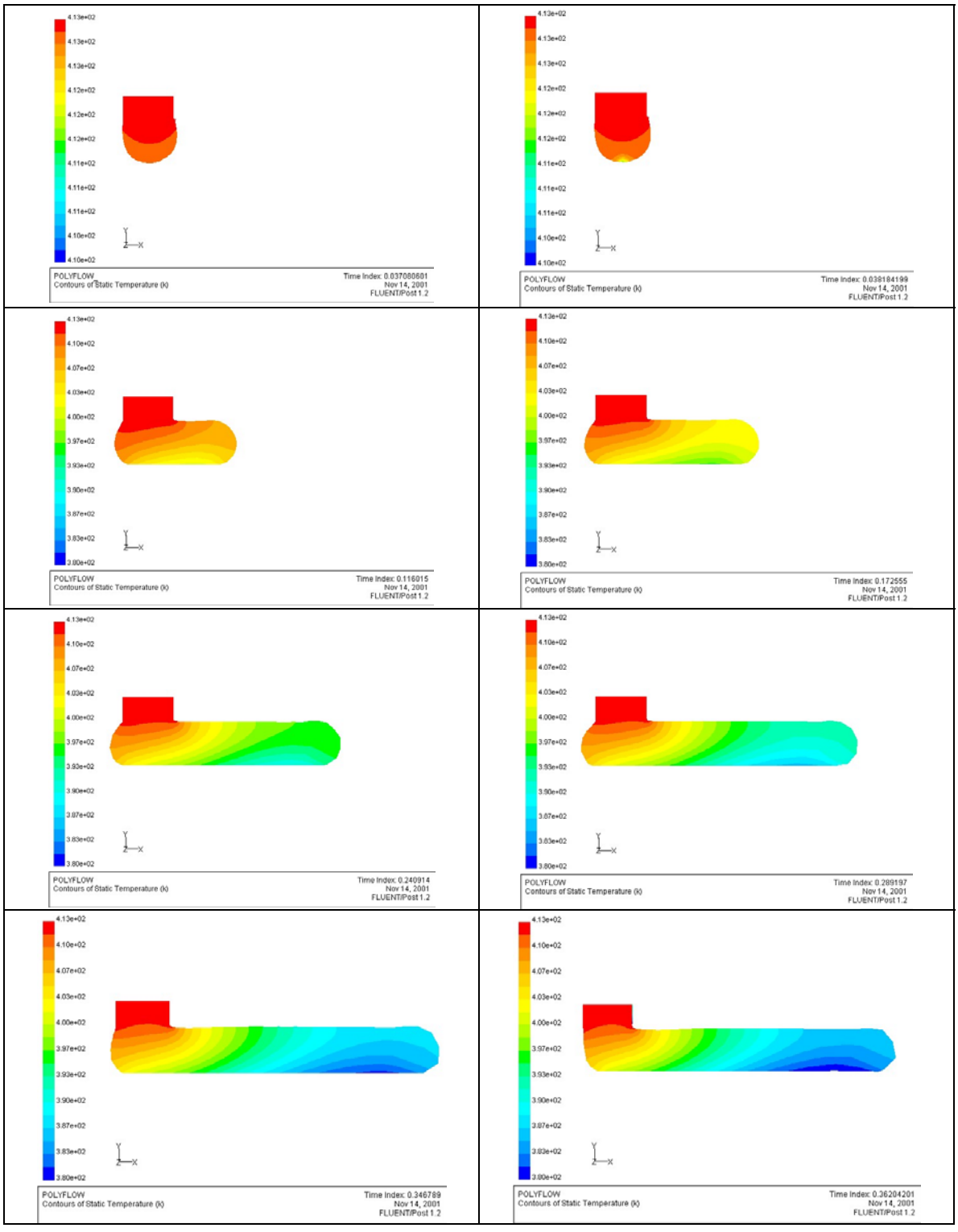

Figure 3.27: Evolution of temperature profile during deposition of a first road ($\alpha=10^3$)

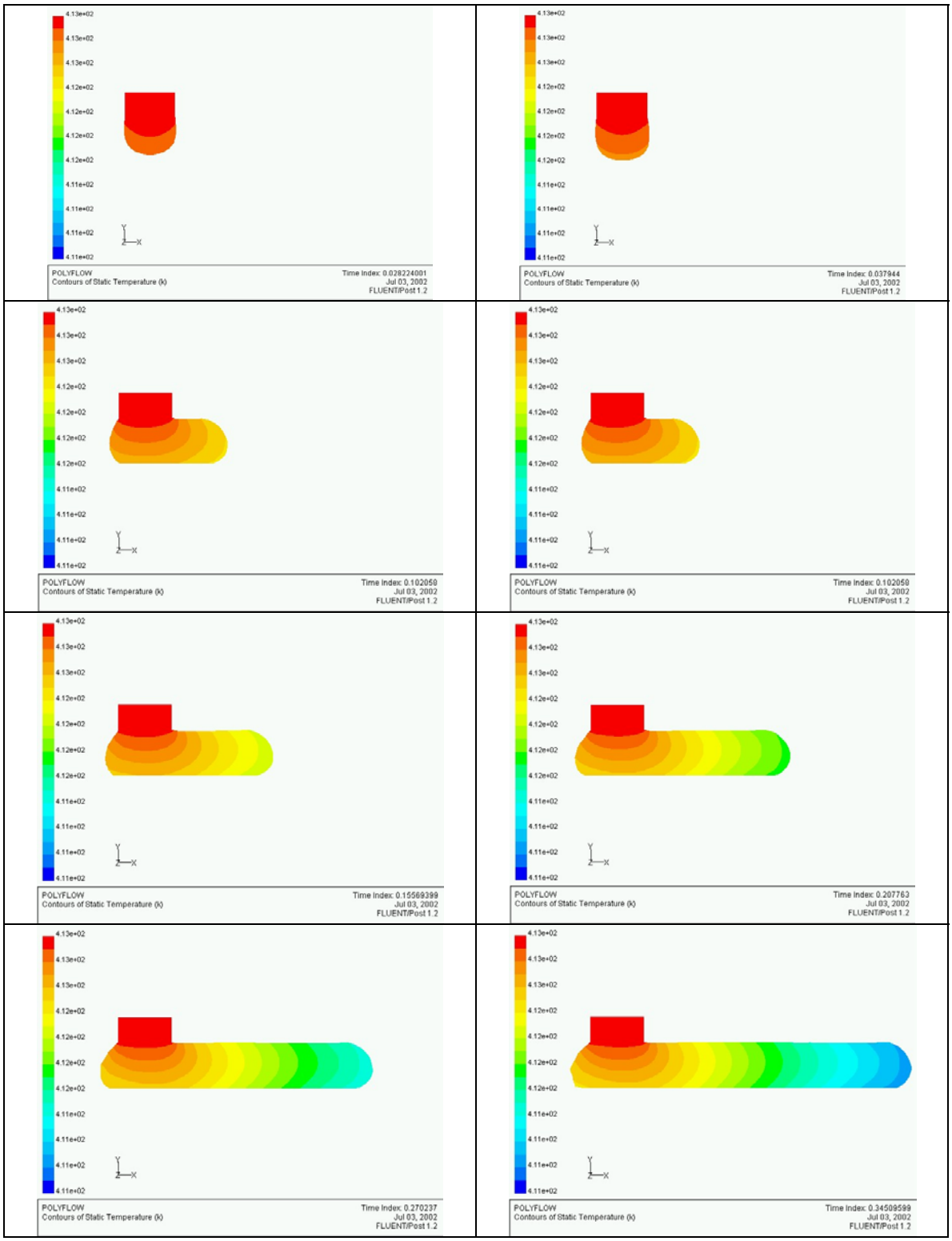

Figure 3.28: Evolution of temperature profile during deposition of a first road (α=10)

In order to capture the evolution of the temperature of the material points at the contact with the platform (on the line reported in Figure 3.29.a), a plot of the temperature distribution as a function of the location *x* has been reported in Figure 3.29.b.

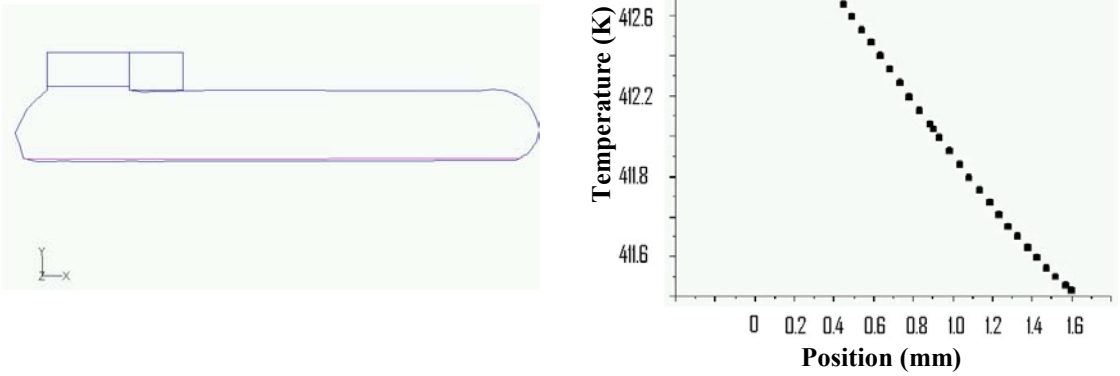

(a) Surface at the contact (b) Temperature plot as a function of x

Figure 3.29: Temperature distribution on the contact with the platform

In Figure 3.30 the temperature distribution has been plotted as a function of time. Considering that the road is deposited at a constant speed of v = *0.005 m/s*, a simple conversion was used to pass from the space domain to time domain.

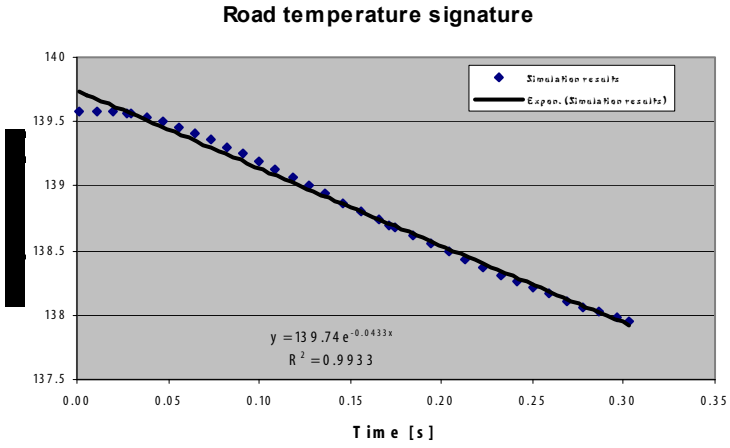

Figure 3.30: Temperature history of a material point during deposition of a single road

According to the developed model, the temperature of a material point in the road decays exponentially as:

$$T[C] = 139.74 \cdot e^{-0.0433 \cdot t}$$

where t represent the time lapsed since the deposition of the considered material point.

In order to have comparable data between the model and the experimental results (see Figure 3.12) in Figure 3.31 a "delayed signal" has been plotted.

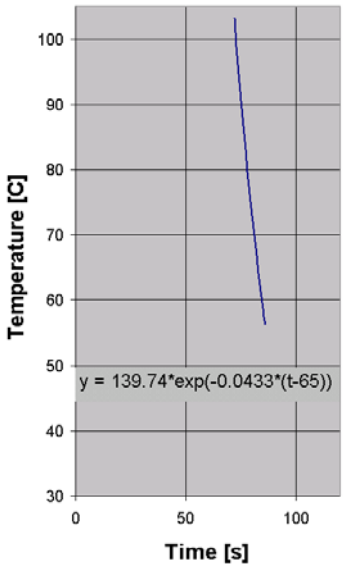

Figure 3.31: Road temperature signature obtained with the simulation

Because of the fin effect of the thermocouple with respect to the low thermomass of the depositing road, it was hypothesized that the captured experimented values are the ones that in reality occur seven seconds later. The prediction of the temperature evolution

derived from the results obtained with the model (see Figure 3.31) is qualitatively similar to the registered signal (Figure 3.12).

In order to verify if the model was able to predict the orientation of particles present in the filament, the pathlines of the flow from respectively a cross-sectional and longitudinal point of view are shown in Figure 3.32.

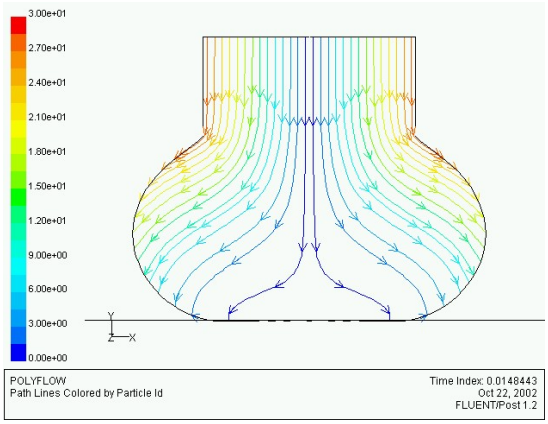

(a) Hybrid cross-sectional flow-field: stagnation & fountain flow

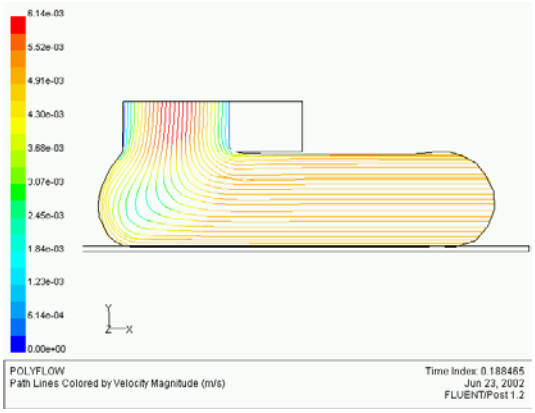

(b) Axial flow-field in the reference frame of moving deposition head

Figure 3.32: Pathlines of flow during deposition: cross-sectional and longitudinal view

A comparison of Figure 3.32 with Figure 3.10 shows a good agreement between the hypothesized and the computed flow field. Furthermore, from the resulted longitudinal flow-field it is possible to predict that if a particle at the exit of the nozzle is angled (with respect to the y direction), it is subjected to a non-uniform velocity field, which tends to orient it.

3.4.5 Evolution of the road in successively deposited layer

In order to build a model for the deposition of consecutive layers, the geometry of the road resulted from the simulation of the deposition of the first layer was imported and

remeshed. Moreover, for consistency with the previous models, the geometry of the nozzle and of the extruded material were imported from the simulation described in the section 3.4.4 (compare Figure 3.24 and Figure 3.33).

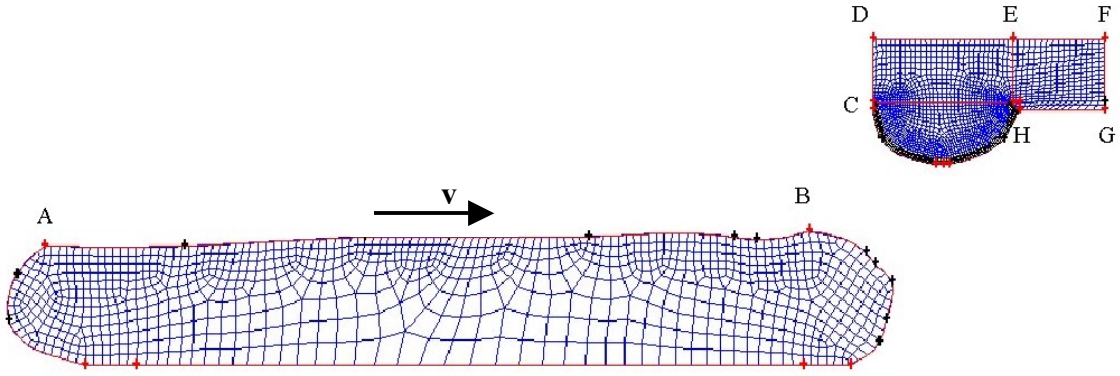

Figure 3.33: Mesh adopted for the model of the deposition of the second layer

Quadrilateral elements with four nodes are applied. The total number of elements for the model is 3074, while the total number of nodes is 3253.

3.4.5.1 Thermal and flow boundary conditions

Due to the repeatability of the deposition process, the flow was considered under the same fluid and thermal boundary conditions applied for the deposition of the first road (see section 3.4.4.1).

For the previous deposited layer it was considered that:

- Its average temperature is $40^{o}C$, because in thermal equilibrium with the envelope atmosphere;
- The road is translating at v = *0.005 m/s*.

A contact detection problem was considered between the free surface CH (see Figure 3.33) of the melt and the top surface AB of the previous deposited road. At contact, it was considered that the heat flow through the interface (see equation (3.8)) is characterized by the parameter of $\alpha=10^2$ W/m^2K. This value was chosen for the simulation of the behavior of the melt, whose thermal conductivity falls between the value typical of the insulating foam and the value characterizing the steel nozzle.

It should be underlined that in the physical problem the surface represented by the line AB is first acting like a *contact target* for the melt, then like an *interface* between the first and the second road. However, since it was not possible to impose a contact detection and an interface problem on the same surface, a *decoupled computation* was performed.

In the first step the simulation was conducted modeling the previous deposited road as a solid, hence AB as a rigid surface. Consequently a contact detection calculation was developed between the free surface of the extruded melt and the top surface of the first layer.

The final geometry obtained with this simulation (see Figure 3.34) was then used to develop the model for the second step. In this case, which aimed to simulate the mutual effects of two consecutive layers, the surface AB was modeled as a moving interface, where continuity of the velocity field and of the contact forces was imposed. This implies that the surface is free to move, under the effect of the incoming flow and of the heat flux, and its final geometry is computed as part of the solution.

In the model the geometry, except for the interface AB, was considered fixed (see top left frame of Figure 3.35) and the following flow boundary conditions were applied:

- A fully developed flow of $Q = 1.3 \times 10^{-6}\ m^3 / s$ was considered on the surface CD and;
- $f_n = f_s = 0$ on the surface EB, in order to simulate that the road is infinitely long in this direction;
- $\mathrm{v}_n = \mathrm{v}_s = 0$ on CA, DC, BF, FG and GA in order to simulate the solidification of the external surface;
- Continuity of the velocity field on the interface.

The thermal boundary conditions were taken as follows:

- Temperature $T = 140^o C$ assumed on CD;
- Heat conduction with $k = 1.5 \frac{W}{mK}$ on EB to simulate the continuity of the road, thus heat conduction in the layer;
- Heat convection with $h = 20 \frac{W}{m^2 K}$ on CA DC, BF and GA to simulate the heat exchange with the environment;
- Temperature $T = 40^o C$ assumed on FG to simulate the contact with the platform;
- Continuity of the temperature field on the interface.

3.4.5.2 Results

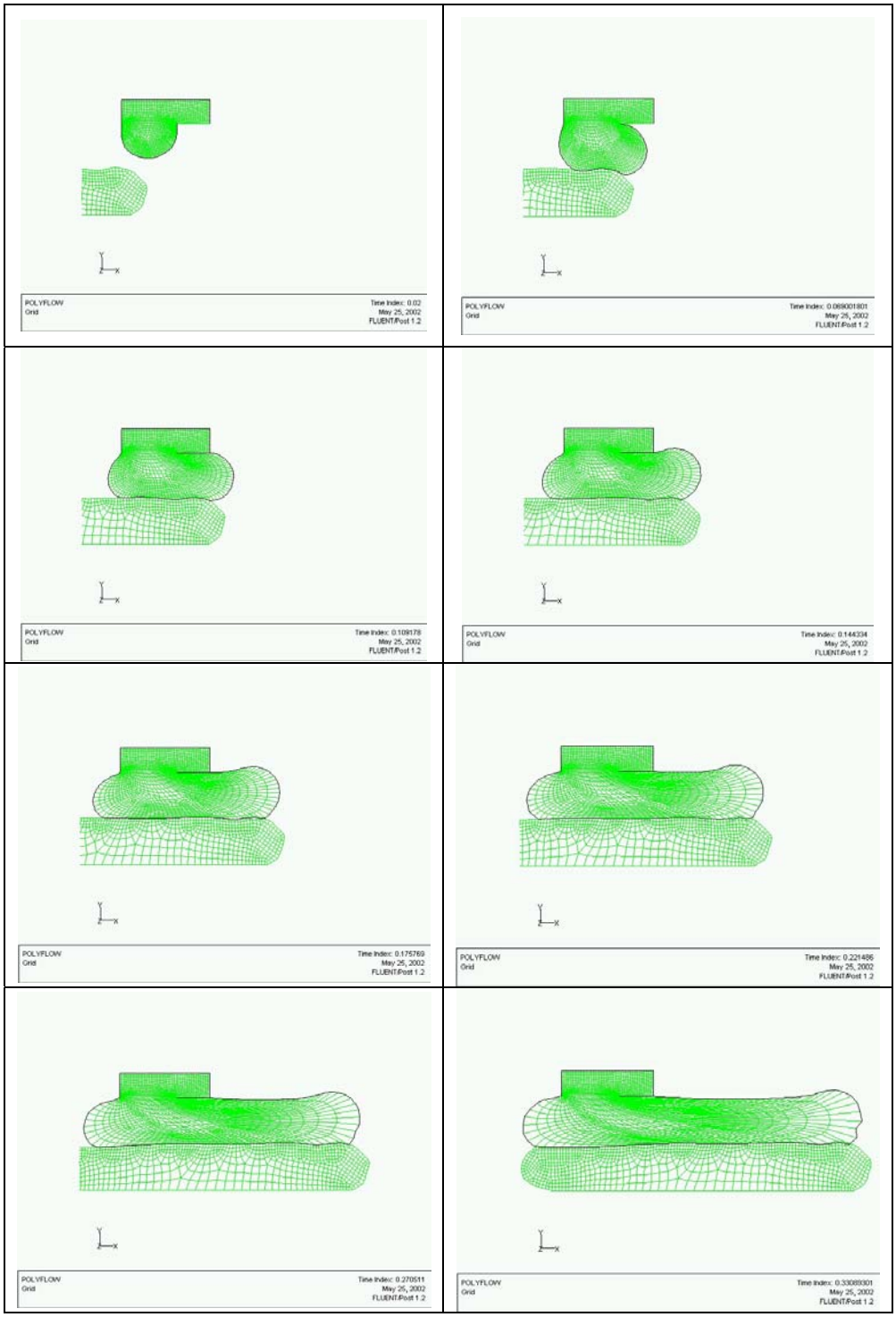

Figure 3.34: Results of the first step of deposition of a second road

In Figure 3.34 the evolution of the geometry obtained with the model developed for the simulation of the first step of the deposition of a second road is reported. It can be observed that the extruded melt adheres to the top surface of the first layer and shapes during its cooling phase.

The Temperature profile and the velocity distribution obtained for the simulation of the second step of deposition of a second road are shown respectively in Figure 3.35 and Figure 3.36.

From the plot of the contour of the velocity magnitude, shown in Figure 3.36, it is possible to observe that the velocity is zero at the interface. This means that with the flow and thermal conditions considered for this simulation the deposition of a second road does not affect the geometry of a previous layer.

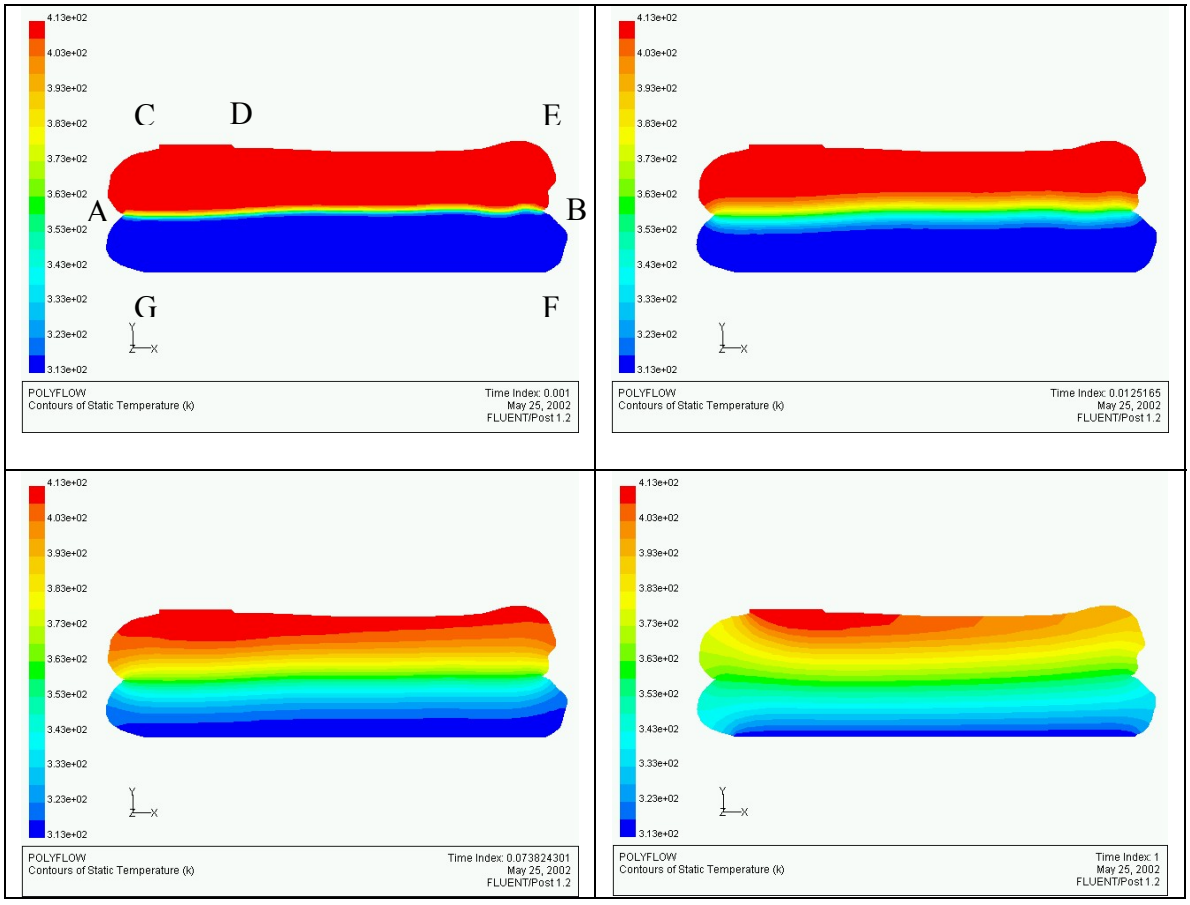

Figure 3.35: Temperature profile of the second step of deposition of a second road

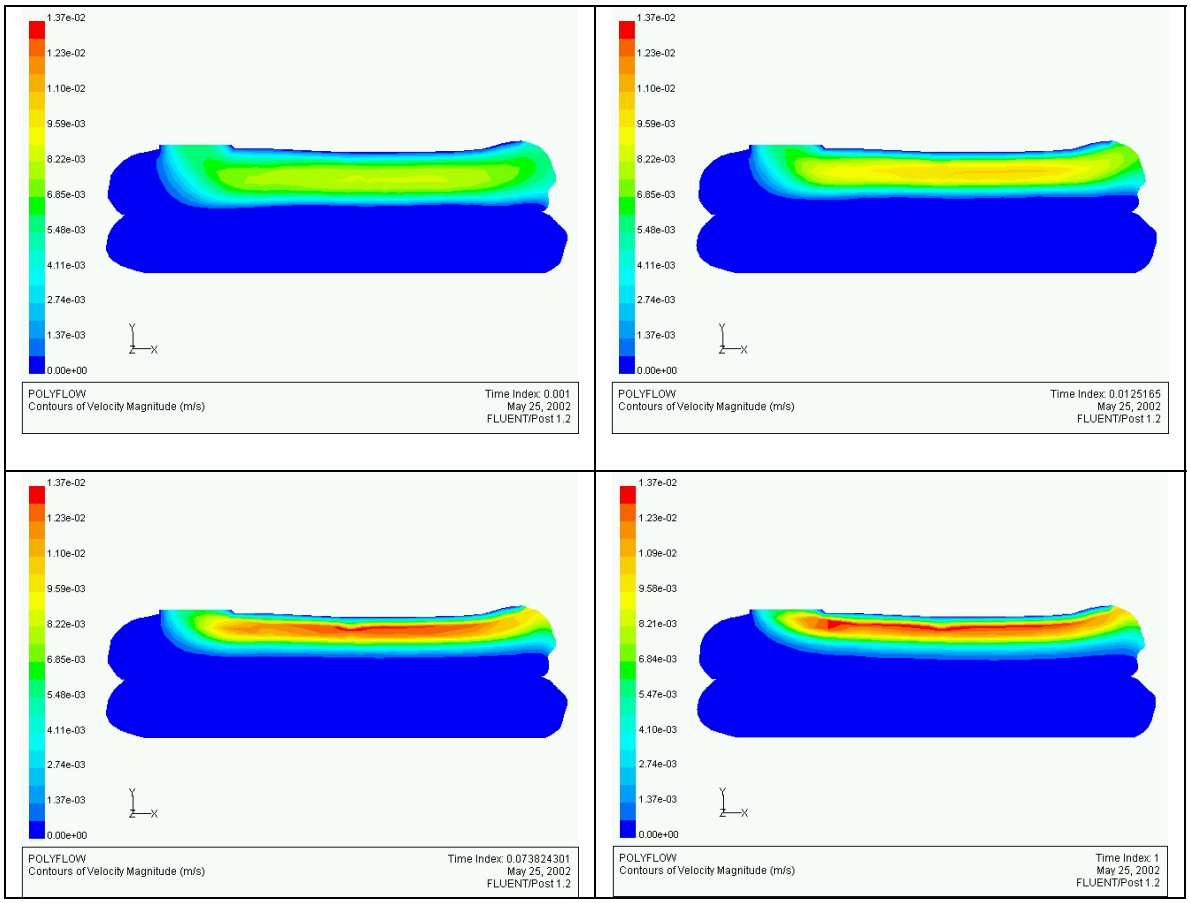

Figure 3.36: Velocity field of the second step of deposition of a second road

However, when higher flow rate and/or higher temperature were assumed on the surface CD it was noticed that the position of the interface, calculated as part of the solution, was affected (see Figure 3.37) by the incoming material.

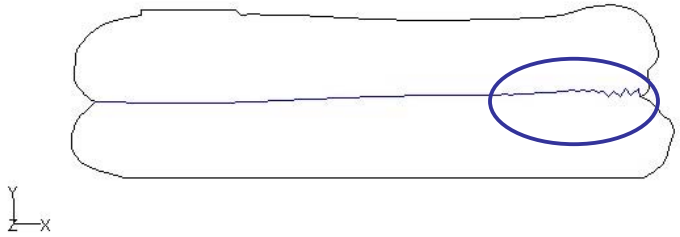

Figure 3.37: Effects on the position of the interface when high flow is applied

3.5 Conclusions

Models described in this chapter have been developed to study and explain the thermo fluid behavior of the material used in fused deposition of ceramics. Since the integrity and quality of parts built with LM processes, i.e. FDC, strictly depend on the thermo fluid dynamic state of the deposited roads, the integration of these models in the design phase of the process will help to achieve the desired performance.

Good agreement obtained in the comparisons with experimental data demonstrated the validity of the models in term of prediction of the geometry, as well as velocity field and temperature distribution in different phases of the process.

As part of further improvements, in the model developed for the evolution of the road in successively deposited layer, a more realistic fluid-rigid body interaction should be explored in order to substitute the two steps approach [55].

The model presented in this paper provide also the opportunity to conduct parametric studies that will lead to the determination of the optimized build strategy for different materials, avoiding a time-consuming trial and error approach.

CHAPTER 4: NOZZLE OPTIMIZATION IN FUSED DEPOSITION

4.1 Abstract

The recent improvements in fused deposition modeling, as described in section 2.3, led to the development of fused deposition of ceramics (FDC) for fabricating ceramic objects directly from CAD files. In this process, once the green body is built, the part goes through post process phases, i.e. binder burn out (BBO) and sintering. In the BBO phase, where the binder disintegrates and is removed, the temperature in the oven reaches 600^{o}C.

It has been observed that in these conditions, the pressure of air trapped in possible voids present in the green body (see Figure 4.1), can cause the failure of the part. It is consequently intuitive that in order to build a successful component it is important to enhance the integrity of the *green body*.

This chapter presents the results of the experimental work aimed to reduce void formation in a finished product by employing different nozzle cross-section configurations to effectively improve the "stacking" of roads. As part of this research two square nozzles have been tested. The results show that with the optimization of some parameters like flow rate, speed and acceleration of the deposition head a significant improvement in the quality of the final part can be achieved.

A finite-element based numerical modeling for the process has been also developed to predict the final shape of the road given a nozzle geometry, as well as to adopt a reverse engineering approach in order to optimize the nozzle configuration.

4.2 Physical problem

In order to obtain roads with cross section independent to the path of motion, the nozzles commercially available for FD processes are characterized by round cross section orifice. Although this design simplifies the configuration of the machine and allows building objects according to any toolpath, it also causes poor bonding between roads. It was observed indeed that a round shape orifice in the nozzle leads to the formation of elliptical cross-section roads. This effect is particularly evident in Figure 4.1, which shows the cross section of a part built with $0/90^{o}$ raster.

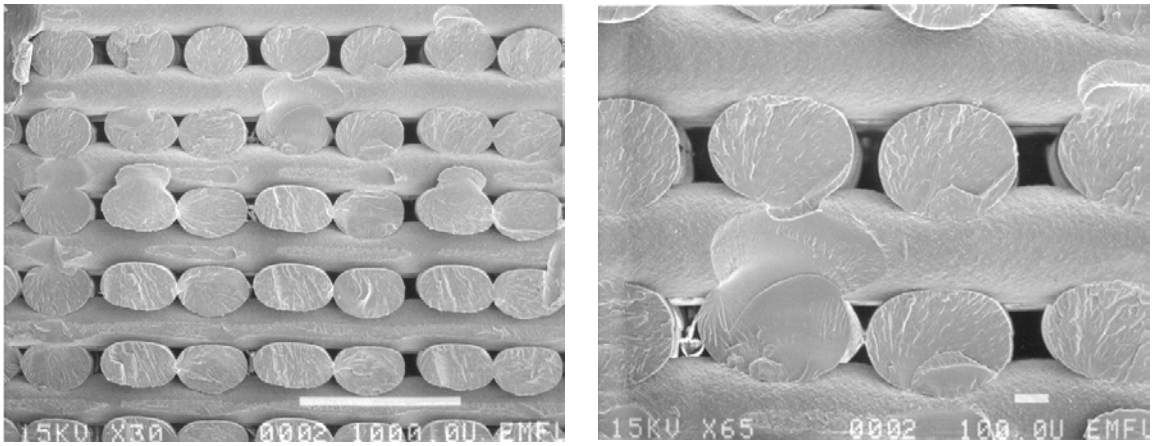

Figure 4.1: Cross-sectional view of ABS part built with $0/90^{o}$ rasters - zero air gap

In the figure it is also notable that the internal architecture of a part, fabricated using FD, reminds the structure of a typical composite material. However, since in this case the “matrix” is constituted by air, the material shows weak behavior in the direction where stresses need to be carried through road-to-road or layer-to-layer adhesion.

For the purpose of increasing the packing of the structure, it is standard procedure, in the FD process, to set an ideally negative distance between two consecutive

roads. Imposing negative air-gaps alters indeed the road cross-sectional geometry by filling the inter-road space with the excess material.

However, previous studies [64] of this process showed that the presence of the heated nozzle at the top surface enforces the filling of the top cavity first, followed by gradually filling of the bottom one (see Figure 4.2). This asymmetry with respect to the horizontal mid-layer is often causing a deformation of the structure and a non-planar bloated top surfaces, totally not acceptable in manufacturing.

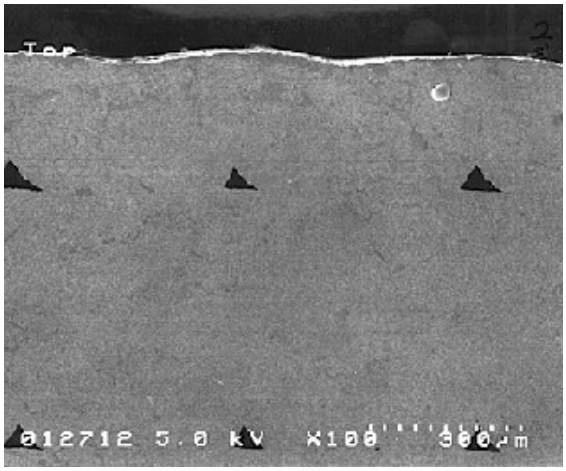

Figure 4.2: Preferential closure of air-gaps across the part cross-section

In order to improve the mechanical properties as well as the quality of the surface of the final part, the attention of this study was focused on the evolution of the road, which is the “building block” of the process.

4.3 Experiments performed with square shaped nozzles

To improve the stacking of the material as well as the surface quality, in this work alternative nozzle designs have been adopted and tested to study their effects on the geometry of the road.

Intuitively, a perfectly square cross-section road would completely eliminate the voids in the structure, considerably improving the mechanical properties of the built part. However, it is widely known that in order to obtain an extruded strand with square cross-section area, a complex nozzle design is required. The shear-thinning viscous behavior of the melt and the non-constant velocity field across the section of the nozzle cause indeed the swelling of the material at the exit. Consequently the nozzle has to be properly designed to compensate the deformation of the strand shape due to the swelling phenomenon.

In order to determine the importance of the swelling phenomenon and its effects on the geometry of the strand according to the shape of the orifice, square cross-section nozzles have been tested at first.

4.3.1 Manufacturing square nozzles

The nozzles employed for these experiments were produced in-house as modification of round nozzles. Electron discharge method (EDM) was applied on T16 (*0.41 mm* in diameter) steel nozzles using a square shaped electrode of *0.41 mm* in size. Pictures of initial nozzles, taken with an optical microscope, showed a misalignment of the new square orifice with respect to the previous round one (see Figure 4.3). The defect was caused by:

- The bending of the EDM electrode during its approaching and centering in the middle of the tip of the nozzle.
- The high accuracy needed in order to place a square of *0.41 mm* in size, around a circle of *0.41 mm* in diameter.

In order to avoid the bending of the electrode, a Copper-Tungsten alloy was used because of its higher stiffness and higher mechanical strength. Moreover, for an easier centering, T16 nozzles were replaced by T12 (0.305 mm in diameter) round nozzles, which allowed a minimum tolerance in the alignment.

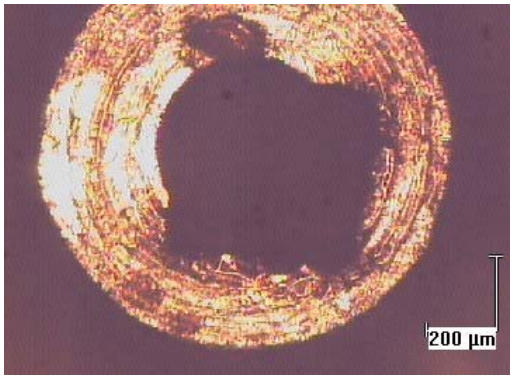

Figure 4.3: EDM positioning problem

The nozzle of Figure 4.4 was manufactured with a Copper-Tungsten electrode, with square cross section of *0.41 x 0.39 mm*, starting from a round nozzle of *0.305 mm* in diameter. The picture in Figure 4.4.a was taken with an optical microscope after the fabrication of the nozzle, while the one in Figure 4.4.b was taken with SEM after use with PZT/ECG9.

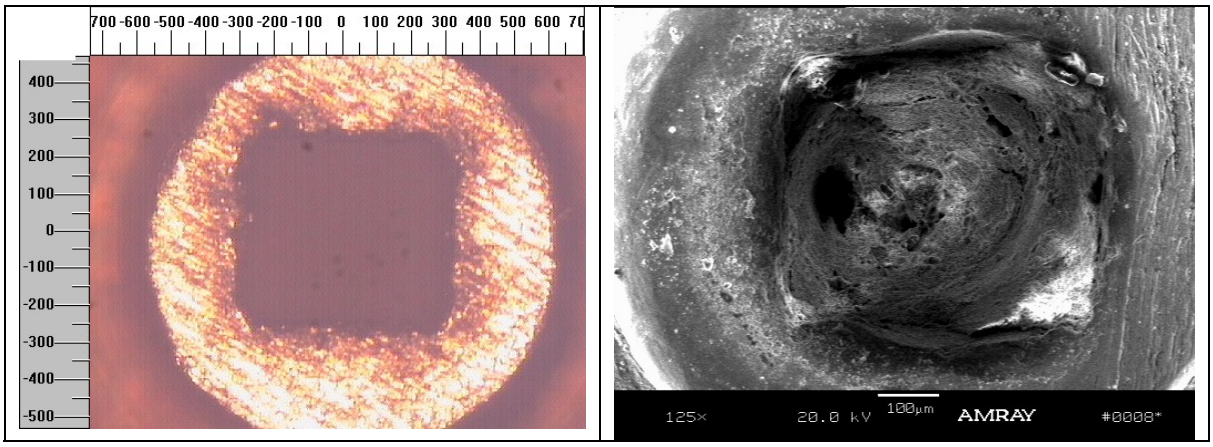

A B

Figure 4.4: Square nozzle manufactured with 0.41x0.39 mm electrode:(A) optical micrograph (after fabrication); (B) SEM (after use)

With the purpose of reducing the manufacturing cost, aluminum square nozzles with bigger orifice dimensions were also fabricated at Rutgers University, one of the co-partners in the development of this MURI project.

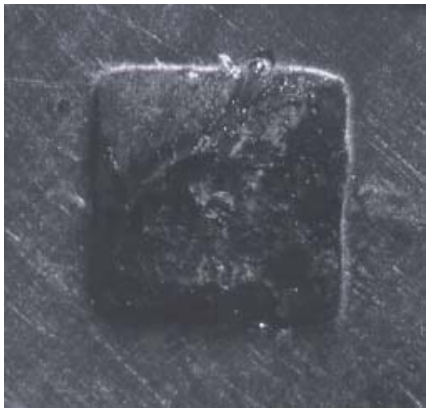

Figure 4.5: Aluminum nozzle (0.76x0.76 mm) [Courtesy of Simona Turcu]

In Figure 4.5 a picture of an aluminum square nozzle with orifice *0.76 x 0.76 mm* is shown. In this case, the nozzle was fabricated in 2 symmetrical parts successively soldered together.

4.3.2 Free extrusion through square nozzles

In order to visualize the swelling of the material due to viscous effects, the cross sections of free extruded strands were analyzed with respect to the size of the nozzle. Pictures taken for the extrusion of PZT/ECG9 through respectively a steel (*0.41 x 0.39 mm*) and an aluminum nozzle (*0.76 x 0.76 mm*) are presented in Figure 4.6.

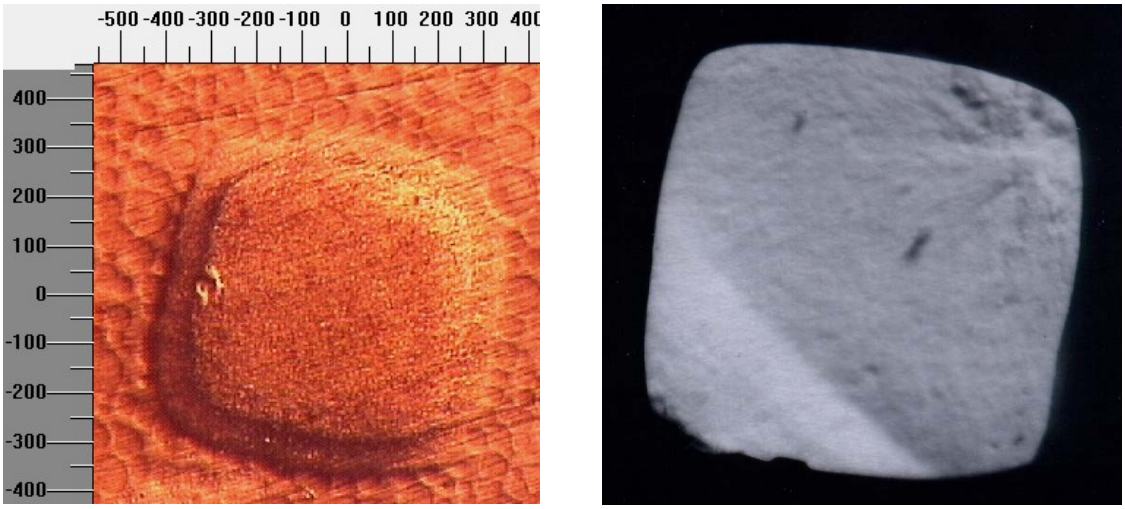

(a) Square road with *0.41 x 0.39 mm* *(Optical microscope)*

(b) Square road with *0.76 x 0.76 mm* [Courtesy of Simona Turcu]

Figure 4.6: Roads extruded through square nozzles

For the picture on the left side, the strands collected during free extrusion were divided in 2 cm long segments and dipped in a 1.5 cm high cup, containing epoxy. During the solidification of the epoxy particular attention was taken in order to keep the strand straight. The samples were then cut, approximately at half its high, and polished to provide a flatter surface. An optical microscope was finally used to generate the images.

The picture on the right hand site was taken in Rutgers University after free extrusion through an aluminum nozzle.

Figure 4.6 shows that the strands obtained using the bigger nozzle present sharper angles, while the strands extruded through the smaller nozzle are characterized by rounded corners. According to the theory of extruded plastics [7] the swelling process (De/D) is proportional to the ratio (L/D), thus it is less pronounced for the bigger cross-sectional nozzle (see equation (4.1)).

$$\frac{De}{D} = 0.1 + \left[1 + \frac{1}{2}\left(\frac{\tau_{11} - \tau_{22}}{2\tau_{21}} \right)^2 \Bigg|_W \right]^{\frac{1}{6}} \qquad (4.1)$$

This effect is due to the extra tension observed along the streamlines of polymeric fluids. Once the fluid is outside the capillary this extra tension cannot be supported and the fluid contract axially and expand radially (proportionally to the difference τ_{11}-τ_{22}).

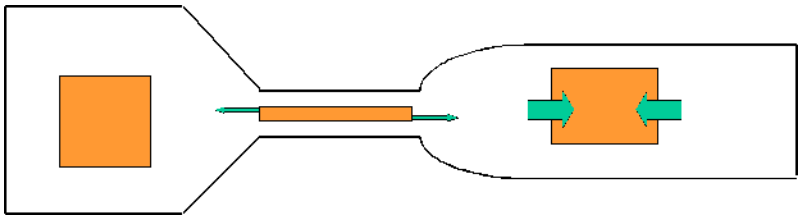

Figure 4.7: Swelling process

Since the normal stress difference of τ_{11}-τ_{22} is related to the extrusion process, during which a cylinder of polymer in the reservoir is squeezed into a long, thin cylinder within the die (see Figure 4.7), the quantity τ_{11}-τ_{22} is proportional to the ratio L/D (where

L represents the length and D the diameter of the tip). Thinner nozzle tips are thus characterized by a more accentuated swell effect.

4.3.3 Experimental results

Even though it was observed that the nozzle with bigger orifice produces strands with sharper edges, hence a cross-section closer to a square shape, the attention of this work was focused on the smaller size nozzle. The choice was the result of a compromise between the need of enhancing the overall surface quality by reducing the stair effect (this requires smaller road width), and the objective to improve part integrity by preventing voids formation (that requires a "more square" road cross-section).

In order to determinate the effect of square orifices on void formation, hence on part integrity and performance, several samples were built with PZT/ECG9 using the steel nozzle (*0.39 x 0.41 mm*). The process parameters applied during the experiments are reported in Table 4-1, while the pictures of the cross-section of the samples are shown in Figure 4.8.

Table 4-1: Parameters for the first set of parts

	Flow Rate [mm^2/s]	**Slice Thickness [mm]**	**Air gap [mm]**	**Acceleration [mm/s^2]**	**Speed [mm/s]**
A	0.157	0.254	0	127	20.32
B	0.157	0.254	-0.076	127	20.32
C	0.157	0.254	-0.13	127	20.32
D	0.157	0.254	-0.18	127	20.32

From Table 4-1 it is observable that, besides the air gaps between consecutive roads, all the process parameters were kept constant in all the experiments. Four parts of at least fifteen layers were built for each case described in Table 4-1, using a 0/0 oriented path in the plane of the support.

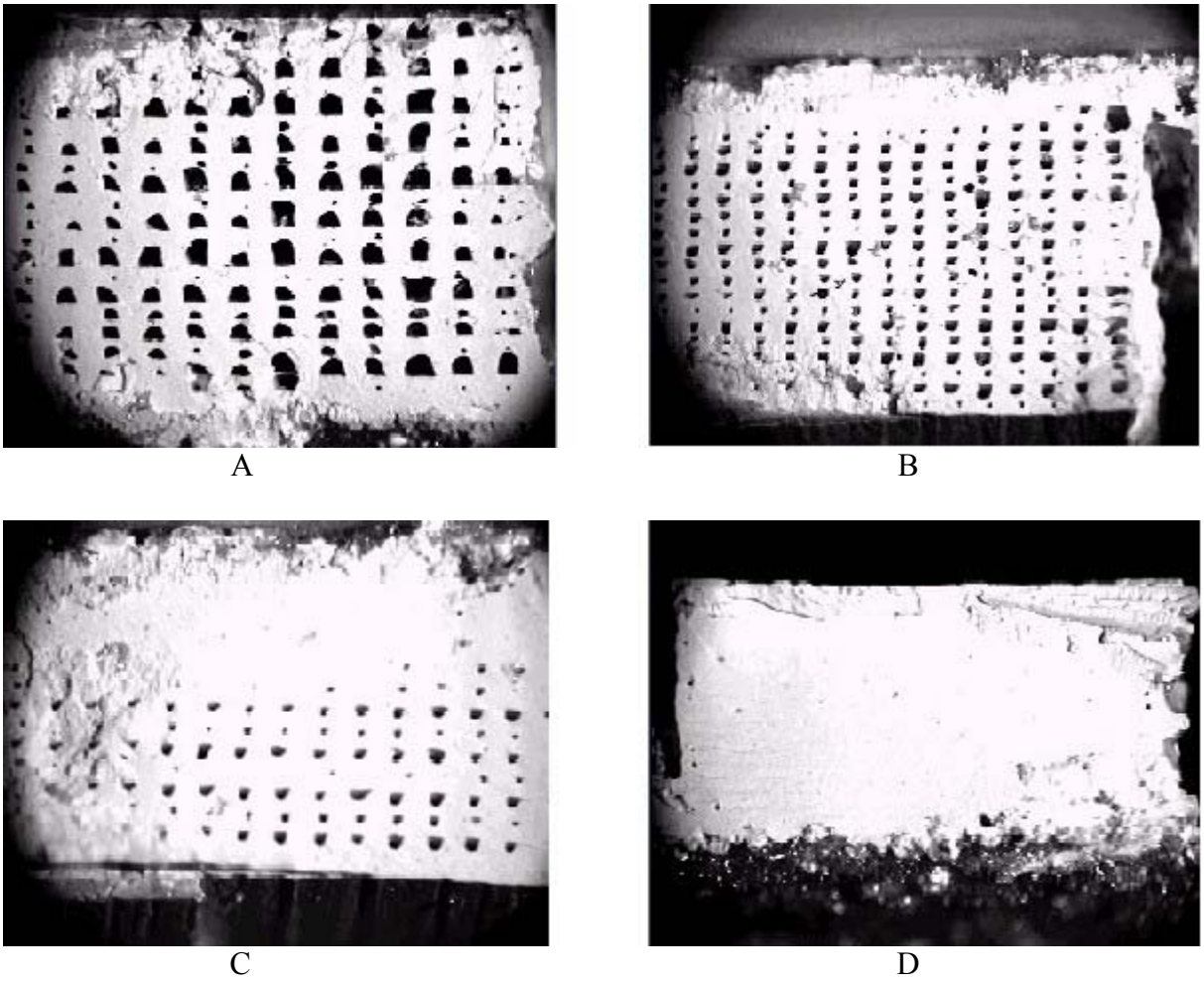

Figure 4.8: Parts built with the square nozzle (0.4x0.4 mm): (A) zero air gap, (B) –0.076 mm, (C) -0.13 mm, (D) –0.18 mm air gap

Following the fabrication, the samples, subjected to cooling due to convection with air at room temperature, were kept on the support in order to avoid any distortion.

Once reached the thermal equilibrium state, the samples were then removed from the foam and dipped in liquid nitrogen for few seconds. The fragility of the material in this condition was such that a sharp knife cut was sufficient to slice the part without affecting the shape of the roads. Pictures of the cross-sections of the samples obtained with this technique are reported in Figure 4.8.

The tendency of void formation resulted from a comparison of the above pictures suggested that a negative air gap should still be applied, when using square nozzles, in order to completely eliminate the void formation. However, intuitively, square cross-sectional roads should be stacked perfectly next to each other to create layers that should be piled easily on top of each other. This geometric consideration suggested that the presence of voids observed in Figure 4.8 was possibly caused by an underestimated flow rate. Increasing the deposition of the material in the unit time, the expansion of the melt, under the constrains of the tip at the exit of the nozzle, would fill the space between consecutive roads.

Several samples were consequently built increasing the flow rate and reducing the speed of deposition, while slice thickness and path orientation were kept identical. Because of the correlation between positioning and delivering system, the deposited cross-section area strictly depends on both the flow rate and the speed of the liquefier. However, since a very large flow rate increases the possibility of buckling failure, a higher mass deposition during the road formation was achieved reducing the speed of the positioning system.

Micrographs of cross-sections of parts built changing the process parameters (i.e. flow area, acceleration and speed of deposition) have been taken and compared. This parametric study led to the fabrication of successful samples (see an example in Figure 4.9) characterized by a apparently "completely dense structure".

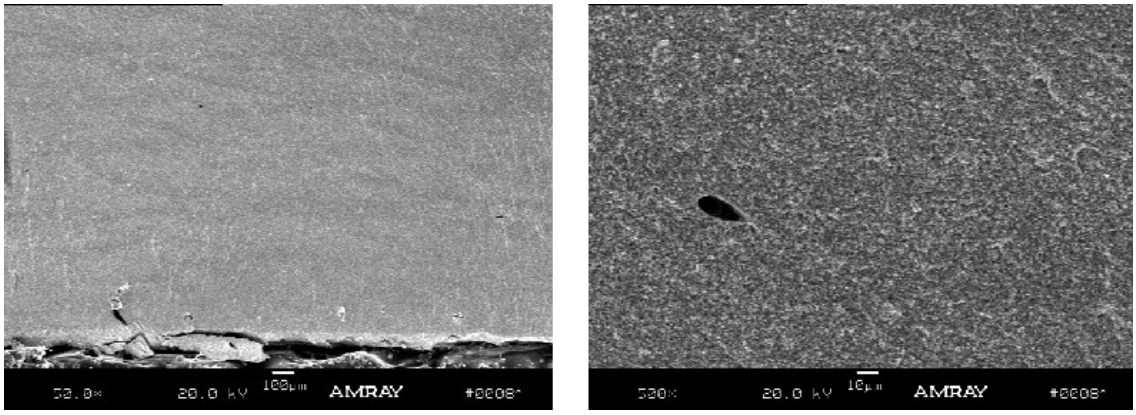

Figure 4.9: Micrograph of the section of a part built with the square nozzle (0.4x0.4 mm) with zoom on the imperfection (10 μm long)

In Figure 4.9, that shows the micrograph of the cross-section of a part obtained with the parameters reported in Table 4-2, no voids are detectable, beside the imperfection in the first layers (see right hand picture).

Table 4-2: Parameters for a successful part

Slice Thickness (*mm*)	0.254
Flow area (mm^2/s)	0.162
Air gap (*mm*)	0
Acceleration (mm/s^2)	76.2
Speed (*mm/s*)	10.16

In order to avoid any dependency of the cutting procedure on the road shape and appearance of the cross-section, micrographs of several slices of the same sample were taken and compared. Since no relevant differences were notable, it was concluded that the cutting procedure does not affect the microstructure of the part.

4.4 Parametric study of free extrusion with square nozzle in FDC

The results of the experiments described in section 4.3 showed that material properties and process parameters strongly affect the shape of the extruded strand. In addition, the theory of excluded plastics [7] explains that the swelling phenomenon is regulated by the surface tension and the rheological behavior of the melt. Moreover, since flow rate and temperature directly affects the rheological properties of the thermoplastic material, they indirectly influence the expansion and shape of the strand.

This section presents the model developed to perform a parametric study aimed to quantitatively determine the importance of process parameters and material properties on the shape of the strand.

4.4.1 Description of the approach

Because of the interest in using PZT/ECG9 to build object with improved performance and surface quality, and also in order to compare the results with the data obtained for a T12 round nozzle, the first step was to simulate the extrusion of the melt through a square nozzle of *0.254 mm x 0.254 mm* in size (whose orifice area is similar to the one typical of T12 nozzles).

The shear-thinning behavior shown by the thermoplastic material was modeled using a power law dependency of the viscosity on the shear rate:

$$\eta(\dot{\gamma}) = K \cdot \dot{\gamma}^{(n-1)} \tag{4.2}$$

where η represents the viscosity, K [$Pa*s^n$] and n (dimensionless) are material parameters while $\dot{\gamma}$ represents the shear rate.

According to the material data and following the discussion reported in Appendix 1, the values of K and n used to model the behavior of PZT/ECG9 were the following:

$$K = 633\ Pa * s^n \qquad \text{and} \qquad n = 0.6$$

Because of the complex problem, which involved the solution of highly non linear equations (i.e. equation (4.2)), and because of the intrinsic three-dimensional characteristic of the geometry, the process was divided in two phases

- The determination of the isothermal flow condition and of the pressure drop in the square nozzle;
- The determination of the shape of the extruded melt.

4.4.2 Model of the square nozzle

The model for the square nozzle was developed to find the conditions of the flow at the exit of the tip. It will be shown in section 4.4.3 that the fluid thermo dynamic state of the melt on this surface will be successively imported on the model for the strand formation. The comparison of the backpressure calculated for the square nozzle was also

confronted with the values determined for the round nozzle in order to verify that the new nozzle configuration would not increase the probability of buckling failure.

4.4.2.1 Mesh and boundary conditions: Definition of "*experimental case*"

Considering that the physical problem presents two planes of symmetry, the mesh used for the simulation was reduced to only one quarter of the entire geometry. Figure 4.10 depicts the mesh and the boundary conditions considered for the simulation: 1280 hexahedron elements with eight nodes were used, resulting in a total number of 1730 nodes for the entire problem.

In order to build a realistic model, the geometry created for the nozzle (see Figure 4.10) is characterized by a sharp change in the section, where the round orifice is suddenly connected to the final square shaped tip. This section was introduced with the purpose of representing the effect of the square pin used for the electron discharge method applied on a round nozzle.

Since the mesh models only one quarter of the total geometry, the flow rate imposed at the entrance of the convergence part represents also only one quarter of the actual flow rate, which was considered equal to $2.5 * 10^{-9}$ m^3/s. This value, that coincides with the one applied for the model of a round nozzle, was chosen in order to obtain comparable results. Moreover because of the results reached with the simulation of the melt front in the liquefier, the inflow was considered fully developed.

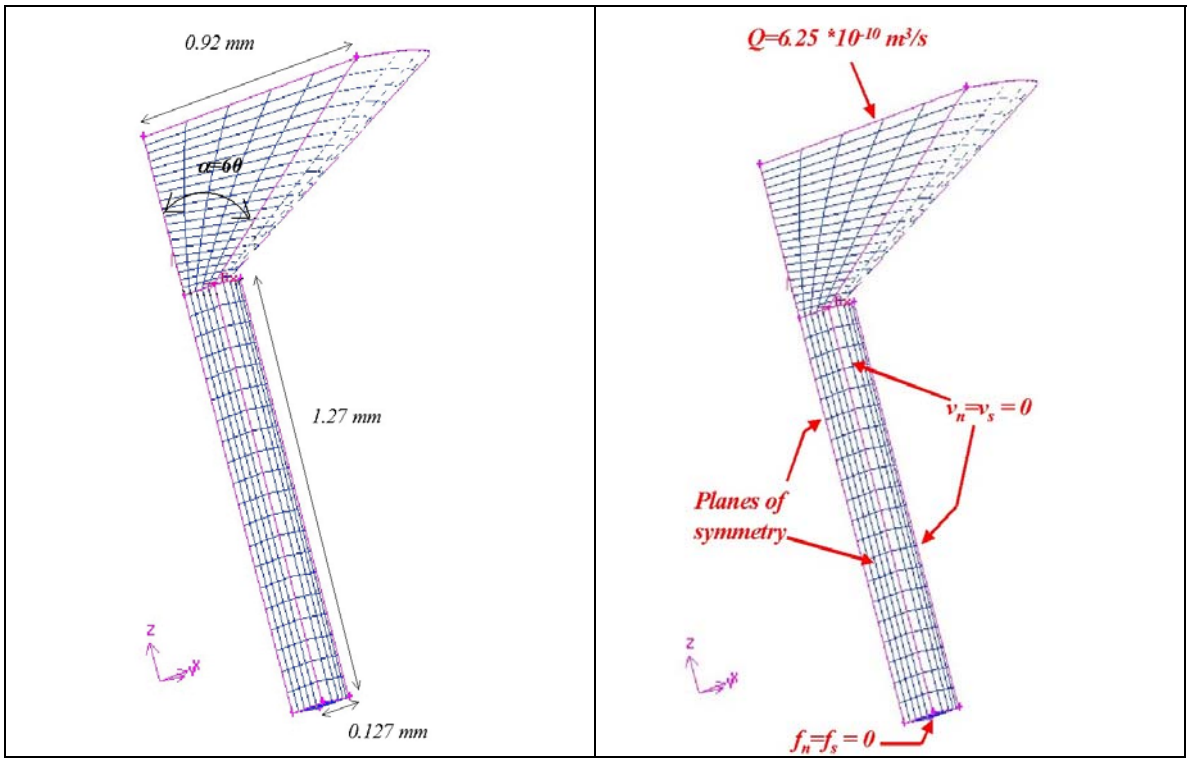

Figure 4.10: Geometry and boundary conditions for the model of the square nozzle

For the other surfaces the following flow conditions were assumed:

- Two plane of symmetry (respectively *xz* and *yz*);
- Zero velocity ($v_n = v_s = 0$) at the contact with the walls of the nozzle, in order to simulate no-slip conditions;
- No surface forces considered at the exit of the nozzle ($f_n = f_s = 0$), to simulate the fact that the flow is free from any constrains.

This simulation was performed to validate the model by comparing the results with the experimental data generated in the conditions described in section 4.3.3. For this reason, it will be referred to as the "*experimental case*".

4.4.2.2 Results

The velocity distribution and the velocity field obtained as part of the solution have been presented in Figure 4.11. Furthermore, Figure 4.12 shows the pressure drop calculated for the conditions reported in section 4.4.2.1.

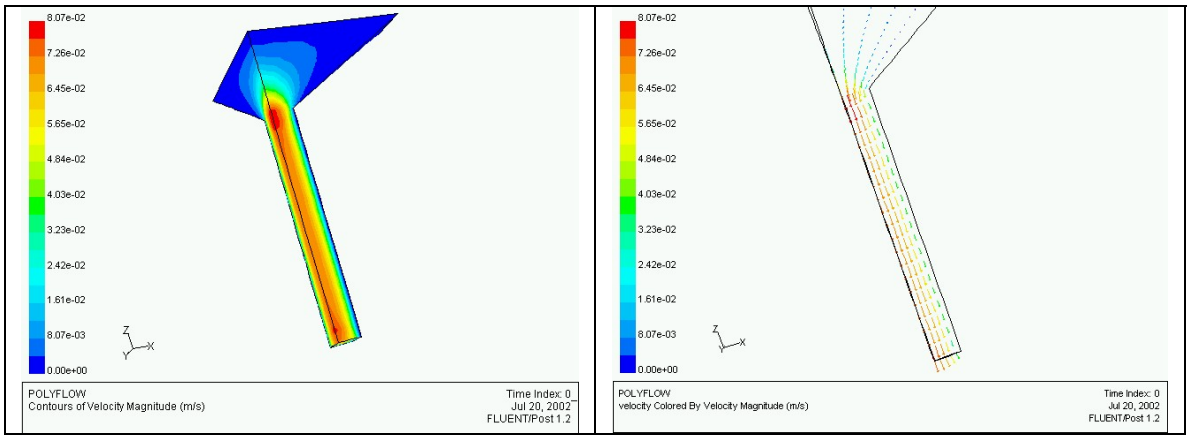

Figure 4.11: Velocity distribution and velocity vectors in the *"experimental case"*

It can be seen that both the profiles of pressure and velocity distribution show zero gradients on the planes *xz* and *yz*, hence they satisfy the conditions of plane symmetry assumed for the model. Moreover it is observable, from the plot of the velocity vectors, as well as from the constant drop of the pressure along the z axis, that the flow becomes fully developed before reaching the end of the tip.

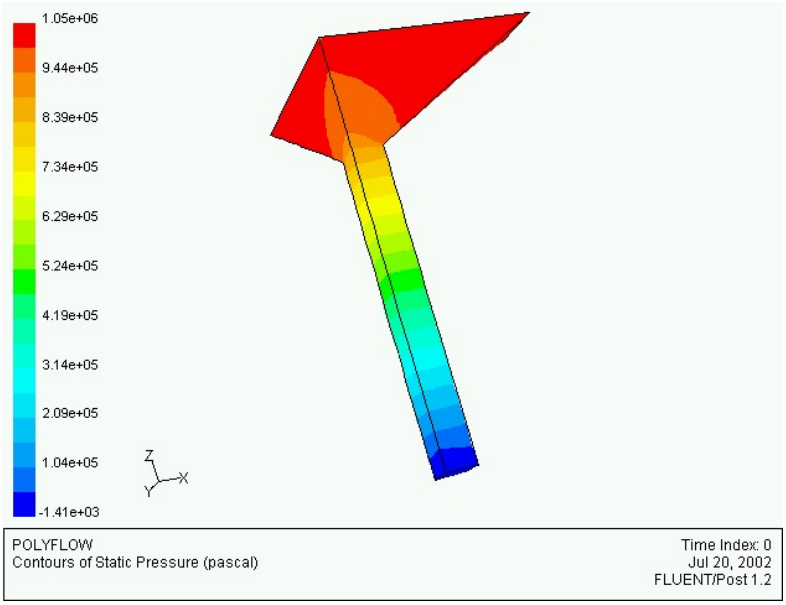

Figure 4.12: Pressure drop in the *"experimental case"*

Comparing the pressure drop obtained with the square nozzle (see Figure 4.12) with the one obtained for the round nozzle (see Figure 3.18), it is possible to conclude that the square nozzle does not affect the pressure drop noticeably, hence does not increase the probability of failure.

4.4.3 The strand formation

Once the thermal flow dynamics state of the melt in the nozzle was calculated and it was concluded that the flow regains its fully developed characteristic few microns after the change of section, the model for the free extrusion was developed.

In this phase, since the nozzle is maintained at a temperature of 140^{o}C, while the envelope temperature is approximately 40^{o}C, the material is subjected to temperature variations that affect its thermal flow dynamic state. In order to take into consideration

the dependence of the melt rheological behavior from the temperature, the Arrhenius relation H(T) was considered as well:

$$\eta(\dot{\gamma}, T) = \eta(\dot{\gamma}) \cdot H(T) \tag{4.3}$$

$$H(T) = \exp\left[\alpha\left(\frac{1}{T} - \frac{1}{T_\alpha}\right)\right] \tag{4.4}$$

where α represents the activation energy and T_α is the reference temperature, for which H(T) =1 [22].

Applying the procedure described in Appendix 1 to the data reported in the same section, the values for the material parameters α and T_α used to model the behavior of PZT/ECG9 were taken as:

$$\alpha = 19800 \quad \text{and} \quad T_\alpha = 413$$

Because of the non-isothermal characteristic of the melt during the extrusion process, its heat capacity and its thermal conductivity had to be determined through experimental analysis and considered in the model. Applying the experimental approach described in Appendix 1, the heat capacity for the melt was considered approximately constant and equal to *500 J/KgK* (value registered for a temperature of 140^oC) while the thermal conductivity was taken as *1.5 W/mK*.

Since the surface tension of the melt is directly affecting the shape of the strand, its value needed also to be experimentally determined and incorporated in the model. Even though the ring method adopted for the measurement did not work very well for PZT/ECG9 and it provided scattering data for the binder (see appendix 1), a parametric

study showed that negligible differences could be detected for value of σ in the range of 0.025 and 0.1 N/m^2. For this reason an average value of σ = 0.05 N/m^2 was considered for the model.

4.4.3.1 Mesh

The geometry and the boundary conditions of the physical problems present two planes of symmetry, hence only one quarter of the total geometry was modeled (see Figure 4.13). Using this approach it was possible to reduce the total number of elements (hexahedrons with eight nodes) to 1980, and the number of nodes to 2744, without sacrificing resolution.

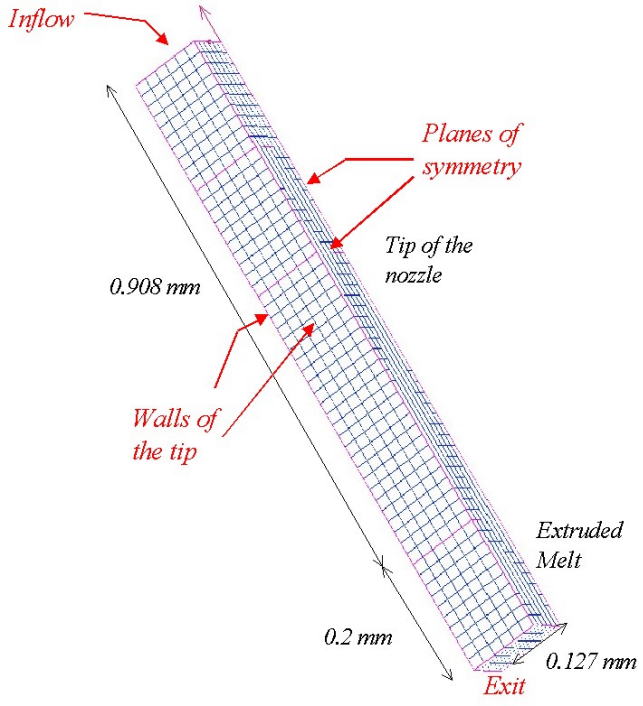

Figure 4.13: Mesh and geometry for the model for the strand formation

4.4.3.2 Experimental case

Flow and thermal boundary conditions

In order to obtain results compatible with the data generated using the square nozzle (see section 4.4.2.2), the boundary conditions applied to the model had to reflect the process conditions used for the test. For this reason it was assumed:

- A fully developed inflow of $Q = 6.25 \cdot 10^{-10} m^3 / s$, which is a quarter of the actual flow rate, on the surface at the entrance;
- No slip conditions at the wall of the nozzle, thus $v_n = v_s = 0$ on the surfaces labeled as wall 1, wall 2 and wall 3 in Figure 4.21;
- No surface forces acting at the exit, thus $f_n = f_s = 0$;
- Free surface conditions on the portion of the geometry representing the extruded material: $\sigma = 0.05 \frac{N}{m^2}$;
- Two planes of symmetry.

The thermal boundary conditions considered for realistic simulations were taken as:

- Temperature assumed on the top surface, which corresponds to the surface at the exit of the conical part of the nozzle, as T = 413 K;
- Two insulated surfaces because of the two planes of symmetry;
- Constant temperature of T = 413 K on the wall surfaces of the tip;

- Flux density $q = 20 * (T - 313)$ considered on the free surface, in order to simulate the heat convection with air at T = 313 K;
- Flux density $q = 0$ assumed on the outflow surface in order to simulate the effect of the contact with the rest of the strand. Since the temperature gradient is undetectable and the value of thermal conductivity is small the conduction through the small section, can be considered negligible.

To achieve the convergence the evolution technique (see Appendix 3) was used on the exponent of the power law as well as on the coefficient α of the Arrhenius relation (see Appendix). The functions used for the two parameters were as follows:

$$n = 0.6 * \frac{1}{s} \text{ and } \alpha = 19800 * \left(-0.59 * s + 1.59 * s^2\right), \text{ with } 0.6 < S < 1.$$

Results

The section of the strand obtained with the developed model, under the conditions above, is shown in Figure 4.14.

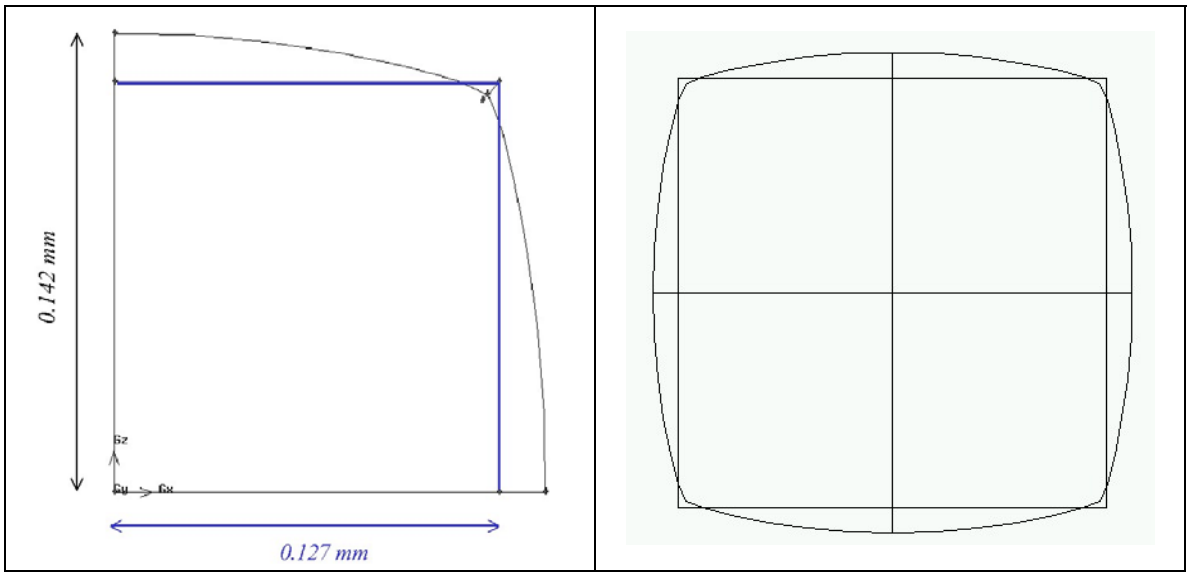

Figure 4.14: Section of the strand (black), computed with a square nozzle (blue)

In order to determine the swelling of the melt, equivalent diameters were defined, both for the nozzle and for the strand, as the diameters of round sections that would lead to the same areas:

$$\pi \cdot \left(\frac{D_e}{2} \right)^2 = A$$

where D_e represents the equivalent diameter and A the area in consideration. The calculation of the equivalent diameter is given by:

$$D_e\big|_{nozzle} = 2 \cdot \sqrt{\frac{(2 \times 0.127)^2}{\pi}} = 0.2866\, mm$$

For the extruded melt the calculation of the area of the strand is more complicated. According to Figure 4.14 the geometry of the cross-section of the strand can

be considered as a combination of a circular and a square shape. For this reason the area was calculated as:

$$A\big|_{extruded} = \pi d^2 + \left[(2d)^2 - \pi d^2\right] \times \frac{50}{100} = 7.2 \times 10^{-2}\ mm^2$$

where d represents the resulted length of the semi-axis (*0.142 mm*). Consequently, the equivalent extruded diameter is:

$$D_e\big|_{extrudate} = 0.303\ \ mm$$

and the calculated parameter S for the swelling phenomenon is:

$$s = \frac{D_e\big|_{extrudate}}{D_e\big|_{nozzle}} = \frac{0.303}{0.2866} = 1.056 \qquad (4.5)$$

In Figure 4.15 to Figure 4.18, the results in term of velocity distribution, pathlines, pressure and temperature distribution have been reported.

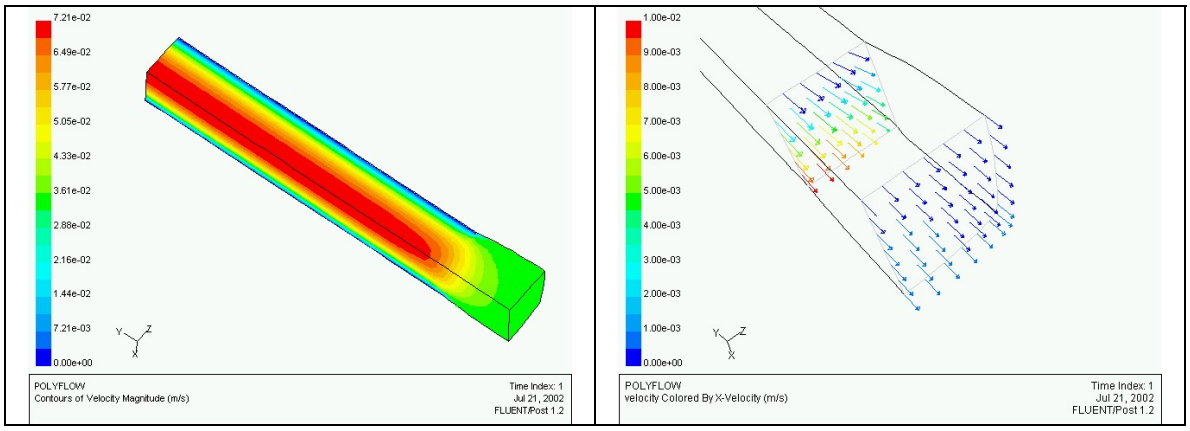

Figure 4.15: Velocity distribution and velocity vectors for stand formation

It can be seen that the profile of velocity distribution show zero gradients on the planes *xz* and *yz*, hence it satisfy the conditions of planes of symmetry assumed for the model. More specifically it is possible to observe that the velocity plot at any section of the tip has a parabolic profile; this suggests a fully developed flow. At the exit of the nozzle, where the melt is subjected only to its surface tension and to the gravitational force, the flow reaches the conditions typical of a *plug flow*: on the whole section the velocity is constant and its magnitude is an average of the values found inside the tip.

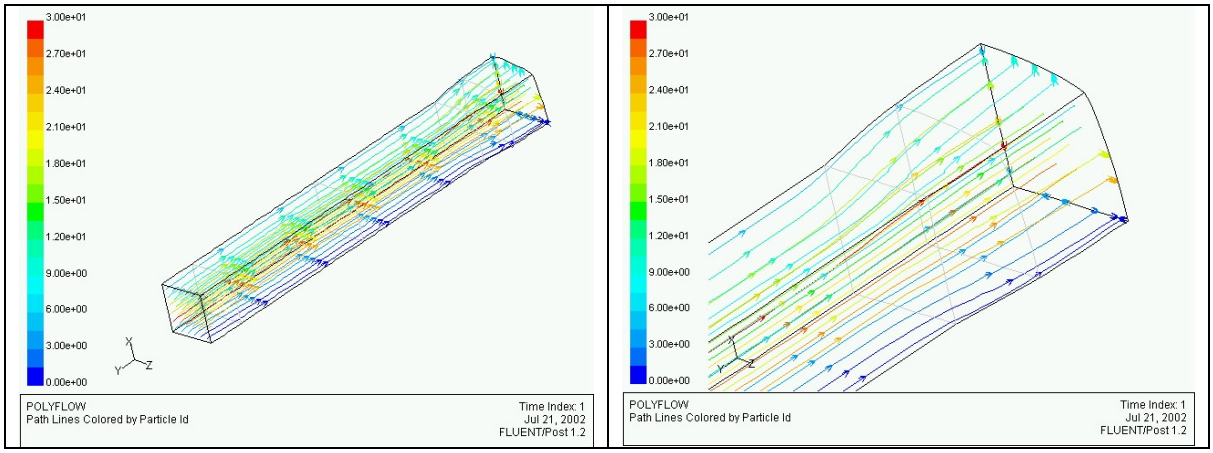

Figure 4.16: Path lines

From the velocity vectors distribution and from Figure 4.16, it can be observed that the flow at the bottom surface of the extruded is moving only perpendicular to the surface ($v_s = 0$). This means that the strand reached an equilibrium in the lateral expansion, hence the swelling process has already ended.

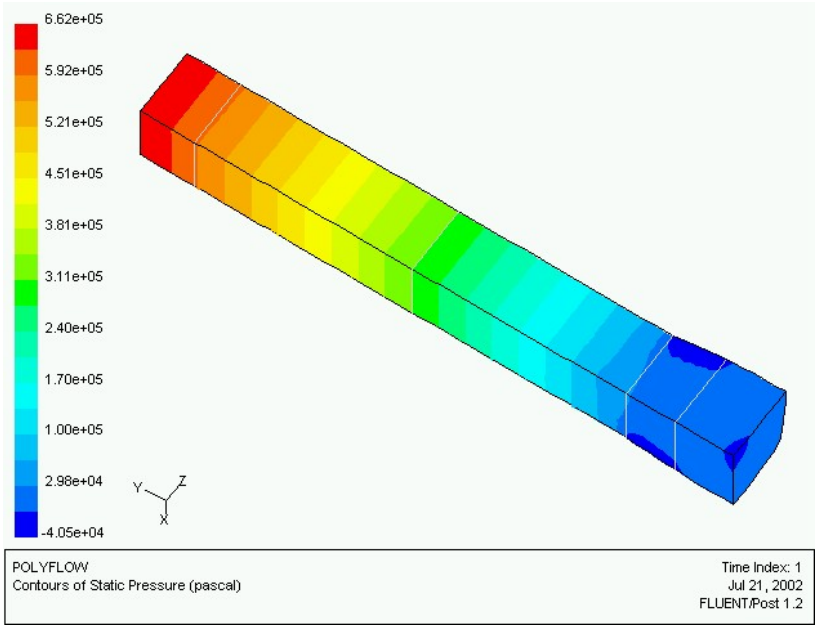

Figure 4.17: Pressure distribution and velocity vectors

The pressure drop gradients of Figure 4.17 correspond to the values obtained for the square nozzle (see Figure 4.12). This result gives evidence of the fact that the flow can be simulated as fully developed at the tip entrance.

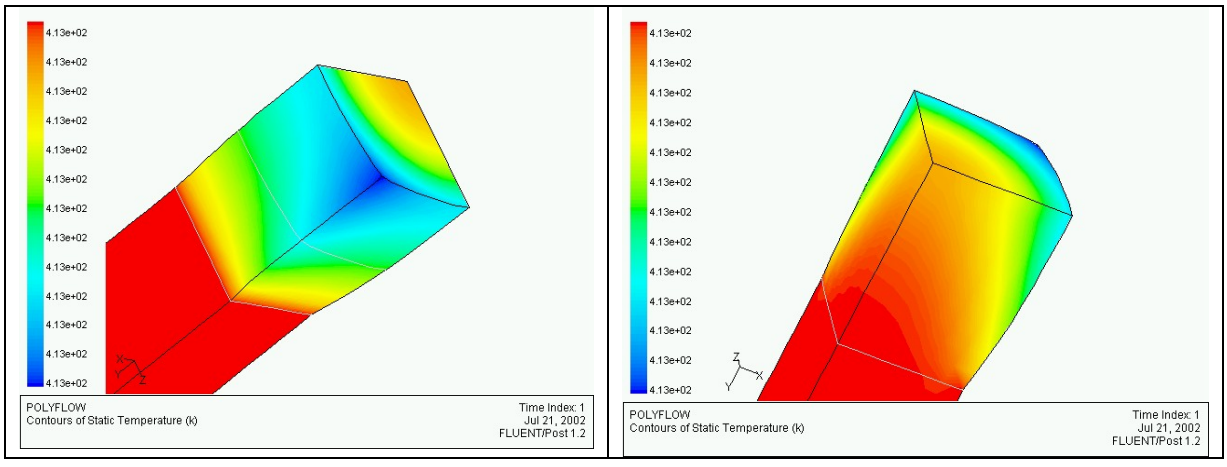

Figure 4.18: Temperature distribution (min. value is 413 K, max 413.15 K)

In Figure 4.18, which shows the temperature distribution in the strand, it is possible to notice that the strand can be considered almost isothermal (the temperature ranges from 413K to 413.15K), both because of the small length of the extruded as well because of the negligible heat flux assumed on the bottom surface.

4.4.3.3 Effect of process parameters

This section describes the parametric study conducted to determine the influence of the different process parameters on the shape of the strand.

Flow rate

In order to quantify the importance of the flow rate on the free extrusion process of the melt, several simulations have been conducted considering three different flow rates:

$Q_1 = 0.625 * 10^{-9}\ m^3/s$, $Q_2 = 1.25 * 10^{-9}\ m^3/s$, $Q_3 = 2.5 * 10^{-9}\ m^3/s$

No significant changes could be detected in the cross section of the strand for these different values of the flow rate. As it could be intuitively expected, the three solutions differ mostly in term of pressure, velocity distribution and vector plot (see Figure 4.19 and Figure 4.20).

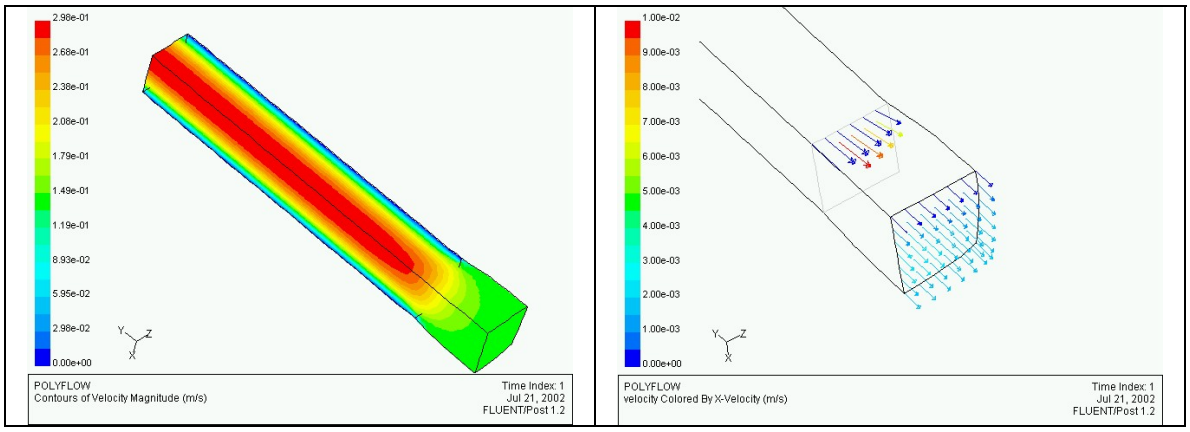

Figure 4.19: Velocity distribution and velocity vectors for Q = 2.5* 10^{-9} m^3/s

The plot of the velocity vectors (see Figure 4.19) shows that at the exit surface the velocity component v_s is slightly greater than zero. This means that a longer portion of the extruded melt should be modeled to capture the change in the shape of the strand

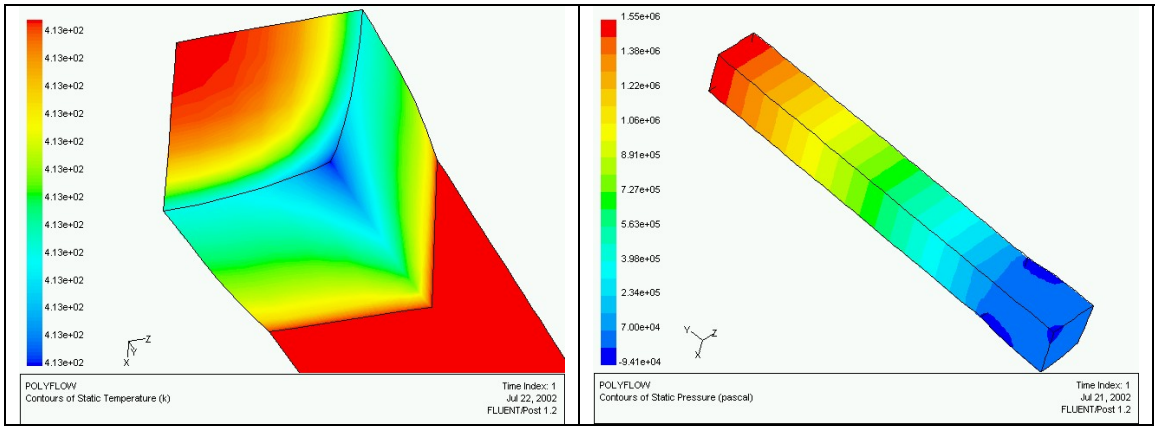

Figure 4.20: Temperature (min value *413.08 K*; max. value *415.15 K*) and pressure distribution for Q = *2.5* 10^{-9} m^3/s*

A comparison of the results obtained for the three different values of the flow rate shows that although different, the plots of velocity, pressure and temperature distribution follow similar profiles.

Conclusions

The results show that the process parameters do not have strong effect on the shape of the strand. Velocity and pressure distribution as well as velocity vectors are qualitatively similar for the three cases of flow rate $Q_1 = 0.625*10^{-9}$ m^3/s, Q2= $1.25*10^{-9}$ m^3/s, $Q_3= 2.5*10^{-9}$ m^3/s. However, as intuitively expected, the quantitative plots change considerably.

In the case of $Q_3= 2.5*10^{-9}$ m^3/s the pressure drop in the nozzle is more twice the pressure drop calculated for $Q_1 = 0.625*10^{-9}$ m^3/s. When a filament filled with ceramic particle is employed, this increase in the pressure drop can cause the buckling failure, thus the interruption for maintenance of the process.

4.5 Reverse engineering approach for optimal nozzle designs

The porous structure typical of parts built using FD technologies is unacceptable when the objective is to manufacture components for direct use. In section 2.3 it was explained that for the fabrication of ceramic parts, for example, the binder burn out process can constitute a critical phase. It was observed that the pressure of the air trapped inside voids present in the green body could cause the failure of the part.

From the studies conducted on the evolution of the road during deposition (see chapter 3) it was concluded that the void formation is mainly caused by the elliptic shape

of the road (see Figure 4.1). Intuitively, the deposition of building blocks with square cross sections will improve the stacking of roads, hence will reduce or even eliminate the presence of voids. Experiments conducted using square nozzles (see section 4.3.2) showed however that in order to obtain square strands the swelling phenomenon couldn't be neglected.

This section presents the reverse engineering approach adopted to determine the nozzle configurations, vis-à-vis of the process parameters and material properties, that will lead to the deposition of the square strands.

4.5.1 Mesh

The reverse engineering approach adopted in this study deals with the computation of the shape of a die that produce an extrudate of a desired shape. Consequently, since the configuration of the nozzle becomes part of the solution as well, a remeshing technique (see Appendix 3) needs to be applied not only on the domain of the strand, for the determination of the geometry of the free surface, but also on a portion of the domain of the nozzle.

For this reason the exit region of a millimeter length of the tip was ideally divided in three zones [39]. In the left hand side of Figure 4.21, zone one, two, three and four represent respectively:

- The portion of the extruded melt;
- The fixed section of the tip: in order to avoid uncontrolled expansion of the melt, the shape of the die had to be maintained fixed for a certain length;

- The adaptive section of the tip: in this zone the shape of the cross section of the nozzle gradually changes from the initial one (in this case square) to the desired one at the exit.
- The starting section of the tip. This part had to be long enough in order to insure fully developed flow at the entrance of the adaptive section.

For purposes of consistency, the mesh used for the reverse engineering approach had the same general characteristics of the one used to determine the strand formation (see section 4.4.3.1). However, in this case, due to the necessity of applying a remeshing technique, the tip of the nozzle had to be divided in three subdomains.

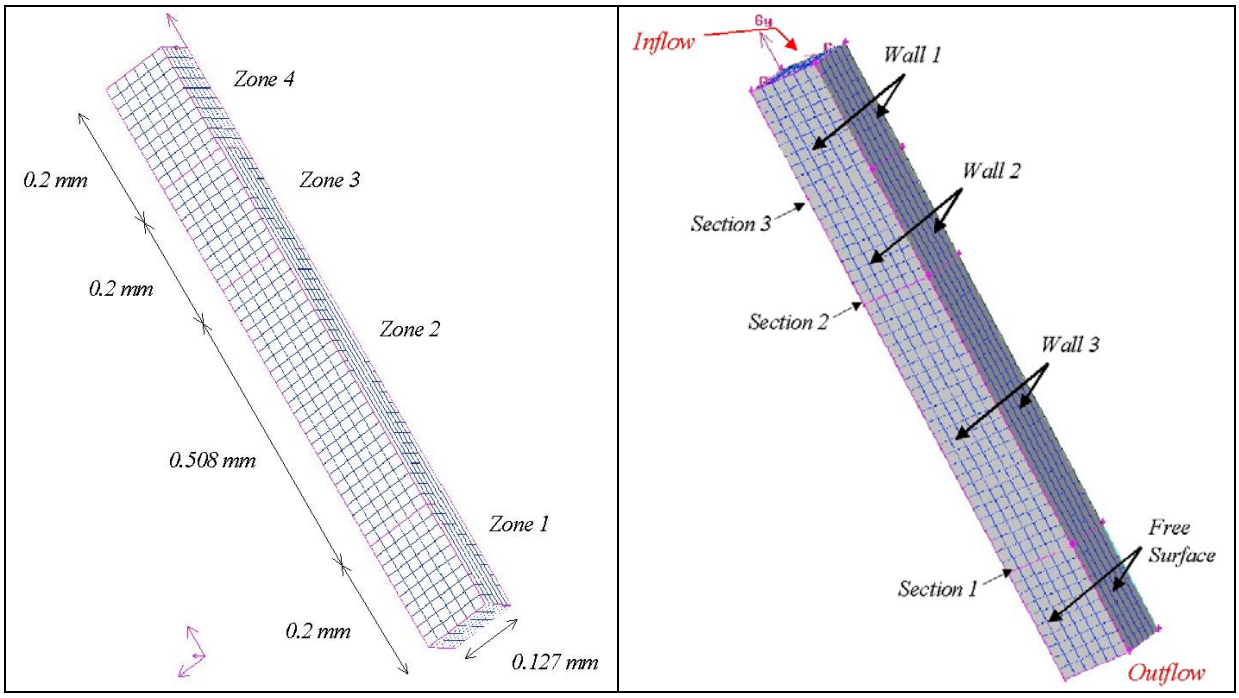

Figure 4.21: Mesh and boundary conditions for the reverse engineering approach

4.5.2 "Experimental case" conditions

This section presents the study conducted to determine the nozzle configuration that, in the conditions referred to as "*experimental case*" (see section 4.4.2.1), will provide a square strand.

Thermal and flow boundary conditions

In order to be consistent with the model developed for the extrusion of the strand, the thermal and flow boundary conditions applied for the "*inverse extrusion*" were the same conditions presented in section 4.4.2.1. However, since the geometry of zone 1, zone 2 and zone 3 of Figure 4.21 were considered part of the solution, a remeshing technique, based on the arbitrary Lagrangian Eulerian approach [39], was applied under the conditions:

- Zone 3: "adaptive section for prediction" with inlet corresponding on section 3 and outlet corresponding on section 2;
- Zone 2: "fixed section for prediction";
- Zone 1: "extrusion", with inlet corresponding with section 1 and outlet the surface at the exit.

Results

Sections of the strand and of the optimized nozzle design obtained with the model, under the described conditions, are presented in Figure 4.22. Because of the variation in the velocity field, due to the no-slip conditions on the wall and to the shear-

thinning behavior of the melt, the nozzle has to be manufactured according to a complex star shape configuration in order to compensate the swelling phenomenon.

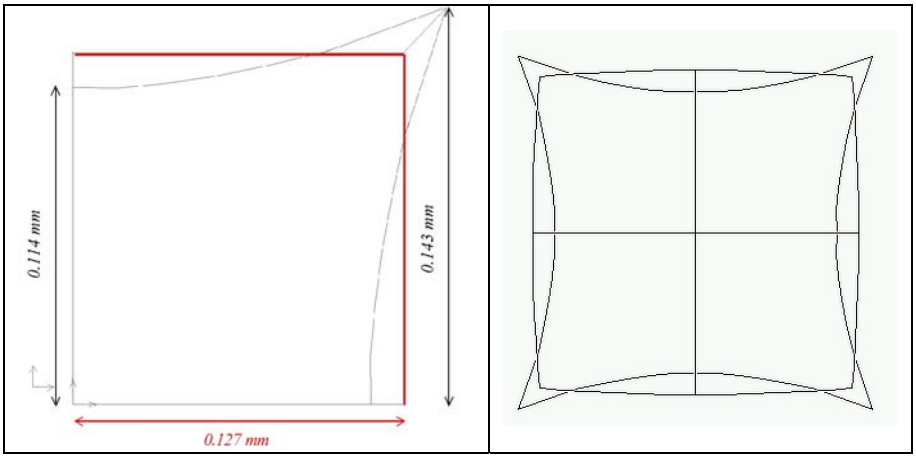

Figure 4.22: Section of the end of the nozzle (black) computed in order to have a square shaped strand. The line in red shows the initial cross section of the nozzle

From the picture on the right hand side of Figure 4.22, it can be seen that the section of the strand is very close to a square cross section. With this shape of the strand, the part integrity would considerably improve.

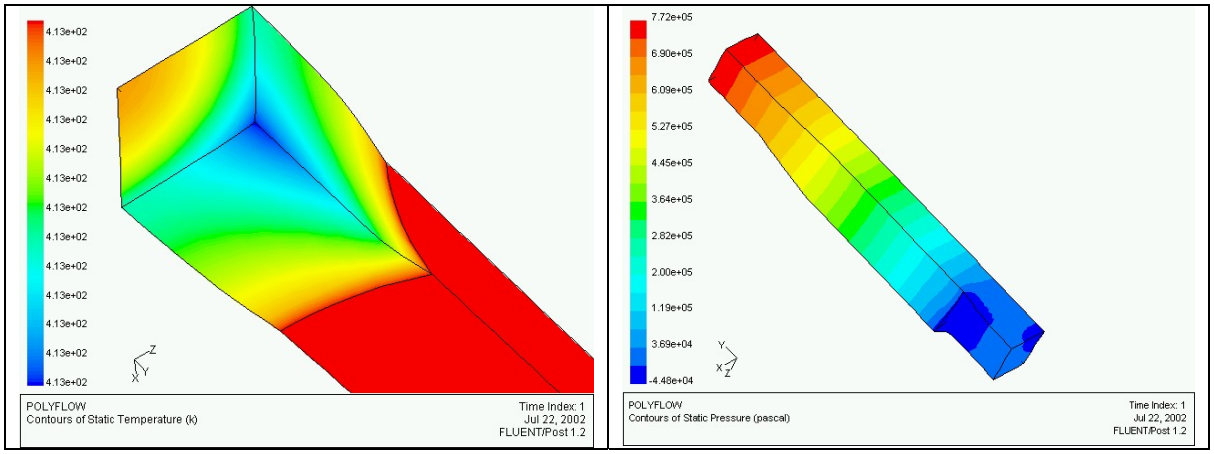

Figure 4.23: Temperature and pressure distribution

In Figure 4.23 the temperature and pressure distribution have been presented in order to determine the thermo fluid dynamic state of the strand. Because of the larger surface subjected to air convection, the melt in proximity of the “corner” of the square shaped nozzle is cooling faster than the rest of the melt (see picture in the left hand side). The contour plots meet the physical expectations, showing that the temperature at the core of the strand is higher and it is gradually decreasing towards the “corner”. It is also possible to observe that the temperature gradient is still negligible for the length of the strand considered.

The plot of the distribution of the pressure drop shows a constant gradient along the direction of the extrusion, hence it reveals a fully developed flow in the tip of the nozzle. At the exit, the melt, subjected only to the surface tension, is free to move in any direction hence the pressure is null.

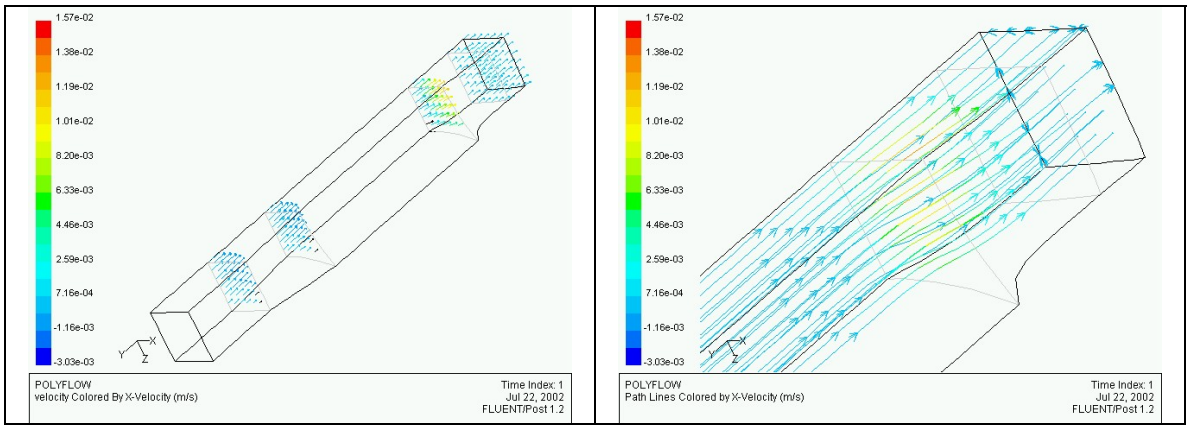

Figure 4.24: Velocity vectors and path lines

The plot of the velocity vector reported in the left hand side of Figure 4.24 shows that at the bottom surface the tangential velocity component $v_s = v_x = 0$, hence the strand

shape is not going to expand any longer. The shape of the strand considered at this section is consequently fully developed.

It should be underlined that in this study the focus was on the free extrusion process. Further development of the model should consider also the simulation of the deposition phase, in order to predict if the square shape is maintained after the contact with the platform.

4.5.3 Parametric study of the shape of the nozzle

In section 4.5.2 it was shown that in order to obtain a square strand, the nozzle had to be manufactured according to a complex star shaped configuration. However, the particular cross-section presented in Figure 4.22 is the optimal design for the conditions assumed for the "*experimental case*". In this section the attention will be focus on the influence of the process parameters and of the material properties on the determination of the optimal nozzle configuration.

4.5.3.1 Influence of the process parameters

Influence of the flow rate: definition of "reference case"

In order to determine the effect of the flow rate on the shape of the nozzle the same mesh described in section 4.5.2 was used assuming the following conditions:

- A fully developed inflow of $Q = 2.5 \cdot 10^{-9} m^3 / s$;
- $v_n = v_s = 0$ on the surfaces labeled as wall 1, wall 2 and wall 3 in Figure 4.21;

- No surface forces acting at the exit, thus $f_n = f_s = 0$;

- Free surface (see Figure 4.21) with $\sigma = 0.05 \frac{N}{m^2}$.

- Two planes of symmetry.

The thermal boundary conditions considered for a realistic simulation were:

- Constant temperature of T = 413 K on the top surface;

- Two insulated surfaces because of the two planes of symmetry;

- Constant temperature of T = 413 K on the wall surfaces of the tip;

- Flux density $q = 20 * (T - 313)$ assumed on the free surface;

- Flux density $q = 0$ taken on the outflow surface.

For these conditions, the results (in term of nozzle design) are presented in Figure 4.25. A comparison between Figure 4.25 and Figure 4.22 shows that, in the case of larger flow rate, the z coordinate of the corner E is shorter ($z_{E\_Qsmall} = 0.143\,mm; z_{E\_Qlarge} = 0.139\,mm$) while the semi-axial length of the nozzle (which corresponds to the z coordinate of the vertex F) is longer ($z_{F\_Qsmall} = 0.114\,mm;\ z_{F\_Qlarge} = 0.1115\,mm$). Geometrically this means that the cross-section of the nozzle should be "closer to a square" when the flow rate is bigger.

This result is caused by the shear thinning behavior of the material: if the same nozzle configuration was applied in the two different conditions, the higher flow rate

would have caused a larger expansion at the corner E, where the gradient of velocity is larger for a larger flow rate, originating round corners.

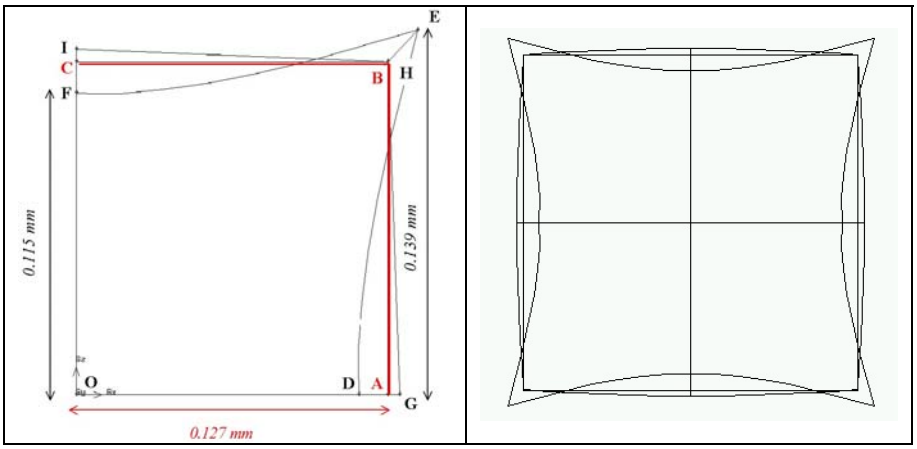

Figure 4.25: Star-shape of the nozzle when $Q = 2.5 \cdot 10^{-9} m^3 / s$ - the *reference case*

For the parametric study described in the next sections, this simulation, defined by the thermal and boundary conditions described above (with $Q = 2.5 \cdot 10^{-9} m^3 / s$), will be considered as the "*reference case*".

4.5.3.2 Influence of the material properties

Influence of the value n and K of the power law

In order to evaluate the effect of the material properties on the shape of the nozzle the same mesh described in section 4.5.2 was used under the conditions of the "*reference case*" described in section 4.5.3.1.

In the simulations run for this study the parameter *K* and *n* of the power law were varied independently. In this section the results have been displayed as a function of *n* for three different values of *K*.

Case of K = 2000

Table 4-3: Geometrical parameters as a function of *n* for *K = 2000*

	E [*mm*] ***Vertex 10***	**D [*mm*]** ***Vertex 11***	**F [*mm*]** ***Vertex 9***	**G [*mm*]** ***Vertex 4***	**I [*mm*]** ***Vertex 1***	**H [*mm*]** ***Vertex 2***
n = 0.4	(0.153,0.153)	(0.120,0)	(0,0.120)	(0.130,0)	(0, 0.130)	(0.125, 0.125)
n = 0.5	(0.141,0.141)	(0.118,0)	(0,0.118)	(0.131,0)	(0, 0.131)	(0.126, 0.126)
n = 0.6	(0.137,0.137)	(0.1115,0)	(0,0.115)	(0.132,0)	(0, 0.132)	(0.127, 0.127)
n = 0.8	(0.133,0.133)	(0.112,0)	(0,0.112)	(0.129,0)	(0, 0.129)	(0.133, 0.133)
n = 0.9	(0.131,0.131)	(0.110,0)	(0,0.110)	(0.134,0)	(0, 0.134)	(0.130, 0.130)
n = 1	(0.130,0.130)	(0.109,0)	(0,0.109)	(0.135,0)	(0, 0.135)	(0.130, 0.130)

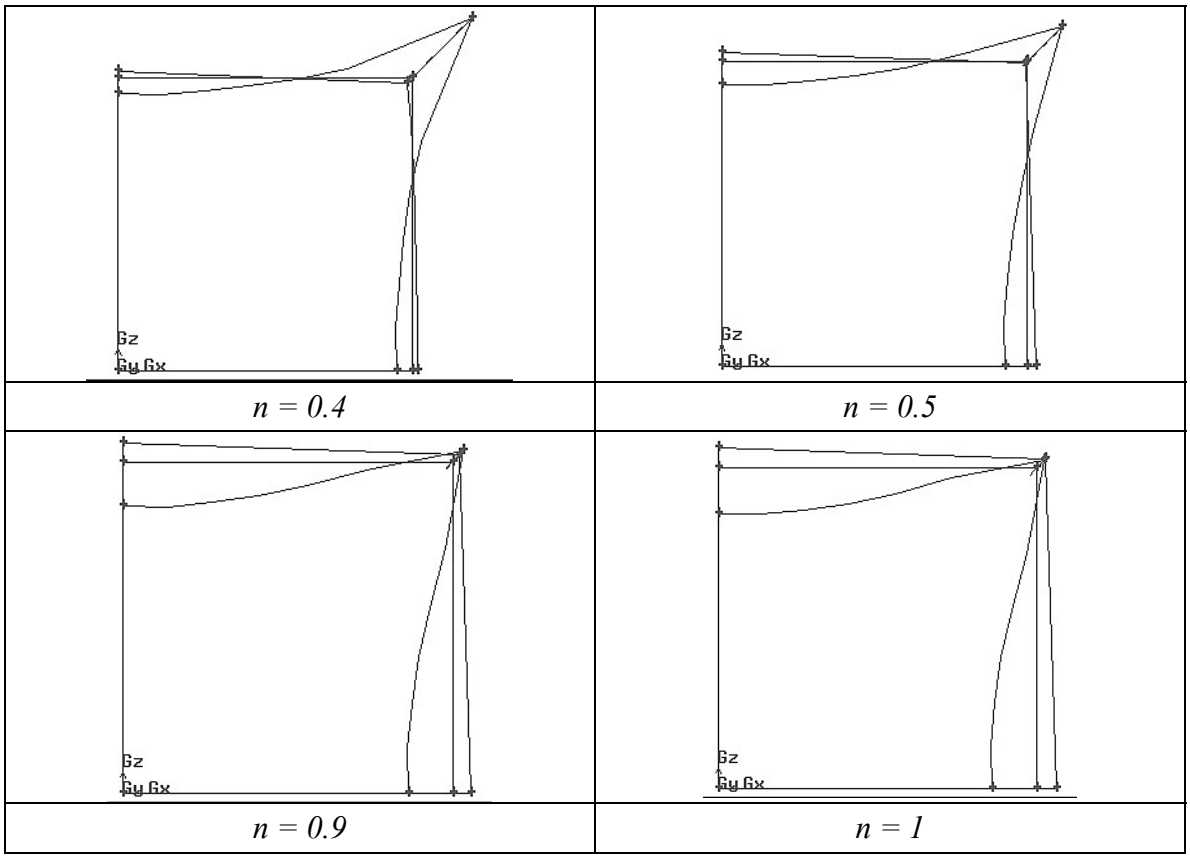

Figure 4.26: Geometry of the nozzle as a function of *n* for *K = 2000*

The results of the simulations for *K = 2000* are summarized in Table 4-3 and the configurations are shown in Figure 4.26. It can be observed that an increasing value of *n* leads to nozzle with smaller area and reduced sharpness of the corners.

Case of K = 1200

Table 4-4: Geometrical parameters as a function of *n* for *K = 1200*

	E [*mm*] ***Vertex 10***	**D [*mm*]** ***Vertex 12***	**F [*mm*]** ***Vertex 9***	**G [*mm*]** ***Vertex 4***	**I [*mm*]** ***Vertex 1***	**H [*mm*]** ***Vertex 2***
n = 0.5	(0.143,0.143)	(0.117,0)	(0,0.117)	(0.131,0)	(0, 0.131)	(0.126, 0.126)
n = 0.6	(0.138,0.138)	(0.115,0)	(0,0.115)	(0.132,0)	(0, 0.132)	(0.127, 0.127)

Table 4-4 (continued)

n = 0.8	(0.133,0.133)	(0.112,0)	(0,0.112)	(0.133,0)	(0, 0.133)	(0.129, 0.129)
n = 0.9	(0.131,0.131)	(0.110,0)	(0,0.110)	(0.134,0)	(0, 0.134)	(0.130, 0.130)
n = 1	(0.130,0.130)	(0.109,0)	(0,0.109)	(0.135,0)	(0, 0.135)	(0.130, 0.130)

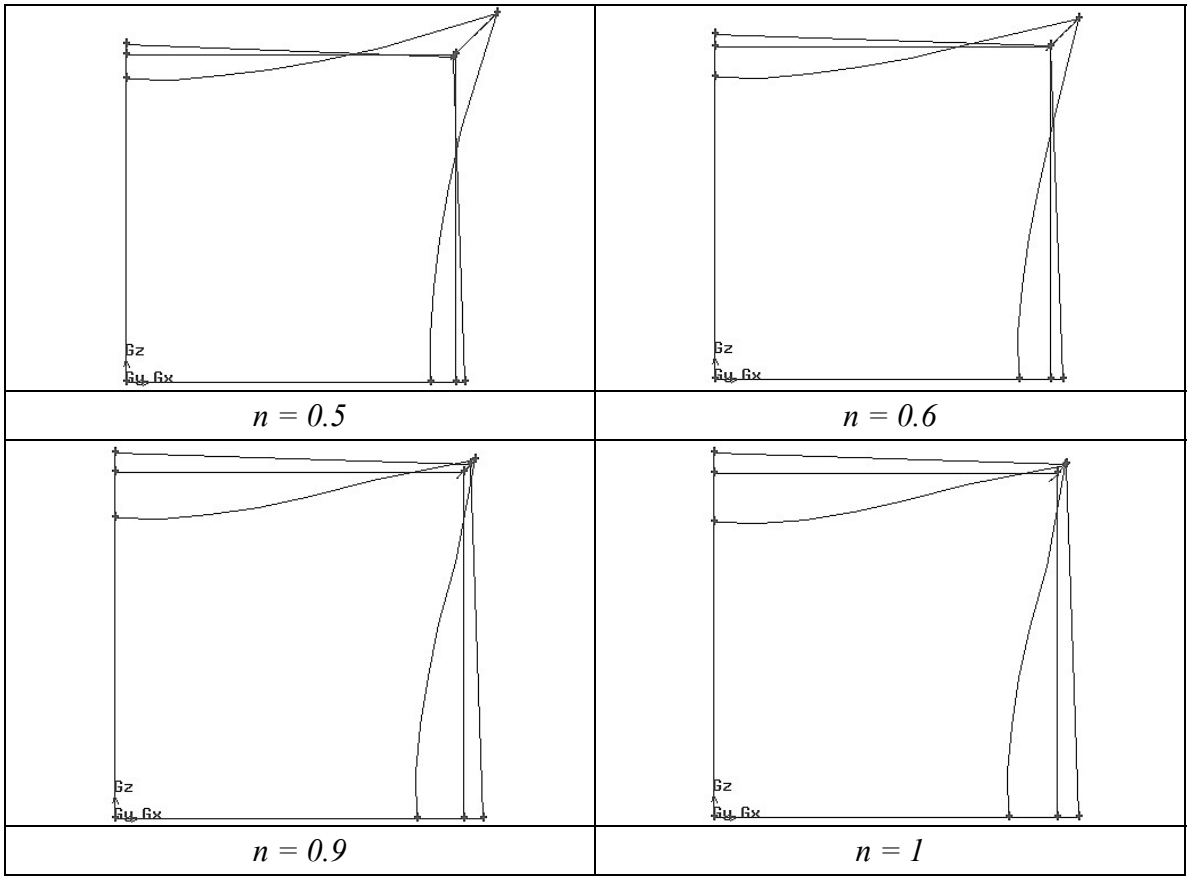

Figure 4.27: Geometry of the nozzle as a function of *n* for *K = 1200*

The results summarized in Table 4-4 and presented in Figure 4.27 show a tendency similar to the one observed for the case with *K = 2000*: nozzles with smaller cross-sectional area and with less sharp corners are optimal for higher values of *n*.

Case of K = 100

Table 4-5: Geometrical parameters as a function of *n* for *K = 100*

	E [*mm*] ***Vertex 10***	**D [*mm*]** ***Vertex 12***	**F [*mm*]** ***Vertex 9***	**G [*mm*]** ***Vertex 4***	**I [*mm*]** ***Vertex 1***	**H [*mm*]** ***Vertex 2***
n = 0.5	(0.258,0.258)	(0.114,0)	(0,0.114)	(0.133,0)	(0, 0.133)	(0.121, 0.121)
n = 0.6	(0.191,0.191)	(0.113,0)	(0,0.113)	(0.133,0)	(0, 0.133)	(0.124, 0.124)
n = 0.8	(0.136,0.136)	(0.111,0)	(0,0.111)	(0.134,0)	(0, 0.134)	(0.128, 0.128)
n = 0.9	(0.133,0.133)	(0.110,0)	(0,0.110)	(0.134,0)	(0, 0.134)	(0.129, 0.129)
n = 1	(0.131,0.131)	(0.109,0)	(0,0.109)	(0.135,0)	(0, 0.135)	(0.130, 0.130)

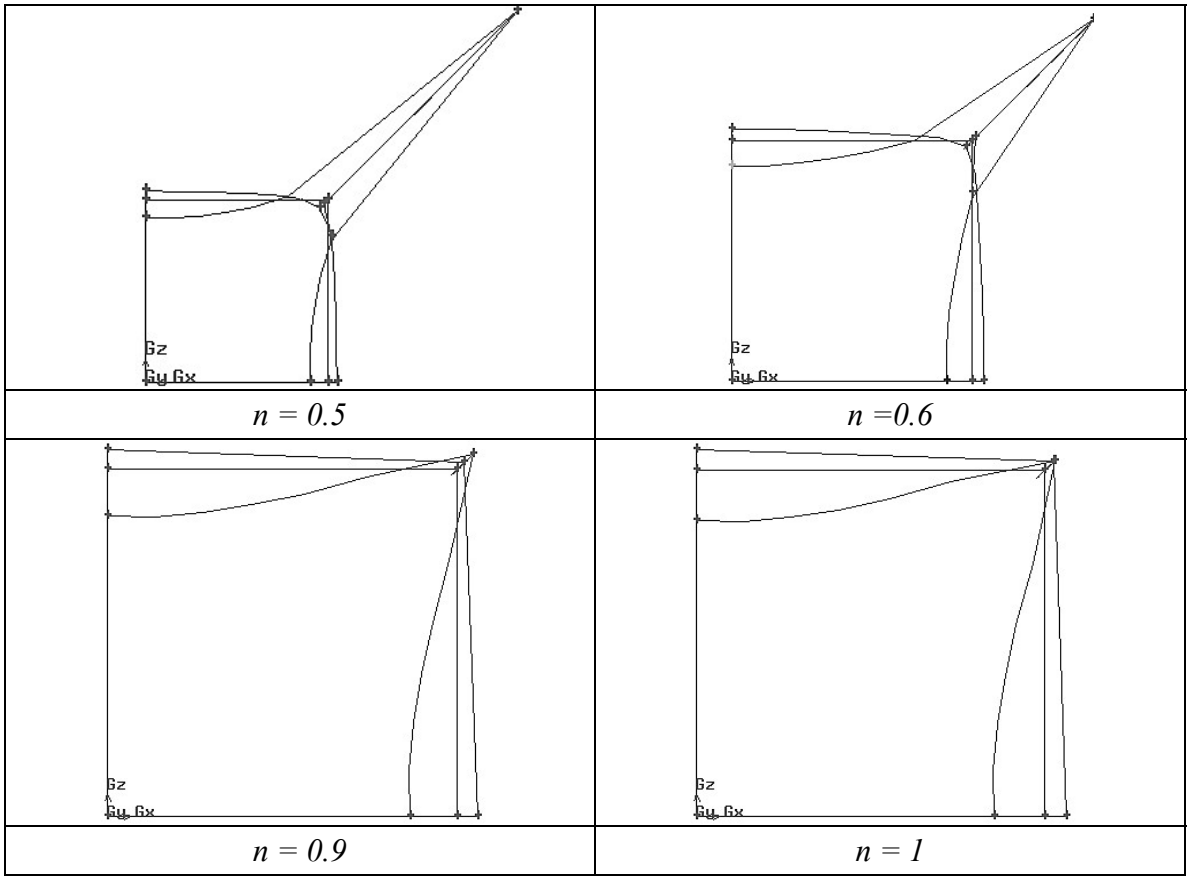

Figure 4.28: Geometry of the nozzle as a function of *n* for *K = 2000*

According to the results summarized in Table 4-5 and the geometries reported in Figure 4.28 the effect of an increasing value of n is more evident in the case with $K = 100$. The geometry of the nozzle that will lead to a square cross sectional strand of approximately *0.254 mm x 0.254 mm* for $K = 1000$ and $n = 0.5$ is so complicated that it can not be considered a realistic possibility.

Conclusions

In conclusion, the optimal design of the nozzle is strongly affected by the material parameters when the material is modeled as a pseudoplastic flow. In case of a Newtonian fluid ($n = 1$) the results do not show any dependency on the parameter K. Since in these cases the viscosity is not dependent on the shear rate, variation of the parameter K are not expected to require different nozzle geometry.

4.5.4 Parametric study of the strand shape through star-shaped nozzle

The experiments reported in section 4.3 showed that the shape of the strand after extrusion is affected by the process parameters and by the material properties. In addition, according to equation (4.1) the swelling of the melts depends on the normal stress difference τ_{11}-τ_{22}. Since the stress field is also dependent on the flow rate and the viscosity of the material, which is affected by temperature and shear rate, it is intuitive the influence of process parameters and material properties.

The objective of this study is to explore the range of material properties and/or process parameters that can be used to obtain a square shaped strand with the same star-shaped nozzle configuration (see in section 4.5.3 the design obtained for

$Q = 2.5 \cdot 10^{-9} m^3 / s$). Hence in this case the shape of the nozzle DEF is maintained constant and the shape of the strand (defined by the contour OGHI in Figure 4.29) is calculated according to the different parameters.

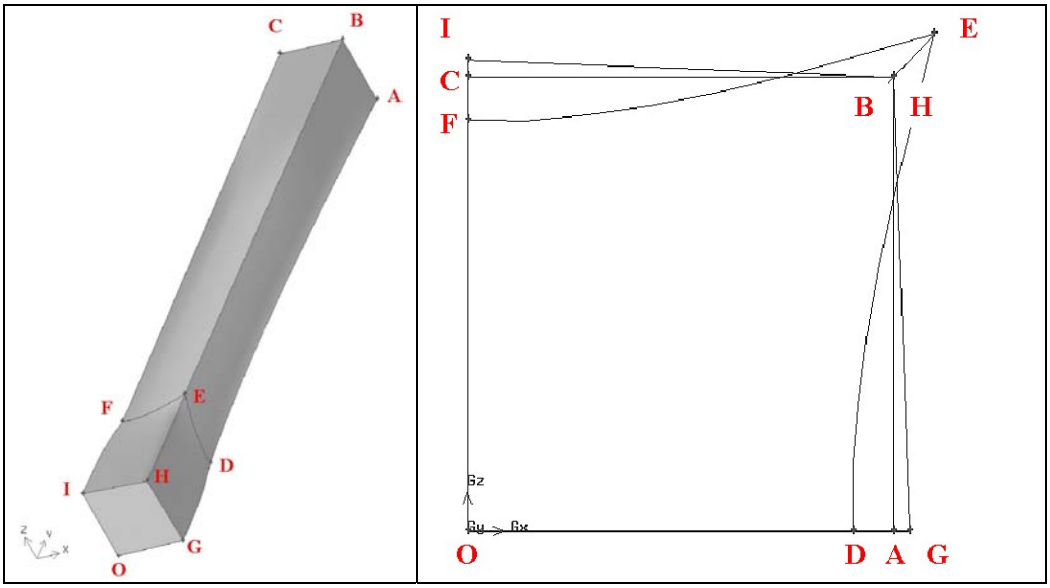

Figure 4.29: Parameters for the study

In order to obtain comparable results, the coordinates of the nodes presented in Figure 4.29 have been explored for the different cases. For an easier comparison with the *reference case,* the parameters obtained in section 4.5.3.1 were summarized in

Table 4-6 and the imposed conditions are listed below:

ρ = Density = *4580 Kg/ m^3*

K = Power law parameter = *633 Pa s^n*

n = Power law index = *0.6*

α = Parameter for the Ahrrenius relation = *19800*

k = Thermal conductivity = *1.5 W/^{o}C m*

Cp = Heat capacity = *500J/KgK*

S = Surface tension = *0.005 N/ m^2*

Q = Flow rate = *2.5 x 10^{-9} m^3/s*

T = Temperature imposed = *413. 15 K*

Table 4-6: Geometrical parameters in the "*reference case"* with Q = 2.5 x 10^{-9} m^3/s

E [*mm*] ***Vertex 10***	**D [*mm*]** ***Vertex 9***	**F [*mm*]** ***Vertex 11***	**G [*mm*]** ***Vertex 2***	**I [*mm*]** ***Vertex 3***	**H [*mm*]** ***Vertex 4***
(0.139,0.139)	(0.115,0)	(0,0.115)	(0.132,0)	(0,0.132)	(0.127, 0.127)

4.5.4.1 Effect of the process parameters

In order to determine the effect of the process parameters, the flow rate and the temperature, at the entrance and on the walls of the nozzle, have been varied and the results have been summarized in the following sections.

Influence of the flow rate

For the parametric study on the flow rate, all the parameters have been kept the same as in the reference case (see section 4.5.3.1), and the flow rate, which represents a quarter of the actual flow rate (see section 4.5.2) was varied from 2.58 * *10^{-10} m^3/s* to 2.58 * *10^{-8} m^3/s.* The results have been reported in Table 4-7.

Table 4-7: Geometrical parameters for flow rate variations

Q [m^3/s]	**E [*mm*]** ***Vertex 10***	**D [*mm*]** ***Vertex 9***	**F [*mm*]** ***Vertex 11***	**G [*mm*]** ***Vertex 2***	**I [*mm*]** ***Vertex 3***	**H [*mm*]** ***Vertex 4***
$2.58*10^{-10}$	(0.139,0.139)	(0.115,0)	(0,0.115)	(0.131,0)	(0, 0.131)	(0.129, 0.127)
$1.29*10^{-9}$	(0.139,0.139)	(0.115,0)	(0,0.115)	(0.131,0)	(0, 0.131)	(0.128, 0.127)
$5.16*10^{-9}$	(0.139,0.139)	(0.115,0)	(0,0.115)	(0.132,0)	(0, 0.132)	(0.127, 0.126)
$2.58*10^{-8}$	(0.139,0.139)	(0.115,0)	(0,0.115)	(0.132,0)	(0, 0.132)	(0.125, 0.124)

From the results of Table 4-7 it seems reasonable to conclude that the nozzle design is not particularly affected by the flow rate. However, the configurations presented in Figure 4.30 show, as expected (see section 4.3.2), that in the case of lower flow rate the strand presents sharper corners.

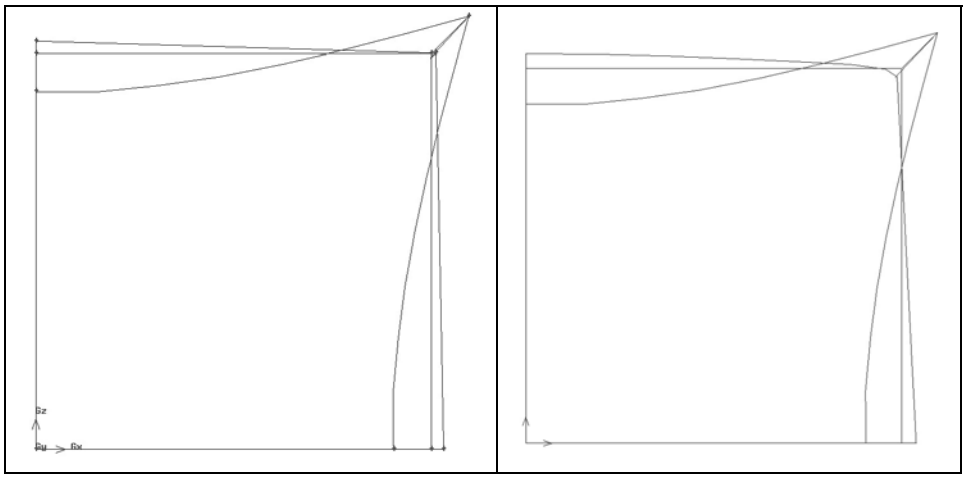

Figure 4.30: Geometry for Q = 2.58 * 10^{-10} m^3/s and Q = 2.58 * 10^{-8} m^3/s.

The fact that the values depicted in Table 4-7 do not show any influence of the flow rate is probably due to the fact that a free extrusion was considered at this point. A model that will simulate the deposition phase will probably demonstrate that the flow rate and the speed of deposition will strongly influence the final shape of the road. It is indeed intuitive that in case of large flow rates, for example, the material will be squeezed between the nozzle and the platform [64]. In Figure 4.31 the picture on the left represents a case where the applied flow rate is much smaller than the one used for the case on the right side.

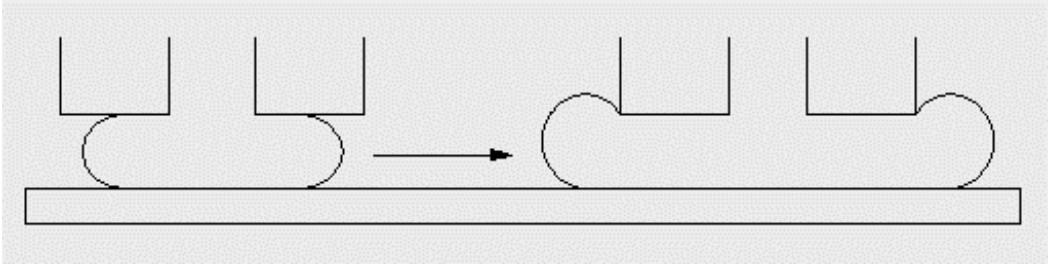

Figure 4.31: Effect of the flow rate on the rad shape during deposition phase

Influence of temperature

In order to determine the influence of temperature applied on the upper surface and on the surface in contact with the walls of the nozzle, two simulations have been conducted with respectively a temperature below and a temperature above the one considered for the *reference case* (T = 413 K). All other parameters were kept identical to the ones described in section 4.5.3.1.

The geometrical parameters resulted from the simulations have been reported in Table 4-8, while the nozzle configurations are depicted in Figure 4.32.

Table 4-8: Geometrical parameters for temperature variations

	E [*mm*] ***Vertex 10***	**D [*mm*]** ***Vertex 9***	**F [*mm*]** ***Vertex 11***	**G [*mm*]** ***Vertex 2***	**I [*mm*]** ***Vertex 3***	**H [*mm*]** ***Vertex 4***
T = 343K	(0.139,0.139)	(0.115,0)	(0,0.115)	(0.132,0)	(0,0.132)	(0.128, 0.126)
T = 600K	(0.139,0.139)	(0.115,0)	(0,0.115)	(0.131,0)	(0,0.131)	(0.128, 0.127)

In this case both the values of the table as well as the geometry configuration seem to agree that a variation of temperature in this range does not affect the geometry.

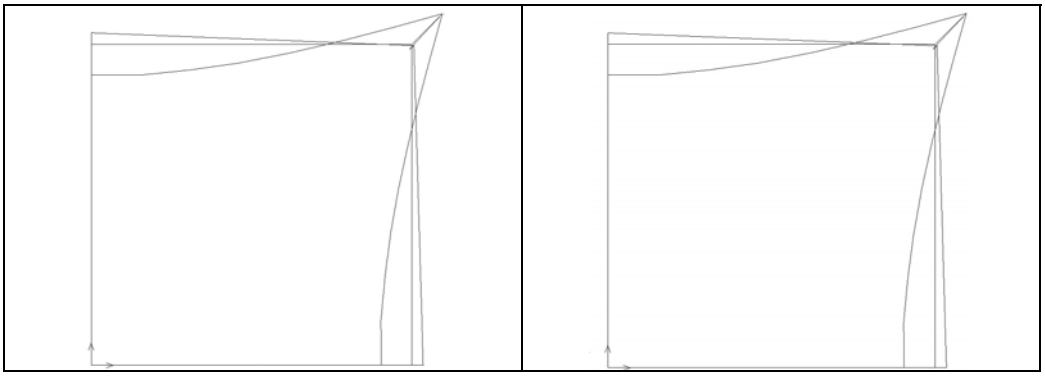

Figure 4.32: Geometry for *T = 343 K* and for *T = 600 K*

4.5.4.2 Effect of material properties

Influence of the exponent n of the power law

In order to consider the effect of the exponent of the power law, several simulations were performed with values of n varying from 0.3 to 2 (see Table 4-9).

Table 4-9: Geometrical parameters for variation of exponent *n*

	E [mm] Vertex 10	***D [mm] Vertex 9***	***F [mm] Vertex 11***	***G [mm] Vertex 2***	***I [mm] Vertex 3***	***H [mm] Vertex 4***
n=0.3	(0.139,0.139)	(0.115,0)	(0,0.115)	(0.123,0)	(0,0.123)	(0.118, 0.117)
n=0.5	(0.139,0.139)	(0.115,0)	(0,0.115)	(0.129,0)	(0,0.129)	(0.125, 0.123)
n=0.6	(0.139,0.139	(0.115,0)	(0,0.115)	(0.134,0)	(0,0.134)	(0.131, 0.129)
n=0.8	(0.139,0.139)	(0.115,0)	(0,0.115)	(0.137,0)	(0,0.137)	(0.133, 0.132)
n=1	(0.139,0.139)	(0.115,0)	(0,0.115)	(0.142,0)	(0,0.141)	(0.138, 0.137)
n=2	(0.139,0.139)	(0.115,0)	(0,0.115)	(0.161,0)	(0,0.158)	(0.160, 0.154)

Since the exponent *n* of the power law is the one that most affects the rheological behavior of the melt (see equation (4.2)), it is expected to have a dominant influence on the shape of the strand. Remembering that [7]:

- $n = 1$ corresponds to the case of a Newtonian fluid;
- $n < 1$ describes a melt with shear thinning behavior;
- $n > 1$ describes a melt with shear thickening behavior;

it can be anticipated that:

- for $n < 1$, the viscosity of the material decreases where higher shear rate values are encountered (near the surfaces of the nozzle), hence the velocity field will be more uniform on the cross-section. Since the swelling is mostly caused by velocity gradients that tend to uniform the velocity of the particle at the exit of the nozzle, a shear thinning behavior will be characterized by a smaller swelling.

- for $n > 1$, the viscosity is proportional to the shear rate, hence higher density is encountered near the surfaces of the nozzle. The resulting velocity field will be characterized by even higher gradients. Since the swelling is mostly caused by a non-uniform velocity field, a shear thickening behavior of the melt will cause a more pronounced swelling phenomenon.

In Figure 4.33 the geometry obtained for a melt modeled as Newtonian flow, i.e. $n = 1$, is depicted.

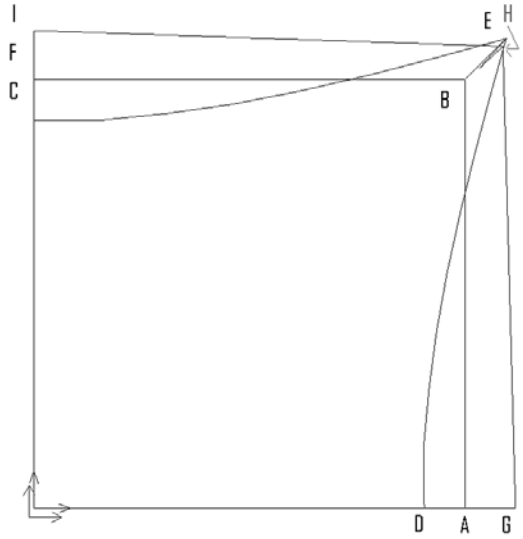

Figure 4.33: geometry for *n=1 (Newtonian fluid)*

This figure shows that the fluid expands at the exit of the nozzle originating a strand shape that is mostly square. The large expansion of the strand in this case is due to the fact that the star-shaped nozzle was calculated for the *reference case*, in which the reological behavior of the melt was described with $n = 0.6$. Consequently, the results

should be interpreted considering *n = 0.6* as the *neutral case* (normalization of the results).

It is because of the "*normalization*" process that in Figure 4.34, the melt characterized by n = 0.3 seems to show a contraction of the section of the strand with respect to the starting section ABC.

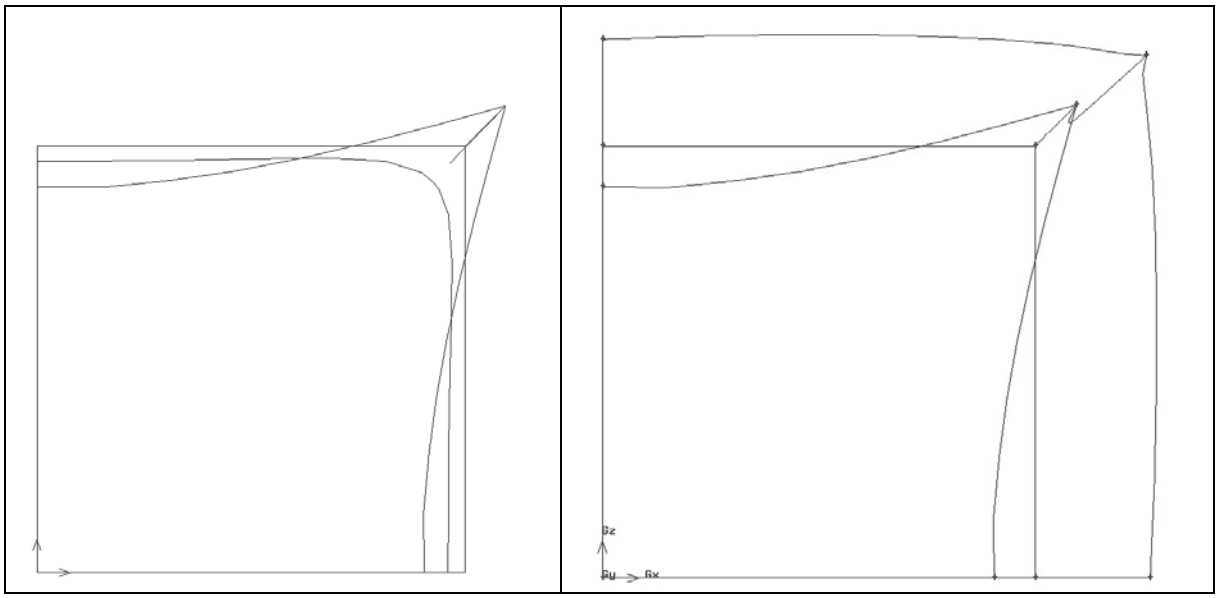

Figure 4.34: Geometry for *n = 0.3* and for *n=2*

The configurations presented in Figure 4.34 support the earlier anticipations: a shear thickening behavior of the melt will cause an expansion of the section of the strand more important that in the case of a shear thinning melt.

Influence of the parameter K of the power law

Since *K* influences the viscosity of the melt, a parametric study is expected to give results with tendency similar to the one obtained for *n*. However, since *K* represents a

constant of proportionality in the power law (see equation (4.1)), while 1-n is the exponent of the shear rate, the effects of variation in the value of *K* are expected to be less important than the one observed for changes in *n*.

Table 4-10: Geometrical parameters for variations of *K*

	E [*mm*] ***Vertex 10***	**D [*mm*]** ***Vertex 9***	**F [*mm*]** ***Vertex 11***	**G [*mm*]** ***Vertex 2***	**I [*mm*]** ***Vertex 3***	**H [*mm*]** ***Vertex 4***
K=100	(0.139,0.139)	(0.115,0)	(0,0.115)	(0.134,0)	(0,0.134)	(0.125, 0.124)
K=300	(0.139,0.139)	(0.115,0)	(0,0.115)	(0.132,0)	(0,0.132)	(0.127, 0.126)
K=500	(0.139,0.139)	(0.115,0)	(0,0.115)	(0.132,0)	(0,0.132)	(0.128, 0.126)
K=1000	(0.139,0.139)	(0.115,0)	(0,0.115)	(0.131,0)	(0,0.131)	(0.128, 0.127)
K=1200	(0.139,0.139)	(0.115,0)	(0,0.115)	(0.131,0)	(0,0.131)	(0.128, 0.127)
K=2000	(0.139,0.139)	(0.115,0)	(0,0.115)	(0.131,0)	(0,0.131)	(0.129, 0.127)

A comparison between Table 4-9 and Table 4-10, where the coordinates of the vertices of the geometry are reported as a function of *K*, shows that increments in either one of the two parameters move the point H of the section of the strand on the upper right corner, causing a sharper edge.

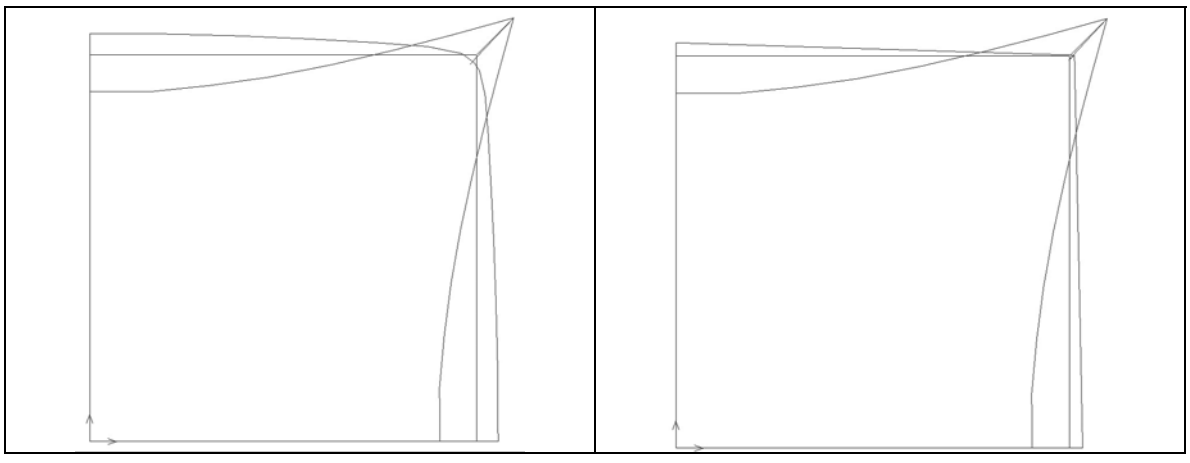

Figure 4.35: Geometries for *K = 100* and *K =2000*

However, comparing Figure 4.35 and Figure 4.34, a different tendency of the effect of *K* and *n* is observed. An increment of *n* always produces a bigger expansion, hence a bigger cross section of the strand; while an increment in *K* results only in a "more square" shape of the strand, without effecting the overall area.

Influence of the surface tension

In order to study the influence of the parameter σ of the surface tension, several simulations were conducted with conditions identical to the one described for the *reference case* (see section 4.5.3.1).

Table 4-11: Geometrical parameters for surface tension variations

$[N/m^2]$	**E [*mm*]** ***Vertex 10***	**D [*mm*]** ***Vertex 9***	**F [*mm*]** ***Vertex 11***	**G [*mm*]** ***Vertex 2***	**I [*mm*]** ***Vertex 3***	**H [*mm*]** ***Vertex 4***
σ=0.0005	(0.139,0.139)	(0.115,0)	(0,0.115)	(0.131,0)	(0,0.131)	(0.129, 0.128)
σ=0.001	(0.139,0.139)	(0.115,0)	(0,0.115)	(0.131,0)	(0,0.131)	(0.129, 0.127)
σ=0.003	(0.139,0.139)	(0.115,0)	(0,0.115)	(0.131,0)	(0,0.131)	(0.128, 0.127)
σ=0.007	(0.139,0.139)	(0.115,0)	(0,0.115)	(0.132,0)	(0,0.132)	(0.127, 0.126)
σ=0.05	(0.139,0.139)	(0.115,0)	(0,0.115)	(0.135,0)	(0,0.135)	(0.124, 0.123)

As mentioned in the Appendix 1, variations of the surface tension do not have strong influence on the geometry of the strand for σ in the range $0.001 < \sigma < 0.01$. However, for values greater than 0.1 N/m^2, the corners of the cross-section of the strand loose their sharp characteristic (see Figure 4.36). Since the surface tension describes the natural tendency of materials to geometrically assume the configuration characterized by the minimum surface, an increment of σ will certainly cause the evolution of a sharp corner towards a "fillet".

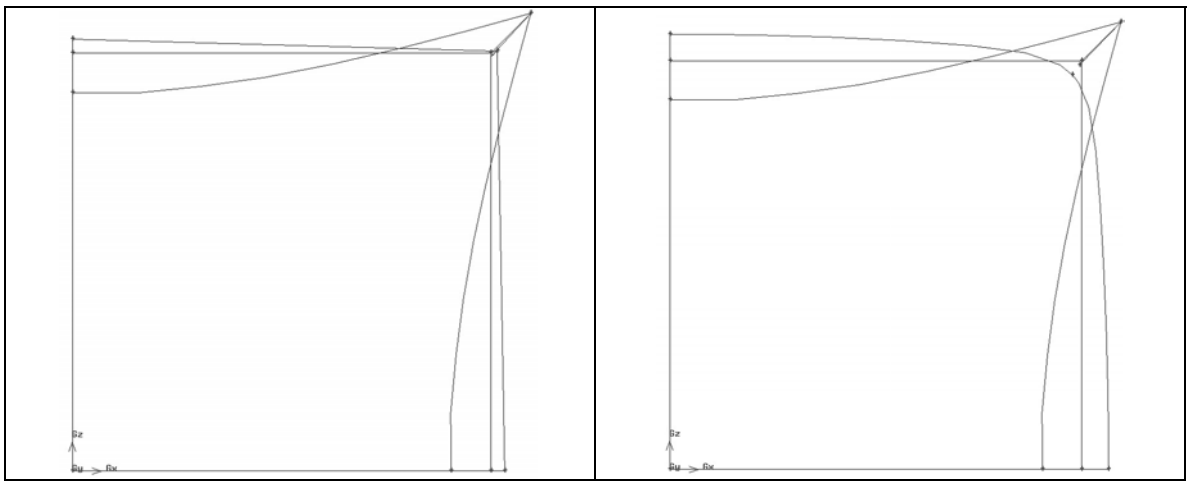

Figure 4.36: Geometry for law (σ=0.0005 N/m2) and high (σ= 0.5 N/m2) values of surface tension

Variation of density

For the study of the influence of the material density on the geometry of the strand two simulations have been conducted respectively with density values smaller and higher than the one considered for the reference case (for which ρ=*4380 Kg/m*^{3}).

Table 4-12: Geometrical parameters for density variations

[Kg/m^3]	**E [*mm*]** ***Vertex 10***	**D [*mm*]** ***Vertex 9***	**F [*mm*]** ***Vertex 11***	**G [*mm*]** ***Vertex 2***	**I [*mm*]** ***Vertex 3***	**H [*mm*]** ***Vertex 4***
ρ=1000	(0.139,0.139)	(0.115,0)	(0, 0.115)	(0.132,0)	(0,0.132)	(0.128, 0.128)
ρ=6000	(0.139,0.139)	(0.115,0)	(0, 0.115)	(0.132,0)	(0,0.132)	(0.128, 0.127)

From the results summarized in Table 4-12 and the configurations depected in Figure 4.37, it is possible to conclude that the density of the material does not play a

strong role in the determination of the strand evolution for values varying from 1000 Kg/m^3 to 6000 Kg/m^3.

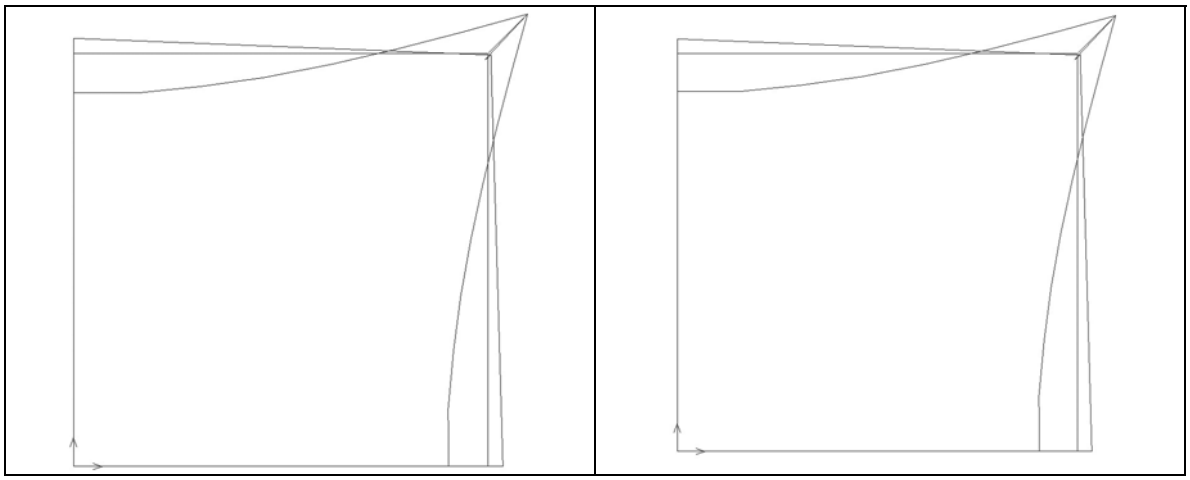

Figure 4.37: Geometries for density $\rho=1000$ and $\rho=6000$

The influence of the density is probably negligible in these simulations where only a few millimeters long strand is modeled. If a simulation were run for a longer time, the density would have played a role in breaking the flow due to the reduction in the cross-sectional area caused by the weight of the extrudate.

4.6 Conclusions and future directions

In this work the influences of the material properties and of process parameters on the shape of the strand were studied. In the first part of the chapter the experiments conducted with square nozzles were described and the results were compared.

It was observed that after extrusion the melt exhibits swelling typical of the pseudoplastic materials. In order to compensate the expansion of the flow at the exit of the nozzle a different configuration of the tip has to be manufactured.

For this reason models of the nozzle and of the extrusion process were developed and described in the second part of the chapter. In the discussion of the results it was concluded that a star-shaped tip would lead to a square-shaped strand.

In order to evaluate the applicability of a star-shaped nozzle in the process, a parametric study on the process condition and on material properties was conducted. The results show that:

- Because of the negligible influence of the temperature on the swelling phenomenon, the same nozzle design could be use for material with different melting temperature.
- The imposed flow rate does not affect the qualitative shape of the strand, but it influences the velocity of the melt and the pressure drop. During the deposition on the substrate, an increasing flow rate will cause the formation of a wider road (that might oversize the tip, hence expand uncontrollably) and it will increase the probability of buckling failure of the filament (because of the increasing pressure drop).
- The density of the material does not influence the shape of the strand, probably because of the small portion of free extrudateconsidered in the model.
- The material parameters K and n that describe the rheological behavior of the melt are most influencing. Affecting the dependence of the viscosity on the shear rate, they directly influence the swelling phenomenon. Furthermore, since K represents a constant of proportionality while $n-1$ is the exponent of

the shear rate in the power law (see equation (4.1)), the effect of variance of n is more evident.

From the results obtained with the model, it can be concluded that the same nozzle design can be applied with the same material for different process conditions without affecting the qualitative shape of the strand. However, when different materials are used, changes in the nozzle design might be necessary in order to maintain a square cross section of the road. For example, in section 4.5.3.2 the results reported in Figure 4.27 show that if two different materials are used, one with $n = 0.4$ and one with $n = 0.9$ two completely different nozzle designs have to be developed in order to obtain similar cross-section of the strand.

It must be underlined that, in the current model, only the relation between shape of the nozzle and shape of the strand was studied in dependency of material properties and process conditions. However, in manufacturing a part, the deposition of the material on the substrate will affect the shape of the strand. Hence, it is important to study further developments of the model that will consider the influences of the platform and of the subsequent roads.

CHAPTER 5: LIQUEFIER DYNAMICS

5.1 Abstract

In chapter 2 Layered manufacturing (LM) was introduced as an evolution of rapid prototyping (RP) technology whereby a part is built in layers as a finish product. Moreover section 2.2 introduced the fused deposition modeling (FDM) process, a form of LM technique in which each section is fabricated through vector style deposition of building blocks, called *roads,* which are then stacked layer by layer to fabricate the final object. The latest improvements in this technology brought about the possibility of fabricating not only a model but even the finished product directly.

The final object is therefore generated through assembly of deposited roads by appropriate motion and flow control commands. Consequently, in order to improve the final quality of a product it is important to closely control the material flow by making dynamic as part of the control strategy.

It was observed that the system, constituted by liquefier filled with thermoplastic material, is characterized by a time constant. With the purpose of improving the control of the flow, two strategies were adopted: 1. improve the time lag by reduction of the uncontrolled volume of the melt, i.e. by shortening the liquefier or by using a *valve nozzle*; 2. understand the time lag in order to develop an integrated control system able of coupling flow with motion.

This chapter presents the analysis of the liquefier dynamics towards establishing control strategies for flow control during the extrusion phase, which is necessary to achieve the objectives mentioned above.

5.2 Introduction

In the FD machine utilized in this study (the Stratasys 1650 Modeler of Figure 2.13) a plastic filament is supplied on a reel and fed into a heated liquefier where it is melted. The melt is then extruded through a nozzle while the incoming filament, still in solid phase, is acting as a "plunger". The nozzle is mounted to a mechanical stage (see Figure 3.1), which can be moved in the *xy* plane [33]. As the nozzle is moved over the table in a prescribed geometry, it deposits a thin bead of extruded plastic, referred to as "roads" which solidify quickly upon contact with substrate and/or roads deposited earlier. Solid layers are generated by following a *rastering* motion, where the roads are deposited side by side within an enveloping domain boundary (Figure 5.1). Once a layer is completed, the platform is lowered in the *z* direction in order to start the next layer. This process continues until the fabrication of the object is completed.

Successful bonding of the roads in the deposition process necessitates control of the thermal environment. Therefore, the entire system is contained within a chamber, which is maintained at a temperature below the melting point of the material being deposited, but above the room temperature.

Several materials are commercially available for this process including polymers such as ABS and investment casting wax. When needed, support structures are fabricated for overhanging geometries using different materials, which are later removed by breaking them away from the object. A water-soluble support material, which can simply be washed away, is also available.

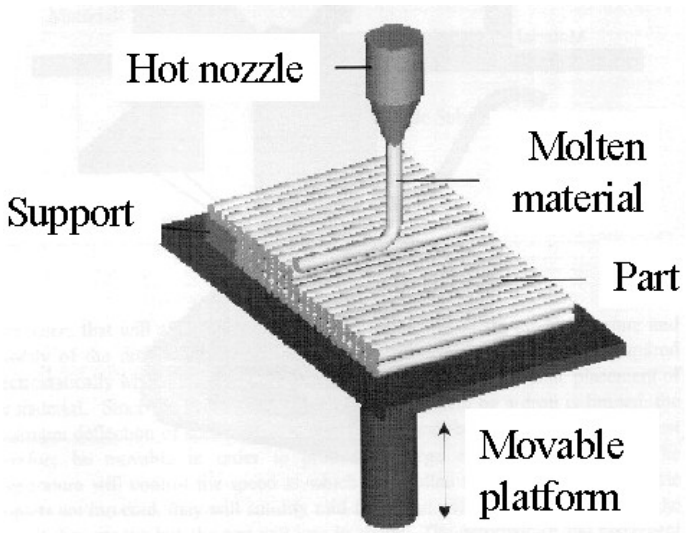

Figure 5.1: Schematic of a FD process

In FD the part is built according to a pre-specified tool-path (Figure 5.2.b), usually determined during the design phase (i.e. Qickslice^{TM}) ([9],[38]). Each tool-path is conceptually divided into five regions (see Figure 5.2.a) [64]:

I. *Pre-movement*: a prescribed volumetric flow rate is started before the deposition begins. A glob of certain size is generated to compensate for the intrinsic deposition delay, due to the internal length of the liquefier, which is the distance between the point of application of the pressure and the point of the material delivery.

II. *Start-up*: as soon as the motion starts, an absolute flow-rate, higher than the steady state flow rate, is established and maintained throughout the acceleration phase;

III. *Steady-state*: once the acceleration phase is complete, a constant flow rate is specified;

IV. *Slow-down*: the main flow rate is stopped and a certain amount of material (empirically determinate and dependent on the deceleration constant and the steady state flow rate) is brought back revolving the motion of the rollers;

V. *Exit-move*: the flow control is turned off and the nozzle is moved to a pre-specified distance from the last point of the tool-path in order to avoid any further interferences.

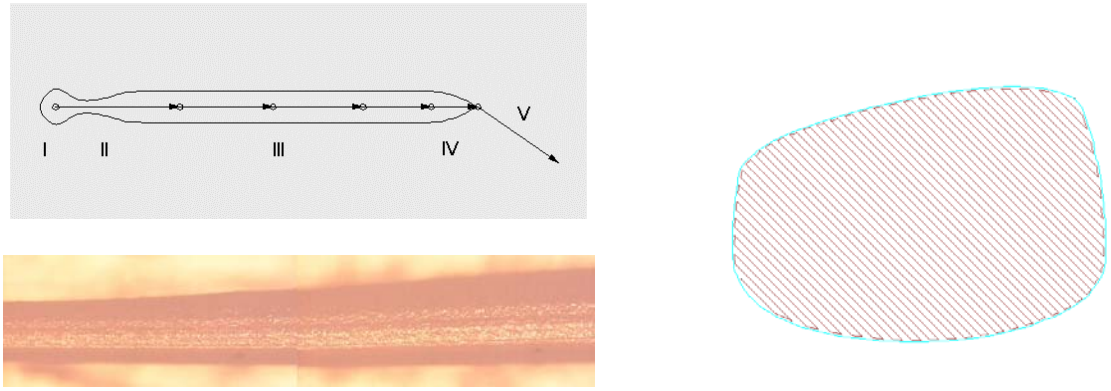

(a) (b)

Figure 5.2: Flow controls regions of a tool-path (a) and sample tool-path (b)

Figure 5.2.a schematically depicts some of the irregularities that are typical during road deposition. An "*under-deposition*" zone can be observed during the acceleration phase and an "*over-deposition*" during deceleration.

In order to reduce these transient effects a better correlation between deposition speed and flow rate is needed. The objective of this chapter is to perform an analysis of the process taking place in the liquefier. A study based on mathematical modeling is presented first. Then a transfer function approach is developed that can be integrated as part of an overall control strategy for an effective flow control and improved part integrity [4]. These two models are then compared with experimental observations that are performed by inducing step changes in deposition rates.

The dynamic of the liquefier (Figure 5.1) is one of the more complicated phenomena to analyze in an FDM process. Inside the liquefier the physical system exhibits a complex behavior due especially to the movement of the non-isothermal, viscous melting fluid. Other possible causes compounding this complex behavior can be due to some and/or all of the following reasons:

- Compressibility of the fluid;
- Slip conditions between the liquefier walls and the melting flow;
- Possible slippage between the feed-rollers and the filament;
- Uneven distribution of heat flux, which is provided by electrical heaters that consist of metal coils wrapped around the aluminum liquefier. Hence, it heats the thermoplastic material once the power is applied. A temperature regulator adjusts the power to the heater, based on temperature measurement at a single point (0.5'' away from the exit tip) [64];

- Change of physical state of the melt. The thermoplastic filament heats up and gradually melts as it travels down the liquefier [64];
- Sticktion effect of the melt while the filament is pushed into the liquefier.

Furthermore, the non-linear dependences of the material properties on the temperature and the shear rate (ABS can indeed be modeled as a generalized Newtonian flow) bring additional difficulties to the modeling process.

5.3 Liquefier dynamics: mathematical model

The extrusion is central to the fused deposition process during which the thermoplastic filament is introduced, via mechanical pressure, into the liquefier, where it melts and is then extruded. Since the rollers are the only drive mechanism in the material delivery system, the filament is under tensile stress upstream to the roller and under compression [60] at the downstream side acting as a plunger. The compressive stress thus becomes the driving force behind the extrusion process (Figure 5.3).

The force required to extrude the melt must be sufficient to overcome the pressure drop across the system, which strictly depends on the viscous properties of the same melt as well as on the geometry of the liquefier and nozzle (Figure 5.4). Because of the fact that melts adhere to the liquefier/die walls, the material is subjected to shear deformation during the flow.

$$\dot{\gamma} = -\frac{dv}{dr} \tag{5.1}$$

Thermoplastic materials currently used in FD exhibit shear thinning behavior, i.e. the viscosity decreases with increasing shear rate [7]. Although more extensive and complex models (i.e. Bird Carreau law, Cross law, etc.) are available, it can be assumed that adopting a power law for generalized Newtonian fluids for modeling of polymers such as ABS, is sufficiently accurate for modeling FD melts, especially in light of other high-order uncertainties in the system. Accordingly, the power law states:

$$\tau = \left(\frac{\dot{\gamma}}{\phi} \right)^{\frac{1}{m}} \tag{5.2}$$

where m and ϕ are material constants, τ is the shear stress and $\dot{\gamma}$ is the shear rate.

The power law parameters m and ϕ indicate the flow exponent and the fluidity respectively. The general flow characteristic of a material and its deviation from the Newtonian behavior is reflected by the flow exponent m.

Applying the Power Law to the momentum flux balance on a fluid element [47] respectively in the zone I, II and III (Figure 5.4), it is possible to determine the total pressure drop:

$$\Delta P_{1\_v} = 2L_1 \left(\frac{\mathrm{v}}{\phi} \right)^{\frac{1}{\mathrm{m}}} \left(\frac{m+3}{\left(D_1 / 2 \right)^{m+1}} \right)^{\frac{1}{\mathrm{m}}} \tag{5.3}$$

$$\Delta P_{2\_v} = \left(\frac{2 \cdot m}{3 \cdot tg\left(\beta / 2 \right)} \right) \left(\frac{1}{D_2^{3/m}} - \frac{1}{D_1^{3/m}} \right) \left(\left(\frac{D_1}{2} \right)^2 (m+3) \cdot 2^{m+3} \right)^{1/m} \tag{5.4}$$

$$\Delta P_{3\_v} = 2L_2\left(\frac{\mathrm{v}}{\phi}\right)^{\frac{1}{\mathrm{m}}}\left(\frac{(m+3)\left(D_1/2\right)^2}{\left(D_2/2\right)^{m+3}}\right)^{\frac{1}{\mathrm{m}}} \tag{5.5}$$

where D_1 and L_1 are respectively the length and the diameter of the liquefier (section I in Figure 5.4), D_2 and L_2 are the length and the diameter of the tip of the nozzle (section III in Figure 5.4), β is the convergence angle of liquefier-tip diameter transition. The velocity v is the velocity of the filament at the entrance of the liquefier. Since at this stage the material is still in solid form, this value is constant and uniform over the cross section (plug flow).

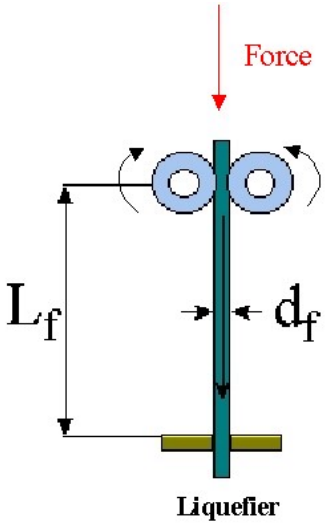

Figure 5.3: Driving force

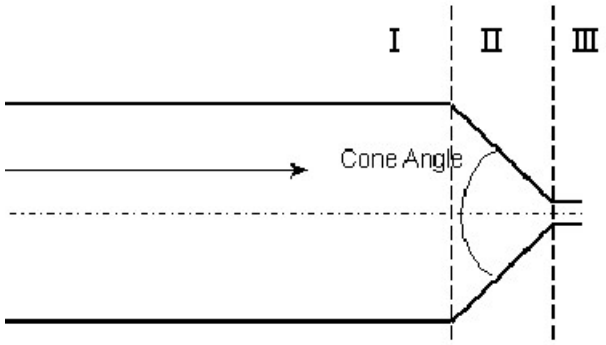

Figure 5.4: Regional decomposition of Liquefier/Extruder

In equations (5.1) - (5.5) the fluid is assumed to be isothermal at a temperature T equal to the temperature of deposition. However, when a sudden change in the flow rate (i.e. step function) is applied at the entrance of the liquefier, the steady state condition of the flow is disturbed. With the introduction of new material in the system, the average velocity of the fluid increases and the average temperature drops. In order to stabilize new steady state conditions, the heat flow rate must be increased. Since the temperature control is based on a single input from a thermocouple reading at the end of the liquefier (12 cm far from where the change has taken place), the response of the system is delayed. Furthermore, the temperature is regulated via heat input from electrical coil heaters. The system continuously adjusts the power supplied to the coils according to the temperature difference between the desired value and the value detected by the thermocouple. The response time of the temperature controlling loops is thus of the order of seconds, due to the thermal inertia of the extrusion assembly.

The necessary heat flow rate, supplied through the wall of the liquefier, $S = 2\pi \frac{D_1}{2} L_1$, can be approximately determined as:

$$q = \left(T - T_i\right) \cdot \frac{\rho \cdot v \cdot A \cdot c_p}{2 \cdot \pi \cdot \left(\frac{D_1}{2}\right) \cdot L_1} \tag{5.6}$$

where T_i is the temperature at the entrance of the liquefier, ρ is the density of the melt, A is the cross section of the inner liquefier and c_p is the specific heat capacity of the melt. In order to simplify the calculation, the melt is considered at the uniform temperature $T = T_f$, that is the temperature at the end of the liquefier, and c_p has been considered constant in the range of temperatures in consideration.

During the time of thermal adjustment, the flow is non-isothermal, so temperature dependence of viscosity must be taken into account along with the shear-rate dependence ([6],[61]). The viscosity expression can be factorized as follows:

$$\eta = H(T) \cdot \eta_0(\dot{\gamma}) \tag{5.7}$$

where *H(T)* accounts for temperature dependence and $\eta_0(\dot{\gamma})$ is the expression for viscosity at some reference temperature T_α (value of the temperature at which the parameters m and ϕ of the power law have been determined). In this study the Arrhenius relation has been adopted to model the behavior of ABS:

$$H(T) = \exp\left[\alpha\left(\frac{1}{T - T_0} - \frac{1}{T_\alpha - T_0}\right)\right] \tag{5.8}$$

where α is the energy of activation, T_α is a reference temperature for which $H(T)=1$ and $T_0=0$ for absolute temperatures T and T_α.

Substituting equation (5.2) into (5.7), various pressure drops in the system can be expressed as:

$$\Delta P_1 = 2L_1\left(\frac{\mathrm{v}}{\phi}\right)^{\frac{1}{\mathrm{m}}}\left(\frac{m+3}{\left(D_1/2\right)^{m+1}}\right)^{\frac{1}{\mathrm{m}}}\cdot e^{\left[\alpha\left(\frac{1}{T}-\frac{1}{T_\alpha}\right)\right]} \tag{5.9}$$

$$\Delta P_2 = \left(\frac{2\cdot m}{3\cdot tg(\beta/2)}\right)\left(\frac{1}{D_2^{3/m}}-\frac{1}{D_1^{3/m}}\right)\left(\left(\frac{D_1}{2}\right)^2(m+3)\cdot 2^{m+3}\right)^{1/m}\cdot e^{\left[\alpha\left(\frac{1}{T}-\frac{1}{T_\alpha}\right)\right]} \tag{5.10}$$

$$\Delta P_3 = 2L_2\left(\frac{\mathrm{v}}{\phi}\right)^{\frac{1}{\mathrm{m}}}\left(\frac{(m+3)\left(D_1/2\right)^2}{\left(D_2/2\right)^{m+3}}\right)^{\frac{1}{\mathrm{m}}}\cdot e^{\left[\alpha\left(\frac{1}{T}-\frac{1}{T_\alpha}\right)\right]} \tag{5.11}$$

$$\Delta P = \Delta P_1 + \Delta P_2 + \Delta P_3 \tag{5.12}$$

From equations (5.9) to (5.12) it can be observed that when a sudden change in the flow rate occurs, the average temperature T drops and the velocity v increases, hence resulting in considerable increase for the pressure drop in the system.

Once total pressure drop is known, the compression force applied to the filament in order to extrude the material can be calculated as:

$$F = \Delta P \cdot A \tag{5.13}$$

where A is the cross section of the filament (which is equal to the cross section of the liquefier). Since the force is imposed by two drive-rollers (see Figure 5.3) driven by a pair of micro stepper motors, the torque Γ and the power required (to each motor) for the extrusion become:

$$\Gamma = \frac{F}{2} \cdot R_r \tag{5.14}$$

$$P = \omega_r \cdot \Gamma \tag{5.15}$$

where R_r is the radius and ω_r is the angular velocity of a roller. The expressions presented above are next arranged and developed into a *MatLab* program.

In the initial approach the following assumptions were made:

1. Perfect adhesion between rollers and filament, thus $\mathrm{v} = \omega_r \cdot R_r$;
2. The angular velocity of the rollers abruptly changes (i.e. step function) in order to provide the specified flow rate (see the Experimental Set Up section);
3. The heat flow rate is increased following a ramp function (in order to model the closed loop control);
4. There is no upper limit to power and torque that drive-motors can provide.

5.4 Mathematical model – results

In Figure 5.5 the results obtained with the first approach (no limitation on power and torque supply), have been grouped. The average velocity (Figure 5.5.a) of the melt is given according to the command provided by the SML file, thus it suddenly changes at half the length of the road.

The heat flow rate is also given and it is assumed to change linearly (Figure 5.5.b)

$$dq = \left(\frac{540 - T_0}{\pi D_1 L_1} \cdot \rho \left(v_{end} - v_0 \right) \cdot A \cdot c_p \right) \cdot \frac{1}{80} \tag{5.16}$$

where *540* represent the exit temperature, in Kelvin, from the liquefier.

The average temperature, that is considered independent of the location, is then calculated using equation (5.6). From Figure 5.5.c it is possible to note that a sudden change in the inflow results in a sudden reduction in temperature. This causes, according to equations (5.7) and (5.8), an abrupt increase of the average viscosity of the melt, thus significant additional pressure (see equations (5.9) – (5.12)) and force (equation (5.13)) are needed to maintain the extrusion. Consequently, to allow continuity in the process, the motors have to provide excessive levels of torque and power. In Figure 5.5.e and Figure 5.5.f it is possible to see that the required power increases from *0.0008 W* to *15000 W* at t = 2.3 seconds (when the flow rate is increased). After this sudden change, the necessary power (and torque) decreases because the average temperature of the melt increases (the flow rate is kept constant, but the heat flow augments).

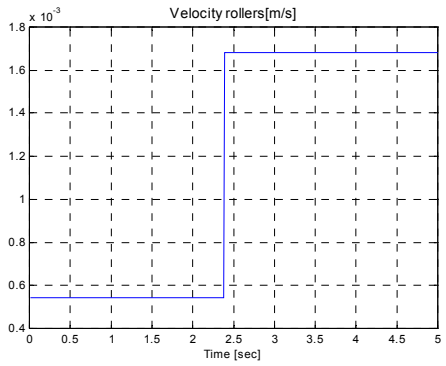
Velocity rollers[m/s]
x 10^-3
Time [sec]

(a)

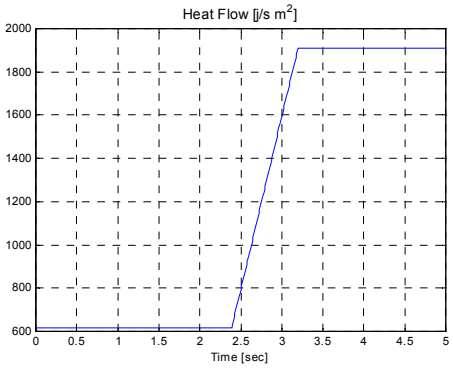
Heat Flow [j/s m^2]
Time [sec]

(b)

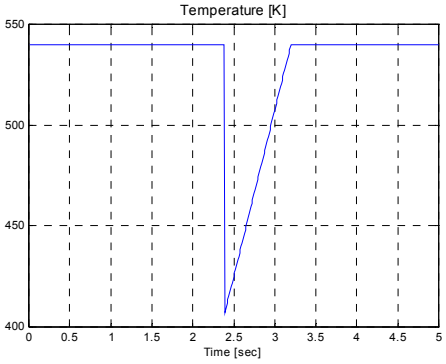
Temperature [K]
Time [sec]

(c)

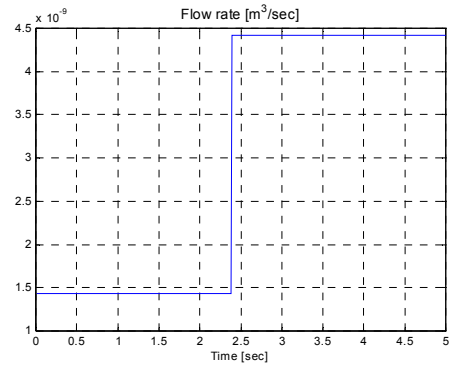
Flow rate [m^3/sec]
x 10^-9
Time [sec]

(d)

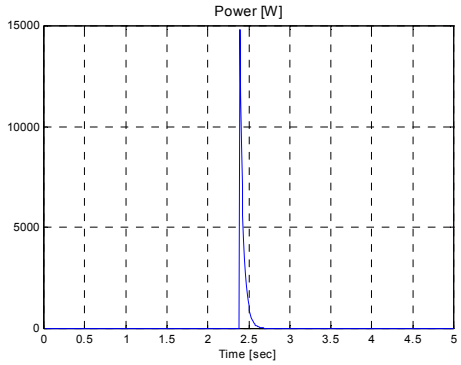
Power [W]
Time [sec]

(e)

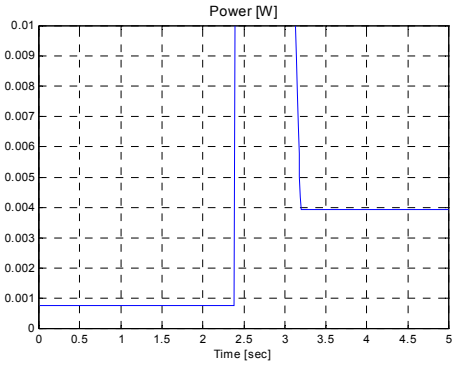
Power [W]
Time [sec]

(f)

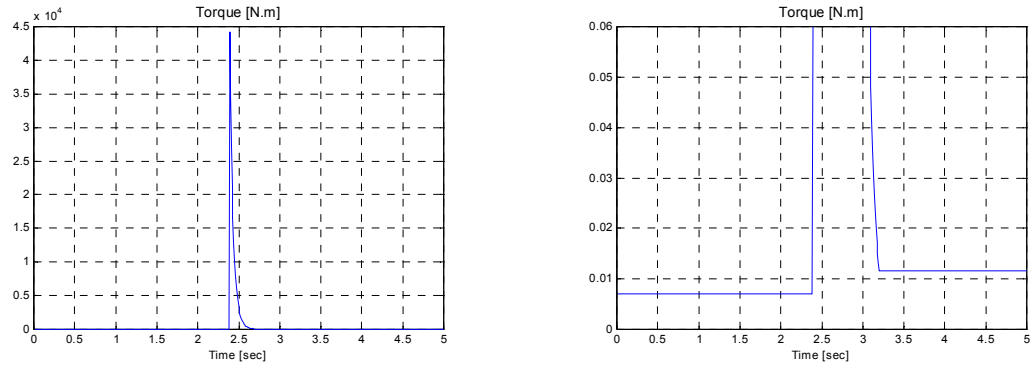

(g) (h)

Figure 5.5: Results for the initial model for a step amplitude = 2.9851

With the assumptions presented earlier, the results show that in order to provide a sudden increase of the angular velocity of the rollers, the stepper motors have to supply excessive levels of torque (because of the increase in the pressure drop, due to the increase in the viscosity) and power. The motors that drive the rollers are MicroMo® Motors, type 2233T012S made by MicroMo® Electronics Inc. The maximum output power that they can supply is 3.66 W, the stall torque is $1.633x\ 10^{-2}\ N/m$ [15] and the most efficient area of operation is for $1.63 \cdot 10^{-3} < \Gamma < 4.9 \cdot 10^{-3}\ N/m$. This indicated that the model has to be modified in order to take into consideration a limitation in power and torque supply.

In the modified approach the following assumptions have been adopted:

1. Slip conditions between rollers and filament, according to the generalized Navier law [22];

2. The angular velocity of the rollers changes in the middle of the deposition process (see the Experimental Set Up section) as much as possible, but without requiring an excessive power supply;
3. The heat flow rate is increased following a ramp function (in order to model the close loop control);

There are prespecified upper bounds for the torque and the power supplied by the stepper motors. Figure 5.6 presents the results obtained with the modified model. In Figure 5.6.a the theoretical response of the velocity of the rollers, according to the command provided by the SML file is shown. However, because of the motor specifications, the speed of the rollers increases until a point when the maximum torque and/or power limits are reached. Beyond this point the rollers maintain a constant velocity on an interval Δt (Figure 5.6.a), during which the desired temperature of the melt is reestablished due to the increase in the heat flow rate (Figure 5.6.c). The necessary heat flow is calculated by specifying the exit temperature which must be kept between *540* and *552 K* (Figure 5.6.d).

The slip condition is taken into account in calculating the melt velocity. The algorithm applied for this case is as follows: (1) the speed of the rollers is increased of a constant value, thus an iteration is performed imposing that the melt is flowing at the same rate (no slip conditions); (2) the force applied by the motor is then calculated using equation (5.13)) and a check on the power and torque is made (equation (5.14) and (5.15)); (3) if the limit on the power and torque is reached, the program proceeds

considering that the applied force is also used to overcome the friction between the rollers and the filament:

$$F_s = \mu \cdot v_r \text{ where } \mu = \mu_0 \cdot v_r^{\,e-1} \tag{5.17}$$

where $\mu_0 = 1, \quad e = 0.48$ are material properties;

(4) the force F applied to extrude the melt is thus reduced by the amount F_s; (5) the new value of F is consequently used to calculate the real average velocity of the melt (see Figure 5.6.b).

These results also indicate that the power and torque necessary to maintain the extrusion process are kept within an acceptable range (Figure 5.6.g and Figure 5.6.h). Thus, it can be concluded that the modified model is more realistic and applicable to physical systems. Furthermore, with these more realistic assumptions the model became capable to better reproduce the experimental observations as will be discussed in a later section.

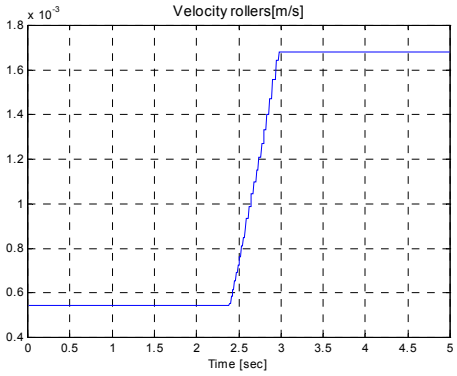

(a)

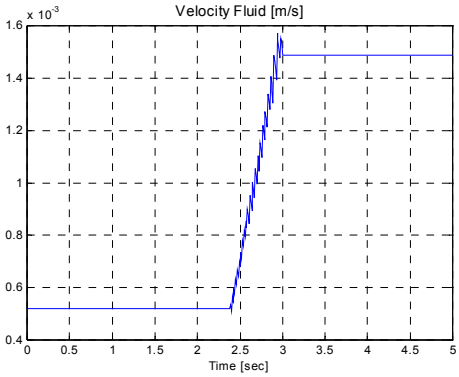

(b)

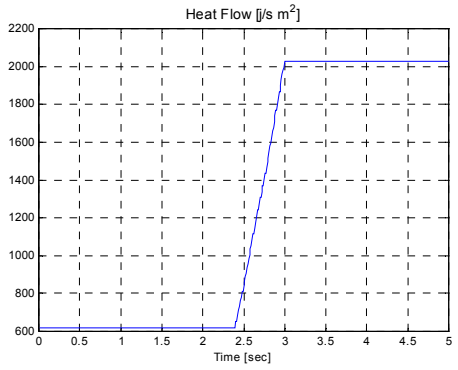

(c)

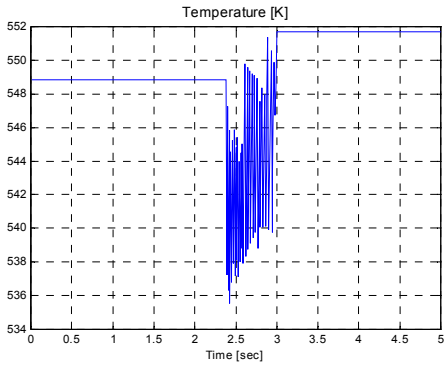

(d)

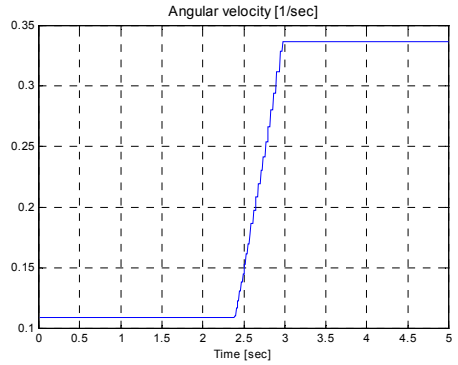

(e)

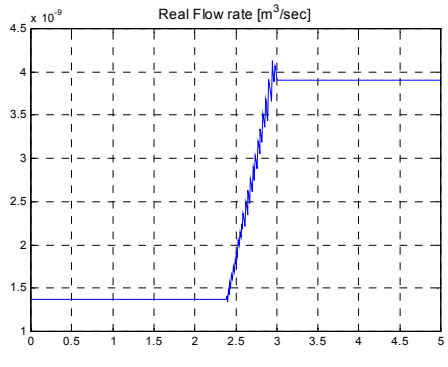

(f)

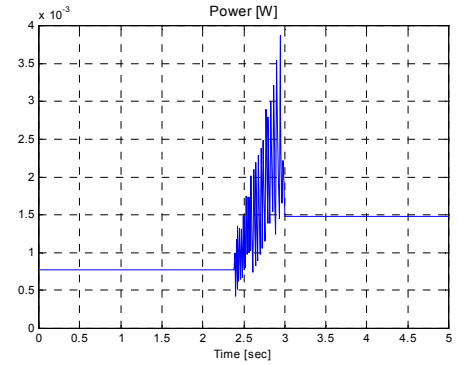

(g)

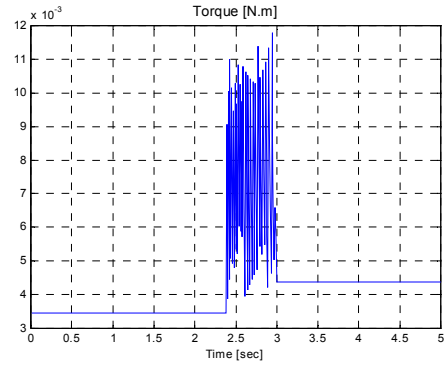

(h)

Figure 5.6: Results from the modified model for step amplitude = 2.9851

5.5 Liquefier dynamics: transfer function approach

In the simplest case the liquefier can be modeled as a dynamic system subjected to the digital SML command, which indicates the desired flow rate, as the input signal and the real flow rate as the output from the system. In the present work the following assumptions have been made:

- the communication between the PC and the controller are instantaneous;
- the Asymtek digital controller is infinitely fast;
- the ABS filament at the entrance of the liquefier is perfectly round, with a diameter of 1.78 mm and the material density is constant;
- the filament is perfectly rigid and does not buckle between the rollers and the liquefier entrance.

In order to develop a model for the transfer function of the liquefier, the response to a step input function has been studied and analyzed. The main objective is that once the time constant, time delay and "gain magnitude constant" of the liquefier system are known, the flow rate can be more accurately regulated according to the deceleration and acceleration of the deposition speed. With this capability it will be possible to significantly reduce some of the irregularities depicted in Figure 5.2, particularly in zones II and IV. In this section the experimental and analytical studies conducted to determinate the liquefier transfer function are presented.

In performing the dynamic modeling for the liquefier, the following variables have been taken in consideration:

- the time delay τ between the signal (change in the material flow rate at the entrance of the liquefier) and the observation of the results (change of the flow rare at the end of the liquefier);
- The slip conditions between the rollers and the filament are accounted for as a delay term;
- The material properties of the ABS (i.e. viscosity, melting flow, thermal conductivity, thermal capacity) ;
- The heat flux that needs to be adapted to the change in the flow rate.

For a better understanding of the dynamics and development of a control strategy, an analog electronic circuit has been developed as shown in Figure 5.7.

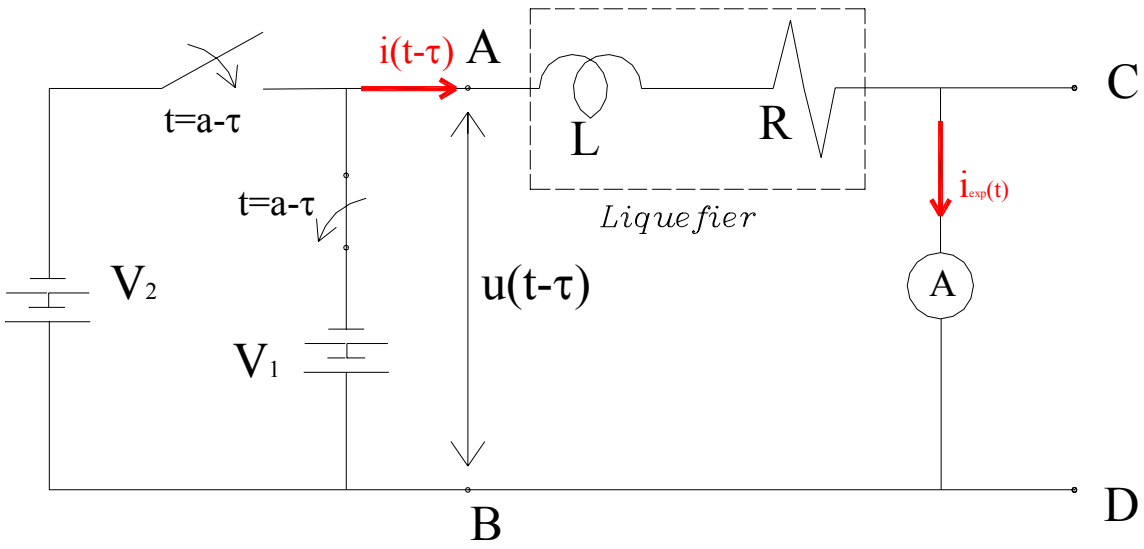

Figure 5.7: The analog electric circuit for dynamic analysis of liquefier

The specified flow rate can be represented as the applied current i (or voltage u, due to the proportional relation between the two entities) at the node A; the slip condition between the rollers and the filament can be modeled as a resistor R; while the material properties and the heat flux can be represented as an impedance L (they can be seen as an opposition to sudden changes in the flow rate).

The response of the liquefier can thus be mathematically expressed using the following equations [46]:

$$\begin{cases} L\dfrac{di(t-\tau)}{dt} + (R)\cdot i(t-\tau) = u(t-\tau) \\ \\ y(t) = i_{\exp}(t) \\ \\ i(t-\tau) = i_{\exp}(t) \end{cases} \tag{5.18}$$

where $i_{\exp}(t)$ is the experienced response of the system, i.e. the current registered at time t by the amperometer. It can be noticed that, due to the time delay τ between the data acquisition of i (current in the node C) and the imposed voltage u (thus the current i) between the nodes A and B, the analyzed response is:

$$y(t) = \quad i(t-\tau) \tag{5.19}$$

Substituting (5.19) into the first equation of the system (5.18):

$$L\cdot \dot{y}(t) + R\cdot y(t) = u\left(t-\tau\right) \tag{5.20}$$

Applying the Laplace transform (indicated with $\mathcal{L}$) to the equation (5.20)

$$\mathcal{L}\{L \cdot \dot{y}(t) + R \cdot y(t)\} = \mathcal{L}\{u(t-\tau)\} \tag{5.21}$$

$$L \cdot s \cdot Y(s) + R \cdot Y(s) = \mathcal{L}\{u(t-\tau)\} \tag{5.22}$$

where $Y(s)$ is the Laplace transform of $y(t)$.

In order to develop a transfer function of the liquefier, a step function has been applied as follows

$$u(t-\tau) = \begin{cases} \mu_1 & t \le a+\tau \\ \mu_2 & t > a+\tau \end{cases} \tag{5.23}$$

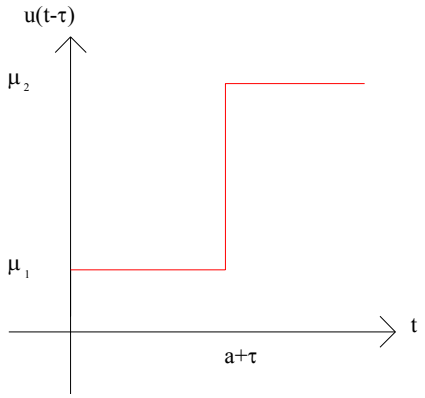

Defining H(t-k) the Heaviside step function:

$$H(t-k) = \begin{cases} 0 & t \le k \\ 1 & t > k \end{cases} \tag{5.24}$$

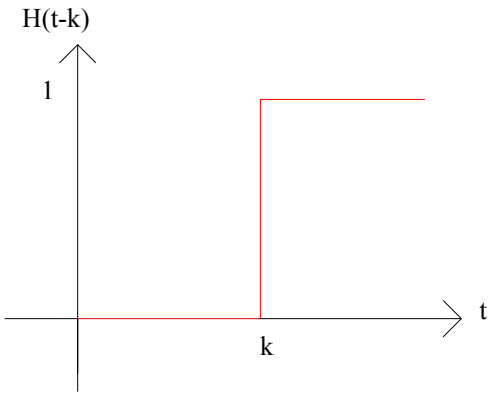

one can write [24]:

$$u(t) = \mu_1 \cdot H(t-0) + (\mu_2 - \mu_1) \cdot H(t-a) \tag{5.25}$$

and similarly

$$u(t-\tau) = \mu_1 \cdot H(t-\tau) + (\mu_2 - \mu_1) \cdot H(t-a-\tau) \tag{5.26}$$

Remembering the Laplace transform of an Heaviside step function H(t)

$$\mathcal{L}\{H(t-k)\} = \frac{e^{-ks}}{s} \tag{5.27}$$

and applying the property of linearity for the Laplace transform of the equation (5.25) and (5.26), it is possible to derive:

$$\mathcal{L}\{u(t)\} = U(s) = \mu_1 \frac{1}{s} (\mu_2 - \mu_1) \frac{e^{-as}}{s} \tag{5.28}$$

Similarly

$$\mathcal{L}\{u(t-\tau)\} = \mu_1 \frac{e^{-\tau s}}{s} + (\mu_2 - \mu_1) \frac{e^{-(a+\tau)s}}{s} = e^{-\tau s}\left[\mu_1 \frac{1}{s} + (\mu_2 - \mu_1) \frac{e^{-as}}{s}\right] \tag{5.29}$$

Substituting equation (5.29) into (5.22):

$$(L \cdot s + R)Y(s) = e^{-\tau s}\left[\mu_1 \frac{1}{s} + (\mu_2 - \mu_1)\frac{e^{-as}}{s}\right] \tag{5.30}$$

Comparing equation (5.28) and (5.30):

$$(L \cdot s + R) \cdot Y(s) = e^{-\tau s} \cdot U(s) \tag{5.31}$$

The *transfer function* G(s) of the system can thus be expressed as:

$$G(s) = \frac{Y(s)}{U(s)} = \frac{\frac{1}{R}}{\left(\frac{L}{R}\right)s + 1} \cdot e^{-\tau s} \tag{5.32}$$

For simplicity, the following constant can be defined:

$$\mu = \frac{1}{R} \tag{5.33}$$

$$T = \frac{L}{R} \tag{5.34}$$

Equation (5.31) can thus be rewritten in the more conventional form [16]:

$$G(s) = \frac{\mu}{Ts + 1} \cdot e^{-\tau s} \tag{5.35}$$

where T is called equivalent time constant,

τ is called equivalent delay and

μ is the gain.

As it is shown in equation (5.35), the transfer function of the liquefier is modeled as a *first order* differential equation. This limits the validity of the studied model to low

frequency responses. The investigation of the II order effects is not indeed part of the goals of the present paper.

5.6 Experimental studies

In order to determine the dynamic response of the liquefier, the relation between the applied value and the actual response in the flow rate during the deposition of a road has been studied. More specifically, a SML file has been written so to deposit a single 10 cm-long-road, at a constant speed of 2 cm/sec. In the same file the command to change the material flow rate is given at the half-length point during building of the road. With accurate measuring of the sectional areas along the extruded filament it was possible to calculate the physical flow rate at the exit of the nozzle, thus enabling comparison with the theoretical predictions.

In order to minimize measurement errors due to the imperfect contact between the extruded material and rough, porous, foam platforms typically used in FD processes, the roads have been deposited on a Plexiglas base. The measurements of the sections of the roads have been performed using Raman spectrometer equipment by determining the road width and thickness respectively at various locations. More specifically, the CC/CD camera attached to the microscope and a computer equipped with Renishaw WIRE software have been used. One of the Renishaw features, the WiRE Video Viewer, allows not only to take pictures of the object set in the microscope stage, but also defines a Cartesian coordinate reference system to read the coordinates of a particular point, to accurately move the stage in *x* and y directions using coordinate inputs, etc. A two-speeds

joystick is also connected to the microscope in order to manually adjust the position of the stage while observing under the microscope.

To generate the sectional data, the roads are first cut very near to the ends with a razor blade and are placed on the microscope stage. Using a 5X magnification lens, the origin of the reference system is defined at one end of the fiber. Following this, the stage can be accurately moved within 1/10 of a μm by entering the desired x-value (distance from one end of the road) in the program.

At each desired location the y coordinates of two opposite points, i.e. points A and B in Figure 5.8, are determined by simply moving the cursor to follow the edges of the road. The width of the fiber is thus calculated as a difference between the two y values. These steps are repeated for different point locations (i.e. points A',B',A",B" etc.) as well as for the side of the road (Figure 5.8.b), in order to also determine its height.

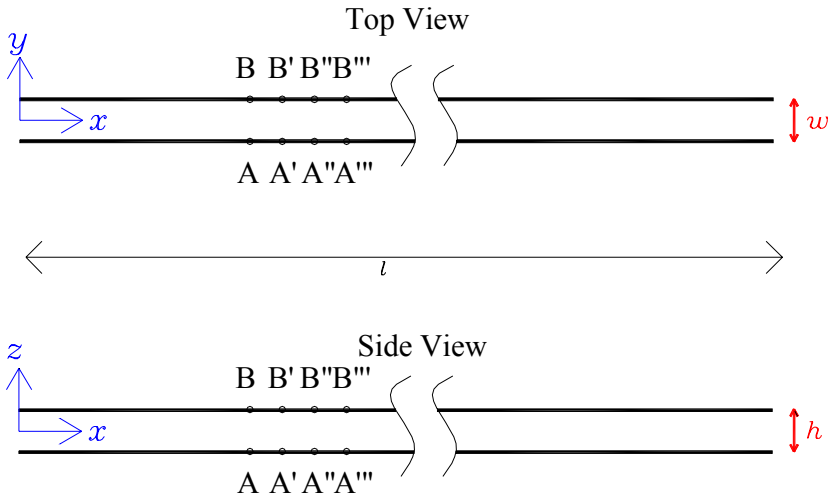

Figure 5.8: a) Top view of the road; b) Side view of the road

For accurate observation of the system response to the step function, the sampling rate has been considerably increased at $x = l/2$ which is the location corresponding to the instant of sudden change in the flow rate.

5.7 Results

The results of the experiments described in the sections above have been assembled in Figure 5.9, Figure 5.10 and Figure 5.11. In these plots, the curves for the step input for the flow rate as well as the curves of the actually measured flow rates can be observed. The only difference between the three experiments depicted in these Figures is the amplitude of the input step functions, while all the other operating parameters are kept the same.

Following observations can be made from these graphs:

- there is a good agreement between the applied flow rate and the physical response of the system for small magnitudes;
- there is a steady state error of approximately the 12% between the input command and the resulting physical flow rate;
- the presence of higher order dynamics will likely improve the dynamic modeling while increasing the complexity of the analysis substantially.

Based on the experimental data, conveniently summarized in Table 5-1, the transfer function for the system, characterized by liquefier filled with ABS, can been obtained (see equation (5.36)) as

$$G(s) = \frac{0.8865}{1 + 0.45s} e^{-0.04s} \tag{5.36}$$

Table 5-1: Parameters of the liquefier transfer function for a step input

Test n.	**1**	**2**	**3**	**Average**
Step Amplitude [mm^3/sec]	3.5645	2.9851	2.4332	2.9946
μ (gain)	0.8994	0.8762	0.8839	0.8865
τ [sec]	0.04	0.06	0.02	0.04
T [sec]	0.47	0.38	0.5	0.45

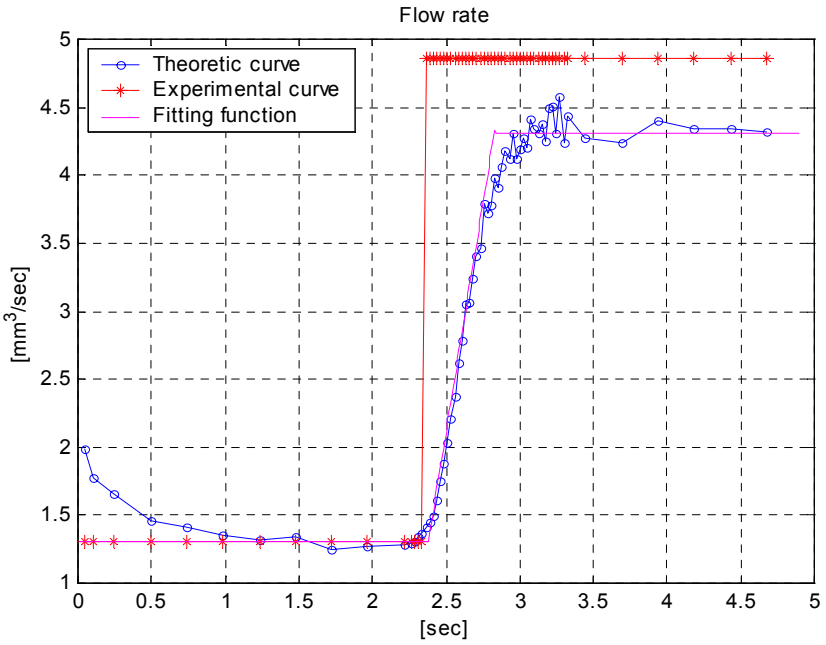

Figure 5.9: Step response, step amplitude = 3.5645

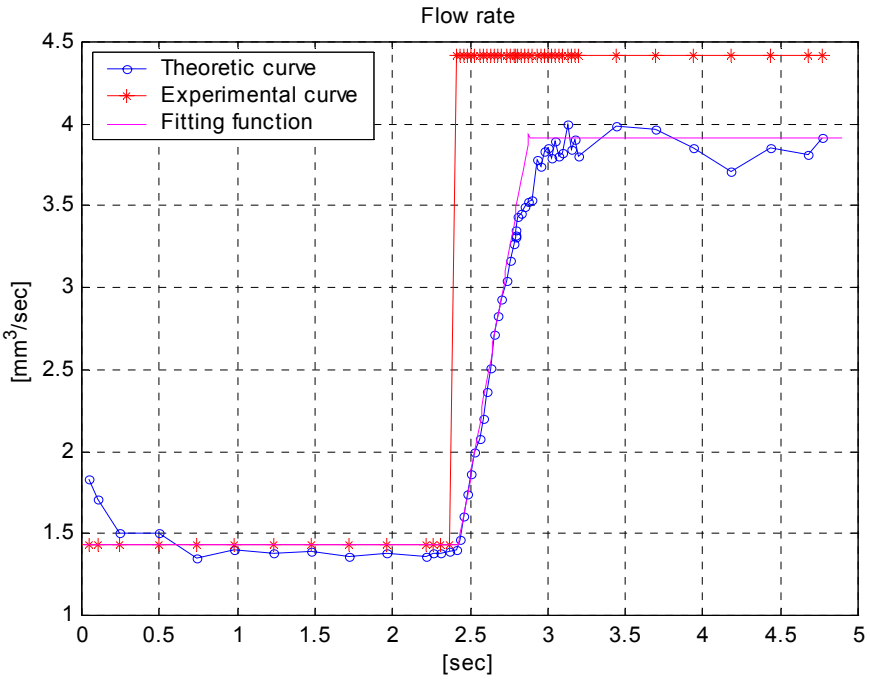

Figure 5.10: Step response, step amplitude =2.9851

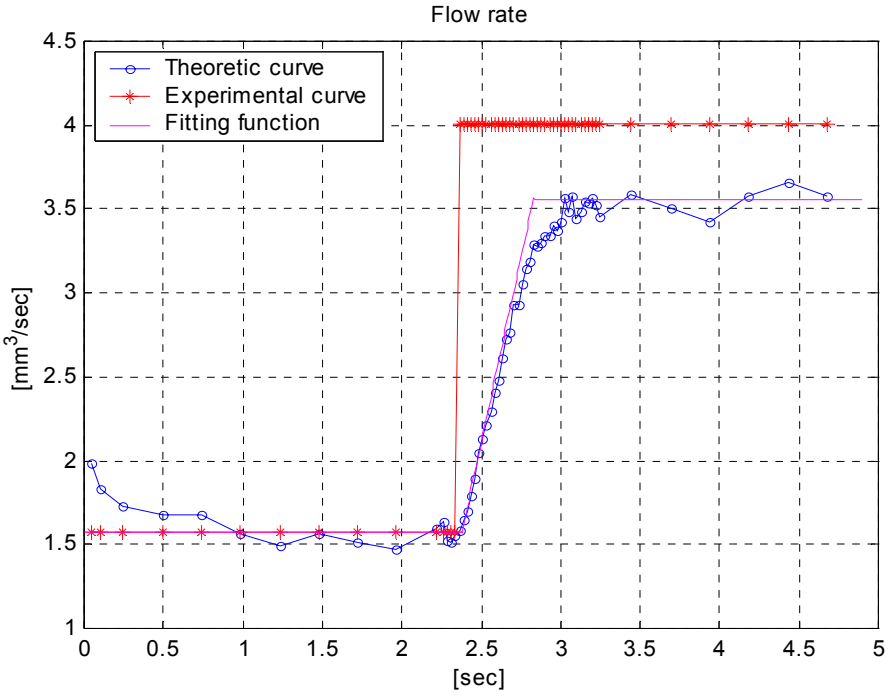

Figure 5.11: Step response, step amplitude =2.4332

5.8 Conclusions

In order to verify the validity of the model, three simulations have been performed for different step amplitude of the input flow rate command. In Figure 5.12, Figure 5.13 and Figure 5.14, the theoretical change in the flow rate (according to the SML file), the experimental curve (determined as described in the previous section) as well as the results obtained with the mathematical model have been assembled.

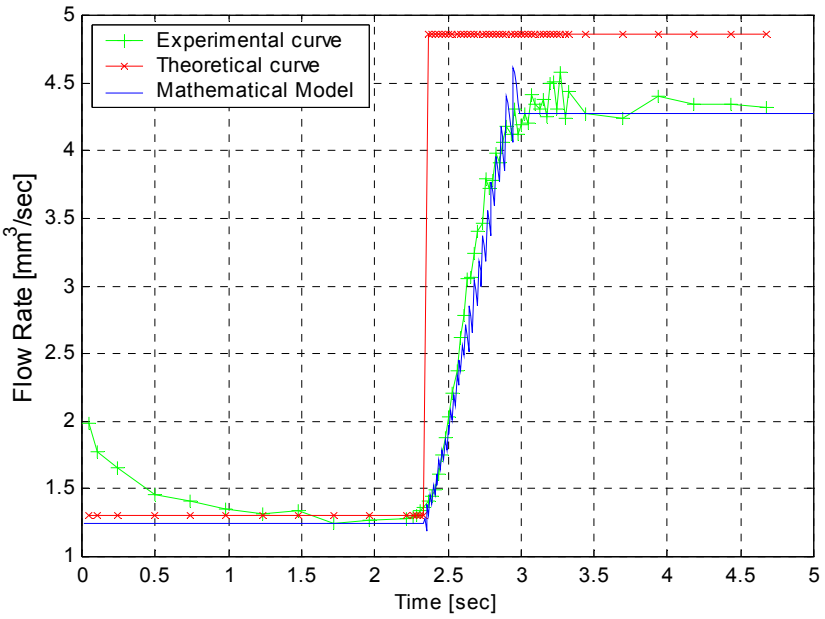

Figure 5.12: Step response, step amplitude = 3.5645

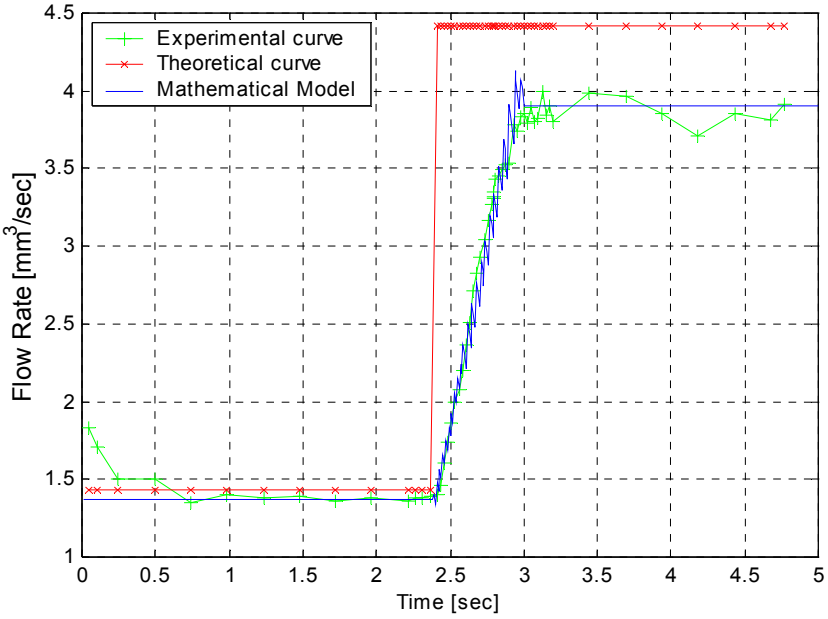

Figure 5.13: Step response, step amplitude =2.9851

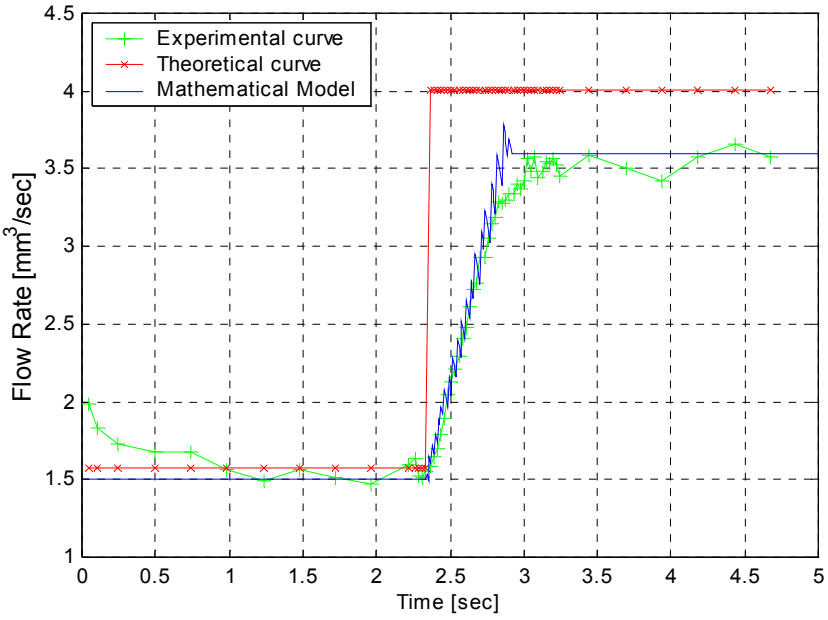

Figure 5.14: Step response, step amplitude = 2.4332

The comparison of the experimental data with the analytical results shows a good agreement for the purpose of integrating a control function describing the dynamic response of a liquefier to changing input commands. The agreement between the mathematical analysis and a transfer function approach provide a sound platform for further refinement of both approaches if needed. However, it should be noted that higher order analysis quickly complicates the development and can be justified only if other factors related to the overall system performance are also accounted for.

CHAPTER 6: MECHANICAL CHARACTERIZATION

6.1 Abstract

The previous chapters focused on the fabrication of the parts using a layered manufacturing approach based on fused deposition. Parts fabricated using this approach exhibit unusual characteristics due to their internal architecture as a result of evolutionary building configuration.

As a finished product, these parts should have predictable behavior under loading conditions and also maintain their dimensional stability especially under vary thermal environments. This necessitates characterization of their mechanical properties and development of suitable analysis tools.

This chapter focuses on mechanical characterization of parts and development of analytical methods based on the similitude with other complex material systems, most notably with fiber-reinforced composite structures. The study focuses on experimental characterization for various built strategies and incorporates the results into a modeling scheme whereby both performance predictions and part dimensional stability can be investigated.

6.2 Introduction

From the description of the fused deposition process, presented in chapter 2, follows that each of the roads and then layers in LM can be considered to be the building blocks of the part. It is quite evident that the layers produced by stacking of roads show anisotropy due to property variations along the direction of the roads and across the roads

where the inter-road adhesion determines the strength. Furthermore, staking of layers to produce the part results in a similar behavior. As a natural consequence of this manufacturing approach, parts fabricated using layered manufacturing exhibit anisotropic properties.

It has been observed that the road shape and the road-to-road interaction, as well as the "trajectory" of deposition strongly affect the properties and performance of the finished product. This implies that determination of the build strategy will have a pronounced effect on the properties and ultimately on the performance of the part. Included in this consideration is the dimensional stability which result form processing related thermal stresses and how a given part responds to it dimensionally.

The internal architecture of a part fabricated using layered manufacturing resembles a fiber reinforced composite structure. Figure 6.1 shows a cross-section of a LM part where this relation is exaggerated. Individual roads are significantly stronger in the axial direction and resemble the fibers in a composite; however, material shows weaker behavior in the direction where stresses need to be carried through road-to-road or layer-to-layer adhesion.

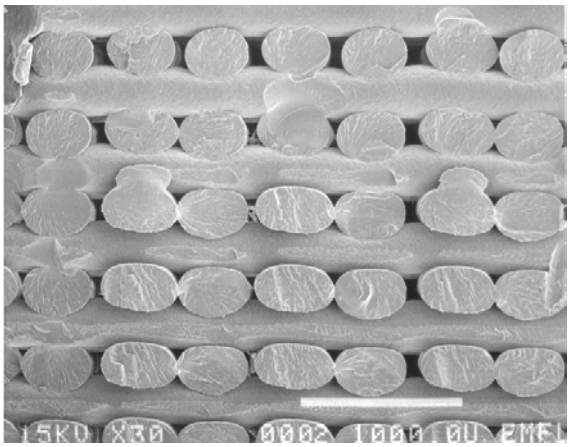

Figure 6.1: Cross-sectional view of ABS part built with 0/90^{o} rasters

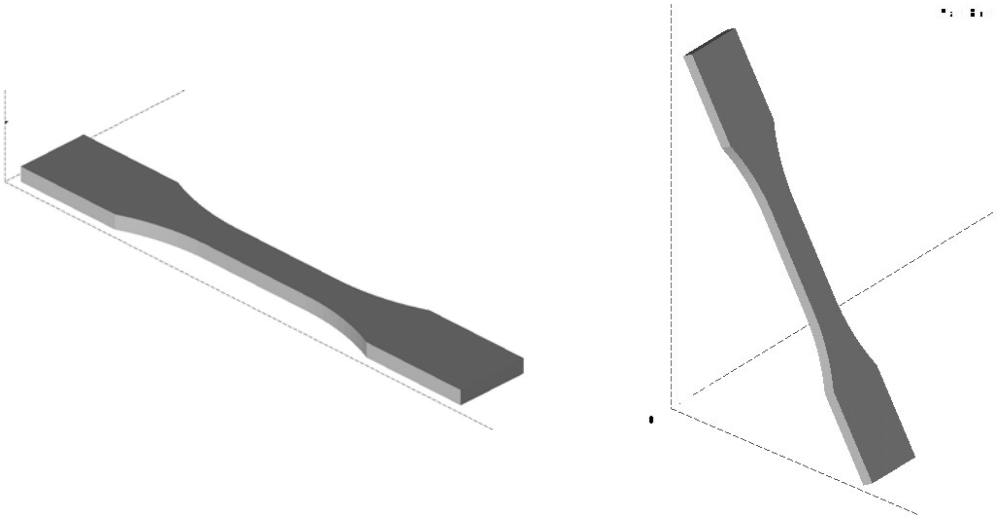

Figure 6.2: Different orientations of the same object

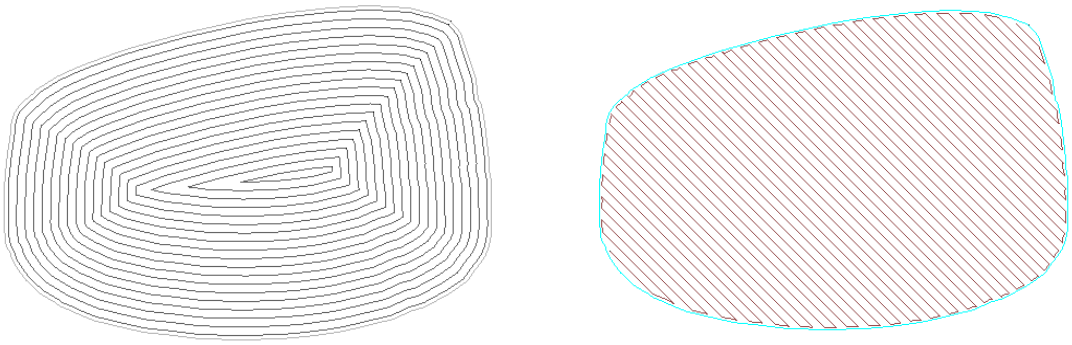

(a) (b)

Figure 6.3: Different toolpath configurations: (a) contour style; (b) raster style

Figure 6.2 shows how different built strategies can result in different property variations depending on producing individual layers.

The analogy between fiber-reinforced composites and parts using layered manufacturing allows for use of some of the analytical tools developed earlier for anisotropic products. In the core of such analysis tools is the determination of the anisotropic stiffness matrix.

This chapter presents a methodology [6] to determine the stiffness matrix for a part built with FDM technique. To make the analysis suitable for conventional composite formulations a pseudo-isotropic path [0 90 +45 –45] has been used to fabricate and test the parts. Experimental investigations are performed on parts made of ABS material and fabricated using the Stratasys 1650 FDM machine.

6.3 Analytical studies

In linear elasticity the relation between stress and strain follows the Hooke's law [36]. It states that, for small strains, stress is linearly proportional to strain. Thus, in order to completely determine the mechanical properties of a material, assuming fully linear behavior, the 36 components of the compliance matrix S of the equation (6.1) must be known

$$\begin{bmatrix} \varepsilon_1 \\ \varepsilon_2 \\ \varepsilon_3 \\ \gamma_{23} \\ \gamma_{13} \\ \gamma_{12} \end{bmatrix} = \begin{bmatrix} S_{11} & S_{12} & S_{13} & S_{14} & S_{15} & S_{16} \\ S_{21} & \cdots & \cdots & & & \\ S_{31} & \cdots & \cdots & & & \\ S_{41} & & & \cdots & & \\ S_{51} & & & & \cdots & \\ S_{61} & & & & & S_{66} \end{bmatrix} \bullet \begin{bmatrix} \sigma_1 \\ \sigma_2 \\ \sigma_3 \\ \tau_{23} \\ \tau_{13} \\ \tau_{12} \end{bmatrix} \tag{6.1}$$

In tensor notation, the equation (6.1) can be also rewritten as:

$$\underline{\varepsilon} = \underline{\underline{S}}\,\underline{\sigma}$$

where the number of underlines specify the dimension of the matrix.

Due to the symmetric properties of the Cauchy's tensor (represented by the matrix $\underline{\underline{S}}$), equation (6.1) can be rewritten in term of only 21 unknowns:

$$\begin{bmatrix} \varepsilon_1 \\ \varepsilon_2 \\ \varepsilon_3 \\ \gamma_{23} \\ \gamma_{13} \\ \gamma_{12} \end{bmatrix} = \begin{bmatrix} S_{11} & S_{12} & S_{13} & S_{14} & S_{15} & S_{16} \\ & S_{22} & \dots & \dots & \dots & \dots \\ & & S_{33} & \dots & \dots & \dots \\ & & & S_{44} & \dots & \dots \\ & sym. & & & S_{55} & \dots \\ & & & & & S_{66} \end{bmatrix} \bullet \begin{bmatrix} \sigma_1 \\ \sigma_2 \\ \sigma_3 \\ \tau_{23} \\ \tau_{13} \\ \tau_{12} \end{bmatrix} \tag{6.2}$$

No assumptions, beside elasticity, have been made until this point, thus equation (6.2) is valid for any anisotropic domain with no symmetry elements present.

For an orthotropic material, which is defined as a material with 3 mutually perpendicular plane of symmetry, equation (6.2) can be simplified in term of the following nine unknowns:

$$\begin{bmatrix} \varepsilon_1 \\ \varepsilon_2 \\ \varepsilon_3 \\ \gamma_{23} \\ \gamma_{13} \\ \gamma_{12} \end{bmatrix} = \begin{bmatrix} S_{11} & S_{12} & S_{13} & 0 & 0 & 0 \\ & S_{22} & S_{23} & 0 & 0 & 0 \\ & & S_{33} & 0 & 0 & 0 \\ & & & S_{44} & 0 & 0 \\ & sym. & & & S_{55} & 0 \\ & & & & & S_{66} \end{bmatrix} \bullet \begin{bmatrix} \sigma_1 \\ \sigma_2 \\ \sigma_3 \\ \tau_{23} \\ \tau_{13} \\ \tau_{12} \end{bmatrix} \tag{6.3}$$

Considering now the conventional engineering constants in three principal directions, equation (6.3) can now be written in terms of the Young's modulus E, the Poisson ratio ν and the shear modulus G:

$$\begin{bmatrix} \varepsilon_1 \\ \varepsilon_2 \\ \varepsilon_3 \\ \gamma_{23} \\ \gamma_{13} \\ \gamma_{12} \end{bmatrix} = \begin{bmatrix} \frac{1}{E_1} & \frac{-\nu_{12}}{E_1} & \frac{-\nu_{13}}{E_1} & 0 & 0 & 0 \\ & \frac{1}{E_2} & \frac{-\nu_{23}}{E_2} & 0 & 0 & 0 \\ & & \frac{1}{E_3} & 0 & 0 & 0 \\ & & & \frac{1}{G_{23}} & 0 & 0 \\ & & & & \frac{1}{G_{13}} & 0 \\ & \textit{sym.} & & & & \frac{1}{G_{12}} \end{bmatrix} \bullet \begin{bmatrix} \sigma_1 \\ \sigma_2 \\ \sigma_3 \\ \tau_{23} \\ \tau_{13} \\ \tau_{12} \end{bmatrix} \tag{6.4}$$

where $\nu_{12} = -\frac{\varepsilon_2}{\varepsilon_1}$, $\nu_{13} = -\frac{\varepsilon_3}{\varepsilon_1}$, $\nu_{23} = -\frac{\varepsilon_3}{\varepsilon_2}$ and we have substituted:

$$\begin{aligned} S_{11} &= \frac{1}{E_1} & S_{12} &= \frac{-\nu_{12}}{E_1} = \frac{-\nu_{21}}{E_2} & S_{13} &= \frac{-\nu_{13}}{E_1} = \frac{-\nu_{31}}{E_3} \\ S_{22} &= \frac{1}{E_2} & S_{23} &= \frac{-\nu_{21}}{E_2} = \frac{-\nu_{12}}{E_1} & S_{33} &= \frac{1}{E_3} \\ S_{44} &= \frac{1}{G_{23}} & S_{55} &= \frac{1}{G_{13}} & S_{66} &= \frac{1}{G_{12}} \end{aligned} \tag{6.5}$$

Converting equation (6.4), the stress matrix can be expressed in term of a product between the general stiffness matrix $\underline{\underline{C}}$ and the strain tensor:

$$\underline{\sigma} = \underline{\underline{C}}\,\underline{\varepsilon} \tag{6.6}$$

or in the explicit form:

$$\begin{bmatrix}\sigma_1\\ \sigma_2\\ \sigma_3\\ \tau_{23}\\ \tau_{13}\\ \tau_{12}\end{bmatrix} = \begin{bmatrix} C_{11} & C_{12} & C_{13} & 0 & 0 & 0\\ & C_{22} & C_{23} & 0 & 0 & 0\\ & & C_{33} & 0 & 0 & 0\\ & & & C_{44} & 0 & 0\\ & sym. & & & C_{55} & 0\\ & & & & & C_{66}\end{bmatrix} \bullet \begin{bmatrix}\varepsilon_1\\ \varepsilon_2\\ \varepsilon_3\\ \gamma_{23}\\ \gamma_{13}\\ \gamma_{12}\end{bmatrix} \tag{6.7}$$

where:

$$C_{11} = \frac{S_{22}S_{33} - S_{23}{}^2}{S} \qquad C_{12} = \frac{S_{23}S_{13} - S_{12}S_{33}}{S} \qquad C_{13} = \frac{S_{12}S_{23} - S_{22}S_{13}}{S}$$
$$C_{22} = \frac{S_{11}S_{33} - S_{13}{}^2}{S} \qquad C_{23} = \frac{S_{12}S_{13} - S_{11}S_{23}}{S} \qquad C_{33} = \frac{S_{11}S_{22} - S_{12}{}^2}{S} \tag{6.8}$$
$$C_{44} = \frac{1}{S_{44}} \qquad C_{55} = \frac{1}{S_{55}} \qquad C_{66} = \frac{1}{S_{66}}$$

and:

$$S = S_{11}S_{22}S_{33} + 2S_{12}S_{23}S_{13} - S_{13}{}^2S_{22} - S_{23}{}^2S_{11} - S_{12}{}^2S_{33}$$

In order to define the mechanical behavior of an orthotropic part, it is thus necessary to determine nine independent constant. Experimental determination of these constants necessitate building six different specimens built in different orientations.

It must be noticed that, according to the Hook's law, the Young's modulus can be obtained from the stress-strain diagram as:

$$E_x = \frac{\Delta\sigma_x}{\Delta\varepsilon_x} \tag{6.9}$$

the Poisson's ratio as:

$$\nu_{xy} = -\frac{\varepsilon_y}{\varepsilon_x} \tag{6.10}$$

The in-plane shear modulus can be obtained from the test of a 45^{o} oriented unidirectional test specimen, according to the following equation:

$$G_{ab} = \frac{E_x}{2(1+\nu_{xy})} \tag{6.11}$$

where x is the direction of applied load and y is the direction perpendicular to it. Furthermore, a and b correspond to 1 and 2 for specimens built in the xy plane, to 1 and 3 for the ones built in xz plane and 2 and 3 for the ones in the yz plane.

6.4 Experimental studies

According to the testing procedures used for composite materials [44], the first step for a better understanding of the mechanical properties is to test a single "*fiber*". Since in FDM technology the extruded road can be considered as the reinforcement of the part, both the bulk feed material as well as the free extruded filament have been tested.

Filament sample preparation

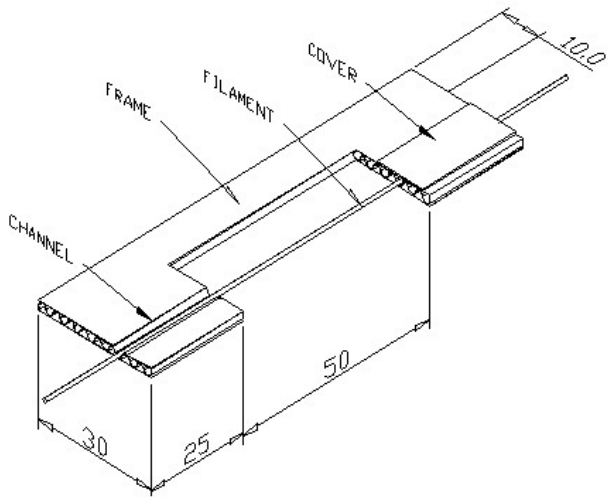

Figure 6.4: Filament sample preparation

The set up used for testing the bulk ABS filament is schematically shown in Figure 6.4. In order to have a larger grip area, the specimen is first glued on an approximately 4 mm thick corrugated cardboard frame of the dimensions specified. To ensure that during the tensile testing, the cardboard is not affecting the results, the frame is cut before applying the load.

In order to attach the sample to the cardboard, 2 channels - 25 mm long and 3 filament diameters wide - are cut through the top layer, leaving the corrugated portion intact. The channels are then filled with epoxy and the filament is laid across them with 10 mm ends overhanging the frame. Comparing the length of the overhang before and after the test will indicate if the filament has slipped through the same frame during the

pulling phase. The covers are successively fastened on the top of the channel using the same epoxy.

Once the epoxy has hardened, the sample is carefully placed on an *INSTRON* machine between pneumatic grips, which can be precisely aligned and can give an accurate control of the gripping pressure, which, in this study, is approximately 500 kPa.

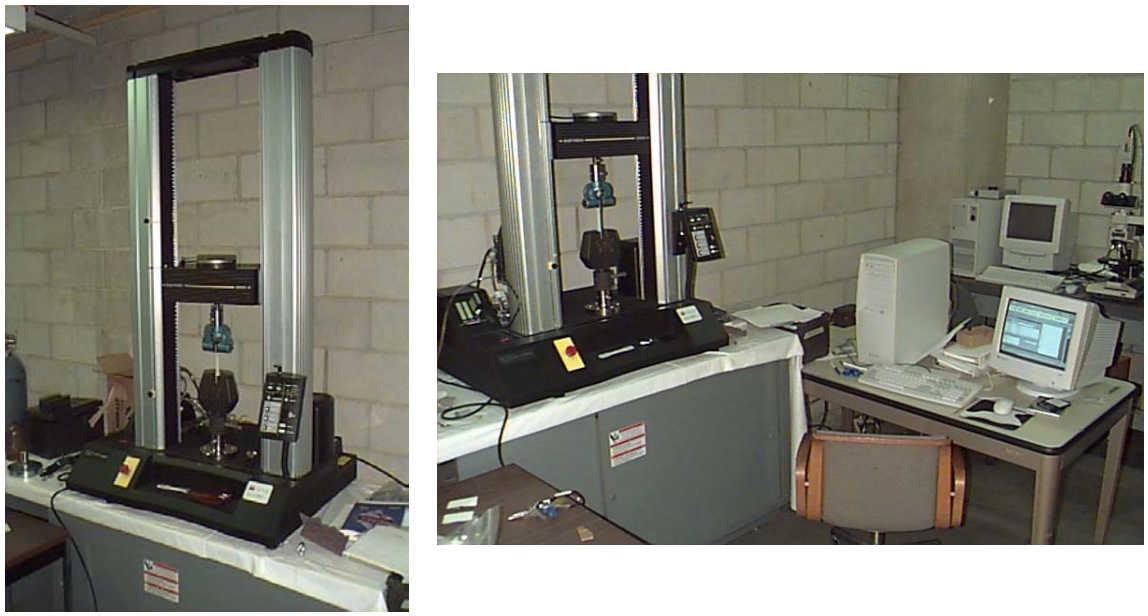

Figure 6.5: Tensile test setup

Sample road preparation

The sample preparation for the road test is very similar to the one used for the filament. Since the sample diameter is much smaller than the previous case, the type of cardboard used for the frame is non-corrugated and it is constituted of thin compressed paper. A tiny channel – 4 road diameters wide and 2 road diameters deep – is cut through the frame. In order to prevent undesirable loading of the filament during frame separation

(before the testing), two pre-cuts are also cut on the sides at the location shown in the picture.

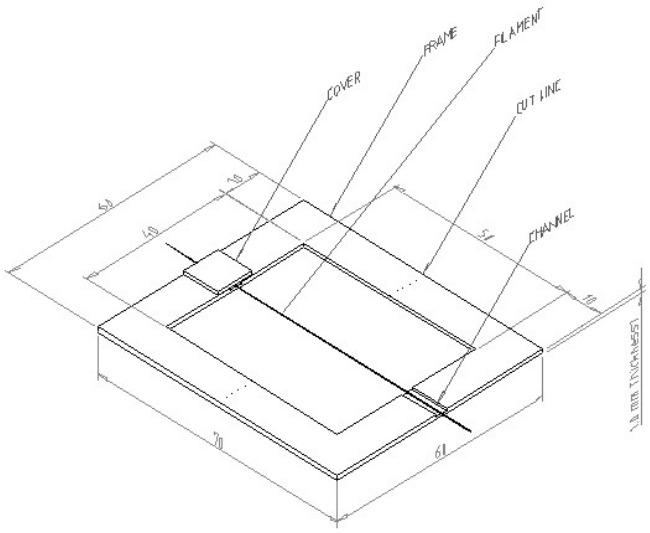

Figure 6.6: Sample road preparation

After filling the channel with epoxy, the road is mounted to the frame and is secured to it by small covers. Once the epoxy has hardened, the sample is mounted in the *INSTRON* grips at the cover location (Figure 6.7).

Figure 6.7: The road tensile test

Tensile test sample preparation

In order to obtain the nine independent constants of the stiffness matrix, six samples built with different orientations (Figure 6.8) have to be tested. Since no special standards exist for RP parts, the samples have been prepared according to the geometry and dimensions specified in the ASTM D 5937-96, the standards for molded plastic parts [18]. The dog-bone sample is designed using a standard 3D CAD program thus it is exported in an STL format. This is the file format that can be imported in QuickSlice, the program provided by Stratasys to slice the part, design the road toolpath and then send the related commands to the RP machine. After slicing the parts, oriented as shown, the toolpath has been chosen first so to obtain a pseudo-isotropic stacking sequence [0 90 +45 –45], then to obtain a domain decomposition raster [66].

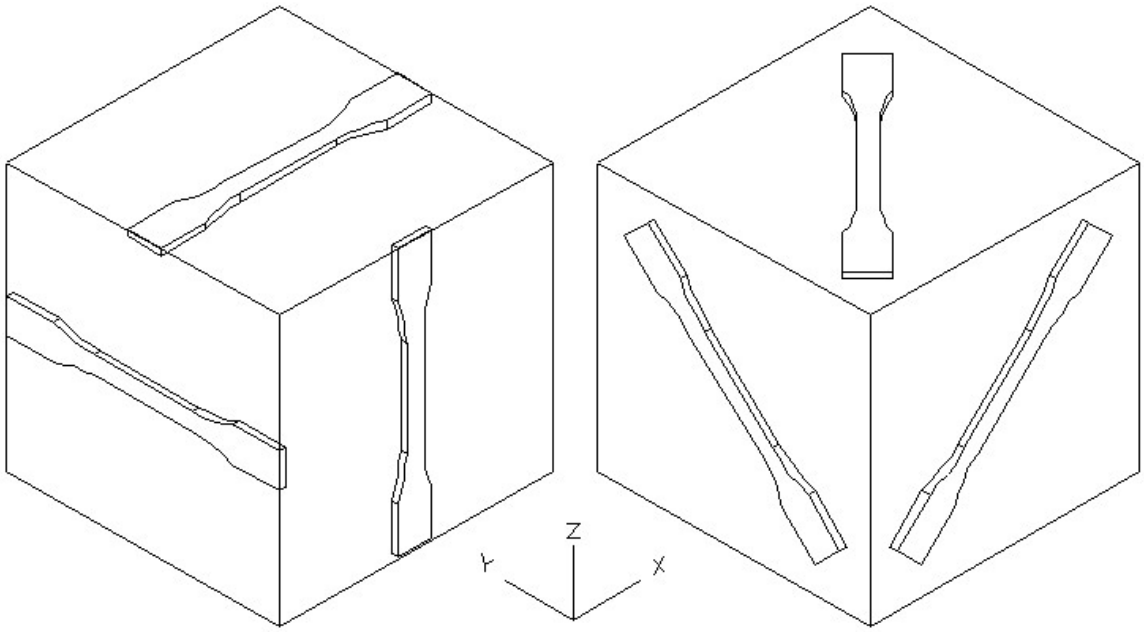

Figure 6.8: Tensile test - orientations of specimens

It must be noted that in the case of domain decomposition raster it was not possible to build a part with 45^{o} orientation, consequently the stiffness matrix is determined only partially.

Flexural test sample preparation

In order to evaluate the flexural properties of the built parts, two specimens with specifications described in ASTM D 790-96 have been built and tested using the 3-points bending procedure [19].

The toolpaths used for the 2 specimens have been [0 90 +45 –45] and the domain decomposition raster.

6.5 Results

The tensile and the 3-points bending tests have been performed using an *INSTRON 5569* machine, equipped with the following features:

- A cross-head screw-driven by a DC servo motor, with a speed range between 0.001 and 500 mm/min;
- A load cell with capacity range between –50 kN to +50 kN;
- Two wedge action grips, for the tensile test on the dog-bone specimens; two pneumatic grips for the tensile test on the filament and on the road;
- One axial strain extensometer with a gauge length of 50 mm;
- One transverse strain extensometer with a gauge length of 10 mm.

The *INSTRON* machine was controlled by software, installed on a Windows-based PC, which allowed adjustment of the test parameters using a closed loop digital controller.

Comparison between ABS filament and ABS road tests:

The results obtained for the tensile test on the filament and on the road were reported respectively in Table 6-1 and Table 6-2.

Table 6-1: Filament tensile test results

Gage length [mm]	Avg. diameter [mm]	Number of specimens tested	Number of specimens considered	Tensile strength [MPa]	Max strain [%]	Elastic modulus [MPa]
50	1.73	11	8	34.3094	53.3290	19.001825

Table 6-2: Road tensile test results

Gage length [mm]	Avg. diameter [mm]	Number of specimens tested	Number of specimens considered	Tensile strength [MPa]	Max strain [%]	Elastic modulus [MPa]
50	0.396	12	10	33.6096	16.8708	19.0172

Comparing the results of the filament and road tensile test, it can be noticed that:

- The values of the tensile strength and the Young's modulus are similar;

- The maximum strain obtained for the road test is almost 1/3 of the one obtained for the filament.

It is possible to conclude that the extrusion process does not have a considerable influence on the strength and modulus of the material, but notably affects the maximum strain.

This last effect can be explained by the viscoelastic behavior of the ABS. It can be hypothesized that during the extrusion through the 0.3 mm diameter nozzle, the polymer is subjected to an orientation [7] of the molecule chains and pre-stretched during solidification, which reduce the elongation characteristics of the material.

The tensile test of the ABS dog-bone specimens built with standard lay-up:

During the tensile test of the dog-bone specimens the data regarding the ultimate tensile strength, the Young's modulus and the Poisson ratio have been collected.

After the collection of the data points obtained in Excel format, a user defined MATLAB function has been developed to perform a least square interpolation of the linear part of the stress-strain curve. Using the interpolating curve, the Young's modulus and the Poisson's ratio (which is the ratio between the slopes of the stress-axial strain and stress-transverse strain) have been calculated with equation (6.9) and equation (6.10) respectively.

The data showed wide scattered plots that can be explained considering the considerable effects of the processing parameters on the measurements. Furthermore, it must be added that a large number of specimens failed prematurely because of the following possible reasons:

- Intra-laminar defects, due to the presence of excess material stuck to the nozzle and then dropped onto a layer;
- Inter-laminar defects due to over or under fill between rasters or between raster and contour;

Surface roughness (initiation of microcracks).

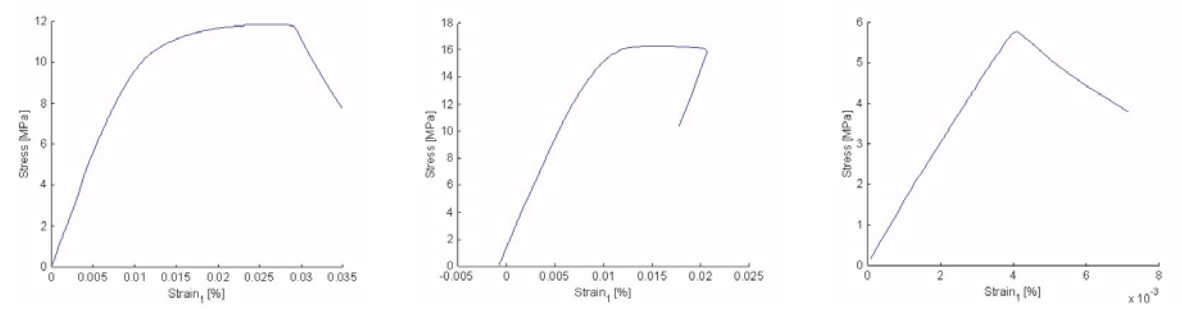

(a) (b) (c)

Figure 6.9: Stress-strain curves for xy (a), yz (b) and xz (c) oriented ABS specimens

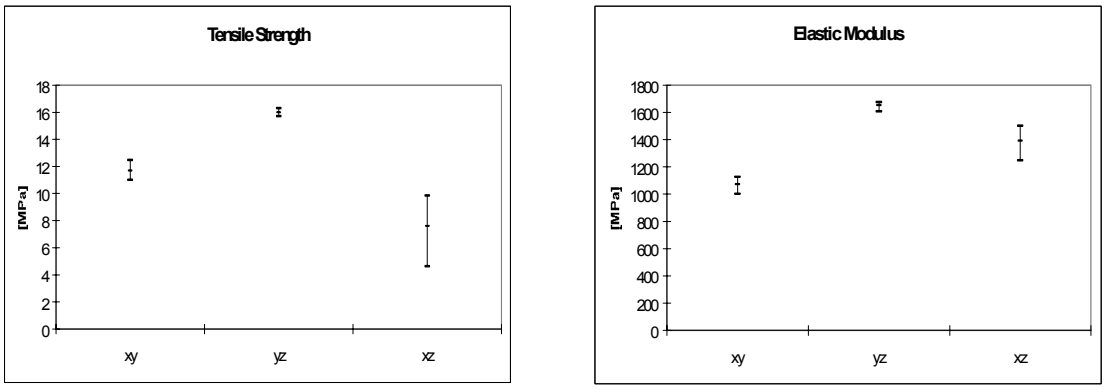

(a) (b)

Figure 6.10: Max, min and average. values: Young's modulus (a) and tensile strength (b)

According to the predictions, the *xz*-oriented samples (see Figure 6.8) show the lowest tensile strength (see Figure 6.9.c). The reason is due to the sample being pulled in

the building directions where the bonding between layers is very weak and where defects are usually present. The *yz* parts (Figure 6.8) on the contrary show the highest values both for the Young's modulus and the tensile strength. It must be also noticed (see Figure 6.10) that the *xz* samples give results with more spread, due probably to the presence of defects in the interlayer bonds. In Table 6-3, the numerical values have been presented.

Table 6-3: Tensile test results – Standard lay-up

Toolpath	**Build plane**	**Orientation**	**Number of specimens tested**	**Number of specimens considered**	**Tensile strenght [MPa]**	**Elastic modulus [MPa]**
[0 90 +45 –45]	xy	X	4	4	11.700	1072.900
[0 90 +45 –45]	yz	Y	4	4	15.987	1652.523
[0 90 +45 –45]	xz	Z	11	6	7.608	1391.448
[0 90 +45 –45]	xy	x+45	5	5	10.808	970.944
[0 90 +45 –45]	yz	y+45	5	4	13.465	1519.115
[0 90 +45 –45]	xz	z+45	3	3	14.702	1527.600

Finally, the stiffness matrix becomes:

$$C = 1.0e+003 * \begin{bmatrix} 1.8530 & 1.4348 & 1.1810 & 0 & 0 & 0 \\ 1.4348 & 3.0843 & 1.6444 & 0 & 0 & 0 \\ 1.1810 & 1.6444 & 2.4141 & 0 & 0 & 0 \\ 0 & 0 & 0 & 0.5540 & 0 & 0 \\ 0 & 0 & 0 & 0 & 0.5405 & 0 \\ 0 & 0 & 0 & 0 & 0 & 0.3696 \end{bmatrix} \text{MPa} \qquad (6.12)$$

and the engineering constants are:

Table 6-4: Engineering constants – Standard lay-up

E_x (MPa)	E_y (MPa)	E_z (MPa)	G_{xy} (MPa)	G_{xz} (MPa)	G_{yz} (MPa)	ν_{xy}	ν_{xz}	ν_{yz}
1072.9	1653	1391.7	369.6	540.5	554	0.3209	0.2707	0.4391

The tensile test of the ABS dog-bone specimens built with domain decomposition lay-up:

In order to evaluate the effects of the toolpath on the mechanical properties of the final part, some dog-bone specimens have been built using a level domain decomposition (see Figure 6.11) and then a different raster for each of the sub-domains.

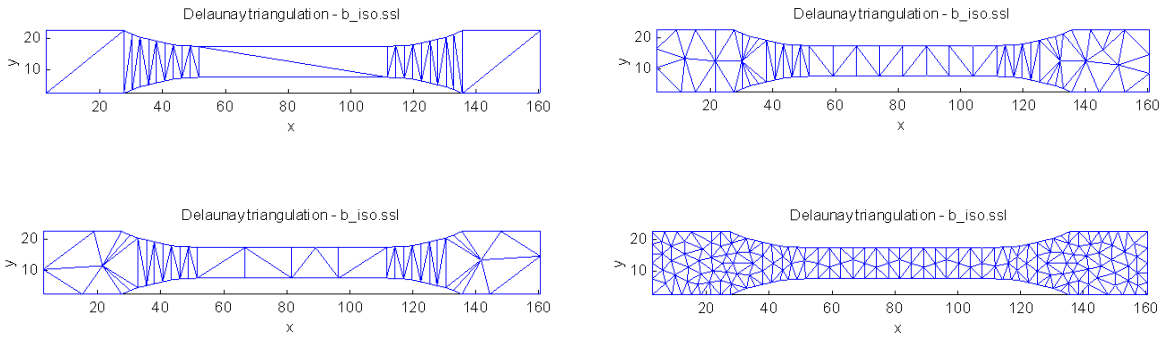

Figure 6.11: Domain decomposition of a tensile test bar

With this approach a more random overall road orientation as well as stronger bonds between adjacent roads (due to the reduction in the road length) are expected because of the higher temperature at the interface (see equations (3.2) and (3.3)). This is reflected (see Figure 6.12) in reduced scatter in data for both the tensile strength and the Young's modulus. It must be noted that for the *xz* oriented samples, the random orientation of the road does not seem to affect the results at all: the Young's modulus and

the tensile strength (see Table 6-5) values are very close to the ones for the standard lay-up (see Table 6-3). Furthermore, for these specimens the results are still very spread out, probably because of the poor intralaminar bonding.

Table 6-5: Tensile test results – Domain decomposition lay-up

Toolpath	Build plane	Orientation	Number of specimens tested	Number of specimens considered	Tensile strenght [MPa]	Elastic modulus [MPa]
Random	xy	X	3	3	10.001	1113.330
Random	yz	Y	3	3	12.506	1514.686
Random	xz	Z	3	3	7.611	1322.250

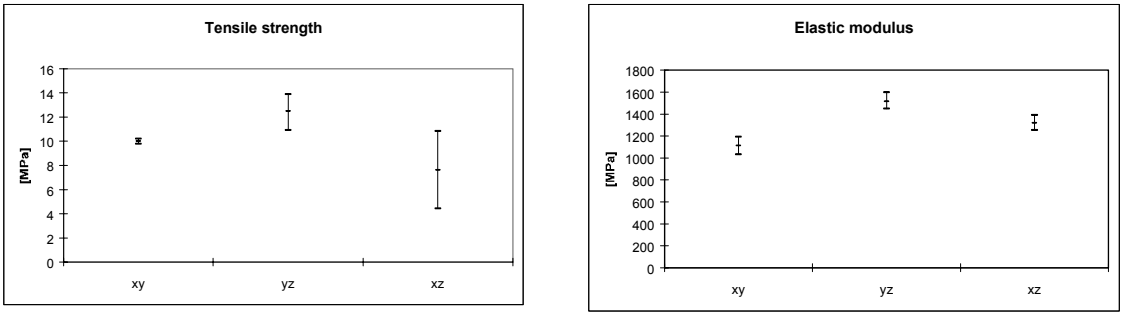

(a) (b)

Figure 6.12: Max, min and average. values: Young's modulus (a) and tensile strength (b)

For the domain decomposition lay-up it was not possible to build specimen oriented at 45^{o} in the *yz* and *xz* planes (see Figure 6.8) because of the small size of the single layer section. Thus the stiffness matrix remains still incomplete:

$$C = 1.0e+003 * \begin{bmatrix} 1.7257 & 1.0975 & 0.9194 & 0 & 0 & 0 \\ 1.0975 & 2.4109 & 1.1293 & 0 & 0 & 0 \\ 0.9194 & 1.1293 & 1.9852 & 0 & 0 & 0 \\ 0 & 0 & 0 & C_{44} & 0 & 0 \\ 0 & 0 & 0 & 0 & C_{55} & 0 \\ 0 & 0 & 0 & 0 & 0 & C_{66} \end{bmatrix} \text{MPa} \qquad (6.13)$$

and the engineering constants are:

Table 6-6: Engineering constants – Domain decomposition lay-up

E_x (MPa)	E_y (MPa)	E_z (MPa)	ν_{xy}	ν_{xz}	ν_{yz}
1113.3	1514.7	1322	0.3248	0.3642	0.3306

The flexure test:

According to [12], in a 3-point bending test the maximum stress occurs in the middle of the span and can be calculated using eq. (6.14).

$$\sigma = \frac{3PL}{2bd^2} \qquad (6.14)$$

where:

- σ is the stress in the outer fibers at a given load [MPa];
- P is the maximum load in the flexure test [N];
- L is the outer support span [mm];
- B is the width of the tested beam [mm];

- D is the specimen thickness [mm].

The results show that the specimens built with a random oriented path are more brittle but much stronger: the ultimate strength is about 8% bigger than the one measured for the standard lay-up specimens (see Table 6-7), but the final deflection is much smaller:

Table 6-7: Flexure test results

Toolpath	Build plane	Orientation	Number of specimens tested	Number of specimens considered	Max load [N]	Max stress [MPa]
[0 90 +45 –45]	xy	X	7	4	79.93	23.290
Random	xy	X	6	4	101.60	25.233

6.6 Computational analysis

In order to demonstrate the importance of the knowledge of the stiffness matrix for the built part, two simulations have been conducted using ANSYS 5.5, to compare the results for an isotropic part and a part built with RP technology.

In the two models a cube of 5 cm is subjected to a negative pressure (thus the "block" is subjected to a tensile stress) of 3 MPa on the top surface. The solid is then constrained (for all the displacement and rotational degrees of freedom) on the middle area of the opposite surface (see Figure 6.13). The mesh element type used for this analysis is a block solid element with 8 nodes, designated as SOLID45.

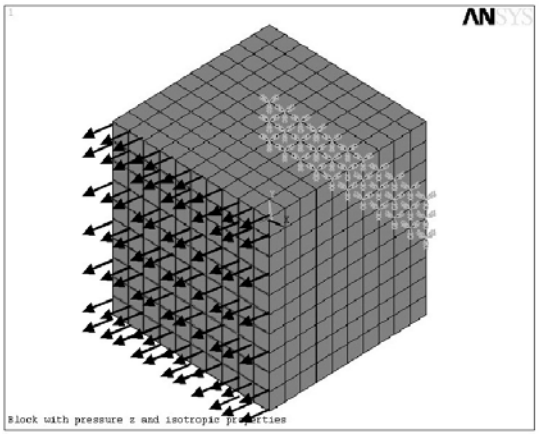

Figure 6.13: Boundary conditions for the two FE models

The two simulations, which are identical for geometry, applied loads and displacements, differ only for the material properties of the model.

In the first case (that in this paper has been designated with the letter *a*) the "block" is considered isotropic:

$$\begin{aligned} E &= 1653 \quad MPa \\ \nu &= 0.4391 \\ G &= 554 \quad MPa \end{aligned} \tag{6.15}$$

In the second case (that in this paper has been designated with the letter *b*) the "block" is considered anisotropic:

$$\begin{aligned} &Ex = 1073 \quad MPa; \quad Ey = 1653 \quad MPa; \quad Ez = 1391.7 \quad MPa; \\ &\nu xy = 0.3209 \qquad \nu xz = 0.2707 \qquad \nu yz = 0.4391 \\ &Gxy = 369.6 \quad MPa; \quad Gyz = 554 \quad MPa; \quad Gxz = 540.5 \quad MPa. \end{aligned} \tag{6.16}$$

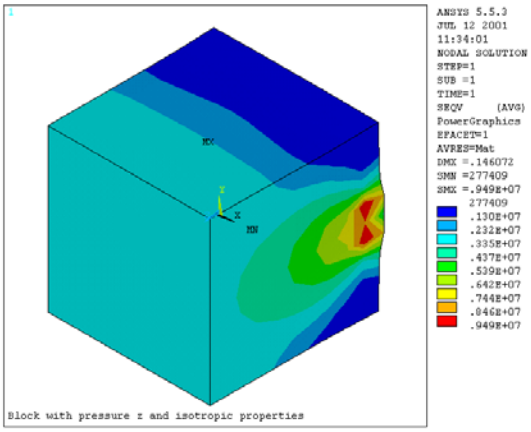

(1a) Von Mises Stress for isotropic properties

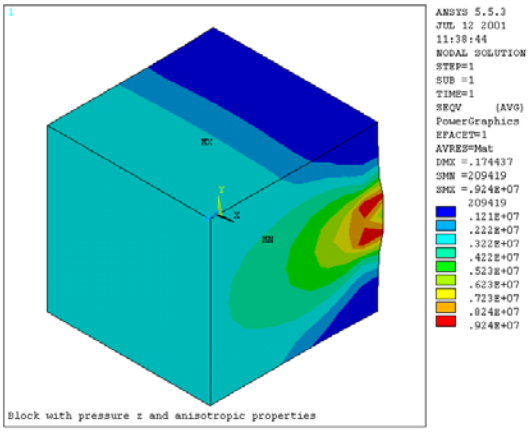

(1b) Von Mises Stress for anisotropic properties

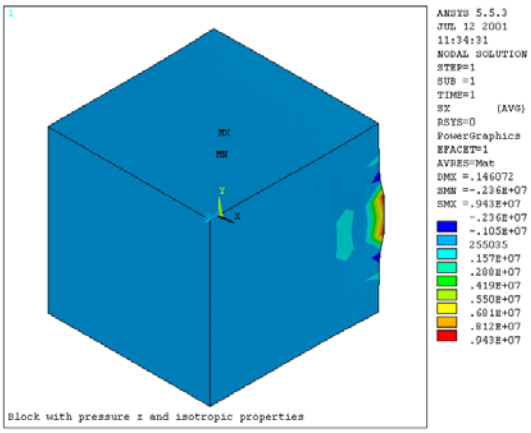

(2a) SX Stress for isotropic properties

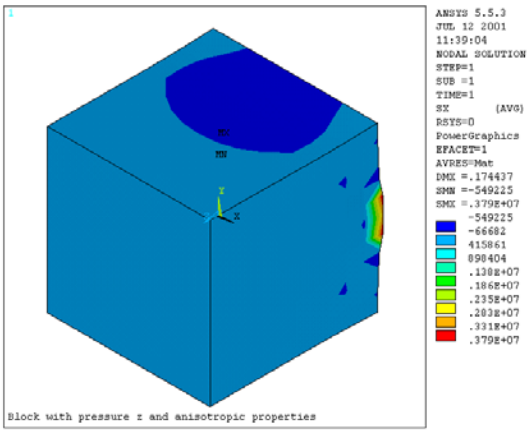

(2b) SX Stress for anisotropic properties

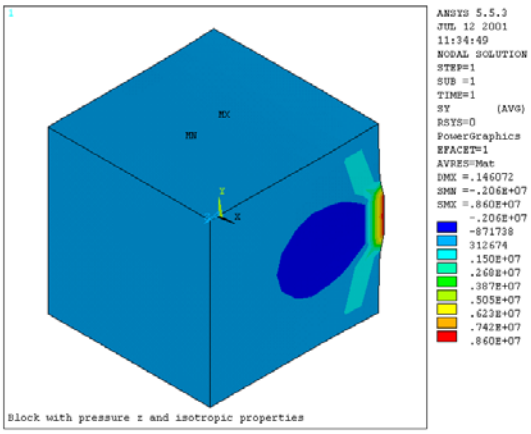

(3a) SY Stress for isotropic properties

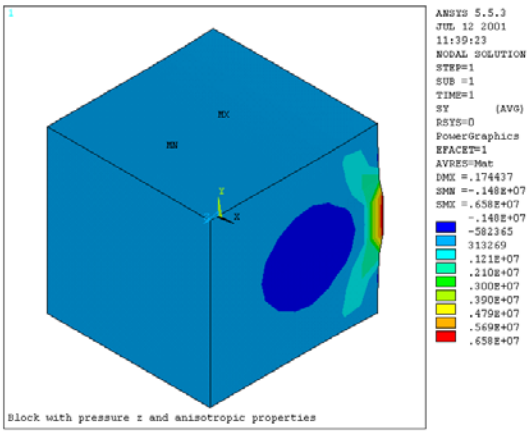

(3b) SY Stress for anisotropic properties

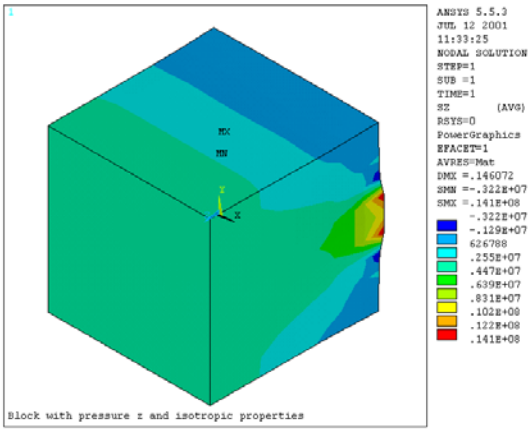

(4a) SZ Stress for isotropic properties

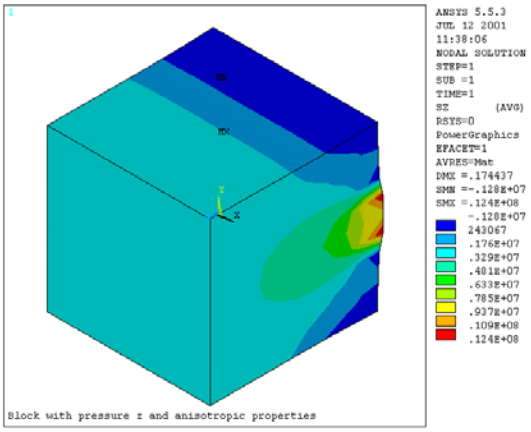

(4b) SZ Stress for anisotropic properties

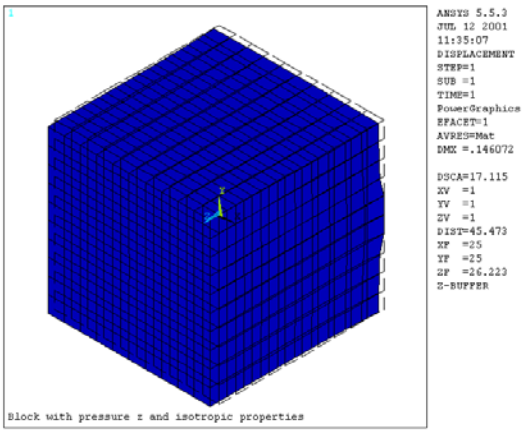

(5a) Deformed shape for isotropic properties

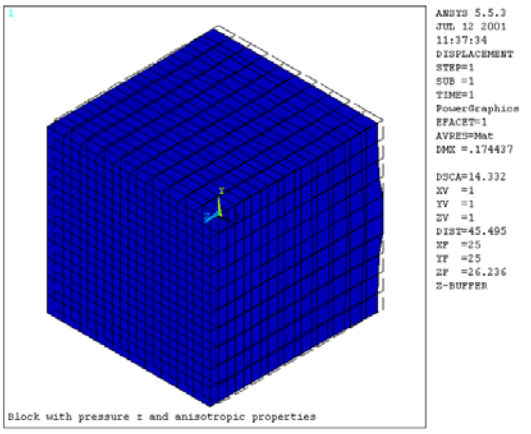

(5b) Deformed shape for anisotropic properties

Figure 6.14: Results for isotropic (a) and anisotropic (b properties

In Figure 6.14 the results obtained on a PC with 600 MHz, 128 MB of RAM, after 3 minutes of CPU time have been reported.

6.7 Finite element analysis - results

The results obtained using ANSYS 5.5 show that failure can be observed if the part is designed considering isotropic material properties. Even if the VM stresses are comparable (see Figure 6.14.1), due to the fact that they are an “average” of the stress

components in every direction, the resistance to failure can be over-evaluated with an isotropic model.

According to the Von Mises criterion ([53] and [66]), when the equivalent stress is less than the yield stress in tension, the material can be consider elastic:

$$\sigma_e = \left(\frac{1}{2} \left[(\sigma_1 - \sigma_2)^2 + (\sigma_2 - \sigma_3)^2 + (\sigma_3 - \sigma_1)^2 \right] \right)^{1/2} \leq \sigma_{yield} \tag{6.17}$$

It must be noticed that when a material reaches the plasticity zone, it is submitted to such large deformations that can be the cause of the system failure, mostly in the case of coupling with other parts. For this reason, equation (6.17) is widely used to determine the applicability of a design under certain stress conditions.

The FE results (see Figure 6.14.1a) show that if the part is considered isotropic with (see Table 6-4)

$$E = E_Y \qquad \nu = \nu_{YZ} \qquad G = G_{YZ} \qquad S_{strength} = 15.9MPa \quad and \quad \sigma_{yield} = (\sigma_{yield})_Y = 14MPa$$

it will reach neither failure, neither the plasticity zone:

$$\begin{aligned} (S_X)_{\max} &= 9.43MPa < S_{strength} = 15.9MPa \\ (S_Y)_{\max} &= 8.6MPa < S_{strength} = 15.9MPa \\ (S_Z)_{\max} &= 14.1MPa < S_{strength} = 15.9MPa \\ \sigma_e &= 9.49MPa < \sigma_{yield} = 14MPa \end{aligned} \tag{6.18}$$

under the mentioned conditions. This result will drive the designer to the conclusion that the object can be safely used for the intended purpose.

However, this chapter demonstrates that a part built using a Fused Deposition Modeling Technique cannot be considered isotropic. As a matter of fact, the FE results reported in Figure 6.14 show that the part will not only reach the plasticity zone, but it will definitely fail under the mentioned load. In Figure 6.14.4b indeed it can be observed that:

$$(S_Z)_{\max} = 12.4MPa > (S_Z)_{strength} = 7.6MPa \tag{6.19}$$

where the value of $(S_Z)_{strength}$ has been taken from the Table 6-3 (tensile strength column).

6.8 Conclusions

FDM is a LM technique where parts are fabricated on an "evolutionary" fashion road by road, layer by layer. As a consequence of layered manufacture, the parts produced are orthotropic. Furthermore, since in FDM every layer is filled by roads according to a certain "path", roads can be considered the real building units of the process.

It has been observed indeed that the road shape and the road to road interaction, as well as the "path", strongly affect the properties and performance of the finished product.

Summarizing, it can be said that two important modeling phases :

- The chosen building direction, hence the orientation of the object with respect to the substrate (see Figure 6.2);
- The chosen path, hence the way every layer is filled by roads (see Figure 6.3);

strongly influence the mechanical properties of the final parts.

The fact that the mechanical properties of the part depend on the orientation and path becomes particularly critical when FDM is used to produce components directly for end use. In this last case it is important to be able to predict and design the object with the desired tolerances and characteristics. The purpose of this study [6] is to determine the stiffness matrix for a part built with FDM technique. It must be noticed that in this study the path influence has not been taken into account. Hence, in order to reduce the anisotropies of the material due to the road-path, only parts built with [0 90 +45 –45] have been tested. All the investigations are based on the standard Stratasys' ABS material used in the FDM 1650 machine.

CHAPTER 7: AN IMPROVED FDC PROCESS

7.1 Abstract

In section 1.1 and in section 2.3 it was explained that the current study is part of a project to adapt a layered manufacturing process to fabricate products for direct use, such as multi material/multi functional components. In order to reach this objective, that requires a shift from rapid prototyping to agile fabrication, it is necessary to improve the flexibility in choice of materials. This chapter presents the development of a novel extrusion system, based on fused deposition technology, which will broaden the range of material selection.

The novel system discussed here avoids most of the material preparation steps. The new set-up, consisting of a mini-extruder mounted on a high-precision positioning system, is fed with bulk material in granulated form. This configuration opens up opportunities for the use of wider range of materials, making the FDM to become a viable alternative manufacturing process for specialty products.

7.2 Introduction

In order to adapt the fused deposition technique to manufacturing purposes, it is important to consider that the product performance often demands use of different materials for specific applications. Therefore, it is necessary to have a technology that is adaptable for a wide selection of materials.

Observations show that the main obstacle for application of new materials with specific characteristics often comes from the use of intermediate precursors such as a

filament. For example, in an FDM process, the advantage of using a precursor filament is thus offset by problems encountered during its preparation and fabrication [61]. Furthermore, during the extrusion phase in road formation, the frequent buckling failures cause interruption of the process (with the necessary cooling down and warming up of the liquefier) and necessitate frequent operator intervention [3]. Consequently, this problem prevents an automatic and continuous process diminishing the main advantage of a filament-based system. In addition, the backpressure encountered during deposition limits the powder volume fraction in the filament [45] reducing the possibility of successful sintering of the built part.

A novel system has been proposed and developed as part of this research to avoid most of the material preparation steps in a filament-based system. The new set-up, called Mini Extruder Deposition (MED) and consisting of a mini-extruder mounted on a high-precision positioning system (see Figure 7.1), operates using with bulk material in granulated form. This configuration opens up opportunities for the use of wider range of materials, making the FDM to become a viable alternative manufacturing process for specialty products.

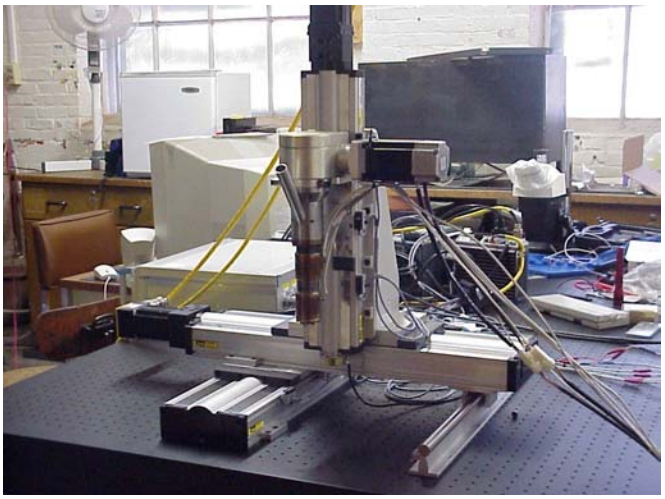

(a) MED hardware

(b) MED screw

Figure 7.1: MED system

7.3 System specifications

In order to generally improve the quality of the entire process, the new extruder has been mounted on three high precision linear motor tables, the 400XR series from Daedal division of Parker Inc.

The tables are characterized [13] by:

- High strength aluminum body;
- Square rails linear bearing, which provide high load carrying capability, and smooth precise motion;
- High efficiency ball screw drive, which offer high throughput, efficiency, accuracy $\pm 10\mu m \div \pm 18\mu m$ and repeatability $(\pm 1.3\mu m)$;
- Encoders that offer direct positional feedback of the carriages location;

- Electromagnetic shaft brake on the vertical axis that halts the carriage motion during a power loss.

The three positioning tables are connected to three Compumotor Gemini [10] digital servo drives, which allow for torque, velocity and encoder tracking modes. They are also equipped with digital notch filters that provide tools to eliminate mechanical resonance.

The three drives are thus connected to one 6K4 Compumotor controller, which communicates to the computer through the serial port SR-232. With the use of the 6K Compumotor it is possible to write only one program to control position, speed, acceleration, deceleration etc. of the three axes at the same time.

A separate unit (see Figure 7.1.a), custom built by Shinko Sellbic Co. in Tokyo, controls the heaters and the motor for the extruding screw (see Figure 7.1.b) . The temperature is checked by two thermocouples at the entrance of the liquefier and approximately at *1.5 cm* from the exit. Because of the two small copper heaters and to the two thermocouples, the thermal inertia of the system is reduced and the temperature of the melt is more uniform than in the FDM Stratasys machine 1650.

The rotational speed of the screw can be regulated either manually or through the interface of a digital device. In this first step of the testing phase of the system, the manual regulation has been preferred. However, in the future the controller will be connected to the same computer used for the positioning system. In this way, only one program will be written for the motion of the platforms and the rotation of the extruding screw, allowing a better correlation between positioning and delivering systems [3].

7.4 System performance

In order to test the performance of the new system, different samples have been built using ECG9/PZT bulk material [45], developed at Rutgers University for fabrication of piezoelectric actuators [1],[48] (see Figure 7.6, Figure 7.8 and Figure 7.10).

7.4.1 Influence of the size of the granules

During the experimental phase, it has been observed that the size of granulates of material fed into the system has a strong influence on the melt flow, even if all other variables, such as temperature and speed of the motors, are maintained constant. To obtain more consistent results, the material has been granulated and sifted using a 1 mm reticulated sieve. Consequently, the powder has been introduced into the liquefier via a pipe and a funnel to get a constant feeding rate. However, with such small size particles, thus with such big ratio surface/volume, the heat at the entrance of the liquefier is high enough to melt the particles together. Therefore, bigger aggregates form, either in the feeding pipe (see Figure 7.1.a) or in the entrance of the liquefier, that prevent the incoming of new material.

At the same time, feeding the extruder with too big pieces of material causes a non-uniform flow rate. When an aggregate of material is indeed trapped between the screw and the chamber of the liquefier, and finally reaches the exit of the nozzle, a very large flow is experimented. Moreover, when air is trapped between two consecutive big aggregates, deposition stops suddenly.

The size of the granulate influences the flow behavior also affecting the temperature of the melt at the entrance of the liquefier. Since the upper thermocouple is

placed on the external surface of the liquefier, the monitored value is an approximation of the temperature of the melt. Consequently when air is trapped between aggregates, the temperature of the melt can increase a couple of degrees even if the outside value is maintained constant. Because of the strong dependency of the viscosity ηon the temperature (see paragraph 7.4.2 and Figure 7.2), it can be concluded that the agglomerate size, affecting the temperature of the melt, influence indirectly also the viscosity, hence the flow during deposition.

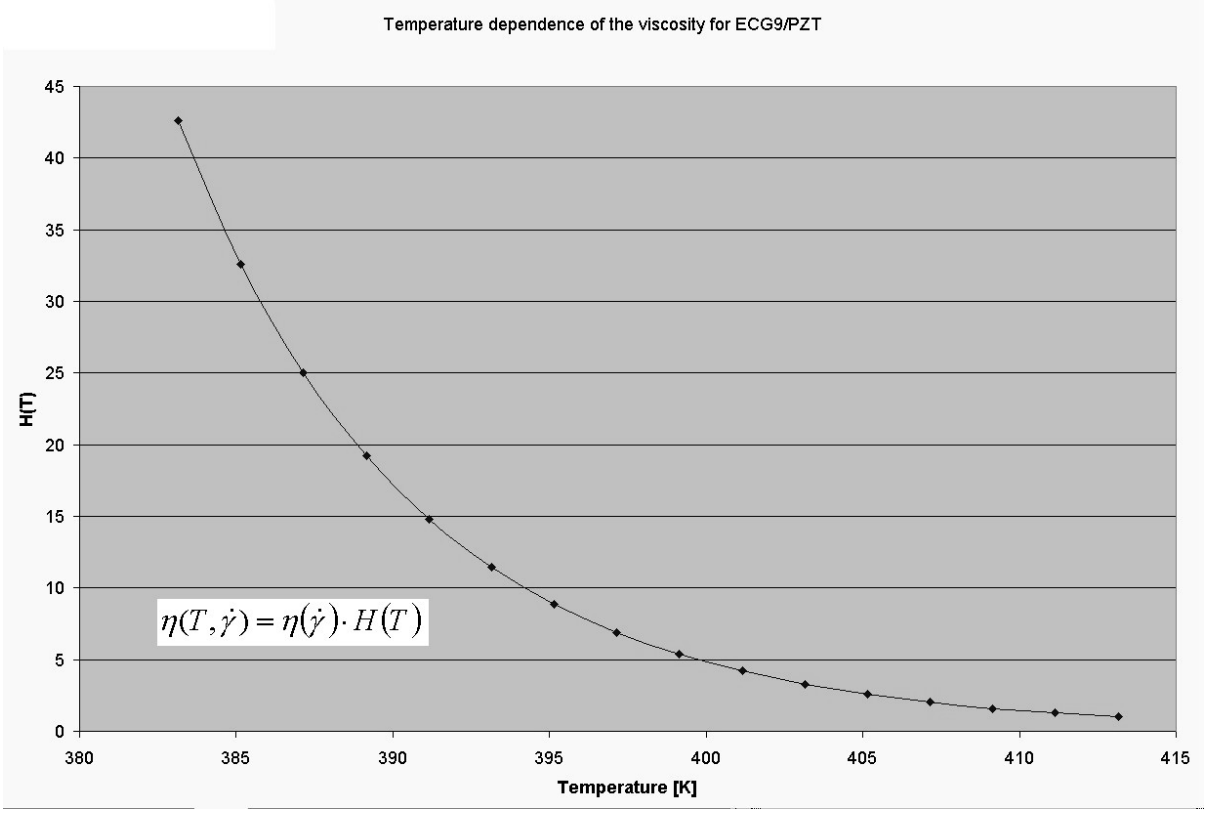

Figure 7.2: Temperature dependence of the viscosity of PZT/ECG9

7.4.2 Influence of the temperature at the entrance of the liquefier

In order to determine the influence of the temperature in the upper part of the liquefier, experiments have been performed varying the values from 145°C to 160°C. The lower boundary value has been decided according to the melting temperature, which is 115°C and the temperature dependence of the viscosity. Since according to Figure 7.2, at 115°C the viscosity of ECG9/PZT is approximately 20 times higher than at 135°C, a melt temperature of 135°C has been considered more acceptable. Furthermore, since the thermocouple checks the temperature outside the cylinder of the liquefier, five extra degrees have been added to account the heat dissipation through the wall. The upper boundary value of the temperature range has been decided according to the material properties of the binder. Values greater than 165°C may lead to chemical degradation of the polymer.

The results show that the viscosity of the material is still too high for extrusion process when the temperature is set below 135°C. In these cases no flow is obtained at the exit of the nozzle (0.3 mm in diameter).

7.4.3 Influence of the temperature at the exit

The influence of the temperature in the lower part of the liquefier was also tested. Experiments have been performed by varying the values from 135°C to 147°C. Results show that for temperatures higher than 145°C the material is too "*fluidic*" after deposition, thus the strand degenerates into a flatter road. For temperatures below 140°C the interface strength between two adjacent roads is not sufficient to ensure satisfactory bonding conditions (see paragraph 7.4.5). In these cases the delivered material does not

adhere to the substrate and remains attached to the external surface of the nozzle. Due to the temperature of the die, this material melts and either clogs the orifice of the nozzle or glues on to previously deposited roads, damaging the already built layers.

7.4.4 Influence of the size and design of the nozzle

In the commercial Stratasys machine four nozzle sizes are available: T10 (7 mills, or 0.1778 mm, in diameter), T12 (12 mills, or 0.3048 mm, in diameter), T16 (16 mills, or 0.4064 mm, in diameter), T20 (20 mills, or 0.508 mm, in diameter). In order to be consistent with previous studies, two nozzles from Stratasys Inc., i.e. the T12 and T16, have been tested with the new system.

It has been observed that with the T12 the continuity of the flow is lost because of clogging problems. This indicated the possibility of the heat dispersion through the walls of the nozzle and of the adapter (the part that connect the nozzle to the liquefier chamber) being too high. At the very end of the nozzle, the volume of the melt presents in the tip "solidifies", causing the flow to stop. In order to use smaller nozzle sizes, the heat convection to the air must be reduced. Thus in the future, we suggest enclosing the working area in a controlled environment to be maintained at a higher temperature (see paragraph 7.4.5).

In the meantime a T16 nozzle has also been tested. Because of the improvement in the continuity of the flow, this size is the one currently used to perform experiments. It has been noticed that when roads are deposited with a positive "gap" (distance between two consecutive roads), the sample is successfully built. However, when the offset is reduced, the interference of the heated tip with a previously built road is such to destroy

the sample. In order to avoid this problem, three different approaches might be taken in consideration for future work: (1) reducing the width of the tip. However, since it has been experimented that the tip function also as “regulator” of the fountain flow (see Figure 7.3), it cannot be completely removed; (2) increasing the room temperature, in order to improve the bonding between deposited layers; (3) controlling the flow during the building process. Until now the extruding screw is manually regulated in an ON/OFF fashion. The flow rate is thus kept constant during the deposition, even if the speed of the nozzle changes according to tool-path [3],[64]. In this case, it is possible to observe for example an overdepoistion of material at the corners of the raster (where the head is accelerating/decelerating); the material in excess interacts consequently with the nozzle and with previously built layers, damaging the sample.

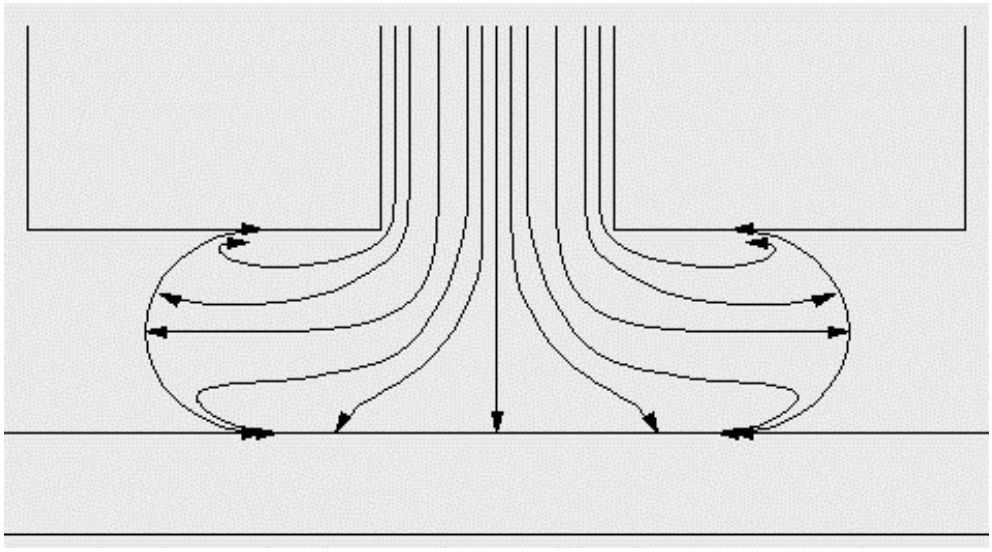

Figure 7.3: Hybrid cross-sectional flow-field

7.4.5 Influence of the room temperature

Self-adhesion of thermoplastic materials, in presence of prolonged exposure to high temperatures is the basics mechanism of part strength in FDM. Conformal movement of polymer chains through interfaces has been proposed as the main mechanism in thermoplastic interface healing by Wool and coworkers [63]. According to this study, the degree of interface healing, defined as the ratio of interface mechanical strength to bulk material strength, depends on ¼ power of residence time *t* spent above a critical bonding temperature (see equations (3.2) and (3.3)).

In order to improve bond between roads and layers, the temperature T_i of the interface and/or the time *t* (equation (3.2)) must be increased. These two effects can be achieved by only increasing the environmental temperature, thus enclosing the work-volumemperature controlled chamber.

7.4.6 Influence of the speed of deposition

Using a T16 nozzle, different experiments have been conducted with different speed of deposition, i.e. speed of the head in x and y direction. The cross section of the deposited road can be indeed reduced increasing the speed of the nozzle. However, in this case the acceleration and deceleration needed for deposition a short road are too big. Consequently, without a regulation of the flow rate, the extra deposited material in the corners of the filling raster may cause the bending of the top surface of the sample (see Figure 7.6.b).

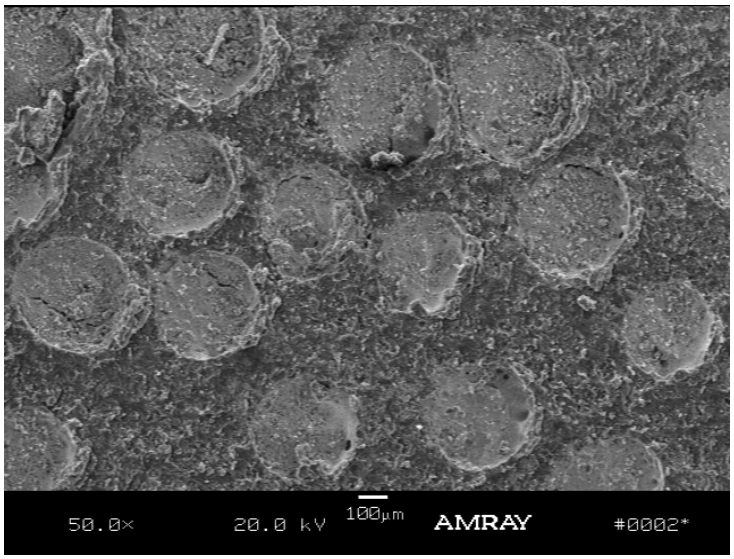

Figure 7.4: Cross-section of free extruded strands

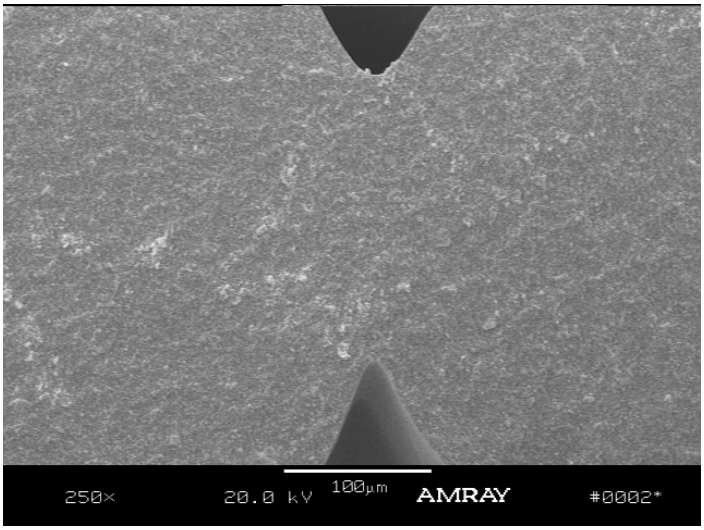

Figure 7.5: Micrograph of contact between two roads

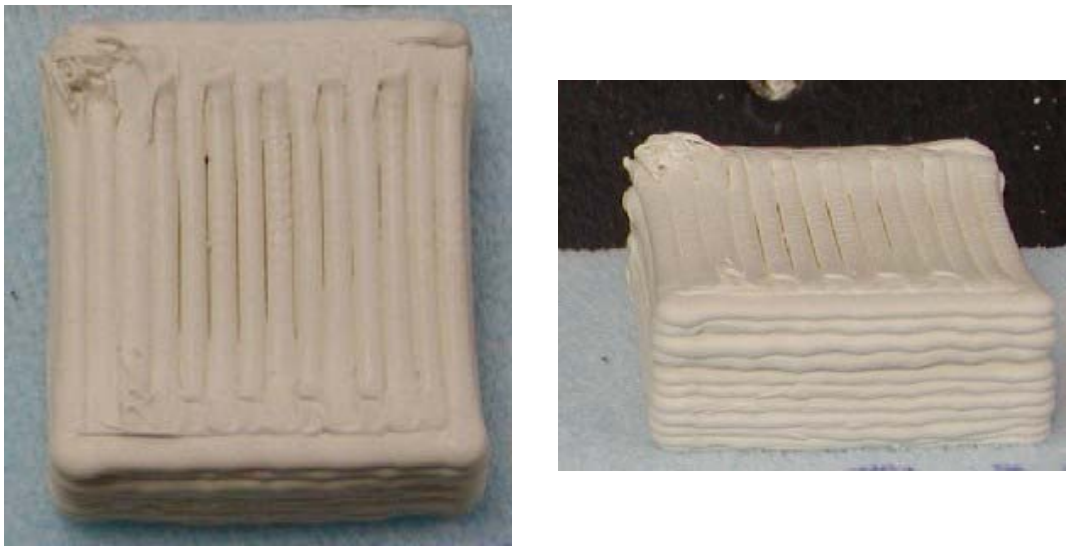

(a) Top view (b) Side view

Figure 7.6: Raster sample with zero gap

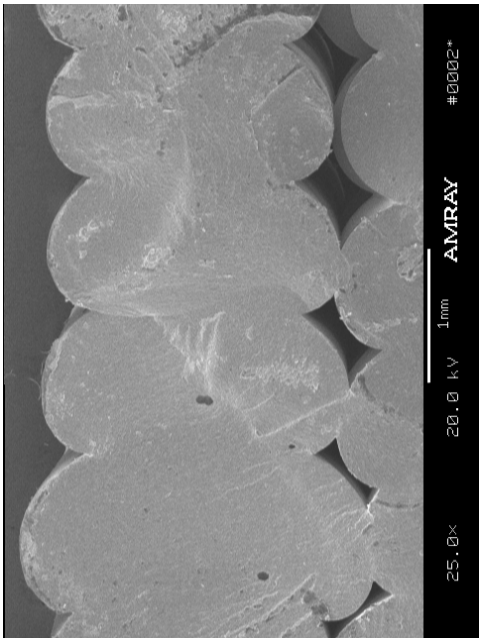

Figure 7.7: Micrograph of raster filled sample – zero gap

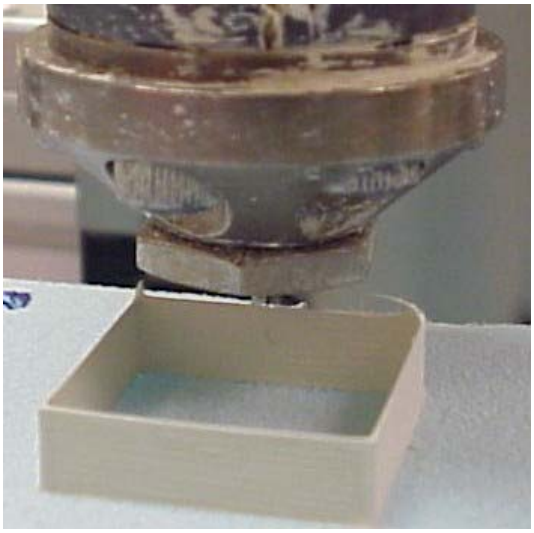

Figure 7.8: Deposition of a single-road wall box

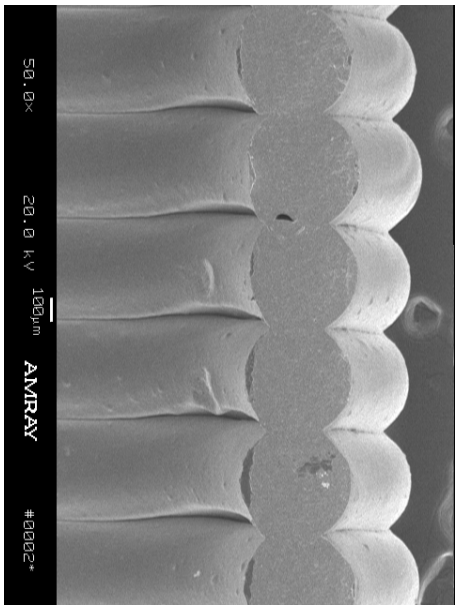

Figure 7.9: Micrograph of the single-road wall box

Figure 7.10: Single-road spiral sample

7.5 Conclusions and future directions

The novel system introduced in this paper, consisting of a mini-extruder mounted on a high-precision positioning system and fed with granulated material, is still under testing, thus significant additional work needs to be done. However, the success obtained in building objects of different configurations (Figure 7.4 to Figure 7.10) is encouraging for further studies in the use of wider range of materials. Future directions could be summarized as follow:

1. A better control of the temperature of the melt could be achieved moving the upper thermocouple inside the liquefier. In this configuration, feeding of material will have less influence on the extruded flow (paragraph 3.4). Furthermore, since the lower thermocouple is acquiring data at 1.5 cm from

the very end of the nozzle, a different mechanism should be used to determine the temperature at deposition. A six channels acquisition data system from Omega will be used for this reason. In order to measure the temperature and also to understand the cooling process in the deposited road, five thermocouples will be incorporate on the top of the platform.

2. In order to obtain a smoother and more automatic process, the correct size of the aggregates must be determined. More experiments thus need to be performed with agglomerate sizes ranging from 3 to 5 mm in diameter.

3. A closer control of the cross section of the deposited road could be achieved improving the correlation between velocity of the positioning system and flow of the melt. The driving motor of the extruding screw must be controlled with the same computer unit and program used for the 3-axis system.

4. In order to have a better visualization, thus control, of the deposition process a CCD camera and a boroscope will be attached to the depositing head. This will allow a more comprehensive understanding of the influence of the different parameters.

5. The study of the effect of nozzle size on various material configurations will give some insights on the road shape that will be possible to obtain.

6. The enclosure if the working platform in a thermally controlled environment will isolate some of the parameters not related to the process (i.e. moisture) and will avoid any contamination of the material.

7. The addition of a rotational stage for the extruder will allow the use of a square nozzle that will have to be oriented continuously to match the path of the motion.

7.6 Future explorations with Ti_3SiC_2

Ti_3SiC_2 , which exhibits properties similar to both of those metals and ceramics, is receiving an increasing attention. Like metals it is an excellent electrical and thermal conductor, easily machinable, relatively soft, good thermal shock resistant and like ceramics it is oxidation resistant and refractory], [20]. Availability of this novel material in powder form increases the possibility of its use in building complex parts based on fused deposition technology as described in this project.

Because of the success obtained for the deposition of relatively complex structures using PZT particles combined with a carrier binder, it is realistic to anticipate the feasibility of building similar architectures using material system based on Ti_3SiC_2 powder. The finished parts are to be produced using processing steps, i.e. binder burnout and sintering, that are similar to fabrication of ceramic components.

It is the intent of this research group to conduct studies with this material system by first characterizing its properties and then implementing necessary system modifications to produce products.

7.7 Applications in tissue engineering

In tissue engineering the need for *scaffolds* with completely interconnected pore network, with large interconnection channels and with highly regular and reproducible

morphology, make them ideal candidates for advanced layered manufacturing applications.

Figure 7.11: Picture of a honeycomb structured sample made with MED

The novel approach under consideration allows for designing and implementing *highly complex internal architectures* (see Figure 7.11), such as scaffolds , into parts through deposition of different materials in a variety of configurations such that the finished product exhibit characteristics to meet the performance requirements. Thus, in principle, one can tailor-make the assemble of materials and structures as per specifications of an optimum design. Moreover, if brought to full maturity, the present technique will be highly automated allowing for unattended operation as well as remotly controlled production.

It has been shown [65] that FDM works well for building honeycomb-like pattern with bioresorbable polymers, such as poly(ε-caprolactone). It would be interesting to also be able to built similar complex structured scaffolds with other specific biodegradable

materials. For example the use of FD could speed up and automate the creation of porous scaffold for bone generation, using the copolymer poly(lactide-co-glycolide) [PLAGA] [8]. Furthermore, the use of this technology, which is compatible with commercially available software, such as MIMICS, allow the direct implementation of MRI images. Thus making it possible to reproduce the three dimensional models of the internal parts

However, as in the previous cases the application of new materials is often encumbered by the use of intermediate material forms. The advantage of a continuous fed filament is thus offset by problems encountered during its preparation and fabrication. In addition, the backpressure encountered during deposition not only limits the use of small size nozzles, but also the microsphere volume fraction in the filament, thus in the built part, reducing the possibility of a successful graft, thus of a new bone regeneration.

The mini-extrusion based system currently under development in Drexel University avoids most of the material preparation steps. The new configuration opens up opportunities for the use of wider range of materials, making the FDM to become a viable alternative for manufacturing specialty products, such as scaffold for bioengineering purposes.

CHAPTER 8: CONCLUDING REMARKS

The research developed and reported in the thesis addressed several important scientific and engineering issues in order to successfully using FD for manufacturing applications.

Among these issues are:

1. The study of mechanical characterization of the part and its relation with building strategies;
2. The study of the liquefier dynamics to insure a close control of the deposited material hence to improve the final quality of the part;
3. The need of a tool that provides guidelines for the determination of process parameters, according to material properties, during the process-planning phase;
4. The need of various nozzle designs and the study of their influence on part quality;
5. The need of an alternative feeding system that reduces problems related to filament fabrication.

In chapter 3 the observations from experimental studies conducted with different process conditions have been reported. The collected data show the influence of material properties and process parameters on the evolution of the road shape, hence on the final quality and performance of the part. Consequently, a comprehensive model of the process was developed and exposed in the same chapter, where a comparison between predicted

and experimented results was also reported. If incorporated in the process-planning phase, the model provides a guide for engineers in the determination of the optimal process parameters, according to material properties, to insure the correct evolution of the road.

In chapter 4 the experiments conducted on various hardware design were reported and described. The studies showed the strong influence of nozzle designs on the evolution of the shape of free extruded strands, hence of roads, and consequently on the final quality of the part. Starting from these observations, a model of free extrusion process was developed and the obtained results were compared with experimental data. The incorporation of the model in a reverse engineering approach constitutes a powerful tool for the determination of optimal nozzle designs, which, providing the desired road shape, will enhance the performance of the part.

In chapter 5 it was shown how a good correlation between positioning and delivery system is important for the quality of the part. It was explained and demonstrated how a mismatch in the control of either one causes over-deposition or under-deposition of delivered material, hence the discharge of the part because of unsatisfactory tolerances requirements. Based on experimental data, a transfer function was originated and reported. Consequently a mathematical model was developed in order to explain, hence control, the dynamics of the system, in particular of the liquefier.

In chapter 6 it was shown that building orientation have a strong impact on the final mechanical properties of the built object. It was also demonstrated that the anisotropy generated during manufacturing by FD could lead to the failure of the product

if underestimated. The fact that the mechanical properties of the part depend on the orientation and path becomes particularly critical when FD technology is used to produce components directly for end use. In this case it is important to be able to predict and design the object with the desired tolerances and characteristics. In the same chapter the results from a study, developed to determine the stiffness matrix for an object built with FD, were reported in order to give directions to engineers during the process-planning phase.

In chapter 7 an improved FDC system is presented. The meticulous study of the process showed that the main obstacle for the application of FD in different areas consists of the use of a filament based feeding system. The advantage of a continuous fed filament is thus offset by problems encountered during its preparation and fabrication: for example, some materials cannot be extruded into a filament, or might not need a polymer as a media for deposition. Furthermore, during the extrusion phase, the frequent buckling causes interruption of the process and necessitate operator intervention. In order to avoid the mentioned problems related to the preparation and application of a filament, a *mini-extrusion system*, fed with pallets of bulk material was developed. From the results described in chapter 7 the system showed good capability and good potential for the application in various fields and with different materials. Shor and coworkers are experimenting the micro-extruder deposititon (MED) for use with biomaterials such as Poly(ε-caprolactone) [PCL] and poly(lactide-co-glycolide) [PLAGA], which can not be extruded, hence it could not be applied in the previous design of the machine.

The achievements of this study not only give an insight of the complexity of FD process through a serial of experimental data, but also, and more important, provide tools that, when incorporated as part of the process planning phase, make FD a suitable technique for manufacturing of high-customized complex architecture product.

With the tools developed during this study, the improvements in quality and performance of the parts are such that FD becomes an attractive technique also for biomedical and eventually nano purposes.

The last developments in biomedical applications, i.e. tissue engineering, requires the manufacturability of very complex structures, such as scaffolds, to use for growing cell in the desired architecture. In order to provide the correct environment for cells growth, i.e. nutrition and oxygen, scaffolds have to present high porosity, constituted by interconnected vessels of very small size, as well as enough strength to support the cells. The models developed in this study, providing a powerful tool in the control of road formations, gives the possibility to engineer the parts with the need requirements. Moreover the new mini-extruder system developed as part of this research, broadening the range of eligible material, opens up the opportunity to use different kinds of biomaterials.

Consequently, it is possible to conclude that the achievements of the research exposed in this thesis make FD a more realistic suitable choice for biomedical applications.

The achievements of this study, in particularly:

- The development of a tool for a close control of the deposition process and of the road to road interaction;
- The development of the mini-extruder system, which eliminating the need of a filament, is not affected by buckling problems. As a consequence the back pressure does not consist a limitation, hence it is theoretically possible to reduce the size of the nozzle to microns in diameter;

make FD an appealing choice for the deposition of nano-roads for fabrication of micro-parts.

List of References

[1] Allahverdi M., Danforth S.C., Jafari M., Safari A., "Processing of advanced electroceramic components by fused deposition technique", Journal of the European Ceramic Society, Vol. 21, (2001), pp 1485-1490.

[2] Ansys 5.5 Theory Manual – Section 2.3.2

[3] Bellini A., Güçeri S. I., Bertoldi M., "Liquefier dynamics in fused deposition", submitted to the Journal of Manufacturing Science and Engineering, (2002).

[4] Bellini A., Güçeri S. I., Bertoldi M., "Mechanical characterization of parts fabricated using layered manufacturing", submitted to Rapid Prototyping Journal, (2002).

[5] Bellini A., Güçeri S. I., Turcu S., Danforth S.C., Safari A., "Nozzle shape, road cross section and space filling in FDM/SFF techniques", Conf. Proc. of EUROMAT 2001, Italy, (2001), ISBN 88-85298-39-7.

[6] Bertoldi M., 1998, *"From Rapid Prototyping to Rapid Manufacturing: analysis of the fused deposition process"*, Tesi di laurea del dipartimento di Ingegneria Aerospaziale del Politecnico di Milano, Milan.

[7] Bird B. R., Armstrong R. C., Hassager O., 1987, "*Dynamics of Polymeric Liquid: second edition– Volume 1: Fluid Mechanics*", Wiley-Interscience, New York, ISBN 0-471-80245-X (v.1)

[8] Borden M., Attawia M., Laurencin C. T., "The sintered microsphere matrix for bone tissue engineering: in vitro osteoconductivity studies", Wiley InterScience, 2002

[9] Bouhal A., Jafari M. A., Han W., Fang T., 1999, "*Tracking control and trajectory planning in layered manufacturing applications*", IEEE Transactions on Industrial Electronics, Vol. 46 No. 2.

[10] Compumotor Catalog, "Motion Control system", Parker automation, USA, 2000.

[11] Cooper K.G., "Rapid Prototyping Technology", Dekker ed., New York 2001, ISBN 0-8247-0261-1

[12] C1341-97, "Standard Test Method for Flexural Properties of Continuous Fiber-Reinforced Advanced Ceramic Composites", American Society for Testing and Materials, Conshohocken, PA 1997.

[13] Daedal Catalog, "Electromechanical Positioning System", Parker automation, USA, (2000).

[14] Danforth S.C., et al., US Patent # 5,738,817, 1998.

[15] DC Micromotors – Brushless DC Sevomotors – Gearheads – Tachogenerators – Encoders – Controllers, MicroMo catalog 1999-2000.

[16] Dean F. K., Chow J. H., 2000, *"Feedback Control Problems: using MATLAB and the Control System Toolbox"*, Brooks/Cole Thomson Learning, Pacific Grove, ISBN 0-534-37175-2

[17] Donea J., Giuliani S., Halleux J. P. "An arbitrary Lagrangian-Eulerian Finite Element Method for Transient Dynamic Fluid-Structures Interactions", *Computer Methods in Applied Mechanics and Engineering*, North Holland, 1982, Vol. 33 – pp 689-723.

[18] D5937-96, *"Standard Test Method for Determination of Tensile Properties of Moulding and Extrusion Plastics"*, American Society for Testing and Materials, Conshohocken, PA 1997.

[19] D790-96a, "Standard Test Methods for Flexural Properties of Unreinforced and Reinforced Plastics and Electrical Insulating Materials", American Society for Testing and Materials, Conshohocken, PA 1997.

[20] El-Raghy T., Barsoum M. W., "Processing and mechanical properties of Ti_3SiC_2, Part I: Reaction Path and Microstructure Evolution", Journal of American ceramic society, vol. 82, pp 1953-56, 1996.

[21] El-Raghy T., Barsoum M. W., "Synthesis and characterization of a remarkable ceramic: Ti_3SiC_2", Journal of American ceramic society, vol. 79, No. 7, pp 1653-58, 1999.

[22] Fluent Incorporation, "*Polyflow 3.9 documentation - Tutorial guide*".

[23] Fluent Inc., "Polyflow Manual: user's guide", August 1999

[24] Greenber M. D., 1998, *"Advanced Engineering Mathematics – second edition"*, Prentice Hall, Upper Saddle River, NJ, ISBN 0-13-321431-1

[25] http://home.att.net/~castleisland/lom_int.htm

[26] http://mtiac.iitri.org/pubs/rp/rp38.htm

[27] http://www.egr.uri.edu/ime/RMC/lens.html

[28] http://www.industrial-lasers.com/archive/2001/03/0301fea6.html

[29] http://www.rci.rutgers.edu/~ecerg/pp_pres/NJCST_files/frame.htm

[30] Huerta A., Liu W. K., "Viscous Flow with large free surface motion", *Computer Methods in Applied Mechanics and Engineering*, North Holland, 1988, Vol. 69 – pp 277-324.

[31] Incropera F. P., DeWitt D. P., "Introduction to heat transfer – third edition", John Wiley & Sons, New York, 1996 – ISBN 0-471-30458-1.

[32] Jaluria Y., Computer Methods for Engineering, Taylor & Francis, Philadelphia, 1978.

[33] Kai C. C., Fai L. K., 1997, "*Rapid Prototyping: Principles and Applications in Manufacturing*", Wiley ed., New York, ISBN 0-471-19004-7

[34] Kalpakjian S., "Manufacturing Processes for Engineering Materials", 3rd Edition, Addison-Wesley Publishing Co.., 1996, ISBN: 0-201-82370-5

[35] Kochan, "Rapid prototyping gains speed, volume and precision", Assembly Automation journal, Volume 20 - Number 4 - 2000, pp 295-299

[36] Krishan K. Chawla, *"Composite Materials: Science and Engineering – Second Edition"*, Springer Edition , New York 1998 – ISBN 0-387-98409-7

[37] Kulkarmi P., Marsan A., Dutta D., "A review of process planning techniques in layered manufacturing", Rapid prototyping journal, Volume 6 - Number 1 - 2000, pp 18-35

[38] Langrana N. A., Qiu D., Bossett E., Danforth S. C., Jafari M., Safari A., 2000, "*Virtual simulation and video microscopy for fused deposition methods*", Material and Design, Vol. 22, pp. 75-82.

[39] Legat V., Marchal J., "Die design: an implicit formulation for the inverse problem", International Journal for Numerical Methods in Fluids, John Wiley & Sons, Vol. 16, pp 29-42 (1993).

[40] Legat V., Marchal J., "Prediction of three dimensional general shape extrudates by an implicit iterative scheme", International Journal for Numerical Methods in Fluids, John Wiley & Sons, Vol. 14, pp 609-625 (1992).

[41] Mani K., Kulkarni P. and Dutta D., "Region-Based Adaptive Slicing", *Computer Aided Design*, Vol. 31, 1999, pp. 317-333

[42] Manufacturing Process Laboratory, "Final Report Anaysis of Fused Deposition of Ceramics", DARPA/ONR Contract, Chicago, 1997.

[43] Marcus S. M., Blaine R. L., "Thermal conductivity of polymers, glasses & ceramics By Modulated DSC", TA instrument.

[44] Matthews F. L., Rawlings R. D., *"Composite Materials: Engineering and Science"*, Chapman & Hall , London 1994 – ISBN 0-412-55970-6

[45] McNulty T. F., Shanefield D. J., Danforth S.C., Safari A., "Dispersion of Lead Zirconate Titanate for Fused Deposition of Ceramics", Journal of the American Ceramic Society, Vol. 82 No. 7, (1999), pp. 1757-1760.

[46] Melsa J. L., Donald S. G., 1969, *"Linear Control Systems"*, McGraw-Hill Book Company, New York, ISBN 07-041481-5

[47] Michaeli W., 1992, "Extrusion Dies: for plastics and Rubber: design and engineering computation – second edition", Hanser ed., New York, ISBN 3-446-16190-2

[48] Mohammadi F., Kholkin A. L., Jadidian B., Safari A., "High-displacement spiral piezoelectric actuators", Applied Physics letters, Vol. 75 No.16, (1999), pp 2488-2490.

[49] Nonaka K, Allahvedi M., Mohammadi F., Safari A., " Fabrication of Grain Oriented Lead Metaniobate Components by Fused Deposition of Ceramics", Proceedingd of the 10th International Meeting on Ferroelectricity, IMF-10, Madrid, Spain, Sept. 3-7, 2001.

[50] Pham D.T., Dimov S. S., "Rapid Manufacturing", Springer ed., London 2001, ISBN 1-85233-360-X

[51] Potsch G., Michaeli W., "Injection Molding: An Introduction", Soho Press Inc., 1995, ISBN: 1-569-90193-7.

[52] "PZT-5H/ECG9 Filaments fabrication protocol", Rutgers University

[53] Rowland R. Jr., *"Principles of Solid Mechanics"*, CRC Press, New York 2001 – ISBN 0-8493-0114-9.

[54] Rock S. J., Gilman C. R., "A new SFF process for functional part rapid prototyping and manufacturing: freeform powder molding", Proceedings of solid freeform fabrication, symposium - Austin 1995, pp 80 –86.

[55] Sarrate J., Huerta A. Donea J., "Arbitrary Lagrangian-Eulerian formulation for fluid-rigid body interaction, *Computer Methods in Applied Mechanics and Engineering*, North Holland, 2001, Vol. 190 – pp 3171-3188.

[56] Schawe J.E.K., "A comparison between evaluation methods in modulated temperature DSC", Termochimica Acta, Volume 260, 1995, Pages 1-16.

[57] Schawe J.E.K, "Principles for the interpretation of modulated temperature DSC measurements. Part1. Glass transition", Termochimica Acta, Volume 261, 1995, Pages 183-194.

[58] Stratasys Inc., "FDM System Documentation (version 5.0)", October 1997.

[59] TA Instruments Inc., "TA Instruments Thermal Analysis & Rheology – A subsidiary of Waterd Corporation", Delaware 1999

[60] Venkataraman N., Rangarajan S., Matthewson M. J., Harper B., Safari A., Danforth S. C., Wu G., Langrana N, Güçeri S., Yardimci A., "Feedstock material property – process relationship in fused deposition of ceramics (FDC)", Rapid Prototyping Journal, Vol.6 No. 4, (200), pp. 244-252.

[61] Venkataraman N., "The Process-Property-Performance Relationships of Feedstock Material Used for Fused Deposition of Ceramic (FDC)", PhD Thesis, Dept. of Ceramic and Materials Engrg., Rutgers University, New Brunswick, (2000).

[62] Westkämper E., Koch K. U., Biesinger B., "Creating of Bio-compatible and structures using multiphase jet", Rapid prototyping and tooling journal, No5, April 2001.

[63] Wool R. P., Yuan B. L., McGrarel O. J., "Welding of Polymer Interfaces", Polymer Engineering and Science, vol. 29, no. 19, (1989), pp. 1340-1366.

[64] Yardimci A., "Process analysis and development for fused deposition", PhD Thesis, Dept. Mech. Engrg, University of Illinois at Chicago, 1999.

[65] Zein W., Hutmacher D. W., Tan K. C., Teoh S. H., 'Fused deposition modeling of novel scaffold architectures for tissue engineering applications", Biomaterials, vol 23, pp 1169-1185, 2002.

[66] Zweben C. H., Tsu-Wei Chou T. H., *"Mechanical behavior and properties of composite materials"*, Delaware Composite Design Encyclopedia – volume 1, Technomic Lancaster, 1996.

Appendix 1: PZT/ECG9 material data

Preparation of thermoplastic material loaded with ceramic powders

In the FDC, like in the FDM process, the filament acts as a plunger in order to provide the pressure for the extrusion of the melt. For this reason it must have certain stiffness, but at the same time it also needs a low viscosity to be extruded through a fine nozzle in the molten phase. In order to obtain these properties a customized thermoplastic carrier, designated as ECG9, has been developed at Rutgers University for PZT powder loaded filament. PZT has been considered for its piezoelectric characteristics because the final objective of this study, under ONR funding, is to develop an LM process to fabricate ceramic and multi-material sensor.

Table A1-1: Composition of the ECG9 binder [61]

Component (Role)	**Weight %**	**Source**
Vestoplat (Backbone)	71.43	Huls America
Escorez 2520 (Tackifier)	14.29	Exxon
Vestowax A227 (Viscosity modifier and stiffener)	10.71	Huls America
Polybutene H1500	3.57	Amoco

Table A1-2: Composition of the PZT coated powder [52]

Component	**Weight %**
Stearic Acid	3
PZT	97

In Table A1-1 and Table A1-2 the components for fabricating the material have been reported. The reason for coating PZT powder with stearic acid is to obtain a more uniform dispersion of particles into the carrier.

Once the powder and the binder have been fabricated, the procedure to prepare the filament continues with the compounding/mixing step according to the chart illustrated in Figure A1.1.

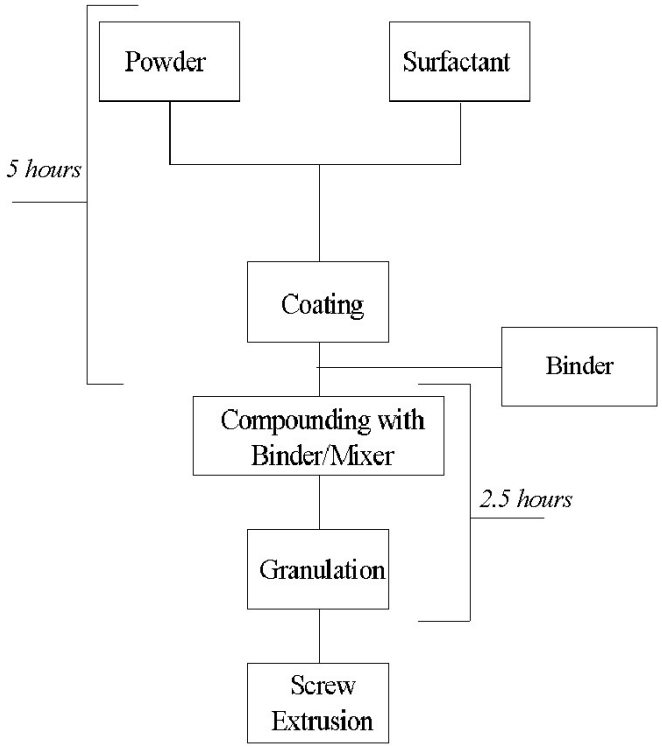

Figure A1.1: Flow chart of the process to make the filament with 20.5 g. of ECG9

The main purpose of this step, accomplished in a torque rheometer (see Figure A1.2 and Figure A1.3), is to obtain a thorough mixing of powder and polymer as well as to break up any eventual agglomerates.

(a) Compounding machine at R.U.

(b) The protection gear

Figure A1.2: The compounding machine at Rutgers University

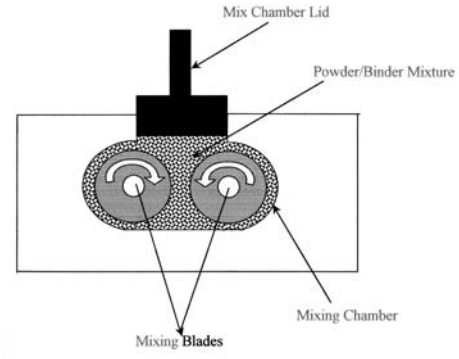

(a) Torque rheometer

(b) Rheometer blades

Figure A1.3: The torque rheometer and the blades

The temperature of the chamber (see Figure A1.1.a) and the rotational speed of the blades (see Figure A1.3.b) are empirical determined, such that sufficient mixing takes place [61].

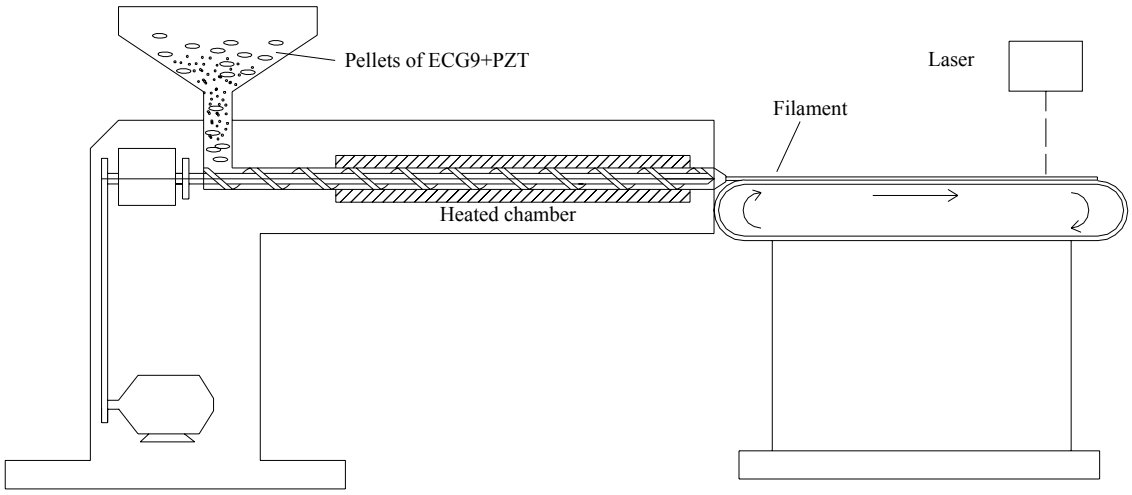

Figure A1.4: The preparation of the filament

The last step for the preparation of the filament is the extrusion of the material through a nozzle of 1.78 mm in diameter. In this case a particular attention has to be given to the relation between the speed of the screw and the speed of the belt. If the two values are not exactly correlated, the filament can break (see Figure A1.4).

The laser posted at the end of the convoy belt makes sure that the diameter of the filament is within $1.78 \pm 0.025 mm$. If this tolerance is not achieved, the filament will break during the FDC process and it will make the process intermittent.

Viscosity as a function of temperature and shear rate

Capillary test developed at Rutgers University

The capillary rheometer (see Figure A1.5) has been used to determine the shear rate dependency of the viscosity of the PZT/ECG9 [61]. The main reason for choosing this type of test is its similitude to the extrusion through the nozzle of the FDM process. Moreover it was experimented that the range of shear rate values in the performed capillary test was comparable to the one obtained in the rapid prototyping process (approximately between 10 s^{-1} and 1000 s^{-1}).

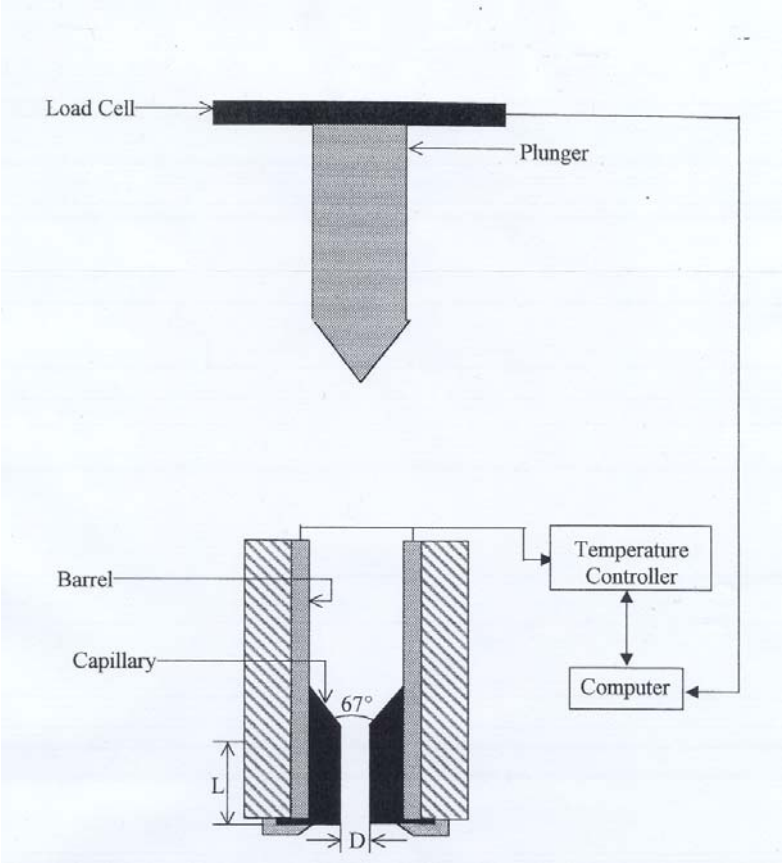

Figure A1.5: Capillary test developed in Rutgers University [61]

In the test the barrel, moved at constant velocity, pushes the polymer through a "nozzle". The apparent viscosity is then calculated from the pressure needed to force the fluid through the capillary at particular flow rate [7]. A load cell, connected to an Instron machine, controls the motion of the plunger [61].

The basic equations are:

$$\Delta P = \frac{F}{A_b} \quad \text{with} \quad A_b = \frac{D_b^{\,2}}{4}\pi \tag{A1.1}$$

where

ΔP	=	Pressure needed for the extrusion
F	=	Force measures by the Instron machine
A_b	=	Cross sectional area of the barrel
D_b	=	Diameter of the barrel

The velocity V with which the fluid is driven through the capillary, is imposed by the barrel, which is connected to the load cell of an Instron machine. The volumetric flow rate is thus determined by:

$$Q = A_b \cdot V \tag{A1.2}$$

In order to calculate the apparent viscosity of the fluid, the melt is first considered Newtonian and the flow is supposed to be laminar:

$$\Delta P = \frac{2 \cdot \tau_w L_c}{\left(\frac{D_c}{2}\right)} \qquad \text{thus} \qquad \tau_w = \frac{\Delta P\left(\frac{D_c}{2}\right)}{2 \cdot L_c} \tag{A1.3}$$

where τ_w represents the shear stress at the tube wall. It can be shown that for steady tube flow, like in this case, the shear stress varies linearly with the distance from the center of the tube:

$$\tau_r = \frac{\tau_w \cdot r}{D_c / 2} \tag{A1.4}$$

Considering that the volume flow rate is given by:

$$Q = 2\pi \int_0^{\frac{D_c}{2}} v_z \cdot r \cdot dr \tag{A1.5}$$

applying the integration by parts and substituting $\dot{\gamma} = \left(\frac{dv_z}{dr}\right)$

$$Q = -\pi \int_0^{\frac{D_c}{2}} \left(\frac{dv_z}{dr}\right) \cdot r^2 \cdot dr = \pi \int_0^{\frac{D_c}{2}} \dot{\gamma} \cdot r^2 \cdot dr \tag{A1.6}$$

With a change of variable and the substitution of equation (A1.4), it is possible to write:

$$\left(\frac{Q}{\pi\left(D_c / 2\right)^3}\right) = \frac{1}{\tau_w{}^3} \int_0^{\tau_w} \dot{\gamma} \cdot \tau_{rz}{}^2 \cdot d\tau_{rz} \tag{A1.7}$$

where the shear rate is to be regarded as a function of shear stress.

Equation (A1.7) indicates that data taken in the tubes of different lengths and radii should collapse onto a single curve when plotted as $\left(\frac{Q}{\pi(D_c/2)^3}\right)$ versus τ_w. In order to obtained the desired expression, equation (A1.7) has to be differentiated with respect to τ_w:

$$\dot{\gamma}_w = \frac{1}{\tau_w^{\,2}} \cdot \frac{d}{d\tau_w}\left[\tau_w^{\,3}\frac{Q}{\pi(D_c/2)^3}\right] \tag{A1.8}$$

This result, called the "Weissenberg-Rabinowitsch equation", shows how the wall shear rate $\dot{\gamma}_w$ can be obtained through the differentiation of pressure drop/flow rate data. Once $\dot{\gamma}_w$ and τ_w are known the viscosity is easily found to be:

$$\eta(\dot{\gamma}_w) = \frac{\tau_w}{\dot{\gamma}_w} \tag{A1.9}$$

Equation (A1.9) gives the viscosity in term of the shear rate at the wall. If in addition one assumes that $\eta(\dot{\gamma}_w)$ obtained at the wall is the same as $\eta(\dot{\gamma})$ through the tube, equation (A1.9) can be used to plot $\eta(\dot{\gamma})$. This assumption appears to be valid for typical polymer fluid, as well as for PZT/ECG9.

In Figure A1.6 the data obtained for different ratio of length to diameter (L/D) and velocity have been reported.

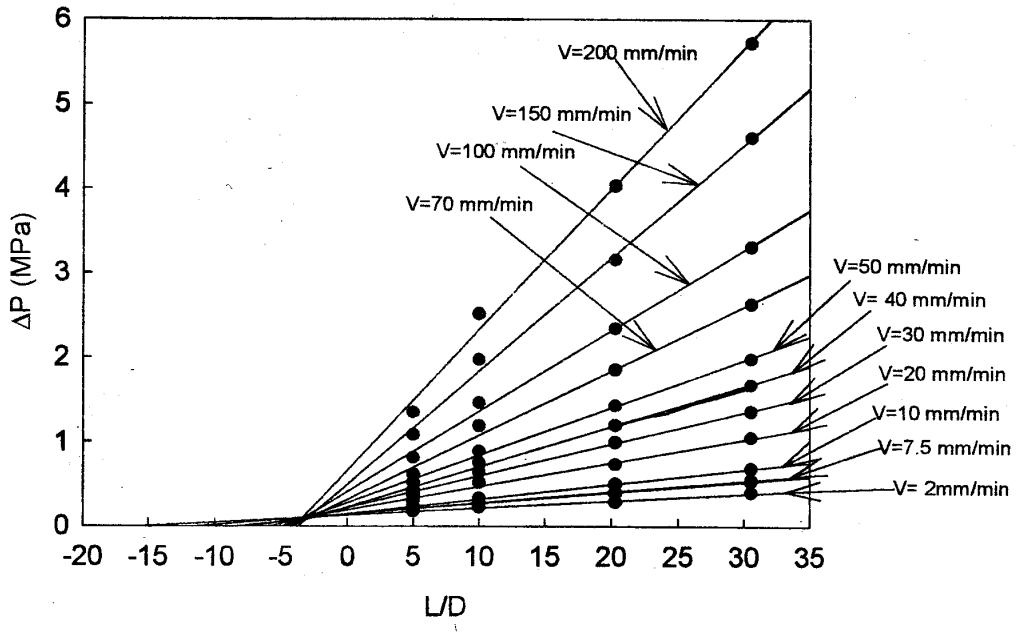

Figure A1.6: Measured Pressure Drop in capillary test (from [61])

Results

Using equations (A1.1) to (A1.9), the viscosity as well as the shear rate have been calculated for the different experiments and have been reported in Table A1-3 to Table A1-5, according to the temperature imposed to the barrel.

Table A1-3: Experimental results (RU) for PZT/ECG9 at temperature of 120 C

Rheology test for ECG9 52% PZT 8/22/98 - Length = 28.85 Temp=120C					
Velocity [mm/min]	**Shear Rate [1/sec]**	**Viscosity [Pa-sec]**	**Final Load [N]**	**Shear Stress [Pa]**	**first run**
2	8.414	677	32.92	5690	
5	21.03	353	42.9	7420	
7	29.45	301	51.33	8880	
10	42.07	242	58.77	10200	
20	84.14	164	79.59	13800	
30	126.2	106	77.54	13400	
40	168.3	76.8	74.75	12900	
50	210.3	64	77.81	13500	
70	294.5	111	189.22	32700	
100	420.7	96.9	235.74	40800	
150	631	82.8	302	52200	
200	841.4	73.4	357.23	61800	
Velocity [mm/min]	**Shear Rate [1/sec]**	**Viscosity [Pa-sec]**	**Final Load [N]**	**Shear Stress [Pa]**	**second run**
2	8.41	640	31.16	5390	
5	21.03	393	47.8	8270	
7	29.45	278	47.32	8180	
10	42.07	231	56.08	9700	
20	84.14	160	77.88	13500	
30	126.2	111	80.67	14000	
40	168.3	134	130.01	22500	
50	210.3	66.1	80.41	13900	
70	294.5	109	185.49	32100	
100	420.7	97.8	237.89	41100	
150	631	82.6	301.25	52100	
200	841.4	74.1	360.3	62300	

Table A1-3 (continued)

Velocity [mm/min]	Shear Rate [1/sec]	Viscosity [Pa-sec]	Final Load [N]	Shear Stress [Pa]	third run
2	8.414	804	39.1	6760	
5	21.03	334	40.61	7020	
7	29.45	273	46.48	8040	
10	42.07	230	55.98	9680	
20	84.14	171	83.26	14400	
30	126.2	116	84.32	14600	
40	168.3	132	128.43	22200	
50	210.3	69.8	84.96	14700	
70	294.5	108	184.33	31900	
100	420.7	95	231.22	40000	
150	631	84.2	307.4	53200	
200	841.4	75.3	366.54	63400	

Velocity [mm/min]	Shear Rate [1/sec]	Viscosity [Pa-sec]	Final Load [N]	Shear Stress [Pa]	fourth run
2	8.414	635	30.91	5350	
5	21.03	367	44.69	7730	
7	29.45	296	50.41	8720	
10	42.07	248	60.21	10400	
20	84.14	206	100.31	17300	
30	126.2	159	116.01	20100	
40	168.3	145	141.25	24400	
50	210.3	152	185.13	32000	
70	294.5	114	194.26	33600	
100	420.7	107	261.34	45200	
150	631	85.4	311.76	53900	
200	841.4	76.1	370.41	64100	

Table A1-4: Experimental results (RU) for PZT/ECG9 at temperature of 130 C

Rheology test for ECG9 52% PZT 8/22/98 - Length = 28.85 Temp = 130C					
Velocity [mm/min]	**Shear Rate [1/sec]**	**Viscosity [Pa-sec]**	**Final Load [N]**	**Shear Stress [Pa]**	**first run**
2	8.414	430	20.92	3620	
5	21.03	229	27.87	4820	
7	29.45	184	31.39	5430	
10	42.07	147	35.76	6190	
20	84.14	102	49.65	8590	
30	126.2	79.5	58.03	10000	
40	168.3	68.6	66.77	11500	
50	210.3	58.6	71.33	12300	
70	294.5	40.4	68.85	11900	
100	420.7	29.4	71.63	12400	
150	631	19.1	69.84	12100	
200	841.1	36.6	178.05	30800	
200	841.4	37.2	182.77	31600	
Velocity [mm/min]	**Shear Rate [1/sec]**	**Viscosity [Pa-sec]**	**Final Load [N]**	**Shear Stress [Pa]**	**second run**
2	8.414	330	16.05	2780	
5	21.03	192	23.34	4040	
7	29.45	160	27.32	4730	
10	42.07	136	33.09	5720	
20	84.14	97.8	47.61	8230	
30	126.2	73.5	53.62	9270	
40	168.3	64.2	62.43	10800	
50	210.3	54.9	66.74	1150	
70	294.5	39.2	66.72	11500	
100	420.7	27.5	66.87	11600	
150	631	18.4	66.97	11600	
200	841.1	37	180.21	31200	

Table A1-4 (continued)

Velocity [mm/min]	Shear Rate [1/sec]	Viscosity [Pa-sec]	Final Load [N]	Shear Stress [Pa]	third run
2	8.414	432	21	3630	
5	21.03	212	25.81	4460	
7	29.45	168	28.54	4940	
10	42.07	138	33.48	5790	
20	84.14	94	45.72	7910	
30	126.2	73.3	53.51	9250	
40	168.3	63.7	62.03	10700	
50	210.3	54.6	66.41	11500	
70	294.5	39.1	66.67	11500	
100	420.7	27.4	66.68	11500	
150	631	18.3	66.88	11600	
200	841.1	36	175.23	30300	
200	841.4	36.4	177.31	30700	

Table A1-5: Experimental results (RU) for PZT/ECG9 at temperature of 140 C

Rheology test for ECG9 52% PZT 8/22/98 - Length = 28.85 Temp=140C					
Velocity [mm/min]	**Shear Rate [1/sec]**	**Viscosity [Pa-sec]**	**Final Load [N]**	**Shear Stress [Pa]**	**first run**
2	8.414	311	15.14	2620	
5	21.03	168	20.45	3540	
7	29.45	140	23.8	4110	
10	42.07	134	32.72	5660	
20	84.14	80	38.91	6730	
30	126.2	55.2	40.29	6970	
40	168.3	43.3	42.15	7290	
50	210.3	38.2	46.46	8030	
70	294.5	32.7	55.63	9620	
100	420.7	27.2	66.27	11500	
150	631	18.1	66.11	11400	
200	841.4	13.7	66.75	11500	
Velocity [mm/min]	**Shear Rate [1/sec]**	**Viscosity [Pa-sec]**	**Final Load [N]**	**Shear Stress [Pa]**	**second run**
2	8.414	243	11.83	2050	
5	21.03	161	19.6	3390	
7	29.45	124	21.11	3650	
10	42.07	103	24.95	4310	
20	84.14	76.2	37.06	6410	
30	126.2	55.4	40.4	6990	
40	168.3	48.7	47.4	8200	
50	210.3	42.8	52.08	9010	
70	294.5	36.9	62.79	10900	
100	420.7	27	65.61	11300	
150	631	18	65.59	11300	
200	841.4	13.5	65.89	11400	

Table A1-5 (continued)

Velocity [mm/min]	Shear Rate [1/sec]	Viscosity [Pa-sec]	Final Load [N]	Shear Stress [Pa]	third run
2	8.414	346	16.86	2920	
5	21.03	164	19.97	3450	
7	29.45	127	21.71	3750	
10	42.07	105	25.62	4430	
20	84.14	67.8	32.97	5700	
30	126.2	56.8	41.45	7170	
40	168.3	50.9	49.55	8570	
50	210.3	46.6	56.65	9800	
70	294.5	37.8	64.41	11100	
100	420.7	30.1	73.3	12700	
150	631	21.2	77.43	13400	
200	841.4	15.3	7.56	12900	
Velocity [mm/min]	**Shear Rate [1/sec]**	**Viscosity [Pa-sec]**	**Final Load [N]**	**Shear Stress [Pa]**	**fourth run**
20	84.14	72.6	35.32	6110	
40	168.3	49.3	47.93	8290	
50	210.3	44.5	54.14	9360	
70	294.5	32.2	54.81	9480	
100	420.7	30.8	75.01	13000	
150	631	21.1	76.9	13300	
200	841.4	15.9	77.47	13400	

From Table A1-3 - Table A1-5 it is clear that the viscosity of PZT/ECG9 decreases with increasing shear rate. This behavior, that is sometime referred as *shear thinning*, while the fluid is said *pseudoplastic*, can be generally modeled with a power law. From the same tables, it can be also observed, as expected, that the viscosity is

highly dependent on the temperature. In order to build a model capable to describe the effect of the temperature, the well known Arrhenius relation has been considered.

Power law

The melt used in the extrusion process has been modeled using the power law. For many of the engineering applications the shear thinning behavior is the most important property of polymeric fluids. When plotted as log(η) versus log($\dot{\gamma}$) the viscosity shear rate curve exhibits a pronounced linear region at high shear rates (see Figure A1.8) . For most of the melts, the slope of the linear section, or ``power-law'' region, is found experimentally to be between -0.4 and -0.9. The tilted straight line can thus be described by a simple ``power law'' expression:

$$\eta = K\dot{\gamma}^{(n-1)} \tag{A1.10}$$

which contains two parameters: K (with units $Pa*s^n$) and n (dimensionless). It can be noticed that when n=1 and K= η the Newtonian fluid is recovered. If n<1, the fluid is said to be ``pseudoplastic'' or ``shear thinning'' and if n>1, the fluid is called “dilatant'' or ``shear thickening''. Experimentally it can be seen that K and n are both temperature dependent, and in general K decreases rapidly with increasing temperature.

The power-law model for $\eta(\dot{\gamma})$ is the most well-known and widely-used empiricism in engineering work, because a wide variety of flow problems have been solved analytically for it.

According to the experimental data obtained from the group in Rutgers University [61], and the mathematical as well numerical model described in the following sections, the values for *K* and *n* used in this project were respectively (see figures 5.13):

$K = 633 \quad Pa \cdot s^n \quad$ and $\quad n = 0.6$

Temperature dependency of the viscosity: Arrhenius relation

If the flow is non- isothermal, the temperature dependence of the viscosity must be taken into account along with the shear rate-dependence [23]. The viscosity law can be factorized as follows:

$$\eta = H(T) \cdot \eta_0(\dot{\gamma}) \tag{A1.11}$$

where *H(T)* is the Arrhenius relation and $\eta_0(\dot{\gamma})$ is the viscosity law at a reference temperature T_α. The Arrhenius relation can be written as:

$$H(T) = \exp\left[\alpha\left(\frac{1}{T - T_0} - \frac{1}{T_\alpha - T_0}\right)\right] \tag{A1.12}$$

where α is the "activation energy for flow" and T_α is the reference temperature for which $H(T) = 1$.

Determination of the material parameters

Matlab programs have been written in order to determine the parameters α, K and n that better fit (minimum square error) the data reported in Table A1-3, Table A1-4 and Table A1-5.

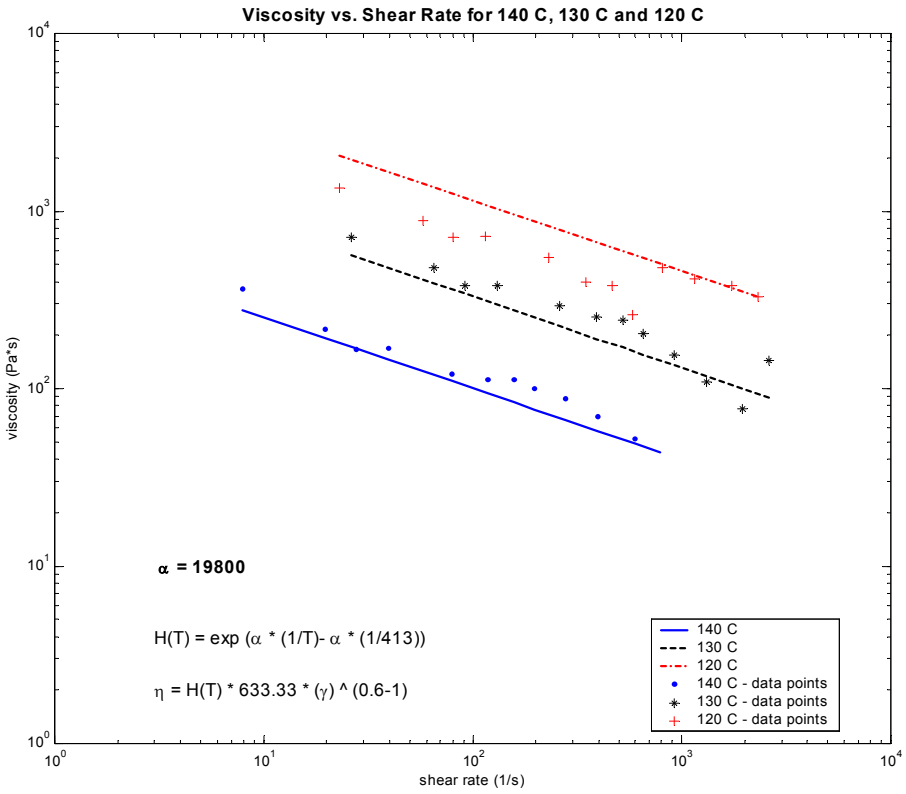

Figure A1.7: Data points and curve fitting for viscosity of PZT/ECG9

In order to verify the validity of the values K and n to use into the power law, a theoretical model was applied to the capillary geometry (see Figure A1.8) and the calculated values for the pressure drop have been compared with the observed ones.

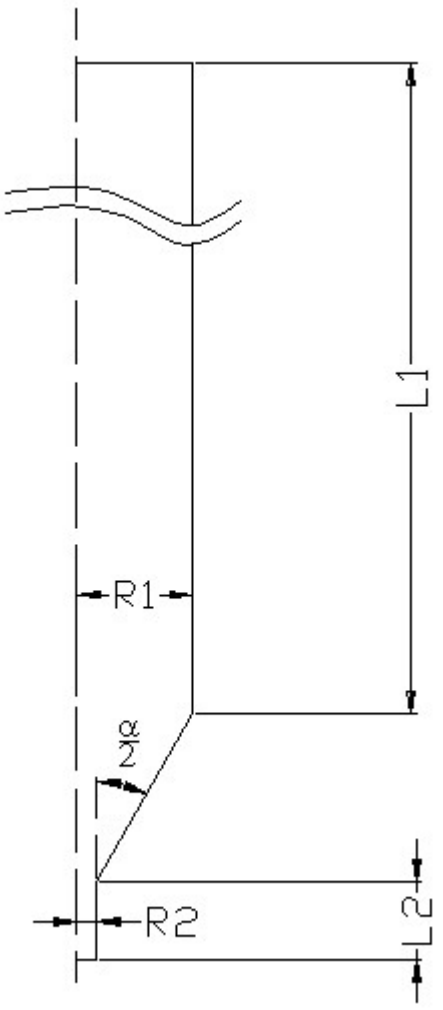

Figure A1.8: Schematic of the capillary test

The capillary geometry can be seen as a series of successively arranged basic geometries, such as a pipe of radius R_1, a conical bore of angle $\alpha/2$ and a pipe of radius R_2. In this case the total pressure drop can be calculated as the sum of the individual pressure drops in each of the three mentioned parts.

The fundamental equations for the flow in a channel with circular or conical bore section can be derived applying the principle of conservation of mass, momentum and energy.

$$\left\{\begin{matrix}\text{Entering momentum}\\ \text{per unit time}\\ \text{(momentum flux)}\end{matrix}\right\}-\left\{\begin{matrix}\text{exiting momentum}\\ \text{per unit time}\\ \text{(momentum flux)}\end{matrix}\right\}+\left\{\begin{matrix}\text{Sum of all}\\ \text{forces acting}\\ \text{on the system}\end{matrix}\right\}=0$$

In general momentum flux can occur as a result of the general motion of the flowing melt or a result of the viscosity of the medium [47]. Under the assumption of incompressibility of the fluid and of laminar flow (melt that flows on straight, parallel paths), the momentum flux balance reduces to a force balance of easy derivation.

The pressure drop at the exit of the pipe of length L and diameter D can be written as:

$$\Delta p=\left[\frac{(m+3)\cdot(2L)^{m}\cdot\dot{V}}{\pi\cdot\left(\frac{D}{2}\right)^{m+3}\Phi}\right]^{\frac{1}{m}} \tag{A1.13}$$

Applying the same procedure to the conical part of the capillary geometry, the volumetric flow rate can be expressed as:

$$\dot{V}=K'\cdot\Phi\cdot\Delta p^{m} \tag{A1.14}$$

where

$\dot{V}$ = the volumetric flow rate

K' = Die conductance applicable to the power law

Δp = Pressure drop in the conical bore

Φ and m are the material parameters for the power law expressed as:$|\dot{\gamma} = \Phi \cdot \tau^m$

From the definition of the $\eta = \frac{\tau}{\dot{\gamma}}$(where represents the τ shear stress and $\dot{\gamma}$ the shear rate), it is possible to derive the viscosity as a function of the material parameters Φ and m:

$$\eta = \left(\frac{\dot{\gamma}^{1-m}}{\Phi} \right)^{\frac{1}{m}} \qquad \text{(A1.15)}$$

Comparing equation (A1.10) with equation (A1.15)), one can correlate the parameter Φ and mw with the previously mentioned n and K.

$$m = \frac{1}{n} \text{ and } \Phi = K^{-\frac{1}{n}} \qquad \text{(A1.16)}$$

Under the assumptions of:

1. *Isothermal flow*, that mean that all particles of the melt stream have the same temperature; the wall of the die has the same temperature as the melt (i.e. there is no heat flow between the melt and the die wall).

2. *Steady state flow*, i.e. no change in flow profile with time.

3. Laminar flow.

4. *Incompressible fluid*, thus melts with constant density.

5. *No slip boundary conditions.*

The die conductance can be derived as [47]:

$$K' = \frac{\pi}{2^m (m+3)} \left(\frac{3\left(\frac{D_1}{D_2} - 1\right)}{m \cdot L \left(1 - \left(\frac{D_2}{D_1}\right)^{\frac{3}{m}}\right)} \right)^m \left(\frac{d}{2}\right)^{m+3} \qquad \text{(A1.17)}$$

where $D_2 < d < D_1$ (see (A1.9)).

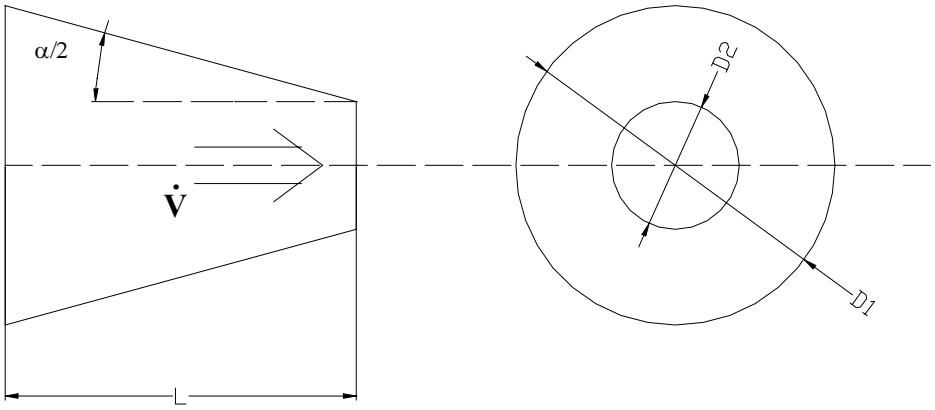

Figure A1.9: parameters for the conical bore part of the capillary

From equations (A1.14) and (A1.17), the pressure drop at the exit of the conical bore is:

$$\Delta p = \left[\frac{\dot{V}\cdot 2^{m+3}(m+3)}{\pi\cdot\Phi}\right]^{\frac{1}{m}}\cdot\frac{2\cdot m\cdot L}{3}\cdot\frac{1-\left(\frac{D_2}{D_1}\right)^{\frac{3}{m}}}{\frac{D_1}{D_2}-1}\cdot\frac{1}{d^{\frac{m+3}{m}}} \qquad (A1.18)$$

$$= \left[\frac{\dot{V}\cdot 2^{m+3}(m+3)}{\pi\cdot\Phi}\right]^{\frac{1}{m}}\cdot\frac{m}{3}\cdot\frac{D_1^{\frac{3}{m}}-D_2^{\frac{3}{m}}}{D_1^{\frac{3}{m}}D_2^{\frac{3}{m}}}\cdot\frac{2L}{D_1-D_2}\cdot\frac{D_2^{\frac{3}{m}}D_2}{d^{\frac{m+3}{m}}}$$

According to the geometry described in figure Die, it is possible to substitute:

$$\frac{D_1-D_2}{2L} = tg\left(\frac{\alpha}{2}\right)$$

Considering the pressure drop at the wall of the exit of the conical bore (i.e. $d=D_2$), equation (A1.18) becomes:

$$\Delta p = \frac{m}{3\cdot tg\left(\frac{\alpha}{2}\right)}\left(\frac{1}{D_2^{\frac{3}{m}}}-\frac{1}{D_1^{\frac{3}{m}}}\right)\left[\frac{\dot{V}\cdot 2^{m+3}(m+3)}{\pi\cdot\Phi}\right]^{\frac{1}{m}} \qquad (A1.19)$$

Equation (A1.13) was incorporated in a Fortran program in order to determine the pressure drop in the first cylindrical part of the capillary (see Figure A1.8). Equation (A1.19) was implemented in the same program for the evaluation of the pressure drop in the conical section of the same test. The calculation was performed for different values of the velocity of the barrel, thus of the melt flow rate:

$$\dot{V} = v \cdot \pi \cdot R_1^{\,2}$$

where v is the velocity of the barrel and R_1 is the radius of the barrel (see Figure A1.5 and Figure A1.8).

In order to better reproduce the same conditions of the capillary test, the numerical calculation was performed for the following values:

		Case 1	**Case 2**	**Case 3**	**Case 4**
L1	=	*50 mm*	*50 mm*	*50 mm*	*50 mm*
D1	=	*4.76*2 mm*	*4.76*2 mm*	*4.76*2 mm*	*4.76*2 mm*
D2	=	*0.965*2 mm*	*0.965*2 mm*	*0.965*2 mm*	*0.965*2 mm*
α	=	*67 degree*	*67 degree*	*67 degree*	*67 degree*
L_2 / D_2	=	*5*	*10*	*20.28*	*31*

The obtained results have been reported in Figure A1.10. The good agreement between the values of Figure A1.10 with the experimental data (see Figure A1.6) lead us to the conclusion that

K = 633.33 and n =0.6

can be considered acceptable for the proposed model.

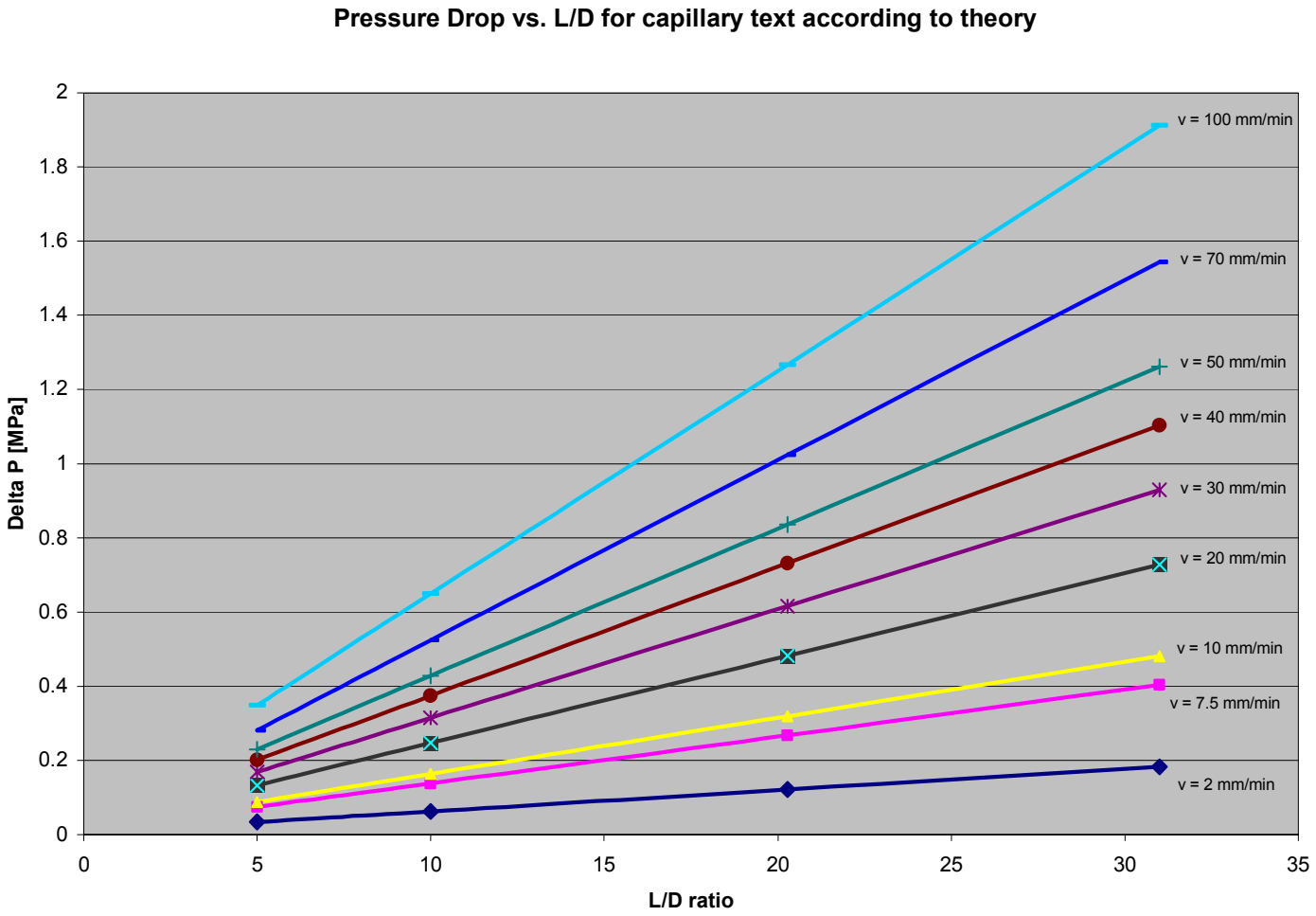

Figure A1.10:Pressure Drop in capillary test (from theory) for K = 633 and n = 0.6

Validity of the numerical simulation: determination of the pressure drop values in a capillary test, using Polyflow.

In order to verify the validity of the finite element model to use for the prediction of the road evolution, road to road interaction and for the determination of the optimal nozzle design, a study was conducted with a capillary test model.

Because of the axisymmetric property of the problem, the mesh reported in Figure A1.11 was used in order to reduce the number of element, thus the size of the calculations.

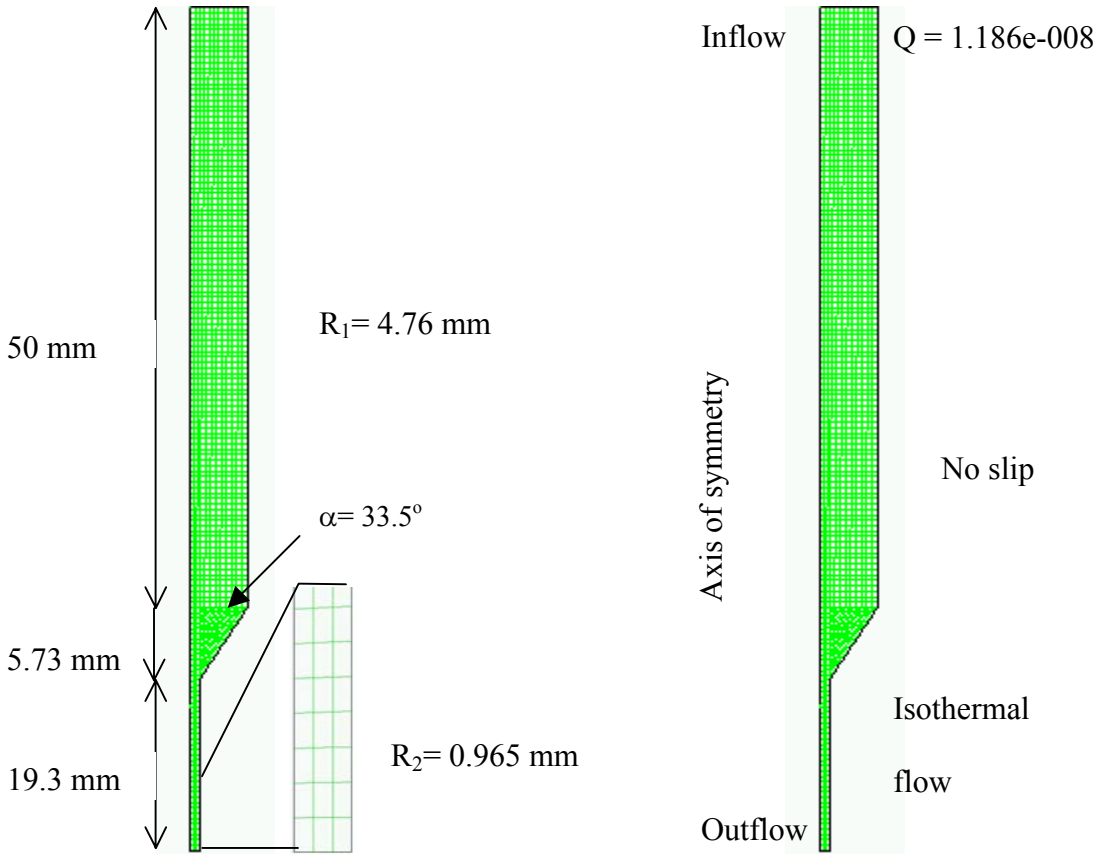

Figure A1.11: Capillary model for L/D = 10

In Figure A1 12, the pressure drop contour and the pressure drop plot have been reported for the case of v= 40 mm/s and L/D = 10. As expected the major contribution to the pressure drop is due to the last part of the cylindrical pipe, where the diameter is extremely small. From Figure A1 12 it is also possible to notice that the pressure drop is varying linearly with respect to *y*, thus it is possible to conclude that the flow is fully developed and it is not particularly affected by the "capillary cone" geometry.

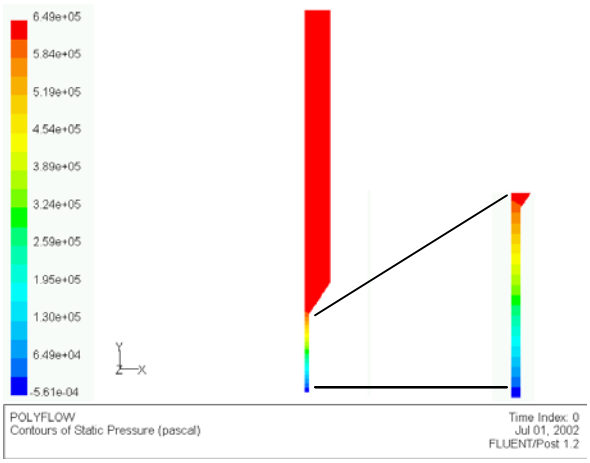

(a) Pressure drop in the capillary

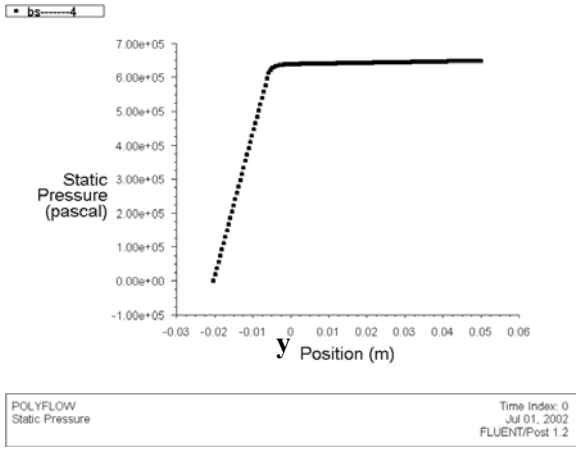

(b) Plot of the pressure drop along y

Figure A1 12: Capillary pressure drop

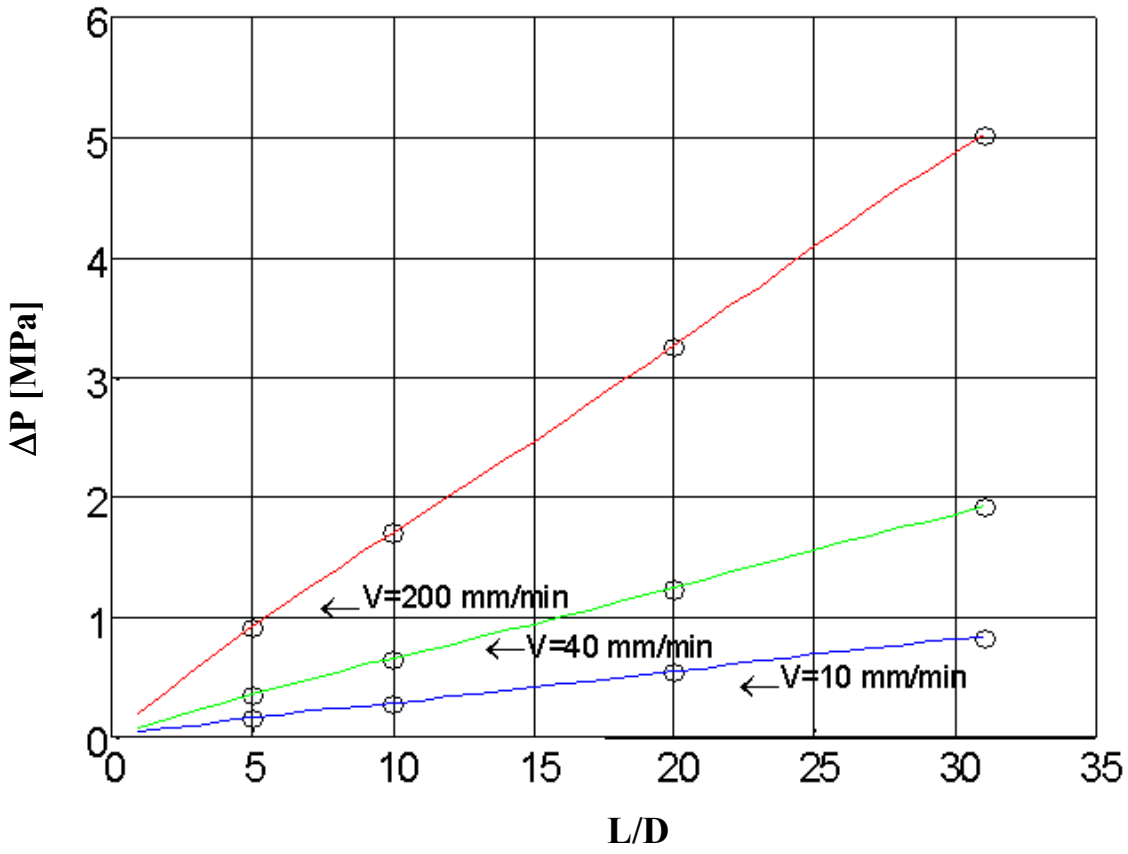

Figure A1.13: Pressure drop in capillary test calculated with polyflow
(K = 633, n = 0.6)

In Figure A1.13, the pressure drop values determinated with the model of the capillary test have been reported.The comparison between Figure A1.6 and Figure A1.13, shows a good prediction of the results obtained with the numerical model. Comparing Figure A1.13 with Figure A1.10 and Figure A1.6 it is possible to see a good agreement. Theory and simulation gives results that are close to experimental data, for K = 633 and n =0.6.

For the dependence of the viscosity on the temperature, we used the Arrhenius relation. When I say that we deposit a semiliquid material is because we deposit on a

substrate enclosed in an envelope maintained at 40 C (313K). From Figure A1.15 (see the excel file) we see that the viscosity is rapidly decreasing with the temperature.

Since experimental data show that during deposition of one road the temperature decreases exponentially:

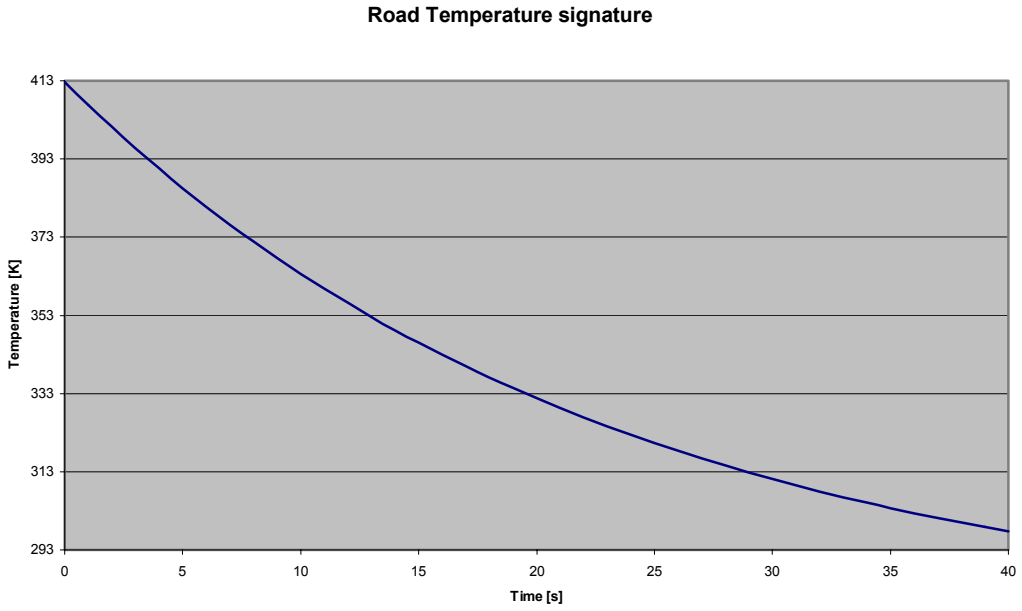

Figure A1.14: Temperature signature of a road during deposition

From the signature of the road (Figure A1.14) we can see that as soon as we deposit the road, the temperature drops to (393K), for which the viscosity is already 1 order of magnitude more than at 140 degree. For this reason we can say that it is semi-liquid.

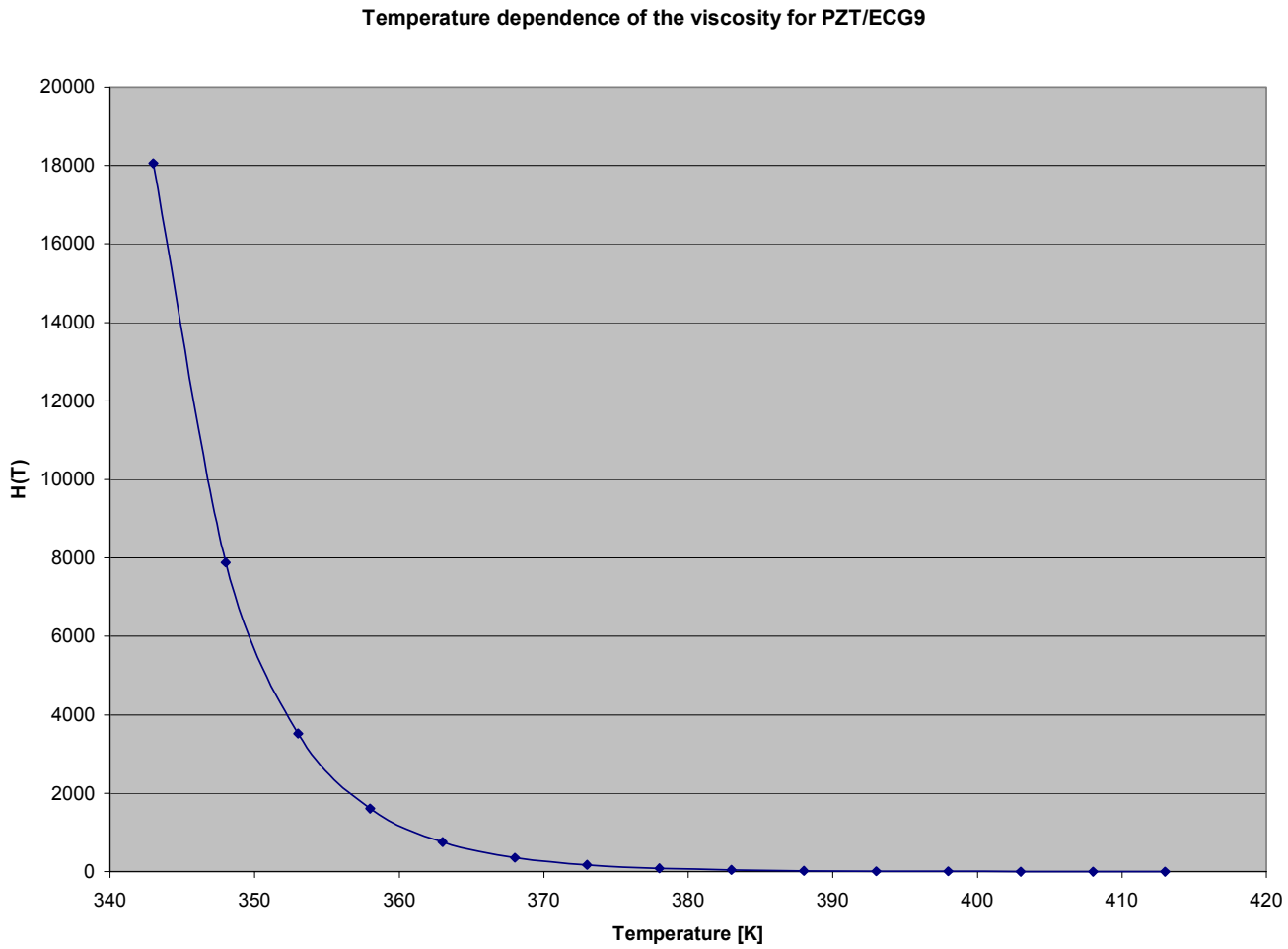

Figure A1.15: Plot of the viscosity dependence from the temperature

The viscosity of the melt during the deposition process has been also estimated using the finite element analysis. The results reported in Figure A1.16 reveal that due to the thermal dissipation, the viscosity increases of almost two orders of magnitude as soon as the melt reach the support platform.

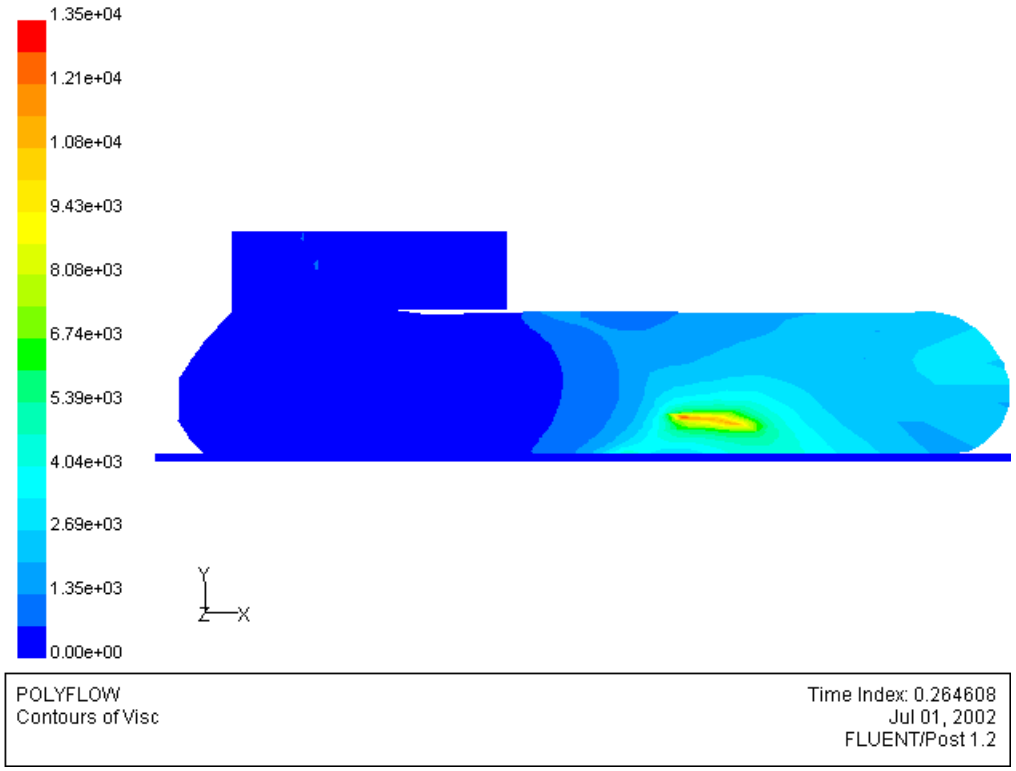

Figure A1.16: Viscosity distribution during deposition [Pa-s]

Because of the large range of values, the viscosity appears to be null in the liquefier. In order to not mislead to inaccurate assumptions, the plot of the viscosity values at the very exit of the nozzle (Figure A1.17.a) has also been reported in Figure A1.17.b.

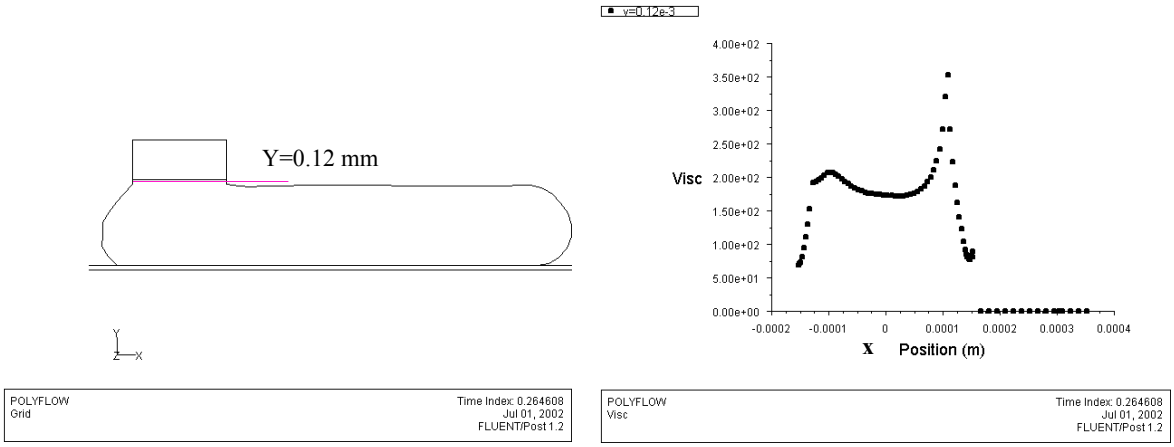

(a) position of the surface at y=0.12 mm (b) plot of the viscosity [Pa-s]

Figure A1.17: Plot of the viscosity during deposition on the line at y = 0. 12 mm

Surface tension for PZT/ECG9

In order to determine the value of the surface tension for PZT/ECG9 a Fisher Surface Tensiomat Model 21 was used. This instrument uses the "*ring method*" approach that utilizes the interaction of a platinum ring with the surface being tested. The ring is submerged below the interface and subsequently raised upwards. As the ring moves upwards it raises a meniscus of the liquid and the instrument measures the maximum force needed for the tearing event. Because of the high viscosity of the material, due to the 52.5 % volume fraction of PZT powder, the collected data showed a large scattered behavior. To have more reliable data the ECG9 binder itself was tested. The results have been reported in Table A1-6:

Table A1-6: Data from the surface tension experiment

	Dyne/cm^2	N/m^2
Surface tension for ECG9	22	0.022
	37	0.037
	29	0.029
	25	0.025
	30	0.030

In order to take in consideration the presence of the PZT particles, whose dispersion, dimension and agglomerate phases directly affect the surface tension, a value of $0.05\frac{N}{m^2}$ has been considered in the developed model. This value was chosen after having run several simulations with surface tension values varying from 0.025 to 1.5. This parametric study did not show relevant differences in the results obtained for surface tensions values in the range of $0.0.25 < S < 1$. When S reaches the unit value the numerical method has convergence problems, probably because of the equilibrium of forces on the free boundary. Under these conditions, the forces exercised by the incoming flow are of the same order of magnitude of the force exercised by the surface tension.

Thermal properties of ECG9/PZT

In order to determine the thermal properties of the ECG9/PZT, experimental tests have been conducted at University of Illinois at Chicago using a Modulated Differential Scanning Calorimetry (MDSC) 2950 from TA Instruments.

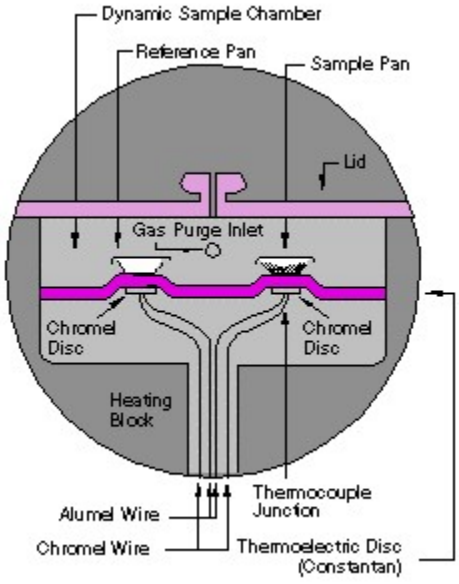

(a) Cell schematic diagram

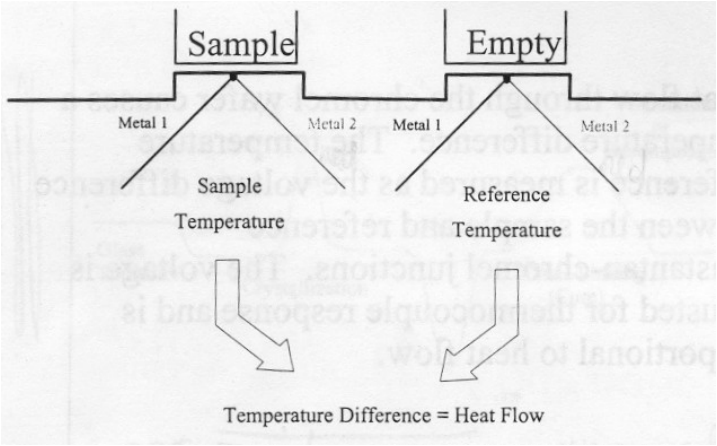

(b) Principal of operation

Figure A1.18: Schematic of the MDSC

In DSC the differential temperature between sample and reference is converted to differential heat flow in the following way:

$$Heat\_Flow = \frac{\Delta T}{R} k_1 k_2$$

where k_1 is the factory-set calibration value;

k_2 is the user-set calibration value (usually a sample of indium is used);

R is the thermal resistance of constantant disk;

ΔT is the temperature difference.

Heat capacity:

A DSC measures the heat of a sample relative to a reference. Heat flow through the cromel wafer (see Figure A1.18) is measured as the voltage difference between the sample and the reference constantan-chromel junctions. The voltage is adjusted for thermocouple response and is proportional to heat flow.

Using the standard DSC with a ramp heating of 15°C/min, the melting point for ECG9/PZT has been determined around 114°C (see Figure A1.19).

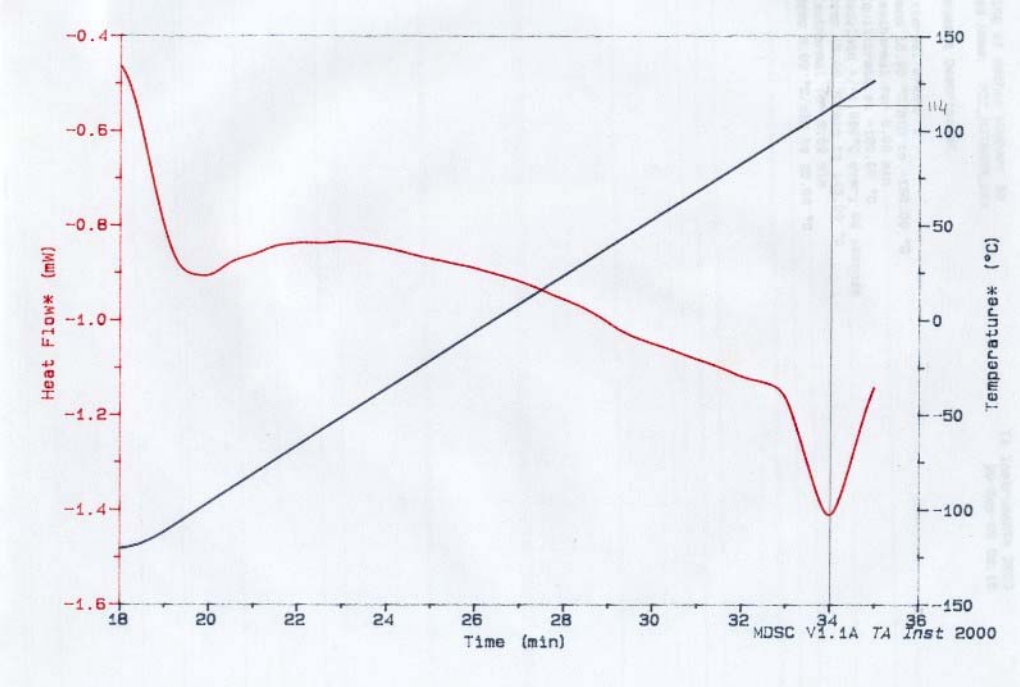

Figure A1.19: ECG9/PZT melting point

To cool down the cell until –150°C without affecting the measurement, liquid Nitrogen was used because of its relatively poor thermal conductivity [59].

Since for the success of deposition process it is important to avoid any hard or brittle conditions of the material, ECG9/PZT has been also tested with the DSC 2950 to determine its glass transition temperature (Tg). In order to increase the sensitivity of the instrumentation to the heat flow absorption through the Tg of the sample, the Modulated DSC has been used (see Figure A1.20).

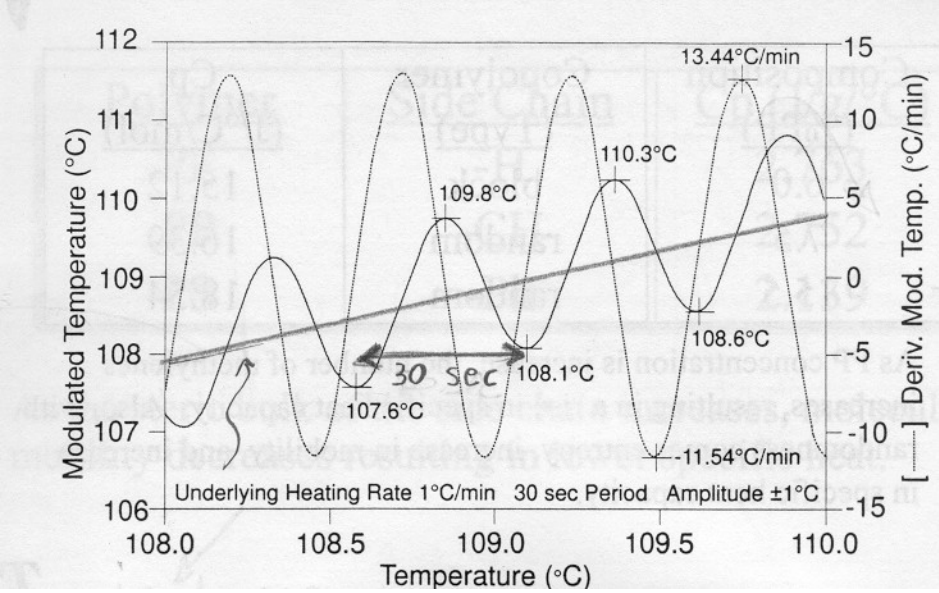

Figure A1.20: Modulated DSC Heating profile

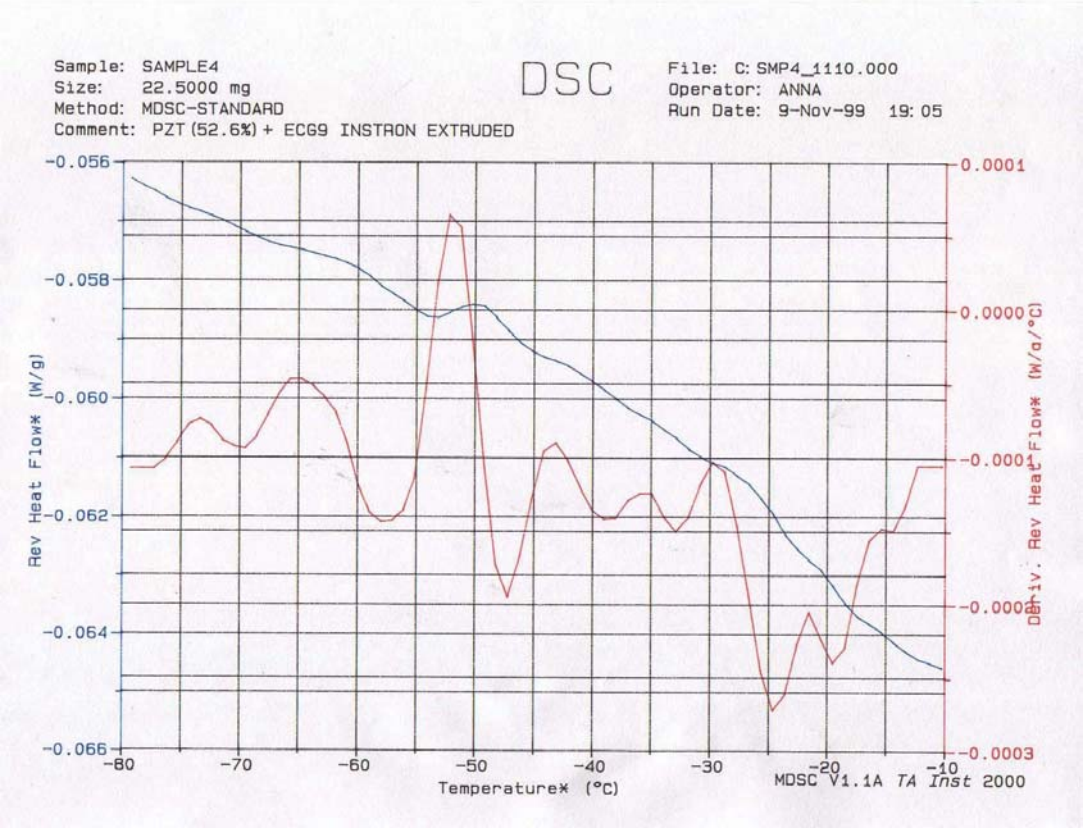

Figure A1.21: ECG9/PZT glass transition

With the MDSC method, the difference in heat flow between reference and sample is measured as a function of both a linear and sinusoidal change in temperature (see Figure A1.20). For this method it is possible to write:

$$dQ/dt = Cp(\beta + A_T\omega\cos(\omega t)) \quad + f(T,t) + A_k \sin(\omega t)$$

where $(\beta + A_T\omega\cos(\omega t)$ is the measured heating rate (dT/dt);

f(T,t) is the kinetic response without temperature modulation;

A_k is the amplitude of the kinetic response to temperature modulation.

Taking the average of the modulated signal:

$$\left.\frac{dQ}{dt}\right|_{av} = Cp\beta + f(T,t)$$

where $Cp\beta$ represents the reversing heat flow signal [56];

β is the average heating rate;

f(T,t) represents the nonreversing signal.

If in the plot of the reversing heat flow signal (see Figure A1.21) an inflection point is detected, than its temperature can be considered the Tg of the sample [57]. In order to better visualize the mentioned point, in Figure A1.21 the derivative of the reversing signal has been reported. From the plotted data, one can conclude that the Tg for ECG9/PZT is -52^{o}C. This means that in the range of temperature (from 20^{o}C to 160^{o}C), used in the FDC process the material will not be subjected to the glass transition phase.

Using the MDSC it is possible to measure also the heat capacity of the sample as the ratio of the modulated heat flow amplitude divided by the modulating heat rate amplitude. In Figure A1.22 the dashed line represents the heat capacity data points obtained for ECG9/PZT.

Table A1-7: Experimental results for PZT/ECG9

Heat capacity for PZT/ECG9		
Temp [Celsius]	**Heat Cap [J/gK]**	**Heat Cap [J/KgK]**
50	0.45	450
90	0.49	490
100	0.52	520
110	0.565	565
115	0.548	548
120	0.55	550
128	0.5	500
140	0.5	500

In Polyflow it is possible to enter the heat capacity as a function of temperature as a polynomial. For this reason I looked for the best fit (according to the data Table A1-7)

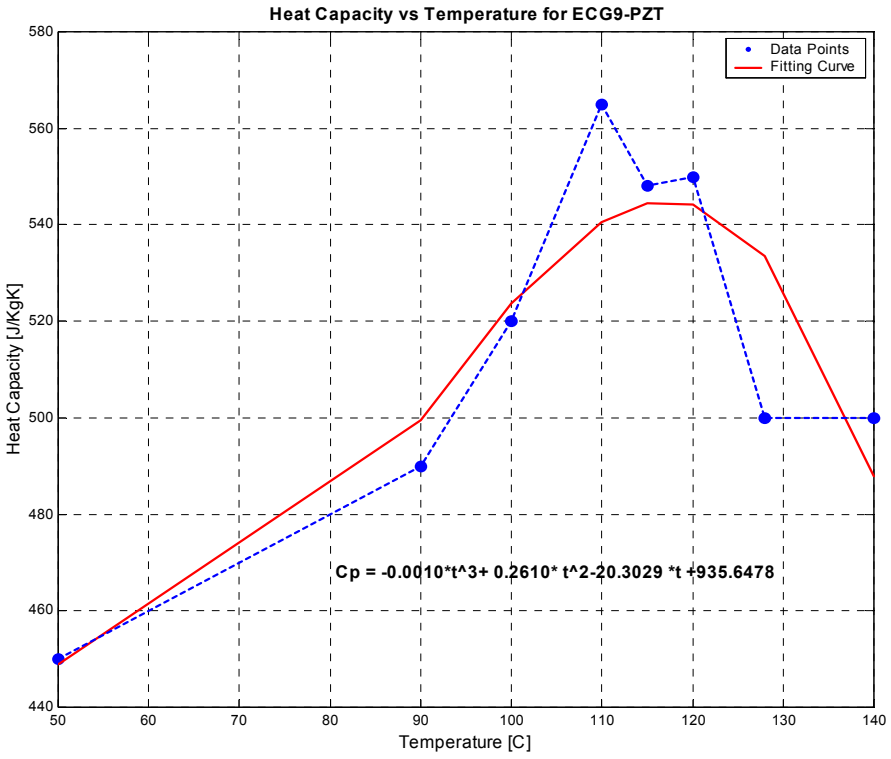

Figure A1.22: Heat capacity curve for ECG9/PZT.

Thermal Conductivity:

The thermal conductivity for the PZT/ECG9 sample was determined using the Modulates DSC from TA instrument described above [43]. Giving the possibility to directly measure the heat capacity of the sample, MDSC provides the possibility to determine the thermal conductivity, property that is closely related to the former one. The modulated heat flow generated in the cell can be expressed as:

$$\left(\frac{dQ}{dt}\right)^2 = 2\cdot(Z\theta_0 kA)^2\left[\frac{1-2\cdot e^{2ZL}\cdot\cos(2ZL)+e^{4ZL}}{1+e^{2ZL}\cdot\cos(2ZL)+e^{4ZL}}\right] \qquad \text{(A2.20)}$$

where:

k	=	Thermal conductivity [W/^{o}C cm]
$\frac{dQ}{dt}$	=	Heat flow amplitude [J/sec]
ω	=	Angular frequency [2π/sec]
ρ	=	Sample density [g/cm^3]
C_p	=	Sample specific heat [J/^{o}C g]
Z^2	=	$\omega\rho C_p / 2k$
θ_0	=	Sample modulation amplitude [^{o}C]

Additional assumption have been considered:

- The specimen is a right circular cylinder with cross sectional area (A) and length (L) with parallel end faces.
- The specimen has a density (ρ) and a specific heat (Cp).
- The face of the specimen at the heat source follows the applied temperature modulation.
- The heat flow through the opposing face is zero.
- There is no heat flow through the side of the specimen.

For samples with low thermal conductivity (like in the case pf PZT/ECG9) the term e^{4ZL} is large, thus dominate the other terms of equation 1. therm_cond. The previous equation yields to:

$$\left(\frac{dQ}{dt}\right)^2 = 2(Z\theta_0 kA)^2 \Rightarrow \left(\frac{dQ}{dt}\right)^2 = 2\frac{\omega\rho C_p}{2k}\theta_0{}^2 k^2 A^2 \Rightarrow \left(\frac{dQ}{dt}\right)^2 = \frac{2\pi}{T} kC_p \rho A^2 \theta_0{}^2 \quad \text{(A2.21)}$$

where $T = \frac{2\pi}{\omega}$ = period.

Since $C = \frac{\left(\frac{dQ}{dt}\right)}{\omega \cdot \theta_0}$, it is possible to write:

$$C^2 = kC_p \rho A^2 \frac{T}{2\pi} \Rightarrow k = \frac{2\pi C^2}{C_p \rho A^2 T}$$

Considering (see assumptions) a cylindrical sample $\rho = \frac{M}{AL} = \frac{4M}{\pi d^4 L}$, equation (A2.21) becomes:

$$k = \frac{8C^2 L}{C_p M d^4 T}$$

Where

L	=	Sample length [cm]
A	=	Sample cross sectional area [cm^2]
M	=	Sample mass [g]
C	=	Apparent heat capacity [J/^oC]

In Figure A1.24 the results obtained using samples with geometry illustrated in Figure A1.23, have been presented:

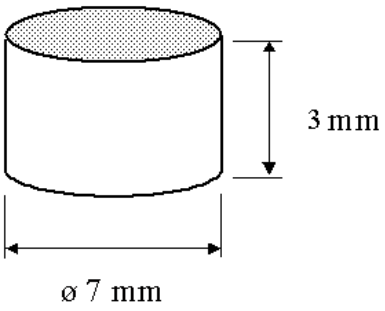

Figure A1.23: Sample of PZT /ECG9 used to determine the thermal conductivity

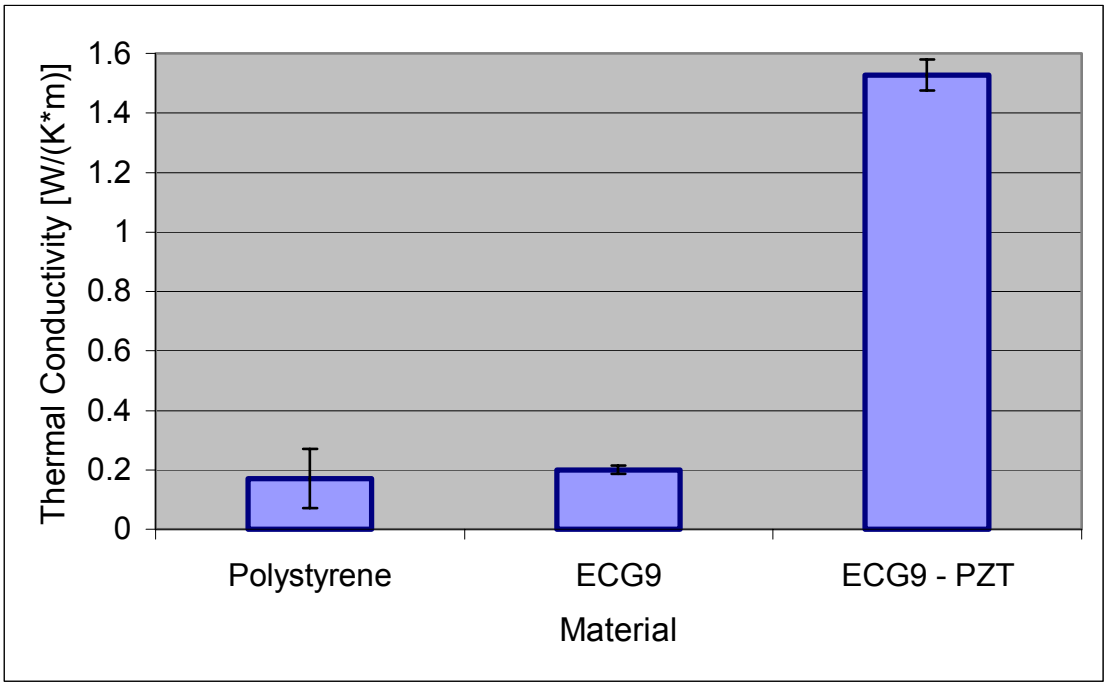

Figure A1.24: Experimental data for the thermal conductivity of PZT/ECG9

Density of ECG9/PZT

The density of ECG9/PZT has been calculated considering that according to [52]:

- The density of PZT-5H (TRS) is approximately 7.9 g/cm^3;
- The density of the binder ECG9 is 0.91 g/cm^3 ;
- The percentage in volume of PZT particles is 52.5 %;
- The percentage in volume of ECG9 is 47.5%.

According to these data, the density of ECG9 filled with PZT particles is:

$$\rho = 7.9 * 0.525 + 0.91 * 0.475 = 4.58 \quad g / cm^3$$

Appendix 2: List of abbreviations

3-D	=	Three-dimensional
3DP	=	Three Dimensional Printing
3DW	=	Three Dimensional Welding
BIS	=	Beam Interference Solidification
BPM	=	Ballistic Particle Manufacture
CC	=	Contour Crafting
CNC	=	Computer Numerical Control
DMD	=	Direct Metal Deposition
DSPC	=	Direct Shell Production Casting
ES	=	Electrosetting
FDC	=	Fused Deposition of Ceramics
FDM	=	Fused Deposition Modeling
FEA	=	Finite Element Analysis
FEM	=	Finite Element Method
FPM	=	Freeform Powder Molding
GPD	=	Gas Phase Deposition
HIS	=	Holographic Interface Solidification
LENS	=	Laser Engineering Net Shaping
LM	=	Layer Manufacturing
LOM	=	Laminated Object Manufacture

LTP	=	Liquid Thermal Polymerization
MJM	=	Multi Jet Modeling
MJS	=	Multi-phase Jet Solidification
Object	=	Object Quadra Process
PLS	=	Paper Lamination System
PLT	=	Paper Lamination Technology
PMS	=	ProMetal System
RFP	=	Rapid Freezing Prototyping
RM	=	Rapid manufacturing
RP	=	Rapid Prototyping
RPS	=	Rapid Prototyping System
SAHP	=	Selective Adhesive and Hot Press
SCS	=	Solid Creation System
SDM	=	Shape Deposition Manufacturing
SF	=	Spatial Forming
SFF	=	Solid Freeform Fabrication
SFP	=	Solid Foil Polymerization
SGC	=	Solid Ground Curing
SL	=	Stereolithography
SLS	=	Selective Laser Sintering
SOUP	=	Solid Object Ultraviolet-laser Plotting
STL	=	Stereolithography File

TSF = Topographic Shell Fabrication

Appendix 3: Finite element theory

Polyflow theory

Since **POLYFLOW** is an unstructured solver, it uses internal data structures to assign an order to the elements, faces, and mesh points in a mesh and to maintain contact between adjacent elements. It does not, therefore, require i,j,k indexing to locate neighboring elements [23].

The element types allowed in Polyflow, for a 2D simulation are:

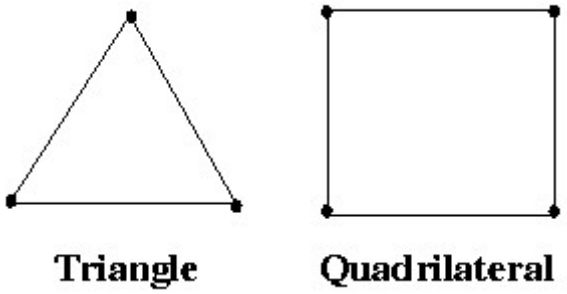

For these elements the equations used for a generalized Newtonian flow with non-isothermal conditions are:

1. Continuity equation;
2. Equation of motion;
3. Constitutive equation;
4. Energy equation.

Because of the strong distortions that typically characterize any extrusion problem, the formulation implemented in Polyflow is Eulerian, thus the mesh is fixed with respect to the library frame and the fluid moves through it.

Conservation of mass - continuity equation:

The mass balance on a small control volume dx, dy, dz is [47]:

$$\begin{Bmatrix}\text{Stored mass}\\ \text{per unit time}\end{Bmatrix} = \begin{Bmatrix}\text{Entering mass}\\ \text{per unit time}\end{Bmatrix} - \begin{Bmatrix}\text{Leaving mass}\\ \text{per unit time}\end{Bmatrix}$$

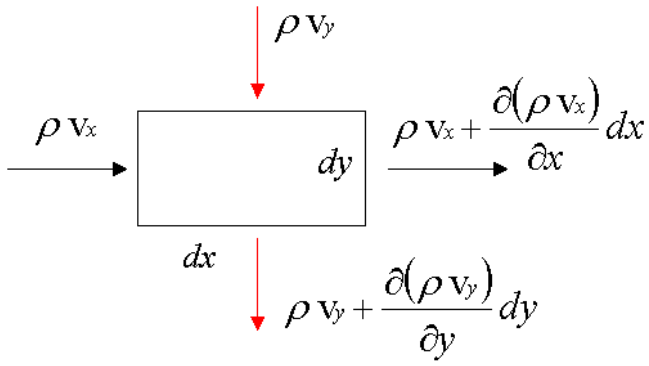

$$\frac{\partial \rho}{\partial t} = -\left(\frac{\partial(\rho \mathrm{v}_x)}{\partial x} + \frac{\partial(\rho \mathrm{v}_y)}{\partial y} + \frac{\partial(\rho \mathrm{v}_z)}{\partial z}\right)$$

$$\frac{\partial \rho}{\partial t} = -(\nabla \rho \vec{\mathrm{v}})$$

$$\frac{\partial \rho}{\partial t} = -\rho\frac{\partial \mathrm{v}_x}{\partial x} - \mathrm{v}_x\frac{\partial \rho}{\partial x} - \rho\frac{\partial \mathrm{v}_y}{\partial y} - \mathrm{v}_y\frac{\partial \rho}{\partial y} - \rho\frac{\partial \mathrm{v}_z}{\partial z} - \mathrm{v}_z\frac{\partial \rho}{\partial z}$$

$$\frac{\partial \rho}{\partial t} + \mathrm{v}_x \frac{\partial \rho}{\partial x} + \mathrm{v}_y \frac{\partial \rho}{\partial y} + \mathrm{v}_z \frac{\partial \rho}{\partial z} = -\rho\left(\frac{\partial \mathrm{v}_x}{\partial x} + \frac{\partial \mathrm{v}_y}{\partial y} + \frac{\partial \mathrm{v}_z}{\partial z} \right)$$

$$\frac{D\rho}{Dt} = -\rho(\nabla \vec{\mathrm{v}})$$

where $\frac{D\rho}{Dt}$ is the substantial derivative of the density.

Since the melt is considered incompressible, then $\frac{D\rho}{Dt} \equiv 0$, thus the continuity equation becomes:

$$\nabla \vec{\mathrm{v}} = \frac{\partial \mathrm{v}_x}{\partial x} + \frac{\partial \mathrm{v}_y}{\partial y} + \frac{\partial \mathrm{v}_z}{\partial z} = 0$$

Conservation of momentum – equation of motion:

The momentum flux balance on a small control volume dx, dy, dz is:

$$\left\{\begin{matrix}\text{Change in the} \\ \text{momentum per unit time}\end{matrix}\right\} = \left\{\begin{matrix}\text{Entering momentum} \\ \text{per unit time}\end{matrix}\right\} - \left\{\begin{matrix}\text{Leaving mass} \\ \text{per unit time}\end{matrix}\right\} + \left\{\begin{matrix}\text{Forces acting} \\ \text{on the system}\end{matrix}\right\}$$

If one consider, for simplicity, the momentum flux balance on the *x* direction:

$$\frac{\partial}{\partial t}(\rho \mathrm{v}_x) = -\left[\frac{\partial}{\partial x}(\rho \mathrm{v}_x \mathrm{v}_x) + \frac{\partial}{\partial y}(\rho \mathrm{v}_y \mathrm{v}_y) + \frac{\partial}{\partial z}(\rho \mathrm{v}_z \mathrm{v}_z) \right] + \\ -\left(\frac{\partial}{\partial x}\tau_{xx} + \frac{\partial}{\partial x}\tau_{yx} + \frac{\partial}{\partial x}\tau_{zx} \right) - \frac{\partial p}{\partial x} + g_x \rho$$

where p represents the pressure, τ represents the surface forces and g the volume forces.

Considering that the stress tensor is always symmetric, it is possible to rewrite similar equations for y and z directions. In a generally valid vector and tensor symbolism (independent on the coordinate system), the momentum equation becomes:

$$\frac{\partial}{\partial t}\left(\rho \bar{\mathrm{v}}\right) = -\left(\nabla\rho \cdot \bar{\mathrm{v}} \cdot \bar{\mathrm{v}}\right) - \nabla p - \nabla \bar{\bar{\tau}} + \rho\vec{g}$$

where it is possible to rewrite as:

$$\left\{\begin{array}{l}\text{Momentum change}\\ \text{per unit time}\\ \text{and unit of volume}\end{array}\right\} = \left\{\begin{array}{l}\text{Change in the motion}\\ \text{(momentum flux)}\\ \text{per unit time}\\ \text{and unit of volumee}\end{array}\right\} + \left\{\begin{array}{l}\text{Pressure forces acting}\\ \text{on the element under}\\ \text{consideration per unit}\\ \text{volume}\end{array}\right\}$$

$$+ \left\{\begin{array}{l}\text{Change in surface forces}\\ \text{per unit time and volume}\\ \text{unit}\end{array}\right\} + \left\{\begin{array}{l}\text{Gravitational force}\\ \text{on the element under}\\ \text{consideration per unit}\\ \text{volume}\end{array}\right\}$$

Considering a incompressible melt, the above equation can be rewritten as follows:

$$\rho\frac{D\,\bar{\mathrm{v}}}{Dt} = -\nabla p - \nabla \bar{\bar{\tau}} + \rho\vec{g}$$

where $\frac{D\,\bar{\mathrm{v}}}{Dt}$ is the substantial derivative of the velocity vector.

Rheological behavior:

For generalized Newtonian fluids:

$$\vec{\vec{\tau}} = 2\,\eta(\dot{\gamma},T)\vec{\vec{D}} \quad \text{with } \vec{\vec{D}} = \frac{1}{2}\left(\nabla\vec{\mathrm{v}} + \nabla\vec{\mathrm{v}}^{\mathrm{T}}\right) \text{ and } \dot{\gamma} = \sqrt{2\,tr\left(\vec{\vec{D}}^{2}\right)}\,.$$

The viscosity law can in general be written as: $\eta(\dot{\gamma},T) = F(\dot{\gamma})\,H(T)$, where $F(\dot{\gamma})$ represents the shear rate dependence of the viscosity ηand $H(T)$ the temperature dependence.

In the simulation used for the PZT/ECG9, the power law has been considered a good approximation of the behavior of the melt:

$$F(\dot{\gamma}) = K\,\dot{\gamma}^{\,n-1}$$

and the Arrhenius law has been taken in consideration for the temperature dependence:

$$H(T) = \exp\left[\alpha\left(\frac{1}{T-T_0} - \frac{1}{T_\alpha - T_0}\right)\right]$$

Energy equation:

The energy equation can be formulated in a similar fashion as the momentum equation:

$$\left\{\begin{array}{l}\text{Change in internal}\\ \text{and kinetic energy}\\ \text{per unit time}\end{array}\right\} = \left\{\begin{array}{l}\text{Increase in internal}\\ \text{and kinetic energy}\\ \text{per unit time}\end{array}\right\} - \left\{\begin{array}{l}\text{Decrease in internal}\\ \text{and kinetic energy}\\ \text{through convection}\\ \text{per unit time}\end{array}\right\}$$

$$+ \left\{\begin{array}{l}\text{Change in internal}\\ \text{energy through}\\ \text{conduction}\\ \text{per unit time}\end{array}\right\} - \left\{\begin{array}{l}\text{Work which the}\\ \text{system carries out}\\ \text{on the environment}\\ \text{per unit time}\end{array}\right\}$$

$$+ \left\{\begin{array}{l}\text{Change in internal}\\ \text{energy due to hear sources}\\ \text{per unit time}\end{array}\right\}$$

where the *internal energy* U is the energy coupled to molecular motions and interactions, thus it depends on local temperature and density of the melt; The *kinetic energy* is the energy directly coupled to the motion of the fluid (thus to the velocity v).

$$\frac{\partial}{\partial t}\left(\rho U + \frac{1}{2}\rho \mathrm{v}^2\right) = -\left(\frac{\partial}{\partial x}\mathrm{v}_x\left(\rho U + \frac{1}{2}\rho \mathrm{v}^2\right) + \frac{\partial}{\partial y}\mathrm{v}_y\left(\rho U + \frac{1}{2}\rho \mathrm{v}^2\right) + \frac{\partial}{\partial z}\mathrm{v}_z\left(\rho U + \frac{1}{2}\rho \mathrm{v}^2\right)\right)$$
$$-\left(\frac{\partial q_x}{\partial x} + \frac{\partial q_y}{\partial y} + \frac{\partial q_z}{\partial z}\right) + \rho\left(\mathrm{v}_x g_x + \mathrm{v}_y g_y + \mathrm{v}_z g_z\right) - \left(\frac{\partial}{\partial x} p\mathrm{v}_x + \frac{\partial}{\partial y} p\mathrm{v}_y + \frac{\partial}{\partial z} p\mathrm{v}_z\right)$$
$$-\left(\frac{\partial}{\partial x}\left(\tau_{xx}\mathrm{v}_x + \tau_{xy}\mathrm{v}_y + \tau_{xz}\mathrm{v}_z\right) + \frac{\partial}{\partial y}\left(\tau_{yx}\mathrm{v}_x + \tau_{yy}\mathrm{v}_y + \tau_{yz}\mathrm{v}_z\right) + \frac{\partial}{\partial z}\left(\tau_{zx}\mathrm{v}_x + \tau_{zy}\mathrm{v}_y + \tau_{zz}\mathrm{v}_z\right)\right) + \phi$$

that can be rewritten as:

$$\frac{\partial}{\partial t}\rho\left(U + \frac{1}{2}\mathrm{v}^2\right) = -\left[\nabla\rho\,\vec{\mathrm{v}}\left(U + \frac{1}{2}\mathrm{v}^2\right)\right] - \nabla\vec{q} + \rho\left(\vec{\mathrm{v}}\cdot\vec{g}\right) - \nabla p\,\vec{\mathrm{v}} - \nabla\left[\vec{\vec{\tau}}\cdot\vec{\mathrm{v}}\right] + \phi$$

where:

$\frac{\partial}{\partial t}\rho\left(U+\frac{1}{2}\mathrm{v}^2\right)$	=	Change in energy per unit time and volume
$-\left[\nabla\rho\,\vec{\mathrm{v}}\left(U+\frac{1}{2}\mathrm{v}^2\right)\right]$	=	Change in energy per unit time and volume through convection
$-\nabla\vec{q}$	=	Change in energy per unit time and volume due to heat conduction
$+\rho(\vec{\mathrm{v}}\cdot\vec{g})$	=	Work per unit time and volume due to gravitational forces
$-\nabla p\,\vec{\mathrm{v}}$	=	Work per unit time and volume due to pressure forces
$-\nabla\left[\vec{\vec{\tau}}\cdot\vec{\mathrm{v}}\right]$	=	Work per unit time and volume due to viscous forces
$+\phi$	=	Change in internal energy due to heat sourced

and $\vec{q}=q_x\vec{i}+q_y\vec{j}+q_z\vec{k}$ is the heat flux vector.

In the case of incompressible flows it is possible to rewrite the above equation:

$$\rho\frac{D}{Dt}\left(U+\frac{1}{2}\mathrm{v}^2\right)=-\nabla\vec{q}+\rho(\vec{\mathrm{v}}\cdot\vec{g})-\nabla p\,\vec{\mathrm{v}}-\nabla\left[\vec{\vec{\tau}}\cdot\vec{\mathrm{v}}\right]+\phi$$

that can be reformulated as:

$$\rho\frac{DU}{Dt}=-\nabla\vec{q}-p(\nabla\vec{\mathrm{v}})-\left(\vec{\vec{\tau}}:\nabla\vec{\mathrm{v}}\right)+\phi$$

where the term:

$$\left(\vec{\vec{\tau}}:\nabla\vec{\mathrm{v}}\right)=\tau_{xx}\frac{\partial\mathrm{v}_x}{\partial x}+\tau_{yy}\frac{\partial\mathrm{v}_y}{\partial y}+\tau_{zz}\frac{\partial\mathrm{v}_z}{\partial z}+\tau_{xy}\left(\frac{\partial\mathrm{v}_x}{\partial y}+\frac{\partial\mathrm{v}_y}{\partial x}\right)+\tau_{yz}\left(\frac{\partial\mathrm{v}_y}{\partial z}+\frac{\partial\mathrm{v}_z}{\partial y}\right)+\tau_{zx}\left(\frac{\partial\mathrm{v}_z}{\partial x}+\frac{\partial\mathrm{v}_x}{\partial z}\right)$$

Considering that at a constant pressure p the internal energy can be expressed as

$dU = c_p dT - p\, dv_p$, where $v_p = \frac{1}{\rho}$ = specific volume, it is possible to write:

$$\rho \frac{DU}{Dt} = \rho\, c_p \frac{DT}{Dt} - \rho\, p \frac{Dv_p}{Dt} = \rho\, c_p \left(\frac{\partial T}{\partial t} + (\vec{\mathrm{v}} \cdot \nabla) T \right) - \rho\, p \left(\frac{\partial \left(1/\rho \right)}{\partial t} + (\vec{\mathrm{v}} \cdot \nabla) v_p \right) =$$

$$= \rho\, c_p \left(\frac{\partial T}{\partial t} + (\vec{\mathrm{v}} \cdot \nabla) T \right) - \rho\, p (\nabla \vec{\mathrm{v}}) v_p = \rho\, c_p \left(\frac{\partial T}{\partial t} + (\vec{\mathrm{v}} \cdot \nabla) T \right) - p (\nabla \vec{\mathrm{v}})$$

for incompressible flows.

The energy equation thus becomes:

$$\rho\, c_p \left(\frac{\partial T}{\partial t} + (\vec{\mathrm{v}} \cdot \nabla) T \right) - p (\nabla \vec{\mathrm{v}}) = -\nabla \vec{q} - p (\nabla \vec{\mathrm{v}}) - \left(\vec{\vec{\tau}} : \nabla \vec{\mathrm{v}} \right) + \phi$$

and with the appropriate simplifications:

$$\rho\, c_p \left(\frac{\partial T}{\partial t} + (\vec{\mathrm{v}} \cdot \nabla) T \right) = -\nabla \vec{q} - \left(\vec{\vec{\tau}} : \nabla \vec{\mathrm{v}} \right) + \phi$$

Degree of freedom

When a thermo fluid simulation is conducted in Polyflow, the degrees of freedom for each node are:

1. Coordinates
2. Velocity
3. Temperature

4. Pressure

In case of a 2D model, therefore there are two components for the node coordinates X and Y, two for the velocity field, one for temperature and one for pressure.

However, in extrusion problems (like the ones modeled during this study) the shape of the extrudate is not known in advance, thus a free surface is used to represent the outer surface of the extrudate. Since the position of a boundary is computed as part of the solution, free-surface problems have additional degrees of freedom (called geometrical degree of freedom) and additional equations, compared with fixed-boundary flow problems. For a free-surface problem, two requirements must be satisfied: the dynamic condition and the kinematic condition.

The dynamic condition imposes that the result of the normal forces is null on the free boundary:

$$f_n = 0$$

The kinematic condition for time-dependent problem, requires that

$$\left(\frac{\partial \vec{x}}{\partial t} - \vec{\mathrm{v}} \right) \bullet \vec{n} = 0$$

where $\vec{x}$ is the position of the node on the free surface. This equation states that a time-dependent free surface must follow trajectories *in the normal direction*; therefore the nodes located on a free surface are Lagrangian in the normal direction. The mixture of a Lagrangian description in the normal direction and an Eulerian description elsewhere is

sometimes referred to as an Arbitrary Lagrangian-Eulerian (ALE) formulation [Polyflow manual].

In the ALE formulation, the computational mesh is treated as a reference frame which may be moving with an arbitrary velocity **w** in the laboratory system (see figure ALE). Depending on the value of w, the following viewpoints may be individuated:

- $\vec{w} = \vec{0}$ the reference frame is fixed in space and this corresponds to the Eulerian viewpoint;
- $\vec{w} = \vec{\mathrm{v}}$ the frame is moving at the same velocity of the particle, thus this corresponds to the Lagrangian viewpoint;
- $\vec{w} \neq \vec{\mathrm{v}} \neq \vec{0}$ the reference frame moves in space at a velocity w. Such a reference frame is called arbitrary Lagrangian-Eulerian and any point of it is identified by its instantaneous position vector ξ_i. In the ALE description a particle is still identified through its material coordinates a_i in the initial configuration of the continuum. However, this identification process is indirect and takes place through the mixed position vector ξ_i which is linked to the material variables a_i by the low of motion of the reference frame: $\xi_i = f_i(a_i, t)$

The ALE description may thus be viewed ad a mapping of the initial configuration of the continuum into the current configuration of the reference frame [17].

With the Arbitrary Lagrangian-Eulerian formulation any law expressed in spatial (Eulerian) variables must be translated into an equivalent law expressed in mixed variables.

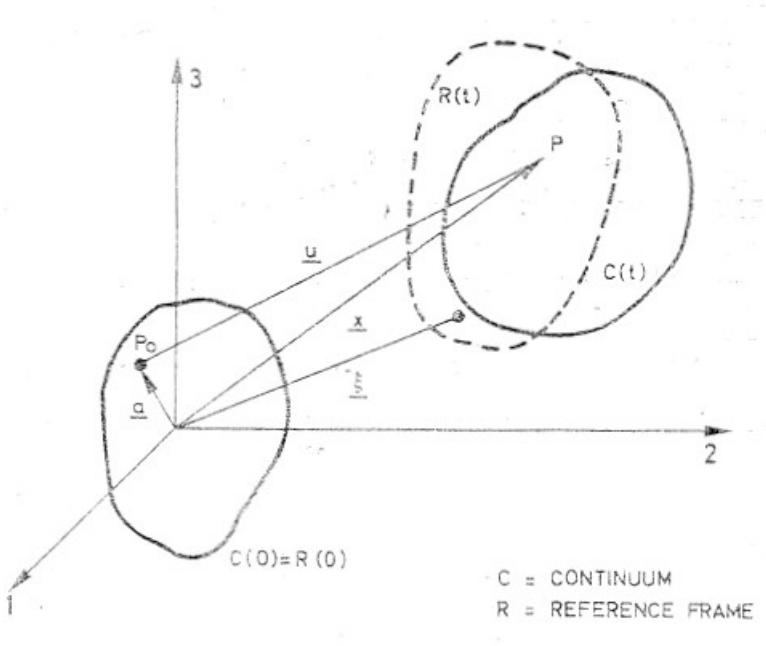

Figure A3.1: Arbitrary Lagrangian-Eulerian formulation

Power law and iterative schemes

The problems considered in this study exhibit highly non –linear characteristics because:

- The viscosity of the material is temperature-dependent, thus causes a non-linearity.

- The flow is generalized Newtonian, thus inertia terms are quadratic in term of the velocity components; also, the viscosity, which depends on the shear-rate, causes non-linearity.
- The flows are non-isothermal, thus heat convection generates terms that are products of velocity components and temperature gradients.

In order to solve the non-linearities, Polyflow normally suggests the use of the Newton-Raphson method. However, in the case of PZT/ECG9, for which the share thinning behavior can be described by the power law with low index n (i.e. n<0.7), the Picard iteration is more suitable. The radius of convergence of this particularly simple method (also known as *successive substitution* or fixed-point iteration) is indeed larger than the one for Newton-Raphson scheme. However its convergence rate is only asymptotically linear, therefore it can be slow [32] and it can require a very large computational time.

Time dependent problems and integration methods

In case of non steady state models, the variables (i.e. degrees of freedom) are functions of the coordinates as well as of the time. Consequently the partial differential equations that govern the problem need to be solved using one of the available numerical integration methods. In order to simplify the computational analysis, the *explicit Euler method* was used during the simulations. This method, which evaluates $\vec{x}_{n+1}$ directly from the known value $\vec{x}$ at the time t_n, does not introduce an additional non-linearity in the problem, thus provides the simplest computational procedure [32]. However, the Euler's

method is conditionally stable: the time step size $\Delta t = t_{n+1} - t_n$ must not exceed a certain value. It is possible to verify that a small value of Δt is also desirable for keeping the truncation error, which is of order Δt, down to a desired level. However, the stability criterion generally limits the time step to a value that is much smaller than that needed for maintaining the accuracy of the solution. Therefore Euler's method constrains the time step and often results in excessive computational time.

Evolution

Non-linearity often makes computations difficult. Non-linear problems frequently have multiple families of solutions. Also, the solution for a given set of parameters cannot generally be extrapolated from an initial, linear solution, since dramatic changes in the nature of the flow can occur with a slight change of flow parameters.

The solution of a non-linear problem is in general surrounded by a domain of convergence. If the initial guess lies within this domain the solution will be reached, but if on the contrary the initial guess is outside, then the iterative procedure will diverge.

In most cases, the only way to solve a non-linear problem is to begin with a solution to a simpler problem, one in which non-linearity is not as troublesome. From this solution, a sequence of problems of increasing non-linearity will be considered, using the solution of one problem as the initial condition for the subsequent problem. Ultimately, the sequence should lead to the original problem and its solution.

If for example the parameter α of the Arrhenius relation is responsible for the non convergence (because of the non –linearity) of the simulation, a sequence of problems

with parameter $\alpha = f(S)$ ($0 \le S \le 1$) could be considered. The sequence begins with $S = 0$ in the case of a direct proportionality characteristic of the function f (if f describes an inverse proportional relation, than the sequence starts with $S = 1$); if a solution is obtained with the parameter having value $f(S)=0$, then S is increased, by a small amount, to $S^i = S + \Delta S$, and a new problem is created with parameter value $f(S^i)$. If a solution is obtained, then the procedure continues incrementing the value of S.

Surface tension

Surface (or interfacial) tension plays an important role in free-surface and moving-interface problems. This section describes the phenomena associated with surface tension, and the equations used to model it in Polyflow [22].

Surface tension force

Consider a curved surface located on the boundary, as shown in Figure A3.1, and let $\bar{n}$ be the outward normal from the surface.

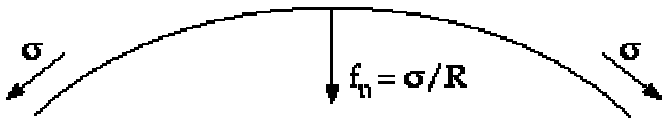

Figure A3.2: Surface tension on a free surface

The surface tension force is a force of amplitude σ, acting *tangent* to the surface, whose net influence (through the vector sum on an elementary surface) is in the normal direction. This normal force (per unit area or length) f_n tends to reduce the surface curvature. The parameter σ is called the surface tension coefficient, and satisfies the following equation:

$$f_n \vec{n} = \frac{\sigma}{R} \vec{n} \tag{A3.1}$$

R is the Gaussian curvature of the surface:

$$\frac{1}{R} = \frac{1}{R_1} + \frac{1}{R_2} \tag{A3.2}$$

where R_1 and R_2 are the two principal radii of curvature (measured in orthogonal directions).

For 2D axisymmetric domains, the surface curvature introduced by the symmetry about the z axis must also be taken into account at the outlet, so that f_n never becomes zero in an axisymmetric geometry when σ is non-zero. In particular, even in the absence of applied external forces, a free jet is subject to a normal surface force given by Equations (A3.1) and (A3.2).

In Polyflow, surface tension forces are introduced on the right-hand side of the momentum equations when a non-zero surface tension coefficient is specified. Introduction of Equation (A3.1) in a finite-element code requires integration by parts (in 2D) in order to use only first-order derivatives of the shape functions that characterize the geometry of the surface.

In 2D, integrating by parts the product of Equation (A3.1) and the velocity shape functions introduces tangential forces at both ends of the free surface. These forces describe the reaction that the ``external world" exerts on the free surface in order to equilibrate the tensile force σ.

It can be shown that, in order to maintain the equilibrium with the tensile force on the free surface, this tangential force f_τ must be defined as

$$f_\tau \vec{\tau} = \sigma \vec{\tau} \tag{A3.3}$$

where $\vec{\tau}$ is the unit vector tangent to the free surface and directed away from the surface (because the surface is in tension, not in compression).

An angle (ϑ) is used to describe the direction of $\vec{\tau}$:

$$\vec{\tau} = \begin{pmatrix} \cos\vartheta \\ \sin\vartheta \end{pmatrix} \tag{A3.4}$$

Positive angles are measured counter-clockwise with respect to a horizontal reference axis. In Figure A3.3, ϑ is a negative angle (e.g., -30^o). This angle allows Polyflow to account for the reaction of the external world on the boundary of the free surface.

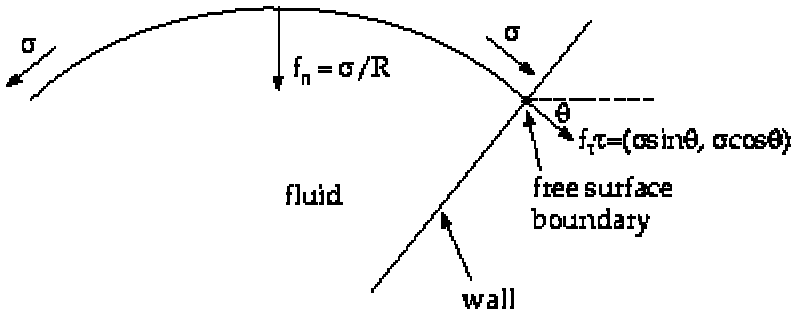

Figure A3.3: Surface tension and traction at the extremities of a free surface

Remeshing Technique (Thompson transformation)

The transformation maps a parent domain into a deformed domain. The transformation begins with the construction of a global coordinate system, defined on a simply-shaped domain. These global coordinates represent a mapping of the irregularly-shaped computational domain into a regular parent domain (such as a square in 2D or a cube in 3D). For example, the irregular domain shown in Figure A3.4 is mapped onto a square by the global-coordinates transformation function $g(\vec{x})$. The coordinates g have the same number of components as the mesh coordinates $\vec{x}$.

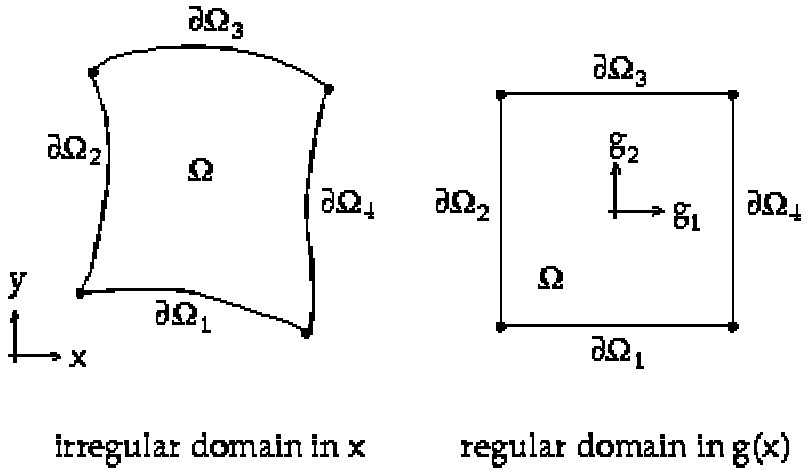

Figure A3.4: Thompson transformation

In the 2D case shown in Figure A3.4 [22] the global coordinates g are constructed on the basis of the following equation:

$$\nabla^2 g(\vec{x}) = 0 \text{ on } \Omega \tag{A3.5}$$

with the following boundary conditions:

$$\begin{aligned} \vec{n}\cdot\nabla g_1 &= 0 \text{ and } & g_2 &= -1 \text{ on } \partial\Omega_1 \\ g_1 &= 0 \text{ and } & \vec{n}\cdot\nabla g_2 &= -1 \text{ on } \partial\Omega_2 \\ \vec{n}\cdot\nabla g_1 &= 0 \text{ and } & g_2 &= -1 \text{ on } \partial\Omega_3 \\ g_1 &= 0 \text{ and } & \vec{n}\cdot\nabla g_2 &= -1 \text{ on } \partial\Omega_4 \end{aligned} \tag{A3.6}$$

The Thompson transformation for this example is simply the inverse mapping $g^{-1}(\vec{x})$. Once $g(\vec{x})$ has been constructed, the Thompson transformation is the solution $\vec{x}$ that satisfies Equation (A3.5) with appropriate boundary conditions. The

calculation of the g field, as well as the Thompson transformation itself, is solved by standard finite-element techniques.

Note that Equation (A3.5) is linear in g, but not in $\vec{x}$. The Thompson transformation is inherently non-linear in $\vec{x}$, even though the Laplacian is a linear operator. The construction of the g field is performed only once at the beginning of the simulation, before the main solver starts. The Thompson transformation is then solved in a coupled fashion, together with the equations governing the flow.

The choice of boundary conditions given to g and $\vec{x}$ in the Thompson transformation governs the remeshing itself. The Thompson transformation is applied to the remeshing subdomain. Each separate sub-boundary of the remeshing subdomain is referred to as a segment. On each segment, one component of the vector g (essential boundary condition) must be specified, while a zero-normal-derivative condition (natural boundary condition) is applied to the other component(s).

VITA

Anna Bellini was born in Bergamo, Italy on 6th January, 1974. She obtained her degree in scientific high school in 1992, with the grade of 52/60.

In September 1992 she enrolled in the Master program in Mechanical Engineering at the Politecnico di Milano, Milan, Italy. In 1996 she was the receiver of a "Programme Européen" scholarship at the prestigious École Polytechnique de Paris, where she attended the last year of "Mechanics of Structures" and "Engineering Sciences and Scientific Computation". In 1998 she worked on a research project about the "Multi-axial fatigue of high-speed trains" in collaboration between the "Laboratoires de Mechanique des Solides" at the École Polytechnique, the "Société Nationale de Chemin de Fer" (SNCF) and the Politecnico di Milano. In 1998, upon the defense of her master thesis "*Methods for the study of the multi-axial fatigue: application to the axle of an high-speed train*" she obtained her master degree in Mechanical Engineering at the Politecnico di Milano with the final grade 100/100 summit cum laude. In 1998 she enrolled in the PhD program in Mechanical Engineering at the University of Illinois at Chicago, where she started developing her research at the Materials Processing Laboratory in collaboration with Dr. Guceri. In the year 2000 she was awarded an Italian scholarship for post-graduate studies in USA. In the same year, she transferred to Drexel University, Philadelphia, at the department of Mechanical Engineering at Mechanics. In 2001 she was the recipient of the Best Poster Award at Drexel University research day. In the academic year 2001/02 she was awarded the George Hill, Jr. Endowell Fellowship for academic achievements.